Mixed and Hybrid Least-Squares FEM in Nonlinear Solid Mechanics

Von der Fakultät für Ingenieurwissenschaften,
Abteilung Bauwissenschaften
der Universität Duisburg-Essen
zur Erlangung des akademischen Grades

Doktor-Ingenieur

genehmigte Dissertation

von

Maximilian Igelbüscher, M.Sc.

Hauptberichter:	Prof. Dr.-Ing. habil. Jörg Schröder
Korreferent:	Prof. Dr. rer. nat. Gerhard Starke

Tag der Einreichung:	16. Februar 2021
Tag der mündlichen Prüfung:	26. August 2021

Fakultät für Ingenieurwissenschaften,
Abteilung Bauwissenschaften
der Universität Duisburg-Essen
Institut für Mechanik
Prof. Dr.-Ing. habil. J. Schröder

Berichte des Instituts für Mechanik, Universität Duisburg-Essen

Nr. 26

Herausgeber:

Prof. Dr.-Ing. habil. J. Schröder

Organisation und Verwaltung:

Prof. Dr.-Ing. habil. J. Schröder
Institut für Mechanik
Fakultät für Ingenieurwissenschaften
Abteilung Bauwissenschaften
Universität Duisburg-Essen
Universitätsstraße 15
45141 Essen
Tel.: 0201 / 183 - 2682
Fax.: 0201 / 183 - 2680

ISBN-13 978-3-9821811-2-7

Vorwort

Die vorliegende Arbeit entstand während meiner Tätigkeit als wissenschaftlicher Mitarbeiter am Institut für Mechanik (Abt. Bauwissenschaften, Fak. Ingenieurwissenschaften) an der Universität Duisburg-Essen im Rahmen der durch die Deutsche Forschungsgemeinschaft (DFG) geförderten Schwerpunktprogramm SPP1748 ("Zuverlässige Simulationstechniken in der Festkörpermechanik - Entwicklung nicht konventioneller Diskretisierungsverfahren, mechanische und mathematische Analyse"). An dieser Stelle möchte ich der DFG für die finanzielle Unterstützung danken und einigen Menschen meinen persönlichen Dank aussprechen, die zum Gelingen dieser Arbeit ihren jeweiligen Anteil beigetragen haben.

An erster Stelle gilt mein Dank meinem geschätzten Doktorvater Prof. Jörg Schröder, der mir die Möglichkeit gab unter seiner Leitung zu promovieren. Für sein intensives fördern und fordern während meiner gesamten Promotionszeit und das mir entgegengebrachte Vertrauen bedanke ich mich sehr. Mein weiterer Dank gilt Prof. Gerhard Starke für die Übernahme des Korreferates und seinen mathematischen Blickpunkt auf die Arbeit sowie für die gute Zusammenarbeit in den gemeinsamen Projekten während meiner Promotionszeit. Ein besonderer Dank gilt Prof. Joachim Bluhm, mit dem ich in gemeinsamen Diskussionen mein Wissen im Bereich der Kontinuumsmechanik und Plastizitt festigen konnte und der sich darüber hinaus immer Zeit für Fragen und Zerstreuung nahm. Für die Begleitung meiner ersten Schritte in der Mechanik und die enge Zusammenarbeit möchte ich Alexander Schwarz und Karl Steeger besonders danken. Die beiden haben mein Interesse an der Mechanik gefördert, meinen Ehrgeiz geweckt und ohne sie hätte ich den Weg der Promotion vielleicht nicht gewagt. Danke sagen möchte ich meinem SPP-Weggefährten Nils Viebahn und Simon Maike für ihre Unterstützung, Ratschläge und intensive Dartrunden. Weiterhin gilt mein Dank Serdar Serdaş und Max Reichel für Zerstreuung Abseits der Mechanik.
Bedanken möchte ich mich auch bei meinen ehemaligen und derzeitigen Kollegen am Institut für Mechanik, Solveigh Averweg, Daniel Balzani, Dominik Brands, Simon Fausten, Markus von Hoegen, Simon Kugai, Matthias Labusch, Veronica Lemke, Petra Lindner-Roullé, Sascha Maassen, Rainer Niekamp, Yasemin Özmen, Mangesh Pise, Sabine Ressel, Mohammad Sarhil, Thomas Schmidt, Carina Schwarz, Steffen Specht, Julia Sunten, Huy Ngoc Thai und Sonja Uebing für die Diskussionen und Atmosphäre am Institut.

Meiner gesamten Familie und Freunden für die Unterstützung in jeglicher Situation, ihre Sicht auf Dinge, offenen Ohren und Ratschläge die mir bei meinen Entscheidungen und Erfolgen sehr geholfen haben. Abschließend danke ich meiner zukünftigen Frau Lisa dafür, dass sie ist wie sie ist und ich sein kann wie ich bin.

Essen, im August 2021 Maximilian Igelbüscher

DOI: 10.17185/duepublico/76121
URN: urn:nbn:de:hbz:465-20220711-084727-3

Abstract

The development of mixed and hybrid finite element formulations with the aim of ensuring reliable, robust and accurate formulations has been an ongoing area of research over the past decades. The present work is intended to contribute to this and deals with the application and analysis of mixed and hybrid formulations for nonlinear material relations. The focus here is on the consideration of mixed stress-displacement formulations and the application for hyperelasticity and plasticity. In particular, the least-squares finite element method (LSFEM) is considered. Among other advantages, the LSFEM results in a minimization problem compared to other mixed methods and thus offers the possibility of direct application of the method in the field of hyperelasticity and finite plasticity without any constraint by stability conditions. For a preliminary investigation of mixed formulations and their fulfillment of plastic material constraints, a Hellinger-Reissner formulation for small deformations is first analyzed. The LSFEM and its challenges are investigated for the small and finite deformation theory and the findings are then considered in the area of finite plasticity. Furthermore, a mixed hybrid finite element formulation based on a hyperelastic least-squares approach is derived and analyzed. For this purpose, continuity requirements are relaxed and enforced by the method of Lagrange multipliers on the inter-element boundaries.

Zusammenfassung

Die Entwicklung von gemischten und hybriden Finite Elemente Formulierungen mit dem Ziel zuverlässige, robuste und genaue Formulierungen zu gewährleisten, stellt in den vergangenen Jahrzehnten einen aktiven Forschungsbereich dar. Die vorliegende Arbeit soll einen Beitrag hierzu liefern und befasst sich mit der Anwendung und Analyse von gemischten und hybriden Formulierungen für nichtlineare Materialzusammenhänge. Der Fokus liegt hierbei auf der Betrachtung von gemischten Spannungs-Verschiebungs Formulierungen und der Anwendung für Hyperelastizität und Plastizität. Insbesondere die Least-Squares Finite Elemente Methode (LSFEM) wird betrachtet. Neben weiteren Vorteilen, resultiert die LSFEM im Vergleich zu anderen gemischten Methoden in einem Minimierungsproblem und bietet somit die Möglichkeit der direkten Überführung der Methode in den Bereich der Hyperelastizität und finiten Plastizität ohne die Einschränkung durch Stabilitätsbedingungen. Für eine Voruntersuchung gemischter Formulierungen und deren Erfüllung der plastischen Materialgleichungen wird zunächst eine Hellinger-Reissner Formulierung für kleine Deformationen analysiert. Die LSFEM und deren Herausforderungen werden sowohl für die Theorie kleiner als auch finiter Deformationen untersucht und die Erkenntnisse anschließend im Bereich der finiten Plastizität berücksichtigt. Des Weiteren erfolgt die Herleitung und Analyse einer gemischten hybriden Finite Elemente Formulierung auf Basis eines hyperelastischen Least-Squares Ansatzes. Hierzu werden Kontinuitätsbedingungen relaxiert und durch die Methode der Lagrangemultiplikatoren auf den Elementkanten eingefordert.

Contents

1 Introduction and outline

Approaches for solving partial differential equations (PDEs) on arbitrary structures are indispensable in today's development and research, e.g., in automotive, aerospace, and industrial products industries, since the equations in these areas are usually no longer analytically solvable. Over the last decades, the finite element method (FEM), among other methods, has proven to be particularly effective and is nowadays included in a large number of simulation tools. First references are given by the pioneering work of Argyris [3], the publication Clough [79] introduce the terminology finite element and the first textbook on finite elements have to be attributed to Zienkiewicz and Cheung [245]. Furthermore, the linear triangular element is introduced in Courant [82] and the six-noded triangle in Fraeijs De Veubeke [101]. The method is characterized by the decomposition of an arbitrary domain into finite subdomains, the so-called finite elements, and based on these simple geometries, the solution of the overall problem can be simulated. In the past decades, great progress has been made in the development of new methods based on the FEM. Nevertheless, the development of the method, also due to the constantly improving computing power, is far from complete and new approaches are constantly being introduced with the aim of developing finite element formulations which provide reliable, robust and accurate solution for all application areas.

Galerkin and mixed Galerkin FEM

For this purpose finite element design is driven by the main goal of improvement of element performance, which is determined by reliability, stability and solution quality as well as accuracy. In Wriggers [236] and Wriggers [237], a general list of requirements is set as criteria for the development of finite elements, which include, e.g., locking free behavior, good solution accuracy for coarse meshes, insensitivity to mesh distortion and simple implementation of nonlinear formulations.

An immense effort has been invested in the development of finite elements based on the variational approach going back to Galerkin [102] over the past decades. In general this approach consider the approximation of one unknown quantity, in solid mechanics given by the displacement field. Such elements are referred as pure displacement elements and are widely used due to their simple implementation. Nevertheless, it has been shown in, e.g., Babuška and Suri [21], pure displacement elements are limited by certain constraints, which can lead to locking behavior and unreliable results in displacement and stress fields.

Due to the mentioned aims in finite element design, a wide range of approaches have been developed to overcome the limitations of the pure displacement elements, considering, e.g., mixed variational principles, reduced integration and stabilization methods, cf. Wriggers [236; 237]. For the mixed variational principles mainly two formulations are applied. The first one is a two-field formulation, with independent displacement and stress approximation for problems in solid mechanics, denoted as the Hellinger-Reissner principle, see Reissner [190] and the early contributions of Hellinger [107] and Prange [183]. A second mixed Galerkin formulation is defined by the Hu-Washizu principle, in terms of displacements, strains and stresses, see the independent contributions of Hu [117] and Washizu [231]. This principle is defined previously in the work of Fraeijs de Veubeke [100], who derived five variational principles based on a four-field approach with respect to displacements, strains, stresses and surface tractions,

cf. Felippa [98] and Braess [50]. An overview of these mixed formulations can be found in Auricchio et al. [17], Wriggers [236] and Braess [50], among others.
The major challenge in the application of these mixed formulations is the choice of appropriate finite element solution spaces and their proper balancing, since they result into matrices with saddle point structures. As a consequence, in general the existence and uniqueness of solutions cannot be guaranteed. In order to ensure these stability requirements for mixed formulations, the so-called LBB-condition or inf-sup condition have to be fulfilled, which is defined independently by Ladyzhenskaya [144], Babuška [20] and Brezzi [55]. For a detailed discussion on the existence and uniqueness of solutions, see, e.g., Boffi et al. [49], Auricchio et al. [17], Brezzi and Fortin [56], Brenner and Scott [53] and Braess [50]. The Hellinger-Reissner formulation can be subdivided in a primal ($\boldsymbol{u} \in \mathcal{H}^1, \boldsymbol{\sigma} \in \mathcal{L}^2$) and dual formulation ($\boldsymbol{u} \in \mathcal{L}^2, \boldsymbol{\sigma} \in \mathcal{H}(\mathrm{div})$), cf. Braess [50]. For the primal formulation stable combinations are presented in Yu et al. [243], Li et al. [151], Braess [50] and for the dual formulation see Arnold et al. [9; 11; 13] and Johnson and Mercier [127]. Further mathematical aspects of the Hellinger-Reissner principle for elasticity can be found in Arnold and Winther [6], Auricchio et al. [17], Lonsing and Verfürth [153], Arnold et al. [9], Boffi et al. [48] and Cockburn et al. [80]. One nowadays well established stress approximation for the primal Hellinger-Reissner principle is presented in Pian and Sumihara [178] and extended to $d = 3$ in Pian and Tong [179]. This discontinuous stress approximation is known to be remarkable insensitive to mesh distortion, locking free for plane strain quasi-incompressible elasticity and yield superconvergent results for bending dominated problems, see Pian and Sumihara [178], Simo et al. [218], Chun et al. [75], Wriggers and Korelc [238] and Schröder et al. [200]. A dual Hellinger-Reissner formulation is discussed in, e.g., Klaas et al. [132] and Schröder et al. [198] using $\mathcal{BDM}$ elements for the stress approximation, see Brezzi et al. [57]. The inf-sup stability of the Hu-Washizu formulation is presented in Braess [50]. Further, finite element developments are based on the Hu-Washizu principle as, e.g., for the framework of the enhanced assumed strain method, cf. Simo and Rifai [216], Andelfinger and Ramm [2], Yeo and Lee [242] and Bischoff et al. [37].
The fulfillment of the stability conditions is often not easy to accomplish and not always possible in an analytical manner, especially for formulations within the field of finite deformations. In order to provide at least a numerical estimate for the conditions, a numerical inf-sup test is presented in Chapelle and Bathe [73] and Bathe [24; 25]. Furthermore, numerical estimates for stability requirements are defined by the count criterion in Zienkiewicz et al. [249; 250].

Least-squares finite element method

Another mixed finite element method is given by the least-squares finite element method (LSFEM). A detailed introduction to the theoretical foundations and discussion on the least-squares finite element method is given in the monographs Eason [92], Jiang [125], Kayser-Herold and Matthies [129] and Bochev and Gunzburger [43].
The method is particularly popular in the field of fluid mechanics based on the inherent advantageous properties of the method, see, e.g., Jiang [125] and Bochev and Gunzburger [43]. These are, inter alia, given by a uniform mathematical procedure applicable for basically all types of PDEs. Furthermore, the resulting system

matrices are symmetric and positive definite and the constructed least-squares (LS) functional can be used as an a posteriori error estimator, which can be applied for adaptive refinement strategies, without additional computational costs, see Berndt et al. [31], Cai and Starke [61] and Bochev and Gunzburger [43], among others. In contrast to mixed Galerkin formulations, the LS formulation results in a minimization problem and is thus not restricted by the LBB-condition and lead to a flexibility in the choice of polynomial order of the finite element approximation. Furthermore, the LS formulation can be applied to non-self-adjoint operators. This is a great advantage compared to the standard Galerkin formulation, especially in fluid mechanics or in transport problems in general, since convection operators are non-self-adjoint operators and result in asymmetric matrices, which in consequence can lead to oscillations and instabilities of the solution for the Galerkin method, cf. Jiang [125], Kayser-Herold and Matthies [129] and Quarteroni and Valli [186]. On the other hand, there are also disadvantages as the weak performance for low order elements and the crucial influence of the solution accuracy on the associated weighting parameters within the formulation, see, e.g., Deang and Gunzburger [89], Pontaza [182] and Schwarz et al. [205]. There are several approaches for weightings, e.g., weighting to obtain norm equivalence proposed by Bochev and Gunzburger [43], Bochev [38], local error weighting by Jiang [124; 125], physical motivated weighting, see Bell and Surana [26; 27], Heys et al. [109] and matrix weighting as proposed in Salonen and Freund [195] and Kayser-Herold [128].

First appearance of the least-squares method (LSM) in correlation with finite element applications and their mathematical analysis are given by Lynn and Arya [155; 156], Zienkiewicz et al. [248], Jespersen [123], Fix et al. [99] and an overview on early developments of LS is given by Eason [92]. A general theory for the LSM for elliptic systems is proposed by Aziz et al. [19] in order to obtain a priori estimates for elliptic systems and to prove optimal convergence rates. Over the past decades, the LSFEM has become a frequently used method, see, e.g., Kayser-Herold and Matthies [129] for an extensive literature review on the development of the method.

The method was first applied for fluid mechanic problems for the Stokes equations in the interrelated works of Jiang and Chang [126] and Chang and Jiang [71]. In the following years, a wide range of work was done using the LSFEM for the Stokes and Navier-Stokes equations with different approaches for the first-order systems. The LSM in terms of a velocity-vorticity-pressure formulation is discussed for the Stokes equations in, e.g., Jiang and Chang [126], Bochev and Gunzburger [40; 41], Bochev [39] and Cai et al. [63], among others. Furthermore, the Navier-Stokes equations are analyzed in a system of first-order which depends on a velocity-pressure-vorticity-temperature-heat-flux system in Tang and Tsang [226] and a velocity-pressure-stress system is presented for Stokes equations in Bochev and Gunzburger [42]. Furthermore, a p-version least-squares approach is investigated in Bell and Surana [26; 27] and Winterscheidt and Surana [234], e.g., for incompressible, non-Newtonian isothermal and non-isothermal fluid flow. The working group led by Prof. Cai, Prof. Manteuffel and Prof. McCormick defined the term first-order system least-squares (FOSLS) in their contributions, see, e.g., Cai et al. [63; 64; 65; 66; 67], Kim et al. [130], Manteuffel et al. [158]. In Cai et al. [64] linear elasticity is considered for a displacement gradient and pressure formulation and further analyzed in Cai et al. [65] with respect to two-stage algorithms, which solve the displacement gradients in a first step

and in a second step the displacements. This approach is further extended and investigated for various boundary value problems in the related publications Cai et al. [66; 67] for multigrid solution methods. The considered field quantities in the latter mentioned publications are mainly approximated in $\mathcal{H}^1$. Furthermore, the LSFEM is applied for linear and nonlinear first-order hyperbolic PDEs in Bochev and Choi [46; 47] and De Sterck et al. [87; 88].

First applications of stress-displacement based LS formulations are introduced for linear elasticity in Cai and Starke [60; 61] and Cai et al. [69]. Therein, the stress approximation is performed with $\mathcal{H}(\mathrm{div})$-conforming Raviart-Thomas functions, see Raviart and Thomas [189]. In Schwarz et al. [205] and Starke et al. [221] a modified LS formulation, characterized by introducing the antisymmetric displacement gradient in the test space, is shown to improve especially the low order element performance. The extended LS formulation, in terms of a mathematically redundant additional stress symmetry conditions, in Cai and Starke [60; 61] is further investigated in Schwarz et al. [207] for static and dynamic problems and in Igelbüscher et al. [120] with an explicit consideration of the balance of angular momentum for the recalculation of reaction forces. Furthermore, the LSFEM for geometrically nonlinear solid mechanics is presented in, e.g., Manteuffel et al. [158] for a St. Venant-Kirchhoff material law and for a Neo-Hookean material law from a more engineering perspective in the publications of Schwarz et al. [206; 208] and Schröder et al. [199] and in Starke et al. [222], Müller et al. [167], Müller [165], Müller and Starke [166] from a mathematical point of view. The work of Schröder et al. [199] gives an overview of small and finite elastic deformations for isotropic and anisotropic material behavior.

The proposed $\mathcal{H}^1 \times \mathcal{H}(\mathrm{div})$ least-squares formulation in Cai and Starke [60; 61] is further investigated by Starke [219; 220] for small strain elasto-plasticity with adaptive mesh refinement in terms of the LS functional as an a posteriori error estimator, where a generalized Gauss-Newton method is applied. In Kwon et al. [143] a meshfree LS approach for elasto-plasticity is discussed and Schwarz et al. [204] proposed a rate-dependent viscoplastic LS formulation. The straightforward utilization of the LSFEM for rate-independent plasticity is shown to lead to drawbacks within the application of the standard Newton-Raphson method, see Kubitz [142] and Schwarz [203] for the case of small strain plasticity and Igelbüscher et al. [119; 121] for finite J_2-plasticity. A possibility to overcome this is introduced in Kubitz [142] by a damped Newton method and in Schwarz [203] and Igelbüscher et al. [119; 121] a modified first variation is applied in order to guarantee a continuous first variation, which is related to the approach in Schwarz et al. [205] and Starke et al. [221].

There is a wide range of further ideas in order to improve the LSFEM for particular cases as, e.g., a formulation introducing a basis of singular functions with local support around singular points is suggested in Berndt et al. [32; 33] for elliptic problems with discontinuous coefficients. Furthermore, weighted norms LSFEM for problems with singularities in order to guarantee optimal converge are proposed in Manteuffel et al. [157], Lee et al. [146; 147], Cai and Westphal [62], which requires knowledge of the arising singularity in the problem, whereas in Hayburst et al. [106] the norms are weighted based on a coarse-scale approximation.

In Bensow and Larson [28; 29] LS formulations are proposed with discontinuous approximation of unknown fields, in which the boundary conditions as well as tangential

and normal continuity is weakly enforced within the LS functional. This is similar to the relaxation of regularity requirements, by replacing the standard $\mathcal{L}^2$ norms by dual space norms as suggested in Bramble et al. [51], Cai et al. [68]. Furthermore, it can be seen to be related to the approaches in discontinuous Galerkin (DG) and discontinuous Petrov-Galerkin (DPG) methods, see Demkowicz and Gopalakrishnan [90]. Therein, jump conditions on the element boundaries, in terms of additional degrees of freedom, enforce the relaxed continuity requirements in the trial and test spaces, see Arnold et al. [12].

Hybrid mixed finite elements

The latter idea represent a further approach in the field of mixed FEM which can be denoted by hybrid FEM. First references for hybrid methods in the engineering community are going back to Pian [176] and Fraeijs De Veubeke [101]. In solid mechanics conforming finite element formulations have to fulfill certain continuity requirements at inter-element boundaries, i.e., normal continuity of the stress field and continuity of the displacements. Throughout this thesis, hybrid FEM is characterized by the simultaneous approximation of at least one field defined on element level and a Lagrange multiplier defined on the union of the boundaries of the elements, cf. Roberts and Thomas [192] and Carey and Oden [70]. This means that the relaxed continuity requirements are enforcement on the inter-element boundaries through Lagrange multipliers, since no continuity is given related to a discontinuous approximation of unknown fields on element level, see Atluri et al. [15; 16], Carey and Oden [70], Roberts and Thomas [192] and Brezzi and Fortin [56]. The idea of mixed hybrid FEM is further discussed for hybrid stress elements in Pian and Chen [177], Punch and Atluri [185] and Xue and Atluri [239] and the existence and stability of general mixed hybrid elements is analyzed in Xue and Atluri [240]. As previously mentioned, a similar approach can be obtained by directly adding the constraint condition to a LS formulation with respect to appropriate norms and rewrite these into equivalent norms in order to achieve a formulation based on the classical $\mathcal{L}^2$ norm, see Bochev and Gunzburger [43]. An approach with an enriched discrete space by discontinuous elements in the vicinity of singularities is studied for the first-order Poisson problem by Bensow and Larson [28] and in Bensow and Larson [29] a discontinuous LS formulation is investigated for the div-curl problem on non-convex domains. In Ye and Zhang [241] a discontinuous LS formulation for general polytopal meshes is introduced and rigorous error analysis is provided. Furthermore, in Igelbüscher and Schröder [118] and Schröder and Igelbüscher [197] a hybrid mixed formulation is derived for linear elasticity based on a least-squares finite element approach. This approach yields physically correct stress distributions for problems with material interfaces by applying a stress approximation with $\boldsymbol{\sigma} \in \mathcal{L}^2$ on each element.

Note that, the term hybrid is widely used for different approaches in the theory of finite elements, e.g., Liu et al. [152] introduce a hybrid LS formulation, where the term hybrid emphasize the fact that two first-order system least-squares formulation are combined by an additional intermediate term, retaining the properties of both formulations.

Outline

The main objective of this work is the application and analyses of mixed and hybrid finite element formulations for material nonlinearities. For this aim mainly the least-squares finite element method is considered as a discretization approach, inter alia, for nonlinear elasticity and finite J_2-plasticity. Therefore, a previous discussion on the enforcement of plastic constraints with respect to mixed formulations is presented in terms of the mixed Hellinger-Reissner principle. Beside this, a hybrid mixed formulation is derived based on a least-squares approach at finite elasticity.
In summary, the present work is structured as follows.

In **Chapter 2** the essential fields of continuum mechanics as the motion and deformation of bodies is presented in terms of the kinematics, the stress concept in a continuum and the fundamental balance principles. Furthermore, the concept of material modeling and the different material descriptions, as finite elasticity and the derivation of plastic material constraints are considered.

As an introduction to the finite element method, the underlying ideas and fundamentals are briefly introduced in **Chapter 3**. In addition, the basic mathematical relations used in this work are defined. In order to classify the methods used, they are briefly explained and their relationship is shown by means of the principle of weighted residuals. The finite element approaches used are presented and a brief explanation of implementation aspects is given.

In order to clarify basic properties of mixed methods, **Chapter 4** first introduces the methods using the theory of small deformations. For this purpose, challenges of LSFEM are discussed and first conclusions for the further analyses are drawn. The enforcement of plastic constraints is presented using a primal mixed Hellinger-Reissner method for small strain J_2-plasticity.

The obtained findings serve as a basis for the extension to finite deformations in **Chapter 5**. For this purpose, the LSFEM is first presented for hyperelastic materials in the two-dimensional case, considering different approaches to improve the accuracy of the solutions and convergence properties by extended functionals and modified first variations. Based on this, a mixed LS formulation for finite plasticity is derived, where the modification of the weak form is essential for the solvability of the method.

In **Chapter 6** the derivation of a hybrid mixed finite element method in terms of a LS approach is presented. For this, discontinuous stress and displacement approaches are introduced, where the essential continuity conditions are enforced via Lagrange multipliers on the element boundaries. The resulting elements allow the application of non-conformal stress approximations at element level for the consideration of problems with material interfaces.

Chapter 7 concludes the present work with a summary of the achieved findings. Furthermore, an outlook is given for future work with respect to the considered fields.

2 Foundations of continuum mechanics

The method of continuum mechanics states the foundation for the description of physical phenomena in solids and fluids. This approach is based on the assumption of a continuum characterized by corresponding physical quantities such as density and temperature. The real molecular structure is replaced and the occurring quantities are only assumed as averaged values, which does not reflect every detail of the structure, but is useful for calculation and application in the engineering field. The essential fields of continuum mechanics are the motion and deformation of bodies, i.e., kinematics, the concept of stresses in the continuum and the mathematical description of the fundamental physical laws denoted as balance principles. The continuum mechanical relations are only given in a short summary for the discussed topic of this work, more detailed descriptions can be found in, e.g., Truesdell and Noll [229], Eringen [93], Noll [173], Marsden and Hughes [159], Ogden [174] and Holzapfel [116].

2.1 Kinematics

A physical body $\mathcal{B}$ with the related surface $\partial\mathcal{B}$ is described as an accumulation of material points or particles in the three-dimensional Euclidean space $\mathbb{R}^3$. For the interpretation of deformations, at least two different states of the body are considered. A reference (undeformed) configuration $\mathcal{B}_0 \subset \mathbb{R}^3$ at time t_0 is stated as material configuration and parameterized in $\boldsymbol{X}$ and a current (deformed) configuration $\mathcal{B}_t \subset \mathbb{R}^3$ at time $t > t_0$ describes the spatial configuration, parameterized in $\boldsymbol{x}$, see Figure 2.1.

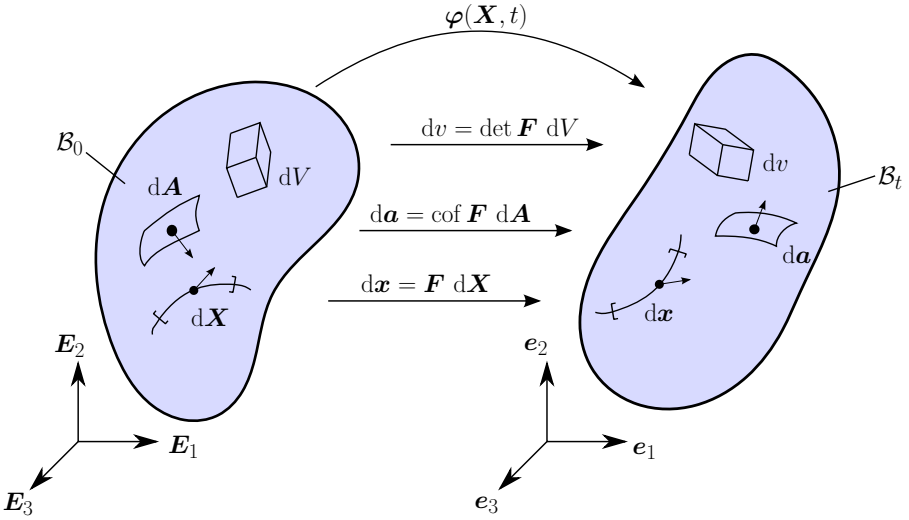

Figure 2.1: Motion of a body in Euclidean space with right-handed orthogonal, cartesian basis system $\boldsymbol{E}_A$ and $\boldsymbol{e}_a$

The transformation of the body from $\mathcal{B}_0$ at t_0 to $\mathcal{B}_t$ at $t > t_0$ is described by a continuous, nonlinear and unique (one-to-one) mapping $\boldsymbol{\varphi}(\boldsymbol{X}, t)$, i.e.,

$$\boldsymbol{\varphi}(\boldsymbol{X}, t) : \mathcal{B}_0 \to \mathcal{B}_t \,. \tag{2.1}$$

This mapping describes a bijective transformation, i.e., every material point $\boldsymbol{X} = X^A\, \boldsymbol{E}_A$ for $A = 1, 2, 3$ on the body $\mathcal{B}_0$ is transferred into exactly one point $\boldsymbol{x} = x^a\, \boldsymbol{e}_a$ with $a = 1, 2, 3$ on the body $\mathcal{B}_t$ at fixed time t, i.e., $\boldsymbol{\varphi} : \boldsymbol{X} \mapsto \boldsymbol{x}$. Since $\boldsymbol{\varphi}$ is assumed to be

uniquely invertible, the description of $\boldsymbol{x}$ and $\boldsymbol{X}$ in terms of $\boldsymbol{\varphi}$ is given by

$$\boldsymbol{x} = \boldsymbol{\varphi}(\boldsymbol{X}, t) \quad \text{and} \quad \boldsymbol{X} = \boldsymbol{\varphi}^{-1}(\boldsymbol{x}, t)\,. \tag{2.2}$$

The difference between the reference $\boldsymbol{X}$ and the actual position vector $\boldsymbol{x}$ is denoted by the displacement vector $\boldsymbol{u}$ and defined as

$$\boldsymbol{u} = \boldsymbol{x} - \boldsymbol{X}\,, \quad \text{thus} \quad \boldsymbol{x} = \boldsymbol{X} + \boldsymbol{u}\,. \tag{2.3}$$

A fundamental kinematic quantity is the deformation gradient given as the gradient of the deformation map $\boldsymbol{\varphi}(\boldsymbol{X}, t)$ and defined by

$$\boldsymbol{F} = \frac{\partial \boldsymbol{\varphi}(\boldsymbol{X}, t)}{\partial \boldsymbol{X}} = \frac{\partial \boldsymbol{x}}{\partial \boldsymbol{X}} = \operatorname{Grad} \boldsymbol{x} = \nabla_X \boldsymbol{x} \quad \text{and} \quad \boldsymbol{F} = \frac{\partial x^a}{\partial X^A}\, \boldsymbol{e}_a \otimes \boldsymbol{E}^A = F^a{}_A\, \boldsymbol{e}_a \otimes \boldsymbol{E}^A\,, \tag{2.4}$$

where $\operatorname{Grad} \boldsymbol{\Upsilon} = \nabla_X \boldsymbol{\Upsilon}$ is introduced as the gradient operator with respect to the reference coordinates $\boldsymbol{X}$ for a second order tensor $\boldsymbol{\Upsilon} \in \mathbb{R}^{n \times n}$. Obviously, the deformation gradient is a two-field tensor with one basis in each configuration, cf. (2.4), and in general not symmetric. Considering Equation $(2.3)_2$ gives a relation for the displacement gradient with respect to the reference placement and the displacement field as

$$\boldsymbol{F} = \nabla_X \boldsymbol{x} = \nabla_X (\boldsymbol{X} + \boldsymbol{u}) = \boldsymbol{1} + \nabla_X \boldsymbol{u}\,, \tag{2.5}$$

in terms of the second order identity tensor $\boldsymbol{1}$. The deformation gradient is a linear transformation map of infinitesimal line elements $\mathrm{d}\boldsymbol{X}$ in the reference configuration to $\mathrm{d}\boldsymbol{x}$ in the current configuration, i.e.,

$$\mathrm{d}\boldsymbol{x} = \boldsymbol{F} \cdot \mathrm{d}\boldsymbol{X} \quad \text{and} \quad \mathrm{d}\boldsymbol{X} = \boldsymbol{F}^{-1} \cdot \mathrm{d}\boldsymbol{x}\,. \tag{2.6}$$

For a unique (one-to-one) transformation map, the existence of $\boldsymbol{\varphi}^{-1}$ has to be ensured. Therefore, the existence of $\boldsymbol{F}^{-1}$ has to be guaranteed, which is done by the necessary and sufficient condition that a non-zero determinant of the deformation gradient $\boldsymbol{F}$ exists, denoted as the Jacobian determinant $J = \det \boldsymbol{F} \neq 0$. The Jacobian determinant describes the volume ratio, which is shown later on. Assuming that volume elements cannot have negative volumes and thus self penetration during motion is omitted leads to $J > 0$. Furthermore, the inverse deformation gradient is defined by

$$\boldsymbol{F}^{-1} = \frac{\partial \boldsymbol{X}}{\partial \boldsymbol{x}} = \nabla_x \boldsymbol{X} = \frac{\partial \boldsymbol{x}}{\partial \boldsymbol{x}} - \frac{\partial \boldsymbol{u}}{\partial \boldsymbol{x}} = \boldsymbol{1} - \operatorname{grad} \boldsymbol{u} = \boldsymbol{1} - \nabla_x \boldsymbol{u}\,, \tag{2.7}$$

where $\operatorname{grad}(\bullet) = \nabla_x(\bullet)$ denotes the gradient operator with respect to the current placement $\boldsymbol{x}$. The mappings of area and volume elements from the reference into the current configuration are defined by

$$\mathrm{d}\boldsymbol{a} = \operatorname{cof} \boldsymbol{F} \cdot \mathrm{d}\boldsymbol{A} = J \boldsymbol{F}^{-T} \cdot \mathrm{d}\boldsymbol{A} \quad \text{and} \quad \mathrm{d}v = J\, \mathrm{d}V\,, \tag{2.8}$$

with $\operatorname{cof} \boldsymbol{F} = \det[\boldsymbol{F}] \boldsymbol{F}^{-T}$ as the definition of the cofactor of $\boldsymbol{F}$ and $\mathrm{d}\boldsymbol{A} = \boldsymbol{N}\, \mathrm{d}A$ and $\mathrm{d}\boldsymbol{a} = \boldsymbol{n}\, \mathrm{d}a$ as the area elements in reference and current placement ($\mathrm{d}\boldsymbol{A} = \mathrm{d}\boldsymbol{X}_1 \times \mathrm{d}\boldsymbol{X}_2$). $\boldsymbol{N}$ and $\boldsymbol{n}$ are the corresponding outward unit normal vectors on the cutting plane of reference and current configuration. Furthermore, the volume elements are defined by a scalar triple product of the line elements $\mathrm{d}\boldsymbol{X}$ with $\mathrm{d}V = (\mathrm{d}\boldsymbol{X}_1 \times \mathrm{d}\boldsymbol{X}_2) \cdot \mathrm{d}\boldsymbol{X}_3$ and

analogously for the current configuration.
The deformation gradient $\boldsymbol{F}$ describes the total deformation of a body consisting of rigid body translations and rotations. Thus, it is not a suitable quantity for the measurement of strains. $\boldsymbol{F}$ can be multiplicative decomposed into

$$\boldsymbol{F} = \boldsymbol{R} \cdot \boldsymbol{U} = \boldsymbol{V} \cdot \boldsymbol{R}\,, \tag{2.9}$$

where rigid body rotations are described by the orthogonal rotation tensor $\boldsymbol{R}$, $\boldsymbol{U}$ and $\boldsymbol{V}$ are the right (material) and left (spatial) stretch tensor, which are symmetric and positive definite, i.e., $\det \boldsymbol{U} > 0$, $\det \boldsymbol{V} > 0$ and consequently $\det \boldsymbol{R} > 0$. A spectral decomposition exemplified the physical meaning of the relations as

$$\boldsymbol{U} = \sum_{i=1}^{3} \lambda_i \, \boldsymbol{N}_i \otimes \boldsymbol{N}_i\,, \quad \boldsymbol{V} = \sum_{i=1}^{3} \lambda_i \, \boldsymbol{n}_i \otimes \boldsymbol{n}_i \quad \text{and} \quad \boldsymbol{R} = \sum_{i=1}^{3} \boldsymbol{n}_i \otimes \boldsymbol{N}_i\,, \tag{2.10}$$

where λ_i, $i = 1, 2, 3$ denote the principal stretches or eigenvalues of the left and right stretch tensor and the eigenvectors in the reference and actual configurations are given by $\boldsymbol{N}_i$ and $\boldsymbol{n}_i$. The decomposition of $\boldsymbol{F}$ reveals that it is inadmissible as a strain measure, since it includes rotations which, in the case of an applied rigid body motion, would lead to unreasonable strain measures in the body. Suitable strain measures are given by the right (material) and left (spatial) Cauchy-Green deformation tensor, i.e.,

$$\begin{aligned} \boldsymbol{C} &= \boldsymbol{F}^T \cdot \boldsymbol{F} = \boldsymbol{U}^T \cdot \boldsymbol{R}^T \cdot \boldsymbol{R} \cdot \boldsymbol{U} = \boldsymbol{U}^T \cdot \boldsymbol{U} \quad \text{and} \quad \boldsymbol{C} = F^a{}_A \, \delta_{ab} \, F^b{}_B \, \boldsymbol{E}^A \otimes \boldsymbol{E}^B\,, \\ \boldsymbol{B} &= \boldsymbol{F} \cdot \boldsymbol{F}^T = \boldsymbol{V} \cdot \boldsymbol{R} \cdot \boldsymbol{R}^T \cdot \boldsymbol{V}^T = \boldsymbol{V} \cdot \boldsymbol{V}^T \quad \text{and} \quad \boldsymbol{B} = F^a{}_A \, \delta^{AB} \, F^b{}_B \, \boldsymbol{e}_a \otimes \boldsymbol{e}_b\,. \end{aligned} \tag{2.11}$$

Both, $\boldsymbol{C}$ and $\boldsymbol{B}$, are rotationally independent and only depend on the stretch of the body. Based on (2.10) and (2.11), $\boldsymbol{C}$ is defined in the reference and $\boldsymbol{B}$ in the current configuration. For completeness, the Green-Lagrange strain tensor $\boldsymbol{E}$ is defined by

$$\boldsymbol{E} = \frac{1}{2}(\boldsymbol{C} - \boldsymbol{1}) = \frac{1}{2}(\boldsymbol{F}^T \cdot \boldsymbol{F} - \boldsymbol{1}) \quad \text{and} \quad \boldsymbol{E} = \frac{1}{2}(F^a{}_A \, \delta_{ab} \, F^b{}_B - \delta_{AB}) \, \boldsymbol{E}^A \otimes \boldsymbol{E}^B\,, \tag{2.12}$$

as a symmetric tensor in the reference configuration and describes the difference of squared distances, i.e., $\mathrm{d}s^2 - \mathrm{d}S^2$ with $\mathrm{d}s = |\mathrm{d}\boldsymbol{x}|$ and $\mathrm{d}S = |\mathrm{d}\boldsymbol{X}|$.

As a fundamental of time-dependent deformation processes, material time derivatives are introduced. For this, the material time derivative of the deformation gradient is considered as a basic kinematic quantity, which is defined as the material velocity gradient, i.e.,

$$\dot{\boldsymbol{F}} = \frac{D}{Dt}\Big(\frac{\partial \boldsymbol{x}}{\partial \boldsymbol{X}}\Big) = \frac{\partial \dot{\boldsymbol{x}}}{\partial \boldsymbol{X}} = \nabla_X \dot{\boldsymbol{x}} = \frac{\partial \dot{\boldsymbol{x}}}{\partial \boldsymbol{x}} \frac{\partial \boldsymbol{x}}{\partial \boldsymbol{X}} = \boldsymbol{L} \cdot \boldsymbol{F} \quad \text{with the velocity} \quad \dot{\boldsymbol{x}} = \frac{D\boldsymbol{x}}{Dt}\,, \tag{2.13}$$

where $\boldsymbol{L}$ denotes the spatial velocity gradient given as

$$\boldsymbol{L} := \nabla_x \dot{\boldsymbol{x}} = \frac{\partial \dot{\boldsymbol{x}}}{\partial \boldsymbol{x}} = \frac{\partial \dot{\boldsymbol{x}}}{\partial \boldsymbol{X}} \cdot \frac{\partial \boldsymbol{X}}{\partial \boldsymbol{x}} = \dot{\boldsymbol{F}} \cdot \boldsymbol{F}^{-1}\,. \tag{2.14}$$

An additive decomposition of $\boldsymbol{L} = \boldsymbol{D} + \boldsymbol{W}$ into the symmetric rate of deformation tensor $\boldsymbol{D}$ and a skew-symmetric spin tensor $\boldsymbol{W}$ yields

$$\boldsymbol{D} = \boldsymbol{L}^{\mathrm{sym}} = \frac{1}{2}(\boldsymbol{L} + \boldsymbol{L}^T) = \boldsymbol{D}^T \quad \text{and} \quad \boldsymbol{W} = \boldsymbol{L}^{\mathrm{skew}} = \frac{1}{2}(\boldsymbol{L} - \boldsymbol{L}^T) = -\boldsymbol{W}^T\,. \tag{2.15}$$

Furthermore, the material time derivative of the Jacobi determinant is obtain by

$$\dot{J} = \frac{\partial}{\partial t} \det \boldsymbol{F} = \frac{\partial \det \boldsymbol{F}}{\partial \boldsymbol{F}} : \frac{\partial \boldsymbol{F}}{\partial t} = J \boldsymbol{F}^{-T} : \dot{\boldsymbol{F}} = J \operatorname{tr} \boldsymbol{L} = J \operatorname{div} \dot{\boldsymbol{x}} \,, \tag{2.16}$$

with the divergence operator $\operatorname{div} \boldsymbol{\Upsilon} = \nabla \cdot \boldsymbol{\Upsilon}$ defined with respect to $\boldsymbol{x}$ and the trace operator $\operatorname{tr}(\boldsymbol{\Upsilon}) = (\boldsymbol{\Upsilon}) : \boldsymbol{1}$ for a second order tensor $\boldsymbol{\Upsilon} \in \mathbb{R}^{n \times n}$.

2.2 Concept of stresses

Deformation processes of a body $\mathcal{B}_t$ caused by internal and external influences, such as, e.g., body forces or external mechanical loads, lead to inner forces and stresses. A visualization of these stresses can be presented by an imaginary cutting plane, separating the body $\mathcal{B}_t$ into two parts. The force acting on a surface element on the cutting plane is denoted by $\mathrm{d}\boldsymbol{f}$ and is calculated by

$$\mathrm{d}\boldsymbol{f} = \boldsymbol{t} \, \mathrm{d}a = \boldsymbol{t}_0 \, \mathrm{d}A \,. \tag{2.17}$$

Here, the Cauchy traction vector $\boldsymbol{t}(\boldsymbol{x}, t, \boldsymbol{n})$ defined by force measured per unit surface area $\mathrm{d}a$ defined in the current configuration is a function of position $\boldsymbol{x}$, time t and the outward unit normal vector $\boldsymbol{n}$ acting on the cutting plane. Analogously, the traction vector $t_0(\boldsymbol{X}, t_0, \boldsymbol{N})$ depends on the reference position $\boldsymbol{X}$, time t_0 and the outward unit normal on the reference configuration $\boldsymbol{N}$. The Cauchy stress theorem postulates the existence of a stress tensor with the linear relation

$$\boldsymbol{t}(\boldsymbol{x}, t, \boldsymbol{n}) = \boldsymbol{\sigma}(\boldsymbol{x}, t) \cdot \boldsymbol{n} \quad \text{and equivalently} \quad \boldsymbol{t}_0(\boldsymbol{X}, t_0, \boldsymbol{N}) = \boldsymbol{P}(\boldsymbol{X}, t_0) \cdot \boldsymbol{N} \,, \tag{2.18}$$

with $\boldsymbol{\sigma}$ as the Cauchy stress tensor and $\boldsymbol{P}$ as the first Piola-Kirchhoff stress tensor. The relation between $\boldsymbol{\sigma}$ and $\boldsymbol{P}$ is obtained by applying Nanson's formula, i.e., $(2.8)_1$ to (2.17), with $\boldsymbol{\sigma} \cdot \boldsymbol{n} \, \mathrm{d}a = \boldsymbol{P} \cdot \boldsymbol{N} \, \mathrm{d}A$ by

$$\boldsymbol{P} = J \boldsymbol{\sigma} \cdot \boldsymbol{F}^{-T} \quad \text{and the inverse relation} \quad \boldsymbol{\sigma} = J^{-1} \boldsymbol{P} \cdot \boldsymbol{F}^{T} = \boldsymbol{\sigma}^{T} \,, \tag{2.19}$$

with $\boldsymbol{P}$ the first Piola-Kirchhoff stress tensor given as a two field tensor and therefore $\boldsymbol{P} \neq \boldsymbol{P}^T$, $\boldsymbol{P}\boldsymbol{F}^T = \boldsymbol{F}\boldsymbol{P}^T$. For convenience, further stress measures are introduced. The symmetric Kirchhoff stress tensor $\boldsymbol{\tau}$ denotes a transformation of the Cauchy stresses to the reference volume in terms of the Jacobian J, and is defined by

$$\boldsymbol{\tau} = J \boldsymbol{\sigma} \,. \tag{2.20}$$

Furthermore, a symmetric stress tensor in the material configuration $\boldsymbol{S}$, the second Piola-Kirchhoff stress tensor, is defined by a pull-back operation of the Kirchhoff stresses, thus

$$\boldsymbol{S} = J \boldsymbol{F}^{-1} \cdot \boldsymbol{\tau} \cdot \boldsymbol{F}^{-T} \,. \tag{2.21}$$

In the literature, further definitions of stress measures can be found, cf., e.g., Holzapfel [116]. An overview of the relation between the different stress quantities is listed in Table 2.1.

Table 2.1: Relation between different stress quantities

		$\boldsymbol{\sigma}$	$\boldsymbol{\tau}$	$\boldsymbol{P}$	$\boldsymbol{S}$
Cauchy stress	$\boldsymbol{\sigma}$	$\boldsymbol{\sigma}$	$J^{-1}\boldsymbol{\tau}$	$J^{-1}\boldsymbol{P}\cdot\boldsymbol{F}^T$	$J^{-1}\boldsymbol{F}\cdot\boldsymbol{S}\cdot\boldsymbol{F}^T$
Kirchhoff stress	$\boldsymbol{\tau}$	$J\boldsymbol{\sigma}$	$\boldsymbol{\tau}$	$\boldsymbol{P}\cdot\boldsymbol{F}^T$	$\boldsymbol{F}\cdot\boldsymbol{S}\cdot\boldsymbol{F}^T$
first P.-K. stress	$\boldsymbol{P}$	$J\boldsymbol{\sigma}\cdot\boldsymbol{F}^{-T}$	$\boldsymbol{\tau}\cdot\boldsymbol{F}^{-T}$	$\boldsymbol{P}$	$\boldsymbol{F}\cdot\boldsymbol{S}$
second P.-K. stress	$\boldsymbol{S}$	$J\boldsymbol{F}^{-1}\cdot\boldsymbol{\sigma}\cdot\boldsymbol{F}^{-T}$	$\boldsymbol{F}^{-1}\cdot\boldsymbol{\tau}\cdot\boldsymbol{F}^{-T}$	$\boldsymbol{F}^{-1}\cdot\boldsymbol{P}$	$\boldsymbol{S}$

2.3 Balance principles

Hereafter, the mathematical description of the fundamental physical principles and foundations of thermodynamics, i.e., conservation of mass, balance laws of linear and angular momentum, balance of energy and entropy inequality are discussed. The presented principles are axioms, i.e., fundamental laws which cannot be derived from other laws, but which are directly comprehensible and correspond to observations in nature without any restriction.

2.3.1 Balance of mass

The balance of mass implies that the change of the mass M of a body $\mathcal{B}_t$ at time t is zero and the mass M over time is constant for a closed system, i.e.,

$$\dot{M} = 0 \quad \text{with} \quad M = \int_{\mathcal{B}_t} \rho \, \mathrm{d}v = \int_{\mathcal{B}_0} \rho \, J \, \mathrm{d}V = \int_{\mathcal{B}_0} \rho_0 \, \mathrm{d}V = \text{const.}\,, \tag{2.22}$$

with ρ as the density of the body in the actual configuration and the reference density denoted by ρ_0, connected by means of the Jacobian $\rho_0 = \rho\, J$. The material time derivative of $(2.22)_2$ is obtained with use of the transport theorem (2.8) and (2.16) in the actual configuration as

$$\dot{M} = \frac{\mathrm{d}}{\mathrm{d}t} \int_{B_t} \rho \, \mathrm{d}v = \int_{\mathcal{B}_t} (\dot{\rho} + \rho \, \operatorname{div} \dot{\boldsymbol{x}}) \, \mathrm{d}v = 0\,, \tag{2.23}$$

and the local statement is given by

$$\dot{\rho} + \rho \, \operatorname{div} \dot{\boldsymbol{x}} = 0\,. \tag{2.24}$$

2.3.2 Balance of linear momentum

The balance of linear momentum postulates that the material time derivative (time rate of change) of linear momentum is equal to the sum of all volume and surface forces acting on the body. A physical representation of this law is

$$\dot{\boldsymbol{I}} = \boldsymbol{k}\,, \tag{2.25}$$

where the linear momentum is denoted by $\boldsymbol{I}$ and $\boldsymbol{k}$ denotes the sum of volume and surface forces on the body, which are defined by

$$\boldsymbol{I} = \int_{\mathcal{B}_t} \rho \, \dot{\boldsymbol{x}} \, \mathrm{d}v \quad \text{and} \quad \boldsymbol{k} = \int_{\mathcal{B}_t} \rho \, \boldsymbol{b} \, \mathrm{d}v + \int_{\partial\mathcal{B}_t} \boldsymbol{t} \, \mathrm{d}a\,. \tag{2.26}$$

Regarding (2.8), (2.16), the local statement of the balance of mass (2.24) and a reformulation of the expression for the external force $\boldsymbol{k}$ by means of the Cauchy theorem leads to

$$\dot{\boldsymbol{I}} = \int_{\mathcal{B}_t} \rho\, \ddot{\boldsymbol{x}}\, \mathrm{d}v \quad \text{and} \quad \boldsymbol{k} = \int_{\mathcal{B}_t} (\rho\, \boldsymbol{b} + \operatorname{div} \boldsymbol{\sigma})\, \mathrm{d}v\,. \tag{2.27}$$

The evaluation of (2.25) with (2.26) yields the global and local statement in the actual configuration as

$$\int_{\mathcal{B}_t} (\operatorname{div} \boldsymbol{\sigma} + \rho\, (\boldsymbol{b} - \ddot{\boldsymbol{x}}))\, \mathrm{d}v = \boldsymbol{0} \quad \Rightarrow \quad \operatorname{div} \boldsymbol{\sigma} + \rho\, (\boldsymbol{b} - \ddot{\boldsymbol{x}}) = \boldsymbol{0}\,, \tag{2.28}$$

which can be transferred into the reference configuration with $\boldsymbol{t}\, \mathrm{d}a = \boldsymbol{t}_0\, \mathrm{d}A$ and $\boldsymbol{t}_0 = \boldsymbol{P} \cdot \boldsymbol{N}$ in $(2.26)_2$ and introducing the body force in terms of the reference density ρ_0, with (2.8), $\rho = J^{-1}\, \rho_0$, yielding

$$\operatorname{Div} \boldsymbol{P} + \rho_0\, (\boldsymbol{b} - \ddot{\boldsymbol{x}}) = \boldsymbol{0}\,, \tag{2.29}$$

where $\operatorname{Div}(\bullet) = \nabla_X(\bullet) : \boldsymbol{1}$ is the divergence operator with respect to $\boldsymbol{X}$.

2.3.3 Balance of angular of momentum

The balance of angular momentum implies that the material time derivative of the moment of momentum, with respect to a fixed reference point $\bar{0}$, is equal to the resulting external moment of all volume and surface forces acting on the body, with respect to the same fixed reference point $\bar{0}$, i.e.,

$$\dot{\boldsymbol{h}}_{\bar{0}} = \boldsymbol{m}_{\bar{0}}\,. \tag{2.30}$$

The moment of momentum $\boldsymbol{h}_{\bar{0}}$ and the external moment $\boldsymbol{m}_{\bar{0}}$ with respect to the fixed reference point $\bar{0}$ are given by

$$\boldsymbol{h}_{\bar{0}} = \int_{\mathcal{B}_t} \boldsymbol{x} \times \rho\, \dot{\boldsymbol{x}}\, \mathrm{d}v \quad \text{and} \quad \boldsymbol{m}_{\bar{0}} = \int_{\mathcal{B}_t} \boldsymbol{x} \times \rho\, \boldsymbol{b}\, \mathrm{d}v + \int_{\partial \mathcal{B}_t} \boldsymbol{x} \times \boldsymbol{t}\, \mathrm{d}a\,. \tag{2.31}$$

Considering (2.24), results for the material time derivative of $\boldsymbol{h}_{\bar{0}}$ in

$$\dot{\boldsymbol{h}}_{\bar{0}} = \frac{\mathrm{d}}{\mathrm{d}t} \int_{\mathcal{B}_t} \boldsymbol{x} \times \rho\, \dot{\boldsymbol{x}}\, \mathrm{d}v = \int_{\mathcal{B}_t} \boldsymbol{x} \times \rho\, \ddot{\boldsymbol{x}}\, \mathrm{d}v\,. \tag{2.32}$$

The reformulation of the external moment $(2.31)_2$ by applying the Cauchy theorem and divergence theorem gives

$$\boldsymbol{m}_{\bar{0}} = \int_{\mathcal{B}_t} \boldsymbol{x} \times \rho\, \boldsymbol{b}\, \mathrm{d}v + \int_{\mathcal{B}_t} (\boldsymbol{x} \times \operatorname{div} \boldsymbol{\sigma} + \nabla_{,x} \boldsymbol{x} \times \boldsymbol{\sigma})\, \mathrm{d}v\,. \tag{2.33}$$

Inserting (2.33) and the local statement of the balance of linear momentum $(2.28)_2$ into (2.32) yields the reformulation of (2.30) as

$$\int_{\mathcal{B}_t} \nabla_{,x} \boldsymbol{x} \times \boldsymbol{\sigma}\, \mathrm{d}v = \int_{\mathcal{B}_t} \boldsymbol{1} \times \boldsymbol{\sigma}\, \mathrm{d}v = \boldsymbol{0} \quad \Rightarrow \quad \boldsymbol{1} \times \boldsymbol{\sigma} = \boldsymbol{0}\,, \tag{2.34}$$

which is fulfilled by the symmetry of the Cauchy stress tensor with

$$\boldsymbol{\sigma} = \boldsymbol{\sigma}^T\,. \tag{2.35}$$

From (2.35), the symmetry of Kirchhoff stress tensor $\boldsymbol{\tau}$ and the second Piola-Kirchhoff stress tensor $\boldsymbol{S}$ can be derived.

2.3.4 Balance of energy - first law of thermodynamics

The balance equation of energy, also known as the first law of thermodynamics, postulates that the material time derivative of the sum of kinetic energy and internal energy is equal to the sum of mechanical work of all inner and outer forces on the body and all other energies acting in or on the body. For the consideration of only mechanical and thermal energies, the balance of energy is given by

$$\dot{K} + \dot{E} = W + Q \,. \tag{2.36}$$

The kinetic energy K and internal energy E of a body are defined as

$$K = \frac{1}{2} \int_{\mathcal{B}_t} \rho \, \dot{\boldsymbol{x}} \cdot \dot{\boldsymbol{x}} \, \mathrm{d}v \quad \text{and} \quad E = \int_{\mathcal{B}_t} \rho \, e \, \mathrm{d}v \,, \tag{2.37}$$

where e denotes the specific internal energy per unit reference mass. Furthermore, the material time derivatives of the kinetic and internal energy is received by applying the transport theorem (2.8), (2.16) and the local statement of the balance of mass (2.24), with

$$\dot{K} = \int_{\mathcal{B}_t} \rho \, \dot{\boldsymbol{x}} \cdot \ddot{\boldsymbol{x}} \, \mathrm{d}v \quad \text{and} \quad \dot{E} = \int_{\mathcal{B}_t} \rho \, \dot{e} \, \mathrm{d}v \,. \tag{2.38}$$

Additionally, the mechanical power W and thermal power Q are defined by

$$W = \int_{\mathcal{B}_t} \dot{\boldsymbol{x}} \cdot \rho \, \boldsymbol{b} \, \mathrm{d}v + \int_{\partial \mathcal{B}_t} \dot{\boldsymbol{x}} \cdot \boldsymbol{t} \, \mathrm{d}a = \int_{\mathcal{B}_t} \dot{\boldsymbol{x}} \cdot \rho \, \boldsymbol{b} \, \mathrm{d}v + \int_{\mathcal{B}_t} (\operatorname{div} \boldsymbol{\sigma} \cdot \dot{\boldsymbol{x}} + \boldsymbol{\sigma} : \boldsymbol{L}) \, \mathrm{d}v \,, \tag{2.39}$$

and

$$Q = \int_{\mathcal{B}_t} \rho \, r \, \mathrm{d}v - \int_{\partial \mathcal{B}_t} \boldsymbol{q} \cdot \boldsymbol{n} \, \mathrm{d}a \,, \tag{2.40}$$

with r as the internal energy source and the heat flow vector $\boldsymbol{q}$. Inserting (2.38), (2.39) and (2.40) into (2.36) and regarding $(2.28)_2$ leads to the balance of energy given as the local statement by

$$\rho \, \dot{e} = \boldsymbol{\sigma} : \boldsymbol{D} + \rho \, r + \operatorname{div} \boldsymbol{q} \,. \tag{2.41}$$

Furthermore, the introduction of a free Helmholtz energy function $\tilde{\psi} = e - \Theta \, \eta$, where Θ is defined as absolute temperature and η as the specific entropy, leads

$$\rho \, (\dot{\tilde{\psi}} + \dot{\Theta} \, \eta + \Theta \, \dot{\eta}) - \boldsymbol{\sigma} : \boldsymbol{D} - \rho \, r - \operatorname{div} \boldsymbol{q} = 0 \,, \tag{2.42}$$

with the material time derivative $\dot{\tilde{\psi}} = \dot{e} - \dot{\Theta} \, \eta - \Theta \, \dot{\eta}$ and for isothermal processes (2.42) reduces to

$$\rho \, \dot{\tilde{\psi}} - \boldsymbol{\sigma} : \boldsymbol{D} = 0 \,. \tag{2.43}$$

An alternative representation of the balance of energy for the framework of pure mechanical energy is defined by

$$\dot{K} + W_{int} = W_{ext} \quad \text{with} \quad W_{int} = \dot{E} \quad \Rightarrow \dot{K} + \dot{E} = W_{ext} \,, \tag{2.44}$$

where the rate of external and internal mechanical power are defined by

$$W_{int} = \int_{\mathcal{B}_t} \boldsymbol{\sigma} : \boldsymbol{D} \, \mathrm{d}v \quad \text{and} \quad W_{ext} = \int_{\partial \mathcal{B}_t} \dot{\boldsymbol{x}} \cdot \boldsymbol{t} \, \mathrm{d}a + \int_{\mathcal{B}_t} \rho \, \boldsymbol{b} \cdot \dot{\boldsymbol{x}} \, \mathrm{d}v \,. \tag{2.45}$$

W_{int} describes the power in $\mathcal{B}_t$ due to the stress field and W_{ext} denotes the power applied on $\mathcal{B}_t$ by the outer forces. This rate of internal mechanical power or so-called stress power is the fundamental equation for detection of work conjugated pairs, i.e., the stress and strain counterpart, which can be identified with

$$W_{int} = \int_{\mathcal{B}_t} \boldsymbol{\sigma} : \boldsymbol{D} \, \mathrm{d}v = \int_{\mathcal{B}_0} \boldsymbol{\tau} : \boldsymbol{D} \, \mathrm{d}V = \int_{\mathcal{B}_0} \boldsymbol{P} : \dot{\boldsymbol{F}} \, \mathrm{d}V = \int_{\mathcal{B}_0} \boldsymbol{S} : \dot{\boldsymbol{E}} \, \mathrm{d}V \,. \tag{2.46}$$

The rate of the Green-Lagrange strain tensor $\dot{\boldsymbol{E}}$ is a pull-back of the rate of deformation tensor $\boldsymbol{D}$ defined by $\dot{\boldsymbol{E}} = \boldsymbol{F}^T \cdot \boldsymbol{L}^{\mathrm{sym}} \cdot \boldsymbol{F} = \boldsymbol{F}^T \cdot \boldsymbol{D} \cdot \boldsymbol{F}$.

2.3.5 Entropy inequality - second law of thermodynamics

The entropy inequality or second law of thermodynamics postulates that the change of the total entropy ($\rho\,\eta$ over $\mathcal{B}_t$) is equal to or greater than the sum of the entropy input by heat production inside $\mathcal{B}_t$ ($\rho\, r/\Theta$ over $\mathcal{B}_t$) and by the heat flow vector over the surface $\partial\mathcal{B}_t$ ($\Theta^{-1}\boldsymbol{q}\cdot\boldsymbol{n}$ on $\partial\mathcal{B}_t$). This relation is given in the inequality

$$\frac{\mathrm{d}}{\mathrm{d}t} \int_{\mathcal{B}_t} \rho\,\eta \, \mathrm{d}v \geq \int_{\mathcal{B}_t} \rho \frac{r}{\Theta} \, \mathrm{d}v - \int_{\partial\mathcal{B}_t} \frac{1}{\Theta}\, \boldsymbol{q}\cdot\boldsymbol{n} \, \mathrm{d}a \,, \tag{2.47}$$

which can be reformulated using the divergence theorem leading to

$$\int_{\mathcal{B}_t} \rho\,\dot{\eta} \, \mathrm{d}v \geq \int_{\mathcal{B}_t} \left(\rho \frac{r}{\Theta} - \mathrm{div}\left(\frac{\boldsymbol{q}}{\Theta}\right)\right) \mathrm{d}v \,. \tag{2.48}$$

The local statement of the entropy inequality, the so-called Clausius-Duhem inequality, reads

$$\rho\,\dot{\eta} - \frac{1}{\Theta}\,\rho\, r + \mathrm{div}\left(\frac{\boldsymbol{q}}{\Theta}\right) \geq 0 \,. \tag{2.49}$$

The reformulation of (2.49) taking into account $\mathrm{div}(\boldsymbol{q}\,\Theta^{-1}) = \Theta^{-1}\ \mathrm{div}\,\boldsymbol{q} - \Theta^{-2}\,\boldsymbol{q}\cdot\nabla_{,x}\Theta$ and the local statement of the balance of energy (2.41) yields the Clausius-Duhem inequality in the form

$$\rho\,(\Theta\,\dot{\eta} - \dot{e}) + \boldsymbol{\sigma} : \boldsymbol{D} - \Theta^{-1}\,\boldsymbol{q}\cdot\nabla_{,x}\Theta \geq 0 \,. \tag{2.50}$$

Inserting the Helmholtz free energy $\tilde{\psi} = e - \Theta\eta$ yields

$$-\,\rho\,(\dot{\tilde{\psi}} - \dot{\Theta}\,\eta) + \boldsymbol{\sigma} : \boldsymbol{D} - \Theta^{-1}\,\boldsymbol{q}\cdot\nabla_{,x}\Theta \geq 0 \,. \tag{2.51}$$

For simplicity, a restriction to isothermal, adiabatic processes, i.e., $\Theta = \text{const.}$, $\dot{\Theta} = 0$, $r = 0$ and $\boldsymbol{q} = \boldsymbol{0}$ reduces the Clausius-Duhem inequality, further denoted by $\mathcal{D}$ as the dissipation inequality, to

$$\mathcal{D} := \boldsymbol{\sigma} : \boldsymbol{D} - \rho\,\dot{\tilde{\psi}} \geq 0 \,. \tag{2.52}$$

A representation of the dissipation inequality in the reference configuration is obtained by multiplying (2.52) by J. Further representations can be obtained by consideration of the work conjugated pairings (2.46) yielding

$$\boldsymbol{\tau} : \boldsymbol{D} - \rho_0\,\dot{\tilde{\psi}} \geq 0 \quad \text{or alternatively} \quad \boldsymbol{P} : \dot{\boldsymbol{F}} - \rho_0\,\dot{\tilde{\psi}} \geq 0 \,. \tag{2.53}$$

2.4 Principles of material modeling

The formulation of material models is restricted by basic principles, which ensure the construction of physically sound material models. These principles, cf., e.g., Noll [173], Truesdell and Toupin [230], Truesdell and Noll [229], Holzapfel [116] and Marsden and Hughes [159], are briefly described in the following. The *principle of causality* is based on the fact that the quantities of motion and temperature of the body are regarded as measurable quantities in any thermomechanical process and are therefore so-called independent process variables. Further quantities, included in the entropy inequality and which cannot be derived from motion and temperature, are considered as dependent constitutive variables, i.e., stresses $\boldsymbol{\sigma}$, heat flow $\boldsymbol{q}$, specific energy e and specific entropy η $(\boldsymbol{\sigma}, \boldsymbol{q}, e, \eta)$, cf. (2.50). Based on this separation of variables, the *principle of determinism* states that these dependent variables in a material point of the body are determined by the history of motion and temperature of all material points in the body. The *principle of equipresence* demands that the maximum number of constitutive variables have to be included in all setup of equations in order to consider their influence on the material behavior as long as the number is not reduced by any restrictive assumptions. Furthermore, a reduction of the number of independent variables is performed by the evaluation of all principles. The *principle of material objectivity* or *material frame indifference* demands for an observer invariant formulation of the constitutive equations, i.e., that the material properties are independent on the change of observer. Therefore, if a rigid body motion $\boldsymbol{Q}$, as a proper orthogonal transformation, is superimposed on the deformed configuration $\mathcal{B}_t$, yielding the superimposed configuration ${\mathcal{B}_t}^+$, the formulation has to fulfill the condition that no alterations occur within constitutive relations, that means e.g., no changes in the stress field.
The superimposed configuration ${\mathcal{B}_t}^+$ contains the actual position vector defined by $\boldsymbol{x}^+ = \boldsymbol{Q}\cdot\boldsymbol{x}$, where the proper orthogonal tensor $\boldsymbol{Q}$ has the properties $\det \boldsymbol{Q} = 1$, $\boldsymbol{Q}^T = \boldsymbol{Q}^{-1}$ and $\boldsymbol{Q}\cdot\boldsymbol{Q}^T = \boldsymbol{1}$, cf. Truesdell and Noll [229] and Holzapfel [116]. The requirement of objective quantities in the reference configuration $\mathcal{B}_0$ and the current configuration $\mathcal{B}_t$ is summarized by

$$\begin{aligned} \{\phi^+, \boldsymbol{v}^+, \boldsymbol{\Upsilon}^+\} &= \{\phi, \boldsymbol{v}, \boldsymbol{\Upsilon}\} \quad \forall\, \{\phi, \boldsymbol{v}, \boldsymbol{\Upsilon}\} \in \mathcal{B}_0\,, \\ \{\phi^+, \boldsymbol{v}^+, \boldsymbol{\Upsilon}^+\} &= \{\phi, \boldsymbol{Q}\cdot\boldsymbol{v}, \boldsymbol{Q}\cdot\boldsymbol{\Upsilon}\cdot\boldsymbol{Q}^T\} \quad \forall\, \{\phi, \boldsymbol{v}, \boldsymbol{\Upsilon}\} \in \mathcal{B}_t\,, \end{aligned} \tag{2.54}$$

which represents a sufficient condition for a scalar, vector and single field tensor ϕ, $\boldsymbol{v}$ and $\boldsymbol{\Upsilon}$. Furthermore, the transformed deformation gradient $\boldsymbol{F}^+$ is given by $\boldsymbol{F}^+ = \operatorname{Grad} \boldsymbol{x}^+ = \boldsymbol{Q}\cdot\boldsymbol{F}$, which fulfills the objectivity condition for a two-field tensor. Consequently, $\boldsymbol{F}$ transforms like a vector based on the condition that none, one or two configurations have to be transformed, due to the fact that the reference configuration is intrinsically independent of the observer. For guaranteeing an objective formulation, it is necessary to choose a stored energy function ψ in terms of frame indifferent values, e.g., the right or left Cauchy-Green deformation tensor $\boldsymbol{C}^+ = (\boldsymbol{F}^T\cdot\boldsymbol{F})^+ = \boldsymbol{F}^T\cdot\boldsymbol{Q}^T\cdot\boldsymbol{Q}\cdot\boldsymbol{F} = \boldsymbol{C}$ or $\boldsymbol{B}^+ = (\boldsymbol{F}\cdot\boldsymbol{F}^T)^+ = \boldsymbol{Q}\cdot\boldsymbol{F}\cdot\boldsymbol{F}^T\cdot\boldsymbol{Q}^T = \boldsymbol{Q}\cdot\boldsymbol{B}\cdot\boldsymbol{Q}^T$. These relations lead to

$$\psi(\boldsymbol{C}^+) = \psi(\boldsymbol{C}) \quad \text{and} \quad \psi(\boldsymbol{B}^+) = \psi(\boldsymbol{Q}\boldsymbol{B}\boldsymbol{Q}^T) \quad \forall\, \boldsymbol{Q} \in SO(3)\,, \tag{2.55}$$

where $SO(3)$ denotes the special orthogonal group, which represents the group of all arbitrary rigid body motions with the previously defined relations for $\boldsymbol{Q}$. A further discussion

on objective quantities and stress rates within the framework of elasto-plastic material deformation is given in Chapter 5.7
Since the motion of a body is described by a reference configuration, the formulation of the constitutive equations has to be unaffected by an applied rotation on the reference configuration with $\boldsymbol{Q} \in \mathcal{G}_k$, which is demanded by the *principle of material symmetry*. The symmetry group $\mathcal{G}_k$ characterizes the symmetry properties of the material with $\mathcal{G}_k \in O(3)$. The rotated reference configuration $\mathcal{B}_0^\star$ is parameterized by $\boldsymbol{X}^\star = \boldsymbol{Q}^T \cdot \boldsymbol{X} \, \forall \, \boldsymbol{Q} \in \mathcal{G}_k$. For an isotropic material, $\boldsymbol{F}^\star = \boldsymbol{F} \cdot \boldsymbol{Q}$ holds without influence on the material behavior. Furthermore, the isotropy of space demands that the stresses on $\mathcal{B}_0$ and $\mathcal{B}_0^\star$ have to be equal. This leads, e.g., for the first and second Piola-Kirchhoff stress tensor as a two- and single-field tensor the relations

$$\boldsymbol{P}(\boldsymbol{F}^\star) = \boldsymbol{P}(\boldsymbol{F}) \cdot \boldsymbol{Q} \quad \text{and} \quad \boldsymbol{S}(\boldsymbol{F}^\star) = \boldsymbol{Q}^T \cdot \boldsymbol{S}(\boldsymbol{F}) \cdot \boldsymbol{Q} \quad \forall \, \boldsymbol{Q} \in \mathcal{G}_k \, . \tag{2.56}$$

Furthermore, the *principle of local agency* states that material points further away than a certain distance to a material point have no significant influence on the independent constitutive variables at that point, in the literature denoted as so-called simple bodies, cf. Noll [173]. In a similar way, the *principle of fading memory* states that the constitutive quantities are not significantly affected by quantities of large temporary distance. The *principle of consistency* demands that all formulated constitutive equations must be in accordance with the basic statements of the balance laws of continuum mechanics and further a model is called thermodynamic consistent if it fulfills the entropy inequality.

2.5 Nonlinear material behavior

The discussed problems in the course of this work are mainly characterized by nonlinear material behavior. These are described by hyperelasticity and elasto-plastic deformations for small and finite strain settings. Material nonlinearities result in a nonlinear stress-strain relation. For elastic materials all deformations are reversible after unloading. In contrast to that, deformations in elasto-plastic materials are partly irreversible, i.e., elastic deformations are reversible and plastic deformations remains in the system after unloading. Here, a short overview on hyperelastic material descriptions is given and an elasto-plastic material model at small and finite strains is briefly discussed, considering a von Mises yield criterion. Moreover, the analysis is restricted to isotropic hardening, which is characterized by an expansion of the yield surface, i.e., an increase of the yield strength, and, in contrast to kinematic hardening effects, independent of the previously applied load direction.

2.5.1 Hyperelastic material description

In the scope of this work, the hyperelastic material description is based on a Neo-Hookean type isotropic free energy function, cf., e.g., Ogden [174] and Ciarlet [78]. It is defined by

$$\psi_{\mathrm{NH}}^{\mathrm{iso}} := \frac{\lambda}{4}(I_3(\boldsymbol{C}) - 1) + \frac{\mu}{2}(I_1(\boldsymbol{C}) - 3) - \left(\frac{\lambda}{2} + \mu\right) \ln \sqrt{I_3(\boldsymbol{C})} \, , \tag{2.57}$$

with respect to the Lamé constants λ and μ and in terms of the first and third principal invariant of the right Cauchy-Green deformation tensor $\boldsymbol{C}$ defined by $I_1(\boldsymbol{C}) = \operatorname{tr} \boldsymbol{C}$ and

$I_3(\boldsymbol{C}) = \det \boldsymbol{C}$ or the left Cauchy-Green deformation tensor $\boldsymbol{B}$ with, $I_1(\boldsymbol{B}) = \operatorname{tr} \boldsymbol{B}$, $I_3(\boldsymbol{B}) = \det \boldsymbol{B}$, where $\psi(\boldsymbol{C}) = \psi(I_1(\boldsymbol{C}), I_2(\boldsymbol{C}), I_3(\boldsymbol{C})) = \psi(I_1(\boldsymbol{B}), I_2(\boldsymbol{B}), I_3(\boldsymbol{B})) = \psi(\boldsymbol{B})$, cf. Wriggers [236]. Furthermore, the principal invariants can be expressed with respect to principal stretches, see, e.g., (2.10), which are

$$I_1(\boldsymbol{C}) = \lambda_1^2 + \lambda_2^2 + \lambda_3^2\,, \quad I_2(\boldsymbol{C}) = \lambda_1^2\,\lambda_2^2 + \lambda_2^2\,\lambda_3^2 + \lambda_3^2\,\lambda_1^2\,, \quad \text{and} \quad I_3(\boldsymbol{C}) = \lambda_1^2\,\lambda_2^2\,\lambda_3^2\,, \tag{2.58}$$

cf. Truesdell and Noll [229]. The representation of the material law based on principal invariants fulfills the requirement of material objectivity for the free energy function, since the principal invariants are independent of a change of the reference system. Further nonlinear elastic material laws are discussed in Ogden [174], which are, e.g., the Mooney-Rivlin model, see Mooney [164] and Rivlin [191] and the Ogden model, see Ogden [175].

2.5.2 Rate-independent elasto-plastic material description at small strains

The brief representation of the basic requirements for elasto-plasticity at small strains are given in detail, e.g., in the contributions by Simo [213], Simo and Hughes [214] and Miehe [162] among others. Elasto-plastic material behavior at small strains is characterized by an additive split of the total strains $\boldsymbol{\varepsilon} = \nabla^s \boldsymbol{u} = \boldsymbol{\varepsilon}^e + \boldsymbol{\varepsilon}^p$ with an elastic part $\boldsymbol{\varepsilon}^e$, a plastic part $\boldsymbol{\varepsilon}^p$ and the symmetric displacement gradient $\nabla^s \boldsymbol{u} = \frac{1}{2}(\nabla \boldsymbol{u} + (\nabla \boldsymbol{u})^T)$. In order to guarantee a thermodynamic consistent model, the second law of thermodynamics (2.50) has to be considered. For isothermal processes, the dissipation inequality is given by (2.52). This can be transferred to the reference configuration with respect to the work conjugated pairs, cf. (2.46), providing $\mathcal{D} = \boldsymbol{S} : \dot{\boldsymbol{E}} - \rho_0\,\dot{\psi}$ and thus for the small strain theory (2.52) is reformulated, with the free energy per reference volume $\psi = \rho_0\,\bar{\psi}$, into

$$\mathcal{D} = \boldsymbol{\sigma} : \dot{\boldsymbol{\varepsilon}} - \dot{\psi} \geq 0\,. \tag{2.59}$$

Here, the additive split of a free energy function with respect to elastic strains $\boldsymbol{\varepsilon}^e$ and internal strain-like variable α yields $\psi(\boldsymbol{\varepsilon}^e, \alpha) = \psi^e(\boldsymbol{\varepsilon}^e) + \psi^p(\alpha)$. Therefore, the dissipation inequality (2.59) reads

$$\begin{aligned} \mathcal{D} &= \boldsymbol{\sigma} : \dot{\boldsymbol{\varepsilon}} - \partial_{\boldsymbol{\varepsilon}^e}\psi : \dot{\boldsymbol{\varepsilon}}^e - \partial_\alpha \psi\,\dot{\alpha} \\ &= (\boldsymbol{\sigma} - \partial_{\boldsymbol{\varepsilon}^e}\psi) : \dot{\boldsymbol{\varepsilon}}^e + \boldsymbol{\sigma} : \dot{\boldsymbol{\varepsilon}}^p + \beta\,\dot{\alpha} \\ &= \boldsymbol{\sigma} : \dot{\boldsymbol{\varepsilon}}^p + \beta\,\dot{\alpha}\,. \end{aligned} \tag{2.60}$$

Furthermore, an abbreviation for the thermodynamic force related to the internal variable is introduced as the conjugated variable $\beta := -\partial_\alpha \psi$. The fulfillment of $\mathcal{D} \geq 0$ yields the Cauchy stress relation $\boldsymbol{\sigma} = \partial_{\boldsymbol{\varepsilon}^e}\psi$, i.e., the stresses are a function of the elastic strains. The resulting equation in (2.60) is referred as reduced dissipation inequality $\mathcal{D}_{\text{red}}$. For reasons of simplicity, the consideration is here restricted to linear isotropic hardening. Thus, the hardening potential $\psi^p(\alpha)$ is given by $\psi^p(\alpha) = \frac{1}{2} h\,\alpha^2$, cf. Miehe and Stein [163], with the hardening modulus h.

For the derivation of the evolution equation of $\boldsymbol{\varepsilon}^p$ and α, which fulfill the Clausius-Duhem inequality, the existence of a convex yield surface in the stress space is postulated. This yield surface Φ characterizes the boundary of the elastic domain of the material deformation and simultaneously the space of admissible stress states. The area in which elastic

and plastic deformations occur is dependent on the choice of the yield criterion. In this work, a von Mises yield criterion is chosen, in which the area of elastic deformations is described in the form of a cylinder in the principle stress space.
One important aspect for the fulfillment of the Clausius-Duhem inequality with respect to the evolution equations is the so-called principle of maximum plastic dissipation, which states that the dissipation becomes maximal for the actual stress state in comparison with all other stress states, cf., e.g., Simo [213]. This approach implies an associated flow rule, the loading/unloading conditions in Kuhn-Tucker form (see (2.63)) and convexity of the elastic domain, cf., e.g., Simo [210; 211] and Simo and Hughes [214]. From a mathematical point of view the principle yields to an optimization problem ($-\mathcal{D}_{\text{red}} \leq 0$) with constraint condition ($\Phi = 0$), which is determined by a Lagrange functional $\mathfrak{L}$ of the form

$$\mathfrak{L}(\boldsymbol{\sigma}, \beta, \gamma) = -\mathcal{D}_{\text{red}} + \gamma\, \Phi(\boldsymbol{\sigma}, \beta)\,, \tag{2.61}$$

where $\gamma \geq 0$ denotes a plastic multiplier and Φ the yield criterion. For the fulfillment of the principle of maximum plastic dissipation, an extreme value for the Lagrange functional $\mathfrak{L}(\boldsymbol{\sigma}, \beta, \gamma) \rightarrow$ stat., i.e., $\partial_{\boldsymbol{\tau},\beta,\gamma}\mathfrak{L} = 0$, is determined by

$$\dot{\boldsymbol{\varepsilon}}^p = \gamma\, \partial_{\boldsymbol{\sigma}}\Phi\,, \quad \dot{\alpha} = \gamma\, \partial_{\beta}\Phi\,, \quad \Phi = 0\,, \tag{2.62}$$

in combination with the fulfillment of the Kuhn-Tucker or so-called loading/unloading conditions and the consistency condition defined by

$$\gamma \geq 0\,, \quad \Phi \leq 0\,, \quad \Phi\,\gamma = 0 \quad \text{and} \quad \dot{\Phi}\,\gamma = 0\,. \tag{2.63}$$

Consequently, $(2.62)_1$ denotes the associated flow rule, which determines the plastic flow, and the evolution of internal variable for the related state $\Phi = 0$. The different states are divided into an elastic unloading ($\dot{\Phi} < 0; \gamma = 0$), plastic loading ($\dot{\Phi} = 0; \gamma > 0$) and a neutral state ($\dot{\Phi} = 0; \gamma = 0$), cf. Simo [213] and Simo and Hughes [214]. Here, the consideration is limited to a von Mises yield criterion

$$\Phi(\boldsymbol{\sigma}, \beta) = \| \operatorname{dev} \boldsymbol{\sigma} \| - \sqrt{\tfrac{2}{3}}(y_0 + \beta)\,, \tag{2.64}$$

where y_0 denotes the initial yield stress and $\operatorname{dev} \boldsymbol{\sigma} = \boldsymbol{\sigma} - \frac{1}{3} \operatorname{tr} \boldsymbol{\sigma}\, \mathbf{1}$. Therefore, the evolution equations of the plastic strains and the internal variable in (2.62) are obtained by

$$\dot{\boldsymbol{\varepsilon}}^p = \gamma \frac{\operatorname{dev} \boldsymbol{\sigma}}{\| \operatorname{dev} \boldsymbol{\sigma} \|} = \gamma\, \boldsymbol{n} \quad \text{and} \quad \dot{\alpha} = \sqrt{\tfrac{2}{3}}\, \gamma\,. \tag{2.65}$$

In order to obtain a complete representation of rate-independent elasto-plasticity the algorithmic treatment is discussed below. Therefore, trial states are introduced, which assumes that the material response is purely elastic. The algorithmic treatment is based on the idea of a return mapping algorithm, in which an elastic predictor step (purely elastic trial step) is followed by a plastic corrector step (return mapping), introduced by Wilkins [233], cf. Simo and Taylor [217]. Here, mainly mixed methods are discussed, where the stresses are an unknown field and thus no trial state of the stresses exist as, e.g., for the case of pure displacement methods, which are extensively described in Simo and Hughes [214].
For the algorithmic implementation a backward Euler integration scheme on the time interval $[t_n, t_{n+1}]$ is applied for the rate equations (2.65), providing

$$\boldsymbol{\varepsilon}^p_{n+1} = \boldsymbol{\varepsilon}^p_n + \Delta_t \gamma\, \boldsymbol{n}_{n+1} \quad \text{and} \quad \alpha_{n+1} = \alpha_n + \sqrt{\tfrac{2}{3}}\, \Delta_t \gamma\,, \tag{2.66}$$

where $\boldsymbol{n}_{n+1} = \operatorname{dev}\boldsymbol{\sigma}_{n+1}/\|\operatorname{dev}\boldsymbol{\sigma}_{n+1}\|$ and the abbreviation $\Delta_t\gamma := \gamma\Delta t$ is introduced with $\Delta t = t_{n+1} - t_n$. Furthermore, if the elastic domain is exceeded ($\Phi^{\text{trial}} > 0$), $\Delta_t\gamma$ as the increment of the plastic multiplier has to be determined based on the relation $\Phi_{n+1} \overset{!}{=} 0$, here given by $\Phi_{n+1} = \|\operatorname{dev}\boldsymbol{\sigma}_{n+1}\| - \sqrt{\frac{2}{3}}(y_0 + h\,\alpha_{n+1})$. This is done by regarding a trial state of the yield criterion as

$$\Phi^{\text{trial}} = \|\operatorname{dev}\boldsymbol{\sigma}_{n+1}\| - \sqrt{\tfrac{2}{3}}(y_0 + h\,\alpha_n)\,, \tag{2.67}$$

with the directly approximated stresses $\boldsymbol{\sigma}_{n+1}$ and $\alpha^{\text{trial}} = \alpha_n$. The stresses $\boldsymbol{\sigma}_{n+1}$ have to be determined with respect to a trial state for pure displacement formulations. As mentioned before, for mixed stress-displacement formulations, with a direct approximation of the stresses, no trial stresses exist. The relation for $\Delta_t\gamma$ is obtained, by inserting the hardening law $(2.66)_2$ into $\Phi_{n+1} \overset{!}{=} 0$, by

$$\Delta_t\gamma = \frac{3\,\Phi^{\text{trial}}}{2\,h} = \frac{3\left(\|\operatorname{dev}\boldsymbol{\sigma}_{n+1}\| + \sqrt{\frac{2}{3}}(y_0 + h\,\alpha_n)\right)}{2\,h}\,. \tag{2.68}$$

This relation for $\Delta_t\gamma$ holds for mixed stress-displacement formulations. A summary of the basic requirements for elasto-plasticity at small strains are listed in Table 2.2.

Table 2.2: Von Mises J_2-plasticity model at small strains

Kinematics	$\boldsymbol{\varepsilon} = \nabla^s\boldsymbol{u} = \boldsymbol{\varepsilon}^e + \boldsymbol{\varepsilon}^p$
Stress relation	$\boldsymbol{\sigma} = \partial_{\boldsymbol{\varepsilon}^e}\psi$
Free energy	$\psi(\boldsymbol{\varepsilon}^e, \alpha) = \psi^e(\boldsymbol{\varepsilon}^e) + \psi^p(\alpha)$
Von Mises yield function	$\Phi(\boldsymbol{\sigma}, \beta) = \|\operatorname{dev}\boldsymbol{\sigma}\| + \sqrt{\frac{2}{3}}(y_0 + \beta)$
Reduced dissipation inequality	$\mathcal{D}_{\text{red}} = \boldsymbol{\sigma} : \dot{\boldsymbol{\varepsilon}}^p + \beta\,\dot{\alpha} \geq 0$
Lagrange functional	$\mathfrak{L}(\boldsymbol{\sigma}, \beta, \gamma) = -\mathcal{D}_{\text{red}} + \gamma\,\Phi(\boldsymbol{\sigma}, \beta)$
Associative flow rule	$\dot{\boldsymbol{\varepsilon}}^p = \gamma\,\partial_{\boldsymbol{\sigma}}\Phi(\boldsymbol{\sigma}, \beta)$
Hardening law	$\dot{\alpha} = \gamma\,\partial_\beta\Phi(\boldsymbol{\sigma}, \beta)$
Optimality conditions	$\gamma \geq 0,\ \Phi \leq 0$ and $\gamma\,\Phi = 0$

2.5.3 Rate-independent elasto-plastic material description at finite strains

The fundamental assumption for the framework of elasto-plasticity at finite strains is the multiplicative decomposition of the deformation gradient into an elastic and a plastic part:

$$\boldsymbol{F} = \boldsymbol{F}^e \cdot \boldsymbol{F}^p\,, \quad \text{with} \quad \boldsymbol{F}^e = F^{e\,a}{}_{\bar{a}}\,\boldsymbol{e}_a \otimes \boldsymbol{Z}^{\bar{a}} \quad \text{and} \quad \boldsymbol{F}^p = F^{p\,\bar{a}}{}_A\,\boldsymbol{Z}_{\bar{a}} \otimes \boldsymbol{E}^A\,. \tag{2.69}$$

This approach considers an intermediate configuration theory, see Simo and Miehe [215] and Miehe and Stein [163], which introduce a third intermediate configuration of the

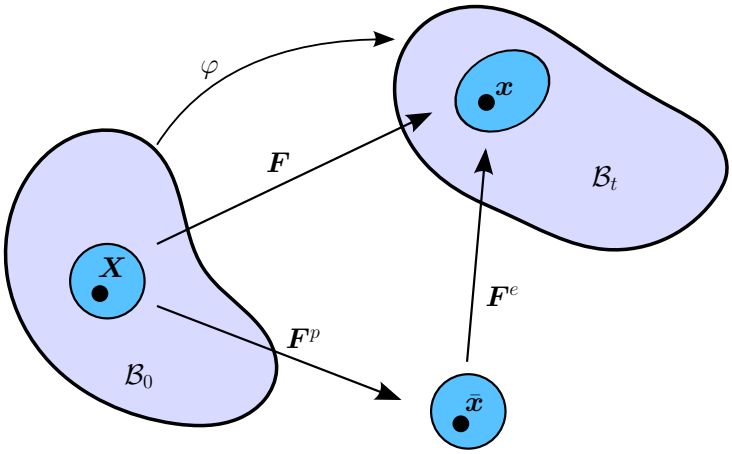

Figure 2.2: Idea of multiplicative elasto-plasticity using an intermediate configuration

body with the corresponding right-handed orthogonal basis system $\boldsymbol{Z}_{\bar{a}}$ for $\bar{a} = 1, 2, 3$, see Figure 2.2.

The intermediate configuration must not be seen as a physically real state of a body and is motivated by the micromechanical behavior, e.g., of metals and the movement of its crystal lattice occurring under deformations. In general, the intermediate configuration is characterized as a stress-free unloaded configuration, in which the plastic deformations are stored. In the intermediate configuration, the elastic strains are given by the elastic right Cauchy-Green tensor

$$\boldsymbol{C}^e = \boldsymbol{F}^{e\,T} \cdot \boldsymbol{F}^e ; \quad \boldsymbol{C}^e = F^{e\,a}{}_{\bar{a}}\, \delta_{ab}\, F^{e\,b}{}_{\bar{b}}\, \boldsymbol{Z}^{\bar{a}} \otimes \boldsymbol{Z}^{\bar{b}} , \tag{2.70}$$

and the plastic strains are determined by

$$\boldsymbol{B}^p = \boldsymbol{F}^p \cdot \boldsymbol{F}^{p\,T} ; \quad \boldsymbol{B}^p = F^{p\,\bar{a}}{}_{A}\, \delta^{AB}\, F^{p\,\bar{b}}{}_{B}\, \boldsymbol{Z}_{\bar{a}} \otimes \boldsymbol{Z}_{\bar{b}} , \tag{2.71}$$

see Simo and Miehe [215] and Miehe and Stein [163]. This assumption was first introduced by Lee and Liu [145] and Lee [148] and is motivated through the micromechanics of crystal plasticity, cf., e.g., Hill [114] and Asaro [14]. A detailed description of the continuum mechanical and kinematical foundations of multiplicative elasto-plasticity as well as a discussion on the micromechanical origins are given, e.g., in Kröner [141], Lee [148], Asaro [14], Lubliner [154], Simo and Hughes [214], Simo [213] and Armero [5].
Furthermore, the application of the multiplicative decomposition of $\boldsymbol{F}$ yields an elastic left and a plastic right Cauchy-Green tensor, i.e.,

$$\boldsymbol{B}^e = \boldsymbol{F}^e \cdot \boldsymbol{F}^{e\,T} = \boldsymbol{F} \cdot \boldsymbol{C}^{p\,-1} \cdot \boldsymbol{F}^T ; \quad \boldsymbol{B}^e = F^{e\,a}{}_{\bar{a}}\, \delta^{\bar{a}\bar{b}}\, F^{e\,b}{}_{\bar{b}}\, \boldsymbol{e}_a \otimes \boldsymbol{e}_b , \tag{2.72}$$

and

$$\boldsymbol{C}^p = \boldsymbol{F}^{p\,T} \cdot \boldsymbol{F}^p = \boldsymbol{F}^T \cdot \boldsymbol{B}^{e\,-1} \cdot \boldsymbol{F} ; \quad \boldsymbol{C}^p = F^{p\,\bar{a}}{}_{A}\, \delta_{\bar{a}\bar{b}}\, F^{p\,\bar{b}}{}_{B}\, \boldsymbol{E}^A \otimes \boldsymbol{E}^B , \tag{2.73}$$

with $\boldsymbol{B}^e$ in the actual and $\boldsymbol{C}^p$ in the reference configuration. Following the concept of thermodynamic a consistent finite elasto-plasticity model is derived based on the fulfillment of the first and second law of thermodynamics, cf. (2.50). In order to guarantee this for the dissipative effects of elasto-plastic deformations, process and internal variables

have to be introduced, which are, for the here considered isothermal and isotropic model, given by the elastic left Cauchy-Green tensor $\boldsymbol{B}^e$, the plastic right Cauchy-Green tensor $\boldsymbol{C}^p$ and the internal plastic variable α.
The Clausius-Duhem inequality, cf. (2.52), for finite isothermal, isotropic deformation processes with respect to the Kirchhoff stresses $\boldsymbol{\tau}$ is given by

$$\mathcal{D} = \boldsymbol{\tau} : \boldsymbol{D} - \dot{\psi} \geq 0\,. \tag{2.74}$$

The considered free energy function $\psi(\boldsymbol{B}^e, \alpha)$ can be additively decomposed into an elastic part $\psi^e(\boldsymbol{B}^e)$ (2.57) and a plastic pseudo potential $\psi^p(\alpha)$. Furthermore, the material time derivative of $\psi(\boldsymbol{B}^e, \alpha)$ reads

$$\dot{\psi}(\boldsymbol{B}^e, \alpha) = \dot{\psi}^e(\boldsymbol{B}^e) + \dot{\psi}^p(\alpha) = \frac{\partial \psi^e}{\partial \boldsymbol{B}^e} : \dot{\boldsymbol{B}}^e + \frac{\partial \psi^p}{\partial \alpha}\,\dot{\alpha}\,, \tag{2.75}$$

where

$$\dot{\boldsymbol{B}}^e = (\boldsymbol{F} \cdot \boldsymbol{C}^{p\,-1} \cdot \boldsymbol{F}^T)^{\cdot} = \boldsymbol{L} \cdot \boldsymbol{B}^e + \boldsymbol{\pounds}(\boldsymbol{B}^e) + \boldsymbol{B}^e \cdot \boldsymbol{L}^T\,, \tag{2.76}$$

denotes the material time derivative of the elastic left Cauchy-Green tensor in dependence of the spatial velocity gradient, cf. (2.14). Furthermore, $\dot{\boldsymbol{B}}^e$ is denoted in terms of the Lie derivative of $\boldsymbol{B}^e$ defined by

$$\boldsymbol{\pounds}(\boldsymbol{B}^e) = \boldsymbol{F} \cdot \frac{\partial}{\partial t}(\boldsymbol{C}^{p\,-1}) \cdot \boldsymbol{F}^T = \boldsymbol{F} \cdot \dot{\boldsymbol{C}}^{p\,-1} \cdot \boldsymbol{F}^T\,, \tag{2.77}$$

see, e.g., the works of Simo [213], Truesdell and Toupin [230] and Marsden and Hughes [159]. The Lie derivative represents a time derivative of coefficients of spatial tensors in a moving base. Therefore, a spatial quantity is transferred into the reference configuration by a pull-back operation, then linearized in this configuration and finally transferred into the current configuration by a push-forward operation. The Lie derivative only describes the coefficient derivative and thus represents only a part of the total time derivative of the quantity. The complete derivative is given by the coefficient derivative $(\boldsymbol{F} \cdot \dot{\boldsymbol{C}}^{p\,-1} \cdot \boldsymbol{F}^T)$ as well as the derivative of the basis vector (here in terms of $\boldsymbol{L} = \dot{\boldsymbol{F}} \cdot \boldsymbol{F}^{-1}$).
The Clausius-Duhem inequality is reformulated using (2.75) and (2.76) and the relation for the symmetric part of the spatial velocity gradient (2.15) to

$$\begin{aligned}
\mathcal{D} &= \boldsymbol{\tau} : \boldsymbol{D} - \dot{\psi} \geq 0 \\
&= \boldsymbol{\tau} : \boldsymbol{D} - \frac{\partial \psi^e}{\partial \boldsymbol{B}^e} : \dot{\boldsymbol{B}}^e - \frac{\partial \psi^p}{\partial \alpha}\,\dot{\alpha} \geq 0 \\
&= \boldsymbol{\tau} : \boldsymbol{D} - \frac{\partial \psi^e}{\partial \boldsymbol{B}^e} : (\boldsymbol{L} \cdot \boldsymbol{B}^e) - \frac{\partial \psi^e}{\partial \boldsymbol{B}^e} : (\boldsymbol{B}^e \cdot \boldsymbol{L}^T) - \frac{\partial \psi^e}{\partial \boldsymbol{B}^e} : \boldsymbol{\pounds}(\boldsymbol{B}^e) - \frac{\partial \psi^p}{\partial \alpha}\,\dot{\alpha} \geq 0 \\
&= \left(\boldsymbol{\tau} - 2\,\frac{\partial \psi^e}{\partial \boldsymbol{B}^e} \cdot \boldsymbol{B}^e\right) : \boldsymbol{D} - \left(2\,\frac{\partial \psi^e}{\partial \boldsymbol{B}^e} \cdot \boldsymbol{B}^e\right) : \left(\frac{1}{2}\,\boldsymbol{\pounds}(\boldsymbol{B}^e) \cdot \boldsymbol{B}^{e\,-1}\right) - \frac{\partial \psi^p}{\partial \alpha}\,\dot{\alpha} \geq 0\,.
\end{aligned} \tag{2.78}$$

Here, the fulfillment of (2.78) directly leads the constitutive relation for the Kirchhoff stress tensor $\boldsymbol{\tau}$ with

$$\boldsymbol{\tau} = 2\,\frac{\partial \psi^e}{\partial \boldsymbol{B}^e} \cdot \boldsymbol{B}^e\,, \tag{2.79}$$

cf., e.g., Miehe [162], which results in the reduced dissipation inequality

$$\mathcal{D}_{\text{red}} = -\boldsymbol{\tau} : \Big(\frac{1}{2}\boldsymbol{\pounds}(\boldsymbol{B}^e)\cdot\boldsymbol{B}^{e\,-1}\Big) + \beta\,\dot{\alpha} \geq 0\,. \tag{2.80}$$

Analogously to the small strain framework, $\beta = -\partial_\alpha \psi^p$ denotes the thermodynamic force associated to the internal variable and $\Phi(\boldsymbol{\tau}, \beta)$ is the yield criterion. The evolution equations for $\boldsymbol{C}^{p\,-1}$ and α, fulfilling the Clausius-Duhem inequality, are determined by a Lagrange functional

$$\mathfrak{L}(\boldsymbol{\tau}, \beta, \gamma) = \boldsymbol{\tau} : \Big(\frac{1}{2}\,\boldsymbol{\pounds}(\boldsymbol{B}^e)\cdot\boldsymbol{B}^{e\,-1}\Big) - \beta\,\dot{\alpha} + \gamma\,\Phi(\boldsymbol{\tau}, \beta) \to \text{stat.} \quad \text{with} \quad \gamma \geq 0\,, \tag{2.81}$$

as an optimization problem with constraint condition. Enforcing stationarity conditions for the Lagrangian functional, $\partial_{\boldsymbol{\tau},\beta,\gamma}\mathfrak{L} = 0$, yields

$$\frac{1}{2}\,\boldsymbol{\pounds}(\boldsymbol{B}^e)\cdot\boldsymbol{B}^{e\,-1} = -\gamma\,\partial_{\boldsymbol{\tau}}\Phi\,, \quad \dot{\alpha} = \gamma\,\partial_\beta\Phi \quad \text{and} \quad \Phi = 0\,, \tag{2.82}$$

which are the flow rule $(2.82)_1$, the evolution equation of the internal variable α $(2.82)_2$ and the consistency condition $(2.82)_3$. For a fulfillment of (2.81), the well-known Kuhn-Tucker conditions must hold. These conditions in combination with the consistency condition are given in (2.63). A reformulation of the flow rule in $(2.82)_1$ and the evolution equation of the internal variable in $(2.82)_2$ with respect to $\boldsymbol{C}^p$ and α yields

$$\dot{\boldsymbol{C}}^{p\,-1} = -2\,\gamma\,(\boldsymbol{F}^{-1}\cdot\partial_{\boldsymbol{\tau}}\Phi(\boldsymbol{\tau}, \beta)\cdot\boldsymbol{F})\cdot\boldsymbol{C}^{p\,-1} \quad \text{and} \quad \dot{\alpha} = \sqrt{\tfrac{2}{3}}\gamma\,. \tag{2.83}$$

As already mentioned in the small strain framework, the region of elastic deformation is dependent on the chosen yield criterion. In the proposed contribution, a von Mises yield criterion for finite deformation, based on the Kirchhoff stresses $\boldsymbol{\tau}$, is defined by

$$\Phi(\boldsymbol{\tau}, \beta) = \|\operatorname{dev}\boldsymbol{\tau}\| - \sqrt{\tfrac{2}{3}}(y_0 + \beta)\,. \tag{2.84}$$

For simplicity, an isotropic linear hardening where the conjugated internal variable $\beta = h\,\alpha$ is chosen, thus $\psi^p = \frac{1}{2}h\,\alpha^2$, if not declared differently. The evolution equations for the internal variable $\dot{\alpha}$ and for the plastic flow, given through the inverse plastic right Cauchy-Green tensor $\dot{\boldsymbol{C}}^{p\,-1}$, are determined by applying the following time integration schemes. Analogously to the small strain framework, a backward Euler scheme is considered for the time integration of the evolution equation of the internal variable see (2.66). In contrast to that, the applied time integration for $\dot{\boldsymbol{C}}^{p\,-1}$ is an exponential map algorithm within an implicit time integration scheme, first introduced by Weber and Anand [232] and Eterovic and Bathe [96] and further regarded, e.g., in Simo [212], Cuitino and Ortiz [84], Simo and Miehe [215] and Miehe and Stein [163]. This exponential map algorithm exactly fulfills plastic incompressibility for the J_2-theory ($\det\boldsymbol{C}^p = 1$), see, e.g., Simo [212]. Furthermore, the implementation is based on a closest-point-projection algorithm and further a radial return method for the associated plasticity model is utilized. The resulting flow rule reads

$$\boldsymbol{C}^{p\,-1}_{n+1} = \exp\Big[-2\,\Delta_t\gamma\,\Big(\boldsymbol{F}^{-1}_{n+1}\cdot\frac{\partial\Phi_{n+1}}{\partial\boldsymbol{\tau}_{n+1}}\cdot\boldsymbol{F}_{n+1}\Big)\Big]\cdot\boldsymbol{C}^{p\,-1}_{n}\,. \tag{2.85}$$

A simplification of the expression for the exponential function is obtained by

$$\boldsymbol{C}_{n+1}^{p\,-1} = \boldsymbol{F}_{n+1}^{-1} \cdot \exp\Big[-2\,\Delta_t\gamma\,\boldsymbol{n}_{n+1}\Big] \cdot \boldsymbol{F}_{n+1} \cdot \boldsymbol{C}_n^{p\,-1}\,, \tag{2.86}$$

regarding the relation for commutating matrices $\boldsymbol{A}$ and $\boldsymbol{D}$, i.e., $\boldsymbol{A}\cdot\boldsymbol{D} = \boldsymbol{D}\cdot\boldsymbol{A}$, by

$$\exp[\boldsymbol{A}\cdot\boldsymbol{D}\cdot\boldsymbol{A}^{-1}] = \boldsymbol{A}\cdot\exp[\boldsymbol{D}]\cdot\boldsymbol{A}^{-1}\,. \tag{2.87}$$

Here, $\Delta_t\gamma := \gamma\Delta t$ with $\Delta t = t_{n+1} - t_n$ and $\boldsymbol{n}_{n+1} = \operatorname{dev}\boldsymbol{\tau}_{n+1}/\|\operatorname{dev}\boldsymbol{\tau}_{n+1}\|$. For the sake of completeness, the requirement of plastic incompressibility given with $\det\boldsymbol{C}^p = 1$ holds, if $\det\boldsymbol{C}_{n+1}^p = \det\boldsymbol{C}_n^p$. This is achieved by computing the determinant of equation (2.86):

$$\det\boldsymbol{C}_{n+1}^{p-1} = \det\boldsymbol{F}_{n+1}^{-1}\,\underbrace{\exp[\operatorname{tr}(-2\Delta_t\gamma\,\partial_{\boldsymbol{\tau}}\Phi_{n+1})]}_{=1}\,\det\boldsymbol{F}_{n+1}\,\det\boldsymbol{C}_n^{p-1} = \det\boldsymbol{C}_n^{p-1}\,, \tag{2.88}$$

with $\det(\exp[\boldsymbol{A}]) = \exp[\operatorname{tr}(\boldsymbol{A})]$ and $\operatorname{tr}[-2\,\Delta_t\gamma\,\partial_{\boldsymbol{\tau}}\Phi_{n+1}] = 0$, based on the chosen von Mises yield criterion in terms of the deviatoric stresses with $\operatorname{tr}(\operatorname{dev}\boldsymbol{\tau}) = 0$, see ,e.g., Simo [212] and Miehe and Stein [163].
The basic equations for elasto-plasticity at finite strains are summarized in Table 2.3. For further derivations, the index $n+1$ is omitted for notational simplicity for quantities at the actual time step t_{n+1}. Quantities at the previous time step t_n are still denoted with the index n.

Table 2.3: Von Mises J_2-plasticity model at finite strains

Kinematics	$\boldsymbol{F} = \boldsymbol{1} + \nabla_X\boldsymbol{u} = \boldsymbol{F}^e\cdot\boldsymbol{F}^p$
	$\boldsymbol{B}^e = \boldsymbol{F}^e\cdot\boldsymbol{F}^{e\,T} = \boldsymbol{F}\cdot\boldsymbol{C}^{p\,-1}\cdot\boldsymbol{F}^T$
Stress relation	$\boldsymbol{\tau} = 2\,\partial_{\boldsymbol{B}^e}\psi^e(\boldsymbol{B}^e)\cdot\boldsymbol{B}^e$
Free energy	$\psi(\boldsymbol{B}^e,\alpha) = \psi^e(\boldsymbol{B}^e) + \psi^p(\alpha)$
Von Mises yield function	$\Phi(\boldsymbol{\tau},\beta) = \|\operatorname{dev}\boldsymbol{\tau}\| + \sqrt{\frac{2}{3}}\beta \le 0$
Reduced dissipation inequality	$\mathcal{D}_{\text{red}} = -\boldsymbol{\tau} : \Big(\frac{1}{2}\boldsymbol{\pounds}(\boldsymbol{B}^e)\cdot\boldsymbol{B}^{e\,-1}\Big) + \beta\,\dot\alpha \ge 0$
Lagrange functional	$\mathfrak{L}(\boldsymbol{\tau},\beta,\gamma) = -\mathcal{D}_{\text{red}} + \gamma\,\Phi(\boldsymbol{\tau},\beta)$
Associative flow rule	$\frac{1}{2}\boldsymbol{\pounds}(\boldsymbol{B}^e)\cdot\boldsymbol{B}^{e\,-1} = -\gamma\,\partial_{\boldsymbol{\tau}}\Phi$
	$\dot{\boldsymbol{C}}^{p\,-1} = -2\,\gamma\,(\boldsymbol{F}^{-1}\cdot\partial_{\boldsymbol{\tau}}\Phi(\boldsymbol{\tau},\beta)\cdot\boldsymbol{F})\cdot\boldsymbol{C}_n^{p\,-1}$
Hardening law	$\dot\alpha = \gamma\,\partial_\beta\Phi(\boldsymbol{\tau},\beta)$
Optimality conditions	$\gamma \ge 0,\ \Phi \le 0$ and $\gamma\,\Phi = 0$

3 Finite element formulations

As already introduced in Chapter 1, the topic of FEM and mixed FEM is extremely comprehensive and the methods have been consolidated and well established over the years. The terminology of the word mixed, in the underlying work, indicates the fact, that the system is depending on more than one unknown quantity. However, this definition does not give any restrictions on the resulting system of equations. This means, mixed formulations include here, e.g., formulations leading to saddle point problems, defined by zero diagonal terms, based on the characterization of constraint variables within the system and minimization problem, in which the main diagonal is unequal to zero.
For convenience, the basic mathematical principles for the underlying work are given at first, as a brief definition of function spaces, their relations and properties. The following representation of different mixed finite element formulations starts with a simple single field problem given as a pure displacement formulation. By means of this, mixed variational or mixed Galerkin formulations as well as mixed least-squares finite element formulations are presented. For simplicity, the formulations are considered for the example of linear elasticity and shall illustrate the classification of LSFEM in the context of other well-known finite element formulations. The main focus in this thesis will be on the LSFEM for several problems in elasticity and physical nonlinearities as hyperelastic and elasto-plastic material behavior.
Furthermore, the basic concept of the finite element method is introduced in terms of discretization of the system with finite elements and some implementation aspects are given for the discussed formulations. The basic aspects of the FEM are given in a variety of textbooks, see, e.g., Zienkiewicz and Taylor [246], Bathe [24], Wriggers [236] and Chen [74], besides others. In addition to that, ideas of standard and mixed finite elements are presented, e.g., in Brezzi and Fortin [56], Bathe [24], Auricchio et al. [17], Braess [50], Wriggers [236], Bochev and Gunzburger [43] and Boffi et al. [49], among others.
In the following, a main focus will be addressed to the established mixed methods of Hellinger-Reissner and Hu-Washizu, see Hellinger [107], Prange [183], Reissner [190], Fraeijs de Veubeke [100], Hu [117] and Washizu [231]. The main objective of this subsequent analysis of different variational methods, which are all based on the weighted residual method, is to place the LSFEM in the context of existing and well established methods. For this purpose, the considered variational formulations and the LSFEM are introduced and discussed using the example of linear elasticity. In addition, basic properties of the methods are listed and a short overview of further formulations and improvements of the presented formulations are given.
In summary, the chapter below includes the following topics:

- The mathematical principles which are applied are briefly presented.
- An overview of basic established methods based on the method of weighted residuals and their context is provided with a special consideration of the primarily discussed LSFEM.
- The idea of a discretization with finite elements is introduced and followed for completeness by a representation of finite element approximation functions in $\mathcal{W}^{1,p}(\mathcal{B})$

and $\mathcal{W}^q(\mathrm{div}, \mathcal{B})$. Approaches for a construction of the functions in the reference and current configuration, based on straight edged elements, are explained.

- Furthermore, general aspects of the finite element implementation and convergence assumptions are discussed.

3.1 Basic mathematical principles

In the procedure of finding the solution of a problem within the finite element method, the unknown field variables have to be given in suitable function spaces. Therefore, some common and well known function spaces are introduced in the following, based on the works, e.g., of Brenner and Scott [53] and Brezzi and Fortin [56]. The here discussed function spaces are restricted to the Sobolev space $\mathcal{W}^{m,p}(\mathcal{B})$ and the related subspaces, all defined by the Lebesque space $\mathcal{L}^p(\mathcal{B})$, which is characterized by p-integrable functions on $\mathcal{B}$. A function υ is embedded in the Lebesque space $\mathcal{L}^p(\mathcal{B})$, if the integral of the p-th power of the function is bounded, cf., e.g., Zienkiewicz et al. [250] and Brenner and Scott [53], which is

$$\mathcal{L}^p(\mathcal{B}) := \{\upsilon : \|\upsilon\|_{\mathcal{L}^p(\mathcal{B})} < +\infty\} \quad \text{for } 0 < p < \infty\,, \tag{3.1}$$

and the corresponding norm is denoted by

$$\|\upsilon\|_{\mathcal{L}^p(\mathcal{B})} := \left(\int_{\mathcal{B}} |\upsilon|^p \,\mathrm{d}V \right)^{1/p} . \tag{3.2}$$

The Sobolev space $\mathcal{W}^{m,p}(\mathcal{B})$ with $m \geq 0$ is defined by

$$\mathcal{W}^{m,p}(\mathcal{B}) := \{\upsilon + \sum_{\alpha=1}^{m} D^{\boldsymbol{\alpha}}\upsilon \in \mathcal{L}^p(\mathcal{B})\} \quad \text{for } 1 \leq p < \infty\,, \tag{3.3}$$

with the relation $\mathcal{W}^{0,p}(\mathcal{B}) = \mathcal{L}^p(\mathcal{B})$ for $m = 0$ and $D^{\boldsymbol{\alpha}}\upsilon$ as the α-th weak differential operator, defining the weak derivative of υ up to order m, where

$$D^{\boldsymbol{\alpha}}\upsilon = \frac{\partial^{|\boldsymbol{\alpha}|}\upsilon}{\partial x_1^{\alpha_1} \partial x_2^{\alpha_2} \partial x_n^{\alpha_n}} \quad \text{with} \quad \left\{ \begin{array}{c} \boldsymbol{\alpha} = (\alpha_1, \alpha_2, \alpha_3) \\ |\boldsymbol{\alpha}| = \alpha_1 + \alpha_2 + \alpha_3 \end{array} \right. , \tag{3.4}$$

cf., e.g., Brezzi and Fortin [56] chapter 3.1. In the framework of finite elements suitable function spaces for the unknown field variables are often given as the Sobolev spaces $\mathcal{W}^{1,p}(\mathcal{B})$ and $\mathcal{W}^q(\mathrm{div}, \mathcal{B})$ with

$$\mathcal{W}^{1,p}(\mathcal{B}) := \{\upsilon \in \mathcal{L}^p(\mathcal{B}) \;:\; D^1\upsilon \in \mathcal{L}^p(\mathcal{B})\} \quad \text{for } 1 \leq p < \infty\,, \tag{3.5}$$

and

$$\mathcal{W}^q(\mathrm{div}, \mathcal{B}) := \{\upsilon \in \mathcal{L}^q(\mathcal{B}) \;:\; \mathrm{div}\,\upsilon \in \mathcal{L}^q(\mathcal{B})\} \quad \text{for } 1 \leq q < \infty\,. \tag{3.6}$$

The associated norms of the Sobolev spaces contain also constraints for the derivatives of the functions denoted by

$$\|\upsilon\|_{\mathcal{W}^{m,p}(\mathcal{B})} := \left(\|\upsilon\|^p_{\mathcal{L}^p(\mathcal{B})} + \sum_{\alpha=1}^{m} \|D^{\boldsymbol{\alpha}}\upsilon\|^p_{\mathcal{L}^p(\mathcal{B})} \right)^{1/p} , \tag{3.7}$$

and

$$\|\upsilon\|_{\mathcal{W}^q(\mathrm{div},\mathcal{B})} := \left(\|\upsilon\|^q_{\mathcal{L}^q(\mathcal{B})} + \|\operatorname{div}\upsilon\|^q_{\mathcal{L}^q(\mathcal{B})} \right)^{1/q} . \tag{3.8}$$

Here, the $\mathcal{L}^p(\mathcal{B})$-norm for vector functions $\boldsymbol{\upsilon} \in [\mathcal{L}^p(\mathcal{B})]^n$ and tensor functions $\boldsymbol{\Upsilon} \in [\mathcal{L}^p(\mathcal{B})]^{n\times m}$ is defined analogously to scalar quantities as

$$\|\boldsymbol{\upsilon}\|_{\mathcal{L}^p(\mathcal{B})} := \left(\sum_{i=1}^{n} \|\upsilon_i\|^p_{\mathcal{L}^p(\mathcal{B})} \right)^{1/p} \quad \text{and} \quad \|\boldsymbol{\Upsilon}\|_{\mathcal{L}^p(\mathcal{B})} := \left(\sum_{i=1}^{n}\sum_{j=1}^{m} \|\Upsilon_{ij}\|^p_{\mathcal{L}^p(\mathcal{B})} \right)^{1/p} , \tag{3.9}$$

where all components of $\upsilon_i, \Upsilon_{ij} \in \mathcal{L}^p(\mathcal{B})$, see, e.g., Brezzi and Fortin [56] and Arnold et al. [10]. The measure p denotes the value of the exponent of the associated function that arises within the considered problem. A suitable measure for p and q in the framework of linear elasticity is $p = q = 2$, which is equivalent to the Hilbert space $\mathcal{H}^m$, as a subspace of the Sobolev space $\mathcal{W}^p$, with the relation

$$\mathcal{W}^{m,2}(\mathcal{B}) = \mathcal{H}^m(\mathcal{B}) \quad \text{and further} \quad \mathcal{W}^2(\mathrm{div},\mathcal{B}) = \mathcal{H}(\mathrm{div},\mathcal{B}) . \tag{3.10}$$

Therefore, all Hilbert spaces are related to the $\mathcal{L}^2(\mathcal{B})$ space and contain functions, which are at least square-integrable functions. The order of Hilbert spaces can be characterized by means of the continuity requirement of the considered functions, where the space $\mathcal{H}^m$ includes all $\mathcal{C}^{m-1}$ continuous square-integrable functions. In the following sections, the mainly considered function spaces, beside $\mathcal{W}^{1,p}(\mathcal{B})$ and $\mathcal{W}^q(\mathrm{div},\mathcal{B})$, are

$$\mathcal{H}^1(\mathcal{B}) = \{\upsilon \,|\, \upsilon \in \mathcal{L}^2(\mathcal{B}) \,:\, D^1\upsilon \in \mathcal{L}^2(\mathcal{B})\} , \tag{3.11}$$

and

$$\mathcal{H}(\mathrm{div},\mathcal{B}) = \{\upsilon \,|\, \upsilon \in \mathcal{L}^2(\mathcal{B}) \,:\, \operatorname{div}\upsilon \in \mathcal{L}^2(\mathcal{B})\} , \tag{3.12}$$

cf. Brenner and Scott [53], Brezzi and Fortin [56] and Boffi et al. [49]. An overview of the relations of the mentioned spaces are illustrated, for $3 \leq m < \infty$, by

$$\begin{array}{ccccccccccc} & & \mathcal{L}^p & \widehat{=} & \mathcal{W}^{0,p} & \supset & \mathcal{W}^{1,p} & \supset & \mathcal{W}^{2,p} & \supset & \mathcal{W}^{m,p} \\ & & \cup & & \cup & & \cup & & \cup & & \cup \\ \mathcal{W}^{0,2} & \widehat{=} & \mathcal{L}^2 & \widehat{=} & \mathcal{H}^0 & \supset & \mathcal{H}^1 & \supset & \mathcal{H}^2 & \supset & \mathcal{H}^m \end{array} \tag{3.13}$$

In addition to the function spaces $\mathcal{W}^{1,p}(\mathcal{B})$ for $0 \geq p \geq \infty$ with p as a integer greater than or equal to 0, there are further function spaces which also apply to $p \in \mathbb{R}$. These function spaces can be expressed by interpolations between two spaces, e.g., $\mathcal{L}^p(\mathcal{B})$ and $\mathcal{W}^{1,p}(\mathcal{B})$ and are generally denoted as Besov spaces, i.e.,

$$\mathfrak{B}^{m,p}(\mathcal{B}) = (\mathcal{L}^p(\mathcal{B}), \mathcal{W}^{1,p}(\mathcal{B}))_{m,p} \quad \text{for } 0 < m < 1, 1 \leq p \leq \infty . \tag{3.14}$$

A more detailed account of these spaces can be found in Bergh and Löfström [30] and Brenner and Scott [54]. The Besov spaces $\mathfrak{B}^{m,p}$ are more general than Sobolev spaces $\mathcal{W}^{m,p}$ and for simplicity are often denoted as Sobolev spaces $\mathcal{W}^{m,p}$ for $0 < m < 1$. Nevertheless, these spaces do not entirely correspond for the limiting case $m \to 1$.

Note that, in general the corresponding fields on a domain $\mathcal{B}$ and the associated finite element space can be projected with respect to so-called trace operators onto the boundaries $\partial\mathcal{B}$, i.e.,

$$\mathrm{tr} : \mathcal{W}^{m,p}(\mathcal{B}) \to \mathcal{W}^{m-1/2,p}(\partial\mathcal{B}) \tag{3.15}$$

see, e.g., Brenner and Scott [53], Bergh and Löfström [30], which defines a surjective but not injective mapping. The trace operators are often considered in the framework of hybrid finite element approaches and thus, define the spaces for the Lagrange multipliers on the boundaries.

3.2 Aspects of displacement and mixed finite element formulations

The basic idea for finding the solution of PDEs is to introduce an approximation, e.g., of the exact solution of the displacement field $\boldsymbol{u}$ as $\boldsymbol{u}_h$, which leads to an error in the fulfillment of the underlying setup of equations, since the approximation is in general not equal to the exact solution. The Galerkin method approximates the solution of operator equations, such as PDEs and represents the most common variant of the so-called weighted residual method, in which the resulting residual equations of an approximate solution is minimized. In the following, the Galerkin method is applied to derive the so-called weak formulation of the PDE, which describes the underlying problem. The method of weighted residuals is defined in terms of residual equations $\mathcal{R}_i$ and arbitrary test functions $\boldsymbol{\eta}_i$, with i denoting the number of residual equations, which have to be solved within the related formulation. Furthermore, the application of the method with

$$\sum_i \int_{\mathcal{B}} \langle \mathcal{R}_i, \boldsymbol{\eta}_i \rangle \, \mathrm{d}V = 0 \,, \tag{3.16}$$

is characterized by a scalar multiplication of $\mathcal{R}_i$ with $\boldsymbol{\eta}_i$ and integration over the whole domain $\mathcal{B}$ of the problem. This reduces the differential equations in a weak sense to zero. Here, the scalar product of two quantities is denoted by $\langle \bullet, \bullet \rangle$. The residual equation $\mathcal{R}$ represents the error in solving the differential equation using the approximation $\boldsymbol{u}_h$. The integration over the domain is in general performed by a numerical integration, which is given throughout this thesis by the well-known Gauss integration scheme, see, e.g., Zienkiewicz and Taylor [246], Wriggers [236].

As a basis for the discussion of different finite element formulations the framework of linear elasticity is considered. The example of linear elasticity is characterized by a set of equations, which is based on the previously presented continuum mechanical fundamentals and is given by

$$\begin{aligned}
\operatorname{div} \boldsymbol{\sigma} &= -\boldsymbol{f} && \text{on } \mathcal{B} \,, \\
\boldsymbol{\sigma} &= \mathbb{C} : \boldsymbol{\varepsilon} && \text{on } \mathcal{B} \,, \\
\boldsymbol{\varepsilon} &= \nabla^s \boldsymbol{u} && \text{on } \mathcal{B} \,, \\
\boldsymbol{\sigma} &= \boldsymbol{\sigma}^T && \text{on } \mathcal{B} \,, \\
\boldsymbol{\sigma} \cdot \boldsymbol{n} &= \bar{\boldsymbol{t}} && \text{on } \partial\mathcal{B}_N \,, \\
\boldsymbol{u} &= \bar{\boldsymbol{u}} && \text{on } \partial\mathcal{B}_D \,,
\end{aligned} \tag{3.17}$$

with the Cauchy stresses defined by Hooke's law and the strain tensor for the infinitesimal theory denoted by $\boldsymbol{\varepsilon}$ and defined by the symmetric displacement gradient $\boldsymbol{\varepsilon} = \nabla^s \boldsymbol{u} = \frac{1}{2}(\nabla \boldsymbol{u} + (\nabla \boldsymbol{u})^T)$, which is the linearized Green-Lagrange strain tensor (2.12). The problem of linear elasticity is characterized by the balance of linear momentum, the

material law, for linear elasticity described by Hooke's law, the compatibility condition of the strains, the balance of angular momentum and corresponding boundary conditions, with the boundary traction and displacement $\bar{\boldsymbol{t}}$ and $\bar{\boldsymbol{u}}$. It should be noted that different types of boundary conditions exist. The boundary $\partial\mathcal{B}$ of the considered body $\mathcal{B}$ is divided into a Neumann boundary $\partial\mathcal{B}_N$ and a Dirichlet boundary $\partial\mathcal{B}_D$ with

$$\partial\mathcal{B} = \partial\mathcal{B}_D \bigcup \partial\mathcal{B}_N \quad \text{and} \quad \partial\mathcal{B}_D \bigcap \partial\mathcal{B}_N = \emptyset \,. \tag{3.18}$$

In general, the Dirichlet boundary is often referred as essential boundary conditions which are directly incorporated into the functional space and the Neumann boundary or natural boundary conditions are conditions for derivatives on the boundary of the domain, cf. Braess [50]. In the following, depending on the formulation under consideration, different setups of boundary conditions occur, each of which is briefly discussed.

3.2.1 Displacement formulation

As a basis for the following presentation of mixed FEM, a single field formulation is considered first. Here, a standard displacement method using the weighted residual method (3.16) is introduced. Therefore, the underlying problem can be characterized by a PDE system given by the balance of linear momentum and corresponding boundary conditions. For this purpose, the system of equations (3.17), which is given as a three-field formulation in displacements, strains and stresses $(\boldsymbol{u}, \boldsymbol{\varepsilon}, \boldsymbol{\sigma})$, have to be converted into a purely displacement dependent setup. For this purpose, the system (3.17) is rewritten, taking into account the material law and the compatibility condition in the balance of linear momentum, leading

$$\begin{aligned} &\operatorname{div}\boldsymbol{\sigma}(\boldsymbol{u}) + \boldsymbol{f} = \boldsymbol{0} && \text{on } \mathcal{B}\,, \\ &\boldsymbol{\sigma}(\boldsymbol{u}) \cdot \boldsymbol{n} = \bar{\boldsymbol{t}} && \text{on } \partial\mathcal{B}_N\,, \\ &\boldsymbol{u} = \bar{\boldsymbol{u}} && \text{on } \partial\mathcal{B}_D\,, \end{aligned} \tag{3.19}$$

with a restriction to homogenous Dirichlet boundary conditions. The balance of angular momentum is directly fulfilled with the symmetry relation for the strains and the related material tensor. Following (3.16) with $i = 1$ and the residual equation $\mathcal{R}$ given by $(3.19)_1$ with $\boldsymbol{\sigma} = \mathbb{C} : \nabla^s \boldsymbol{u}$, yields

$$\int_{\mathcal{B}} (\operatorname{div}\boldsymbol{\sigma}(\boldsymbol{u}) + \boldsymbol{f}) \cdot \boldsymbol{\eta} \, \mathrm{d}V = \int_{\mathcal{B}} (\operatorname{div}(\mathbb{C} : \nabla^s \boldsymbol{u}) + \boldsymbol{f}) \cdot \boldsymbol{\eta} \, \mathrm{d}V = 0\,. \tag{3.20}$$

For convenience, a restriction to equations of first-order, i.e., only derivatives of first-order are part of the treated equations, is considered in the course of this work. Nevertheless, $(3.19)_1$ respectively (3.20) could be solved as a second-order system, utilizing $\mathcal{C}^1$-continuous functions, see Bank and Scott [23] and Ern and Guermond [94], which will not be discussed here. The application of integration by parts, introducing the divergence theorem and Cauchy's theorem (2.18) yields the weak form

$$\int_{\mathcal{B}} \nabla^s \boldsymbol{u} : \mathbb{C} : \nabla \boldsymbol{\eta} \, \mathrm{d}V = \int_{B} \boldsymbol{f} \cdot \boldsymbol{\eta} \, \mathrm{d}V + \int_{\partial\mathcal{B}_N} \boldsymbol{t} \cdot \boldsymbol{\eta} \, \mathrm{d}A\,. \tag{3.21}$$

The gradient of the test function $\nabla\boldsymbol{\eta}$, with $\boldsymbol{\eta}$ often called virtual displacements and stated as $\delta\boldsymbol{u}$, can be interpreted as the directional derivative of the virtual displacement, which is $\nabla^s\delta\boldsymbol{u}$. Thus, the weak form is denoted by

$$\mathcal{G}_{\boldsymbol{u}} := \int_{\mathcal{B}} \nabla^s\boldsymbol{u} : \mathbb{C} : \nabla^s\delta\boldsymbol{u}\,\mathrm{d}V - \int_B \boldsymbol{f}\cdot\delta\boldsymbol{u}\,\mathrm{d}V - \int_{\partial\mathcal{B}_N} \bar{\boldsymbol{t}}\cdot\delta\boldsymbol{u}\,\mathrm{d}A = 0\,. \tag{3.22}$$

For the given problem (3.22) the solution is sought for $\boldsymbol{u}\in\mathcal{V}$ such that $\mathcal{G}_{\boldsymbol{u}} = 0\;\forall\;\delta\boldsymbol{u}\in\mathcal{V}$ with $\mathcal{V} := [\mathcal{H}^1(\mathcal{B})]^3$. Taking into account $\mathcal{C}^0$-continuous functions for the displacement field $\boldsymbol{u}$, the derivatives of $\boldsymbol{u}$ given by $\boldsymbol{\varepsilon}$ and $\boldsymbol{\sigma}$, since $\boldsymbol{\sigma}$ is a function of the strains, are not continuous over the complete domain. This remark of the standard displacement formulation will be considered again later on.
For completeness, if the underlying problem is given by (3.20) it yields, finding a solution $\boldsymbol{u}\in\mathcal{V}$ such that $\mathcal{G}_{\boldsymbol{u}} = 0\;\forall\;\delta\boldsymbol{u}\in\mathcal{V}$ with $\mathcal{V} := [\mathcal{H}^2(\mathcal{B})]^3$.
However, following the principle of the minimum of the total elastic potential, an alternative approach for the derivation of the weak forms depending on the free energy function and the applied loads can be formulated. Here, the energy potential is

$$\Pi(\boldsymbol{u}) = \int_{\mathcal{B}} \frac{1}{2}\nabla^s\boldsymbol{u} : \mathbb{C} : \nabla^s\boldsymbol{u}\,\mathrm{d}V - \int_{\mathcal{B}} \boldsymbol{f}\cdot\boldsymbol{u}\,\mathrm{d}V - \int_{\partial\mathcal{B}_N} \bar{\boldsymbol{t}}\cdot\boldsymbol{u}\,\mathrm{d}A\,, \tag{3.23}$$

with the free energy function for linear elasticity $\psi(\boldsymbol{u}) = \frac{1}{2}\nabla^s\boldsymbol{u} : \mathbb{C} : \nabla^s\boldsymbol{u}$. The solution for $\boldsymbol{u}$ with $\boldsymbol{u}\in[\mathcal{H}^1(\mathcal{B})]^d$, which minimizes the potential, or leads to a stationary potential for the framework of finite deformations, fulfills the differential equations and thus the equilibrium.

3.2.2 Hellinger-Reissner principle

For the analysis of mixed variational principles, the well-known Hellinger-Reissner principle as a two-field problem is presented, based on the works of Reissner [190] and the early contributions of Hellinger [107] and Prange [183], which is therefore also known as the Hellinger-Prange-Reissner principle, cf., e.g., Braess [50]. It should be noted, that there are two different forms of the Hellinger-Reissner formulation referred as the primal and dual or modified Hellinger-Reissner formulation, which are presented below. The difference in the formulations is that they lead to different natural boundary conditions, cf. Braess [50]. Both are defined as mixed problems in terms of displacement and stress field $(\boldsymbol{u},\boldsymbol{\sigma})\in\mathcal{V}\times\mathcal{S}$ and result into system matrices with a saddle point structure and therefore, the considered solution spaces and their combination $\mathcal{V}$ and $\mathcal{S}$ have to be chosen carefully, in order to guarantee existence and uniqueness of the solution. For a mathematical discussion on the existence and uniqueness of solutions, see, e.g., Brezzi and Fortin [56], Brenner and Scott [53], Auricchio et al. [17] and Braess [50].
The setup of equations characterizing linear elasticity (3.17) is reformulated for the two-field problem ($(\boldsymbol{u},\boldsymbol{\sigma})\in\mathcal{V}\times\mathcal{S}$) with $(3.17)_3$ inserted in $(3.17)_2$ providing

$$\begin{aligned}
&\operatorname{div}\boldsymbol{\sigma} + \boldsymbol{f} = \boldsymbol{0} && \text{on}\,\mathcal{B}\,,\\
&\mathbb{C}^{-1} : \boldsymbol{\sigma} = \nabla^s\boldsymbol{u} && \text{on}\,\mathcal{B}\,,\\
&\boldsymbol{\sigma} = \boldsymbol{\sigma}^T && \text{on}\,\mathcal{B}\,,\\
&\boldsymbol{\sigma}\cdot\boldsymbol{n} = \bar{\boldsymbol{t}} && \text{on}\,\partial\mathcal{B}_N\,,\\
&\boldsymbol{u} = \bar{\boldsymbol{u}} && \text{on}\,\partial\mathcal{B}_D\,.
\end{aligned} \tag{3.24}$$

Since the Cauchy stress tensor is now an independent field quantity, the symmetry condition is not fulfilled a priori by the symmetry of the strains and have to be considered separately within the chosen approximation space. The primal Hellinger-Reissner principle, hereinafter referred to as pHR, is constructed by means of (3.16). The two residual equations are given by the balance of linear momentum $(3.24)_1$ and the material law $(3.24)_2$. These are multiplied by the test functions $\boldsymbol{\eta}_i$, given as virtual displacements $\delta\boldsymbol{u}$ and virtual stresses $\delta\boldsymbol{\sigma}$, leading to the weak forms $\mathcal{G}_{\boldsymbol{u}}$ and $\mathcal{G}_{\boldsymbol{\sigma}}$ by

$$\begin{aligned} \mathcal{G}_{\boldsymbol{u}} &:= \int_{\mathcal{B}} \boldsymbol{\sigma} : \nabla^s \delta\boldsymbol{u} \, \mathrm{d}V - \int_{\mathcal{B}} \boldsymbol{f} \cdot \delta\boldsymbol{u} \, \mathrm{d}V - \int_{\partial\mathcal{B}_N} \bar{\boldsymbol{t}} \cdot \delta\boldsymbol{u} \, \mathrm{d}A = 0 \,, \\ \mathcal{G}_{\boldsymbol{\sigma}} &:= \int_{\mathcal{B}} (\nabla^s \boldsymbol{u} - \mathbb{C}^{-1} : \boldsymbol{\sigma}) : \delta\boldsymbol{\sigma} \, \mathrm{d}V = 0 \,, \end{aligned} \tag{3.25}$$

with integration by parts and introduction of the divergence and Cauchy's theorem. The terms relating to the applied forces on $\mathcal{B}$ are the same for pHR formulation as for the displacement formulation (3.22), since the natural boundary conditions are derived by reformulation of the balance of linear momentum. Based on the properties of the given weak form (3.25) the solution of the problem is sought by finding $(\boldsymbol{u}, \boldsymbol{\sigma}) \in \mathcal{V} \times \mathcal{S}$ such that $\mathcal{G}_{\boldsymbol{u}} = 0 \; \forall \; \delta\boldsymbol{u} \in \mathcal{V}$ and $\mathcal{G}_{\boldsymbol{\sigma}} = 0 \; \forall \; \delta\boldsymbol{\sigma} \in \mathcal{S}$ with $\mathcal{V} := [\mathcal{H}^1(\mathcal{B})]^3$ and $\mathcal{S} := [\mathcal{L}^2(\mathcal{B})]^{3\times3}_{\mathrm{sym}}$. These types of elements are also referred as assumed stress elements, based on the work of Pian [176].

The weak forms $\mathcal{G}_{\boldsymbol{u}}$ and $\mathcal{G}_{\boldsymbol{\sigma}}$ of the dual Hellinger-Reissner (dHR) principle, formulated in a similar way as the pHR, lead

$$\begin{aligned} \mathcal{G}_{u} &:= \int_{\mathcal{B}} \operatorname{div} \boldsymbol{\sigma} \cdot \delta\boldsymbol{u} \, \mathrm{d}V - \int_{\mathcal{B}} \boldsymbol{f} \cdot \delta\boldsymbol{u} \, \mathrm{d}V = 0 \,, \\ \mathcal{G}_{\boldsymbol{\sigma}} &:= \int_{\mathcal{B}} (\boldsymbol{\sigma} : \mathbb{C}^{-1} : \delta\boldsymbol{\sigma} + \boldsymbol{u} \cdot \operatorname{div} \delta\boldsymbol{\sigma}) \, \mathrm{d}V - \int_{\partial\mathcal{B}_D} \bar{\boldsymbol{u}} \cdot (\delta\boldsymbol{\sigma} \cdot \boldsymbol{n}) \, \mathrm{d}A = 0 \,, \end{aligned} \tag{3.26}$$

where the natural boundary conditions result from the transformation of the material law. The function spaces for the dHR formulation are chosen such that $\mathcal{G}_{\boldsymbol{u}} = 0 \; \forall \; \delta\boldsymbol{u} \in \mathcal{V}$ and $\mathcal{G}_{\boldsymbol{\sigma}} = 0 \; \forall \; \delta\boldsymbol{\sigma} \in \mathcal{S}$ with $\mathcal{V} := [\mathcal{L}^2(\mathcal{B})]^3$ and $\mathcal{S} := [\mathcal{H}(\operatorname{div}, \mathcal{B})]^{3\times3}_{\mathrm{sym}}$.

The related representation of the pHR energy potential yields

$$\Pi^{\mathrm{pHR}}(\boldsymbol{u}, \boldsymbol{\sigma}) = \int_B \left(-\frac{1}{2} \boldsymbol{\sigma} : \mathbb{C}^{-1} : \boldsymbol{\sigma} + \boldsymbol{\sigma} : \nabla^s \boldsymbol{u} \right) \mathrm{d}V - \int_{\mathcal{B}} \boldsymbol{f} \cdot \boldsymbol{u} \, \mathrm{d}V - \int_{\partial\mathcal{B}_N} \bar{\boldsymbol{t}} \cdot \boldsymbol{u} \, \mathrm{d}A \,, \tag{3.27}$$

and furthermore, the dHR energy potential leads to

$$\Pi^{\mathrm{dHR}}(\boldsymbol{u}, \boldsymbol{\sigma}) = \int_B \left(\frac{1}{2} \boldsymbol{\sigma} : \mathbb{C}^{-1} : \boldsymbol{\sigma} + (\operatorname{div} \boldsymbol{\sigma} + \boldsymbol{f}) \cdot \boldsymbol{u} \right) \mathrm{d}V - \int_{\partial\mathcal{B}_D} \bar{\boldsymbol{u}} \cdot (\boldsymbol{\sigma} \cdot \boldsymbol{n}) \, \mathrm{d}A \,. \tag{3.28}$$

As mentioned before, the difference between the primal and dual HR formulation given by the natural boundary conditions becomes obvious in the weak forms and the energy potential. The stress boundary conditions are naturally imposed within the primal formulation. For the dual formulation these stress boundary conditions have to be imposed within the function space with $\boldsymbol{\sigma} \cdot \boldsymbol{n} = \bar{\boldsymbol{t}}$ on $\partial\mathcal{B}_N$, cf. Braess [50], since the displacement boundary conditions are directly incorporated within the formulation.

In the following, primal and dual mixed formulations are classified according to their

continuity properties and the type of natural boundary conditions. The primal mixed formulations are closely related to the pure displacement formulations, in which $\boldsymbol{u} \in \mathcal{H}^1(\mathcal{B})$ such that a $\mathcal{C}^0$-continuous displacement field is obtained and the stress boundary conditions have no continuity requirements. For the dual mixed formulations, the stresses are in $\mathcal{H}(\mathrm{div}, \mathcal{B})$ and thus $\mathcal{C}^0$-continuity is required in normal direction for the stresses and the displacement boundary conditions are applied as natural boundary conditions, cf. Atluri et al. [16] and Bertóti [34] among others as well as (3.25), (3.26).

Especially, the symmetry of the stress tensor $\boldsymbol{\sigma}$ has to be considered, in the construction of Hellinger-Reissner based finite elements for elasticity. Therefore, a range of approximations are introduced, see, e.g., Stenberg [224], Arnold et al. [10], Arnold et al. [9] and Kober and Starke [135], in which the stress symmetry condition is additionally controlled in terms of a Lagrange multiplier. In Kober and Starke [135] an exact symmetry is enforced by application of Lagrange multipliers based on a non-symmetric version of the nonconforming stress space in Gopalakrishnan and Guzmán [104]. Therefore, the Raviart-Thomas space is enhanced by bubble functions, referred as bubble-curls, which are not globally continuous on the edges in $d = 2$. For the stress approximation in Gopalakrishnan and Guzmán [104] symmetric basis functions are introduced, yielding a nonconforming formulation with respect to $\mathcal{H}(\mathrm{div}, \mathcal{B})$ but exact symmetric stresses. Application of the Raviart-Thomas space for the stress approximation lead in general only to weakly symmetric stresses, cf. Boffi et al. [48]. Furthermore, a weak enforcement of stress symmetry, which leads to approximation functions of lower polynomial order, is considered in Arnold et al. [10], Arnold et al. [9], Boffi et al. [48] and Klaas et al. [132]. For the dual Hellinger-Reissner formulation, stable finite elements with strong symmetry enforcement are presented, e.g., in Arnold et al. [11], Johnson and Mercier [127], Kober and Starke [135] for $d = 2$ and for $d = 3$ in Arnold et al. [9], Arnold et al. [13]. For the pHR formulation, an often used stress approximation is given by the discontinuous 5-parameter stress approach by Pian and Sumihara [178] for $d = 2$ and extended to $d = 3$ by Pian and Tong [179]. In Yu et al. [243] and Li et al. [151] stability and an a posteriori error estimator is discussed for the primal formulation. For completeness and since the mathematical proof of stability is avoided in this work, a proof of the inf-sup stability of a primal and dual HR formulations can be found in Braess [50].

3.2.3 Hu-Washizu principle

The second presented mixed Galerkin formulation is referred as the Hu-Washizu (HW) principle, based on the works of Hu [117] and Washizu [231]. However, the formulation can already be found in Fraeijs de Veubeke [100], cf. Felippa [98], and thus, is sometimes denoted as the de Veubeke-Hu-Washizu principle, see Braess [50]. It is defined as a three-field formulation in terms of displacements, strains and stresses for the considered framework of linear elasticity. As in the Hellinger-Reissner formulation, the application of the Hu-Washizu principle leads to a saddle point problem, which requires a careful choice and balancing of applied solution spaces to ensure uniqueness and existence of the solution. For completeness, a proof of the inf-sup stability as well as coercivity is given in Braess [50]. A discussion on the limitation of the Hu-Washizu formulation

in relation with the Hellinger-Reissner and pure displacement formulations are given in Stolarski and Belytschko [225].
The three-field formulation can be directly applied to the setup of equations for the problem of linear elasticity given in (3.17). The residual equations in (3.16) are given by the balance of linear momentum, material law and compatibility condition. Application of integration by parts and introduction of the divergence and Cauchy's theorem, yield the weak forms $\mathcal{G}_{\boldsymbol{u}}, \mathcal{G}_{\boldsymbol{\sigma}}$ and $\mathcal{G}_{\boldsymbol{\varepsilon}}$ by

$$\begin{aligned}
\mathcal{G}_{\boldsymbol{u}} &:= \int_{\mathcal{B}} \boldsymbol{\sigma} : \nabla^s \delta\boldsymbol{u} \, \mathrm{d}V - \int_{\mathcal{B}} \boldsymbol{f} \cdot \delta\boldsymbol{u} \, \mathrm{d}V - \int_{\partial\mathcal{B}_N} \bar{\boldsymbol{t}} \cdot \delta\boldsymbol{u} \, \mathrm{d}A = 0 \,, \\
\mathcal{G}_{\boldsymbol{\sigma}} &:= \int_{\mathcal{B}} (\nabla^s \boldsymbol{u} - \boldsymbol{\varepsilon}) : \delta\boldsymbol{\sigma} \, \mathrm{d}V = 0 \,, \\
\mathcal{G}_{\boldsymbol{\varepsilon}} &:= \int_{\mathcal{B}} (\mathbb{C} : \boldsymbol{\varepsilon} - \boldsymbol{\sigma}) : \delta\boldsymbol{\varepsilon} \, \mathrm{d}V = 0 \,.
\end{aligned} \tag{3.29}$$

The Hu-Washizu principle can be defined by find $(\boldsymbol{u}, \boldsymbol{\sigma}, \boldsymbol{\varepsilon}) \in \mathcal{V} \times \mathcal{S} \times \mathcal{X}$, such that $\mathcal{G} = 0 \; \forall \; (\delta\boldsymbol{u}, \delta\boldsymbol{\sigma}, \delta\boldsymbol{\varepsilon}) \in \mathcal{V} \times \mathcal{S} \times \mathcal{X}$ with $\mathcal{G} = \mathcal{G}_{\boldsymbol{u}} + \mathcal{G}_{\boldsymbol{\sigma}} + \mathcal{G}_{\boldsymbol{\varepsilon}}$, $\mathcal{V} := [\mathcal{H}^1(\mathcal{B})]^3$, $\mathcal{S} := [\mathcal{L}^2(\mathcal{B})]^{3\times3}_{\mathrm{sym}}$ and $\mathcal{X} := [\mathcal{L}^2(\mathcal{B})]^{3\times3}_{\mathrm{sym}}$. The symmetry of the strains and stresses have to be incorporated in the function spaces, since both are unconstrained by the formulation. Furthermore, the energy potential for the Hu-Washizu principle is denoted by

$$\Pi^{\mathrm{HW}}(\boldsymbol{u}, \boldsymbol{\sigma}, \boldsymbol{\varepsilon}) = \int_{\mathcal{B}} \left(\frac{1}{2} \boldsymbol{\varepsilon} : \mathbb{C} : \boldsymbol{\varepsilon} + \boldsymbol{\sigma} : (\nabla^s \boldsymbol{u} - \boldsymbol{\varepsilon}) \right) \mathrm{d}V - \int_{\mathcal{B}} \boldsymbol{f} \cdot \boldsymbol{u} \, \mathrm{d}V - \int_{\partial\mathcal{B}_N} \bar{\boldsymbol{t}} \cdot \boldsymbol{u} \, \mathrm{d}A \,. \tag{3.30}$$

Analogously to (3.22) and (3.25) the stress boundary conditions are naturally imposed within the principle. Thus, the Hu-Washizu principle is a primal formulation, based on the previously given classification.
The Hu-Washizu principle is an often used basis for the development of finite element formulations as, e.g., for the framework of the enhanced assumed strain method, cf. Simo and Rifai [216], Andelfinger and Ramm [2], Yeo and Lee [242] and Bischoff et al. [37].

3.2.4 Least-squares finite element method

The mixed LSFEM in general is not dependent on a fixed number of field variables and like the just presented Galerkin and mixed Galerkin methods, is defined as a formulation based on the method of weighted residuals. However, referring to (3.16) the test functions $\boldsymbol{\eta}_i$ are chosen to be the first variations of the residual equations $\delta\mathcal{R}_i$, which yields

$$\mathcal{G} = \sum_i \int_{\mathcal{B}} \langle \mathcal{R}_i, \delta\mathcal{R}_i \rangle \, \mathrm{d}V = 0 \,. \tag{3.31}$$

The first variations $\delta\mathcal{R}_i$ are defined as the derivatives of the residual equations with respect to all unknown field variables considered in the underlying problem and multiplied by the variational expression of the unknown quantity. For the considered problem (3.17), the application of (3.31), by restriction to a two-field problem find $(\boldsymbol{u}, \boldsymbol{\sigma}) \in \mathcal{V} \times \mathcal{S}$, such that

$\mathcal{G} = 0 \; \forall \; (\delta\boldsymbol{u}, \delta\boldsymbol{\sigma}) \in \mathcal{V} \times \mathcal{S}$ with $\mathcal{R}_{1,2}$ as $(3.24)_{1,2}$, yields

$$\begin{aligned} \mathcal{G}_{\boldsymbol{u}} &= -\int_{\mathcal{B}} (\boldsymbol{\sigma} - \mathbb{C} : \nabla^s \boldsymbol{u}) : (\mathbb{C} : \nabla^s \delta\boldsymbol{u}) \, \mathrm{d}V = 0 \,, \\ \mathcal{G}_{\boldsymbol{\sigma}} &= \int_{\mathcal{B}} (\operatorname{div} \boldsymbol{\sigma} + \boldsymbol{f}) \cdot \operatorname{div} \delta\boldsymbol{\sigma} \, \mathrm{d}V + \int_{\mathcal{B}} (\boldsymbol{\sigma} - \mathbb{C} : \nabla^s \delta\boldsymbol{u}) : \delta\boldsymbol{\sigma} \, \mathrm{d}V = 0 \,, \end{aligned} \tag{3.32}$$

where $\mathcal{V} := [\mathcal{H}^1(\mathcal{B})]^3$ and $\mathcal{S} := [\mathcal{H}(\operatorname{div}, \mathcal{B})]^{3\times 3}_{\mathrm{sym}}$. The comparison of the weak forms (3.25), (3.26) and (3.29) with (3.32) directly depicts the difference in the resulting system matrices. Since all independent variables are given as quadratic terms in (3.32), the stiffness matrix will not have zero diagonal terms as it is the case for the mixed Galerkin formulations. Therefore, the resulting system is not characterized as a saddle point problem, but is considered as a minimization problem.

As the main aspect of the presented work, a more detailed description of the LSFEM is given below and overviews of the method are given in Bochev and Gunzburger [43], Jiang [125], Kayser-Herold and Matthies [129] and Eason [92]. The construction of a LS functional can be performed with respect to different norms applied to the underlying system of equations and based on the requirements of the PDEs, cf. Bochev and Gunzburger [43]. Following the key points for the construction of a practical LSFEM, defined by Bochev and Gunzburger [43], the basis is given by the application of the squared $\mathcal{L}^2(\mathcal{B})$- and $\mathcal{L}^2(\partial\mathcal{B})$-norm, with the squared $\mathcal{L}^2(\mathcal{B})$-norm defined by

$$\| \bullet \|^2_{\mathcal{L}^2(\mathcal{B})} = \| \bullet \|^2_{0,\mathcal{B}} = \int_{\mathcal{B}} | \bullet |^2 \, \mathrm{d}V \,. \tag{3.33}$$

The LSFEM is characterized by finding the minimizer $\mathcal{U}_{\mathrm{LS}}$ of a quadratic functional $\mathcal{F}(\mathcal{U})$ in terms of the unknowns $\mathcal{U}$, with respect to the minimization space $\bar{\mathcal{V}}$, given by

$$\mathcal{U}_{\mathrm{LS}} = \underset{\mathcal{U} \in \bar{\mathcal{V}}}{\operatorname{argmin}} \, \mathcal{F}(\mathcal{U}) \,. \tag{3.34}$$

For further steps, $\langle \bullet, \bullet \rangle_{\mathcal{L}^2(\mathcal{B})}$ defines the inner product on $\mathcal{L}^2(\mathcal{B})$, which is the integral over the body $\mathcal{B}$ of the inner product $\langle \bullet, \bullet \rangle_{\mathcal{L}^2(\mathcal{B})} = \int_{\mathcal{B}} \langle \bullet, \bullet \rangle \, \mathrm{d}V$. Therefore, the $\mathcal{L}^2(\mathcal{B})$- and squared $\mathcal{L}^2(\mathcal{B})$-norm (3.2) and (3.33) are written as $\| \bullet \|_{\mathcal{L}^2(\mathcal{B})} = (\int_{\mathcal{B}} \langle \bullet, \bullet \rangle \, \mathrm{d}V)^{1/2}$ and $\| \bullet \|^2_{\mathcal{L}^2(\mathcal{B})} = \int_{\mathcal{B}} \langle \bullet, \bullet \rangle \, \mathrm{d}V$. The construction of a LS functional $\mathcal{F}(\mathcal{U})$, based on a first-order system of PDEs given as residual equations $\mathcal{R}_i$, is defined, according to the method of weighted residuals (3.16), by

$$\mathcal{F}(\mathcal{U}) = \sum_i \| \omega_i \mathcal{R}_i \|^2_{\mathcal{L}^2(\mathcal{B})} = \sum_i \frac{1}{2} \int_B \omega_i^2 \langle \mathcal{R}_i, \mathcal{R}_i \rangle \, \mathrm{d}V \to \min. \tag{3.35}$$

Here, ω_i denote the weighting parameters, applied separately for each residual equation $\mathcal{R}_i$, which is skipped for notational simplicity but will be discussed later on. The solution of the unknown field $\mathcal{U}$, which minimizes the LS functional, is determined by utilization of the variational calculus and calculated by the condition that the first variation of the functional $\delta_{\mathcal{U}}\mathcal{F}$, is equal to zero and is represented in accordance with (3.31) by

$$\delta_{\mathcal{U}} \mathcal{F} = \frac{\partial \mathcal{F}}{\partial \mathcal{U}} \delta\mathcal{U} = \sum_i \int_{\mathcal{B}} \delta_{\mathcal{U}} \langle \mathcal{R}_i, \mathcal{R}_i \rangle \, \mathrm{d}V = 0 \,. \tag{3.36}$$

The construction procedures for the functional itself (3.35) and the weak form (3.36) can be applied for all types of problems and without any limitation of the unknown field quantities. Application of (3.35) on problem (3.17), as a two-field problem with $(3.17)_3$ inserted in $(3.17)_2$, leads to

$$\mathcal{F}(\boldsymbol{u},\boldsymbol{\sigma}) = \frac{1}{2}\int_{\mathcal{B}} \Big(\langle \operatorname{div}\boldsymbol{\sigma} + \boldsymbol{f}, \operatorname{div}\boldsymbol{\sigma} + \boldsymbol{f}\rangle + \langle \boldsymbol{\sigma} - \mathbb{C} : \nabla^s \boldsymbol{u}, \boldsymbol{\sigma} - \mathbb{C} : \nabla^s \boldsymbol{u}\rangle \Big)\, \mathrm{d}V\,, \tag{3.37}$$

with $\boldsymbol{u} \in \mathcal{H}^1(\mathcal{B})$ and $\boldsymbol{\sigma} \in \mathcal{H}(\operatorname{div}, \mathcal{B})$. Analogously to the case of the standard displacement formulation, a direct solution of the second-order problem (3.19) is also achievable by the LS formulation as a single field problem, i.e.,

$$\mathcal{F}(\boldsymbol{u}) = \frac{1}{2}\int_{\mathcal{B}} \Big(\langle \operatorname{div}(\mathbb{C} : \nabla^s \boldsymbol{u}) + \boldsymbol{f}, \operatorname{div}(\mathbb{C} : \nabla^s \boldsymbol{u}) + \boldsymbol{f}\rangle \Big)\, \mathrm{d}V\,, \tag{3.38}$$

with $\boldsymbol{u} \in [\mathcal{H}^2(\mathcal{B})]^3$. As previously noted, only first-order problems will be considered further on, due to the simpler utilization of the $\mathcal{H}^1(\mathcal{B})$ function space, according the lower continuity requirements within the space. Furthermore, a requirement for practical LS formulations is the restriction to a first-order system of equations, given by i PDEs in residual form $\mathcal{R}_i$. The problem here relates to the construction of the first-order system, by the recast of the given system of PDEs into a first-order system of equations, which is unfortunately not unique, since a norm-equivalent formulation can be achieved with respect to different norms, cf. Bochev and Gunzburger [43] for an illustration on the Poisson problem. As discussed in Bochev and Gunzburger [43], the chosen norms could lead to a not straightforward assembling of the system matrices, e.g., by consideration of a negative Sobolev norm $\| \bullet \|_{-1}$. For a circumvention of using different norms a proper mesh-dependent scaling factor can be introduced to obtain a quasi norm-equivalent formulation, e.g., with $\| \bullet \|^2_{1/2,\partial\mathcal{B}} = h^{-1} \| \bullet \|^2_{0,\partial\mathcal{B}}$.
It has to be noted, that for an explicit consideration of boundary conditions in the LS functional, the related trace norms or fractional norms with $\mathcal{H}^{1/2}$ and $\mathcal{H}^{-1/2}$, have to be transferred into norm-equivalent formulations by a mesh-dependent weighted $\mathcal{L}^2(\partial\mathcal{B})$-norm, to ensure a straightforward assembling operation. Consequently, in order to circumvent these difficulties as far as possible, only first-order systems formulated in the squared $\mathcal{L}^2(\mathcal{B})$-norm are considered in the following.

3.2.5 Advantages and disadvantages of the LSFEM

As briefly presented in the introduction, LSFEM, like any other method, offers advantages and disadvantages, which are discussed below. Despite the freedom in the construction of LS functionals, several aspects must be considered, in order to understand the behavior of the method. These include the choice of the polynomial order of the applied approximation functions, the construction of the functional itself and the physical meaning of the underlying equations as well as the weighting factors as part of the functional.
The construction of least-squares functionals is given by an uniform mathematical procedure for basically all types of PDEs. In contrast to other well established mixed finite element formulations, the LSFEM yields an unconstrained minimization problem. Therefore, a restriction or proper balancing of function spaces is unnecessary, at least from the point of stability, and a proof of stability of the method in terms of the

inf-sup condition is not necessary. Thus, the combination of polynomial orders of the single fields must not be carefully balanced. The possibility of unlimited combinations of functions of different orders can lead to combinations, in which the approximation quality of a individual quantity limits the global order of convergence and the chosen approximation approaches must be questioned. Nevertheless, when considering individual quantities, such as the displacement convergence of a particular point, the choice of polynomial orders does not lead to any limitation, but can additionally improve the result, cf. Schwarz et al. [207; 208], among others. Furthermore, the unconstrained minimization problem yields the flexibility to design suited functionals, which directly approximate the unknown field variables of interest, e.g., stresses and displacements. The quantities of interest can be chosen freely and the first-order system is constructed with respect to these assumptions. Based on the construction of the method, the resulting system matrices are symmetric and positive (semi-) definite, which is of interest for the applicability of different iterative solution strategies. The occurrence of the term positive semi-definite can be observed, e.g., in the analysis of stability problems for hyperelastic formulations. Therein, eigenvalues occur, which are in the vicinity of zero. A further advantage is an a posteriori error estimator provided by the LS functional itself and without additional computational costs, cf., e.g., Bochev and Gunzburger [43] and Cai and Starke [61]. Based on this, adaptive mesh refinement can be applied. Furthermore, the applicability of this error estimator to nonlinearities is shown in, e.g., Starke [219], Münzenmaier and Starke [169], Müller et al. [167], Münzenmaier [168] and Müller [165]. For the LSFEM, in comparison with Galerkin and mixed Galerkin formulations, the finite element solution space for the fulfillment of boundary conditions does not have to be limited, since the boundary conditions can be directly included in the functional as residual equations.

It is in the nature of the formulation that each selected functional minimizes the sum of the squared norms of the PDEs and leads to the best possible solution. Since the solution of a LS functional can be seen as the best possible balance between the solutions of the individual parts. Therefore, also overdetermined systems can be solved. However, the solution depends on the choice of residual equations and scalar weighting factors, which can be chosen independently and freely for each of the differential equations under consideration. Therefore, weighting factors have a crucial impact on the solution, which can influence or emphasize different properties of the formulation. Thus, they can be seen as both, an advantage and a disadvantage of the method. In the past, several different approaches for weighting factors appeared in the literature. Bochev and Gunzburger [43] and Bochev [38] introduce weightings based on the approach of equivalent norms. A reduction of the local error by weighting is discussed in Jiang [124; 125] and physical motivated weights are considered, e.g., by Bell and Surana [26; 27], Heys et al. [109] and Winterscheidt and Surana [234]. In Deang and Gunzburger [89], mesh-dependent weights for an improved accuracy are analyzed and the idea of a matrix weighting parameter is introduced in Salonen and Freund [195] and Kayser-Herold [128]. This matrix weighting is, e.g., considered for a diffusion problem, where the matrix entries are calculated with respect to the analytical solution of the problem, leading to a significant increase of solution accuracy. However, this type of weighting requires the knowledge about the sought solution, which generally cannot be calculated analytically. Furthermore, a weighted norm LSFEM is investigated, e.g., in

Bidwell et al. [36] and Jeong and Lee [122]. Lee and Chen [149] present a nonlinear weighting for a velocity-pressure-stress formulation for Stokes equations.
Furthermore, the choice of weightings is also related to the differential equation under consideration. In the following chapters, the weighting factors of the investigated LS functionals are chosen by physically motivated scaling of the units of the residual equations and based on parameter studies. An example is given by investigating weighting factors, which consider unit-dependent factors that scale the respective PDE to be independent of units, see, e.g., Bell and Surana [26] and Igelbüscher et al. [120]. The influence of the weighting parameters in the field of solid and fluid mechanics can be reduced by a higher order polynomial approach.
Another disadvantage of the LSFEM is the poor approximation quality of low order elements, see, e.g., Chang and Nelson [72], Deang and Gunzburger [89], Pontaza [182], Pontaza and Reddy [181], Schwarz et al. [205]. Besides the possibility of an improvement in terms of individual weighting parameters, there are various approaches to overcome this disadvantage, such as a modification of the functional, as for fluid mechanics, e.g., proposed in Chang and Nelson [72], Nelson and Chang [172] and for solid mechanics investigated by Schwarz et al. [206; 208]. The modification often includes an extension of the functional by additional terms, which are mathematically redundant but lead to an improvement in the finite element performance as, e.g., improved mass conservation in fluid applications, see Bochev et al. [44; 45] and Heys et al. [110; 111; 112]. The LSFEM leads, compared with pure displacement formulations, to a rapidly increasing system size. However, all mixed finite element formulations result in large system matrices due to the additionally introduced variables. For a reduction of the system size, static condensation of system matrices on element level can be applied for discontinuous approximated variables. Therefore, this approach is not applicable for standard LSFEM with continuous approximations of the unknown fields. Nevertheless, discontinuous LSFEM are introduced, e.g., in Bensow and Larson [28], Bensow and Larson [29] and Ye and Zhang [241], which could provide the possibility of reduced systems by static condensation.
The LSFEM often leads to a high condition number compared to Galerkin formulations, see Bochev and Gunzburger [43], which can result in a poor convergence behavior in the iterative solution procedure.

3.2.6 Linearization of the variational formulations

The derived weak forms for the pure displacement (3.22), primal and dual Hellinger-Reissner (3.25), (3.26) and Hu-Washizu formulation (3.29) as well as the first variation of the LS functional (3.32) are leading to linear systems of algebraic equations for the here depicted example of linear elasticity. Since mainly nonlinear problems are considered in the following, the derivation of a linearized weak form is necessary, in order to solve the nonlinear system of equations. Therefore, the variational problems for the Galerkin, mixed Galerkin and LSFEM are solved iteratively to find the approximate solution by means of, e.g., the Newton-Raphson method. For convenience, only the linearized form of (3.32) is presented below. For the linearization of the LS functional a general procedure is given by

$$\Delta_{\mathcal{U}}\delta_{\mathcal{U}}\mathcal{F} = \frac{\partial(\delta_{\mathcal{U}}\mathcal{F})}{\partial\mathcal{U}}\Delta\mathcal{U} = \sum_i \int_{\mathcal{B}} \langle \Delta_{\mathcal{U}}\delta_{\mathcal{U}}\mathcal{R}_i, \mathcal{R}_i\rangle + \langle \delta_{\mathcal{U}}\mathcal{R}_i, \Delta_{\mathcal{U}}\mathcal{R}_i\rangle \,\mathrm{d}V\,, \tag{3.39}$$

which yields, applied for the depicted linear elastic example (3.32), with respect to the unknown fields $\boldsymbol{u}$ and $\boldsymbol{\sigma}$, the equations

$$\begin{aligned}
\Delta_u \delta_u \mathcal{F} &= \int_{\mathcal{B}} \nabla^s \delta\boldsymbol{u} : \nabla^s \Delta\boldsymbol{u} \, \mathrm{d}V \,, \\
\Delta_u \delta_\sigma \mathcal{F} &= -\int_{\mathcal{B}} \delta\boldsymbol{\sigma} : (\mathbb{C} : \nabla^s \Delta\boldsymbol{u}) \, \mathrm{d}V \,, \\
\Delta_\sigma \delta_u \mathcal{F} &= -\int_{\mathcal{B}} (\mathbb{C} : \nabla^s \delta\boldsymbol{u}) : \Delta\boldsymbol{\sigma} \, \mathrm{d}V \,, \\
\Delta_\sigma \delta_\sigma \mathcal{F} &= \int_{\mathcal{B}} \operatorname{div} \delta\boldsymbol{\sigma} \cdot \operatorname{div} \Delta\boldsymbol{\sigma} \, \mathrm{d}V + \int_{\mathcal{B}} \delta\boldsymbol{\sigma} : \Delta\boldsymbol{\sigma} \, \mathrm{d}V \,.
\end{aligned} \tag{3.40}$$

The representation of weak forms and linearization of the considered formulations will be given separately for the formulation under investigation.

3.2.7 Discretization

The determination of an analytical solution of each of the presented weak forms on arbitrary domains is in general not possible. Therefore, the FEM is applied for solving the PDEs, see, e.g., Zienkiewicz and Taylor [247], Braess [50], Bathe [24] and Wriggers [236]. The fundamental idea of the FEM is to replace the given physical domain under consideration by a finite number of polygonal elements. The considered continuum body of interest $\mathcal{B}$ is replaced by an approximation $\mathcal{B}_h$, which consists of n_{elem} finite elements $\mathcal{B}_{\text{e}}$. This approach can be represented by

$$\mathcal{B} \approx \mathcal{B}_h = \bigcup_{\text{e}=1}^{n_{\text{elem}}} \mathcal{B}_{\text{e}} \,. \tag{3.41}$$

Furthermore, each of these finite elements approximates the unknown variables on its domain by the consideration of approximation or so-called shape functions in combination with nodal values at certain points on the element domain. These points are denoted as interpolation sites, which can represent nodes, edges, surfaces or even the volume of the element, depending on the selected approximation space and the choice of functions, which are usually given by piecewise polynomial interpolation functions. Therefore, the unknowns at each point of the real body are reduced to a certain number on the applied finite element mesh. For the assumption of a refinement of the finite element mesh with $h_{\text{e}} \to 0$, where h_{e} is a characteristic element length (e.g., diameter), it is assumed that the approximation quality of the physical fields increases.
A suitable finite element can be characterized, following Ciarlet [77], by the triplet $(\mathcal{B}_{\text{e}}, \mathcal{N}_{\text{e}}, \mathcal{U}_{\text{e}})$ with the following properties:

- The element domain $\mathcal{B}_{\text{e}}$ is a polyhedron in $\mathbb{R}^d$
- $\mathcal{N}_{\text{e}}$ are the local approximation or shape functions on $\mathcal{B}_{\text{e}}$
- $\mathcal{U}_{\text{e}}$ defines the local degrees of freedom on $\mathcal{B}_{\text{e}}$

Furthermore, $\mathcal{B}_h$ is also referred as the triangulation of $\mathcal{B}$ such that:

- If $\mathcal{B}_h = \cup_{\mathrm{e}=1}^{n_{\mathrm{elem}}} \mathcal{B}_\mathrm{e}$, $\mathcal{B}_1 \cap \mathcal{B}_2 = \emptyset$, where a vertex of $\mathcal{B}_1$ and $\mathcal{B}_2$ is given, if $\mathcal{B}_1 \cap \mathcal{B}_2$ consists of exactly one point and for $\mathcal{B}_1 \cap \mathcal{B}_2$ consisting of more than one point, it defines an edge in $d = 2$ or face in $d = 3$ shared by both elements.
- $\mathcal{B}_\mathrm{e}$ has straight edges, if $\mathcal{B}_\mathrm{e} \subset \mathcal{B}$,
- $\mathcal{B}_\mathrm{e}$ can include curved edges, if it is located at the boundary $\partial\mathcal{B}$,
- The vertex angles are greater than 0,

cf., e.g., Brezzi et al. [57] and Braess [50]. Consequently, the finite element space in which the solution is sought is a discrete counterpart of the continuous approximation space $\mathcal{V}$, which is selected with respect to the partial differential equation on the continuous body, denoted, e.g., by $\mathcal{V}_h \subset \mathcal{V}$ with $\boldsymbol{u}_h \in \mathcal{V}_h$ and $\boldsymbol{u}_h$ is the discrete counterpart of $\boldsymbol{u}$. For convenience, an often used approach within the finite element method is the isoparametric concept, which consists of the idea of introducing an isoparametric subspace or so-called parameter space. In this subspace each finite element is defined and is mapped into the reference or actual configuration with respect to the transformation maps, given by the Jacobian matrices $\boldsymbol{J} = \partial\boldsymbol{X}/\partial\boldsymbol{\xi}$ and $\boldsymbol{j} = \partial\boldsymbol{x}/\partial\boldsymbol{\xi}$. Here, $\boldsymbol{X}, \boldsymbol{x}$ and $\boldsymbol{\xi}$ denote the coordinate vectors in the reference, actual and parameter space. The approximations of the geometry $\boldsymbol{X}_h$ and $\boldsymbol{x}_h$ are defined by

$$\boldsymbol{X}_h = \sum_{j=1}^{n_{u,\mathrm{elem}}} \mathbb{N}^j(\boldsymbol{\xi})\, \hat{\boldsymbol{X}}^j \quad \text{and} \quad \boldsymbol{x}_h = \sum_{j=1}^{n_{u,\mathrm{elem}}} \mathbb{N}^j(\boldsymbol{\xi})\, \hat{\boldsymbol{x}}^j\,, \tag{3.42}$$

where $\mathbb{N}(\boldsymbol{\xi})$ denotes a matrix consisting of Lagrange type approximation functions defined in the parameter space $\boldsymbol{\xi} = \{\xi, \eta, \zeta\}^T$, cf. Appendix 8.1. The number of displacement related nodes per element is defined by $n_{u,\mathrm{elem}}$ and the nodal coordinate vectors in reference and actual configuration $\hat{\boldsymbol{X}}$ and $\hat{\boldsymbol{x}}$.
The advantages of the isoparametric concept are the known geometry of the considered finite element in the isoparametric subspace and consequently the approximation functions as well as the numerical integration points and weights, by considering, e.g., Gauss quadrature for integration, are known a priori. Furthermore, the geometry and the displacements can be approximated by the same shape functions, see, e.g., Zienkiewicz and Taylor [247] and Wriggers [236].

The discrete form of the mixed LS formulation (3.37) with the related first variation (3.32) and linearization (3.40) is exemplarily presented below, which holds, in a similar manner, for all following finite element approaches. The considered approximation functions are discussed in Chapter 3.3.
For the discretized problem, approximation matrices are introduced. They are depending on the underlying element type, regarding the number of nodes and the dimension associated to the related degree of freedom. Here, the tensorial quantities are restored into a vector structure performed in the following. Since a discussion on two and three dimensional problems will be presented afterwards, an introduction of the approximated field quantities and interpolation matrices are given for completeness for the three dimensional framework, which can be reduced straightforward to two dimensions. For the LSFEM the

necessary vector representation of displacements $\boldsymbol{u}_h$, strains $\boldsymbol{\varepsilon}_h = \nabla^s \boldsymbol{u}_h$, stresses $\boldsymbol{\sigma}_h$ and divergence of stresses $\operatorname{div} \boldsymbol{\sigma}_h$ are given by

$$\begin{aligned} \boldsymbol{u}_h &:= \{u_1, u_2, u_3\}^T \,, \\ \boldsymbol{\varepsilon}_h &:= \nabla^s \boldsymbol{u}_h = \{\varepsilon_{11}, \varepsilon_{12}, \varepsilon_{13}, \varepsilon_{21}, \varepsilon_{22}, \varepsilon_{23}, \varepsilon_{31}, \varepsilon_{32}, \varepsilon_{33}, \}^T \,, \\ \boldsymbol{\sigma}_h &:= \{\sigma_{11}, \sigma_{12}, \sigma_{13}, \sigma_{21}, \sigma_{22}, \sigma_{23}, \sigma_{31}, \sigma_{32}, \sigma_{33}\}^T \,, \\ \operatorname{div} \boldsymbol{\sigma}_h &:= \{\operatorname{div} \sigma_1, \operatorname{div} \sigma_2, \operatorname{div} \sigma_3\}^T \,., \end{aligned} \tag{3.43}$$

The vectors of degrees of freedom $\boldsymbol{d}_u^j$ and $\boldsymbol{d}_\sigma^{j,i}$, related to the unknown discrete field quantities, here $\boldsymbol{u}_h$ and $\boldsymbol{\sigma}_h$, are

$$\begin{aligned} \boldsymbol{d}_u^j &:= \left\{d_{u1}^j,\ d_{u2}^j,\ d_{u3}^j\right\}^T \,, && \text{for } j = 1, .., n_{u,\text{elem}} \,, \\ \boldsymbol{d}_\sigma^{j,i} &:= \left\{d_{\sigma 1}^{j,i},\ d_{\sigma 2}^{j,i},\ d_{\sigma 3}^{j,i}\right\}^T \,, && \text{for } j = 1, .., n_{\text{edge}} \text{ and } i = 1, .., n_{\sigma,\text{edge}} \,, \end{aligned} \tag{3.44}$$

where j in $\boldsymbol{d}_i^j$ denotes the number of displacement nodes $n_{u,\text{elem}}$ within one finite element and j and i in $\boldsymbol{d}_\sigma^{j,i}$ are given by the number of edges n_{edge} and number of stress nodes on each edge as well as on the interior face $n_{\sigma,\text{edge}}$. The approximation of $\boldsymbol{u}_h, \nabla^s \boldsymbol{u}_h, \boldsymbol{\sigma}_h$ and $\operatorname{div} \boldsymbol{\sigma}_h$, for the linear elastic mixed finite element formulation, with $\boldsymbol{\sigma} \in [\mathcal{H}(\operatorname{div}, \mathcal{B})]^{3\times 3}$ and $\boldsymbol{u} \in [\mathcal{H}^1(\mathcal{B})]^3$ are

$$\begin{aligned} \boldsymbol{u}_h &= \sum_j^{n_{u,\text{elem}}} \mathbb{N}^j(\boldsymbol{\xi})\, \boldsymbol{d}_u^j = \mathbb{N}(\boldsymbol{\xi})\, \boldsymbol{d}_u \,, & \boldsymbol{\sigma}_h &= \sum_j^{n_{\text{edge}}} \sum_i^{n_{\sigma,\text{edge}}} \mathbb{S}^{j,i}(\boldsymbol{\xi})\, \boldsymbol{d}_\sigma^{j,i} = \mathbb{S}(\boldsymbol{\xi})\, \boldsymbol{d}_\sigma \,, \\ \boldsymbol{\varepsilon}_h &= \sum_j^{n_{u,\text{elem}}} \mathbb{B}^j(\boldsymbol{\xi})\, \boldsymbol{d}_u^j = \mathbb{B}(\boldsymbol{\xi})\, \boldsymbol{d}_u \,, & \operatorname{div} \boldsymbol{\sigma}_h &= \sum_j^{n_{\text{edge}}} \sum_i^{n_{\sigma,\text{edge}}} \mathbb{S}'^{j,i}(\boldsymbol{\xi})\, \boldsymbol{d}_\sigma^{j,i} = \mathbb{S}'(\boldsymbol{\xi})\, \boldsymbol{d}_\sigma \,, \end{aligned} \tag{3.45}$$

and analogously the virtual and incremental variables, omitting the summation over the related nodes, are defined by

$$\begin{aligned} &\delta \boldsymbol{u}_h = \mathbb{N}\, \delta \boldsymbol{d}_u \,, \quad \Delta \boldsymbol{u}_h = \mathbb{N}\, \Delta \boldsymbol{d}_u \,, \quad \delta \boldsymbol{\varepsilon}_h = \mathbb{B}\, \delta \boldsymbol{d}_u \,, && \Delta \boldsymbol{\varepsilon}_h = \mathbb{B}\, \Delta \boldsymbol{d}_u \,, \\ &\delta \boldsymbol{\sigma}_h = \mathbb{S}\, \delta \boldsymbol{d}_\sigma \,, \quad \Delta \boldsymbol{\sigma}_h = \mathbb{S}\, \Delta \boldsymbol{d}_\sigma \,, \quad \operatorname{div} \delta \boldsymbol{\sigma}_h = \mathbb{S}'\, \delta \boldsymbol{d}_\sigma \,, && \operatorname{div} \Delta \boldsymbol{\sigma}_h = \mathbb{S}'\, \Delta \boldsymbol{d}_\sigma \,. \end{aligned} \tag{3.46}$$

Herein, the matrix $\mathbb{N}$ consists of conforming continuous piecewise polynomial functions, Lagrange type functions ($\mathcal{P}$, $\mathcal{Q}$) and $\mathbb{B}$ includes the derivative of the functions with respect to $\boldsymbol{\xi} = \{\xi, \eta, \zeta\}^T$, in the literature often referred as $\mathbb{B}$-matrix. Furthermore, $\mathbb{S}$ consists of suitable $\mathcal{H}(\operatorname{div}, \mathcal{B})$-conforming functions, e.g., Raviart-Thomas ($\mathcal{RT}$) or Brezzi-Douglas-Marini ($\mathcal{BDM}$) functions, while $\mathbb{S}'$ includes directional derivatives of these functions. For completeness, these matrices are defined in Appendix 8.1.1.
For simplicity the summations over n_{edge}, $n_{\sigma,\text{edge}}$ and $n_{u,\text{elem}}$ are omitted in the following

representations. Thus, the element vectors and matrices are constructed by

$$\begin{aligned}
&\boldsymbol{d}_u := \left\{ \boldsymbol{d}_u^{1\,T},\ \boldsymbol{d}_u^{2\,T},\ \ldots\ \boldsymbol{d}_u^{j\,T} \right\}^T && \text{for } j = 1, ..., n_{u,\text{elem}}\,, \\
&\mathbb{N} := \left\{ \mathbb{N}^1,\ \mathbb{N}^2,\ \ldots\ \mathbb{N}^j \right\}^T && \text{for } j = 1, ..., n_{u,\text{elem}}\,, \\
&\mathbb{B} := \left\{ \mathbb{B}^1,\ \mathbb{B}^2,\ \ldots\ \mathbb{B}^j \right\}^T && \text{for } j = 1, ..., n_{u,\text{elem}}\,, \\
&\boldsymbol{d}_\sigma := \left\{ \boldsymbol{d}_\sigma^{1,1\,T},\ \boldsymbol{d}_\sigma^{1,2\,T},\ \ldots\ \boldsymbol{d}_\sigma^{j,i\,T} \right\}^T && \text{for } j = 1, ..., n_{\text{edge}} \text{ and } i = 1, ..., n_{\sigma,\text{edge}}\,, \\
&\mathbb{S} := \left\{ \mathbb{S}^{1,1},\ \mathbb{S}^{1,2},\ \ldots\ \mathbb{S}^{j,i} \right\}^T && \text{for } j = 1, ..., n_{\text{edge}} \text{ and } i = 1, ..., n_{\sigma,\text{edge}}\,, \\
&\mathbb{S}' := \left\{ \mathbb{S}'^{1,1},\ \mathbb{S}'^{1,2},\ \ldots\ \mathbb{S}'^{j,i} \right\}^T && \text{for } j = 1, ..., n_{\text{edge}} \text{ and } i = 1, ..., n_{\sigma,\text{edge}}\,.
\end{aligned} \tag{3.47}$$

Analogously, the virtual and incremental vectors $\delta\boldsymbol{d}_{u,\sigma}$ and $\Delta\boldsymbol{d}_{u,\sigma}$ are defined. For the calculation of the displacement gradient the derivative of the approximation function, with respect to the reference configuration $\boldsymbol{X}_h$, is necessary, which is

$$\nabla \boldsymbol{u}_h = \frac{\partial \boldsymbol{u}_h}{\partial \boldsymbol{X}_h} = \frac{\partial \boldsymbol{u}_h}{\partial \boldsymbol{\xi}} \boldsymbol{J}^{-1}\,, \quad \text{with} \quad \frac{\partial \mathbb{N}}{\partial \boldsymbol{X}_h} = \frac{\partial \mathbb{N}}{\partial \boldsymbol{\xi}} \frac{\partial \boldsymbol{\xi}}{\partial \boldsymbol{X}_h} = \frac{\partial \mathbb{N}}{\partial \boldsymbol{\xi}} \boldsymbol{J}^{-1}\,, \tag{3.48}$$

by application of the chain rule.
Consequently, the discrete form of the LS formulation (3.37) on element level, denoted by $\delta_u \mathcal{F}^{\text{e}}$, $\delta_\sigma \mathcal{F}^{\text{e}}$, with $\delta_u \mathcal{F} = \mathcal{G}_u$ and $\delta_\sigma \mathcal{F} = \mathcal{G}_\sigma$, cf. (3.32), (3.36), reads

$$\begin{aligned}
\delta_u \mathcal{F}^{\text{e}} = \delta \boldsymbol{d}_u^T\, \boldsymbol{r}_u^{\text{e}} \quad &\Rightarrow \quad \boldsymbol{r}_u^{\text{e}} = -\int_{\mathcal{B}} \mathbb{N}^T\, \underline{\mathbb{C}}^T (\mathbb{S}\, \boldsymbol{d}_\sigma - \underline{\mathbb{C}}\, \mathbb{B}\, \boldsymbol{d}_u)\, \mathrm{d}V\,, \\
\delta_\sigma \mathcal{F}^{\text{e}} = \delta \boldsymbol{d}_\sigma^T\, \boldsymbol{r}_\sigma^{\text{e}} \quad &\Rightarrow \quad \boldsymbol{r}_\sigma^{\text{e}} = \int_{\mathcal{B}} \mathbb{S}'^T (\mathbb{S}'\, \boldsymbol{d}_\sigma + \boldsymbol{f})\, \mathrm{d}V + \int_{\mathcal{B}} \mathbb{S}^T (\mathbb{S}\, \boldsymbol{d}_\sigma - \underline{\mathbb{C}}\, \mathbb{B}\, \boldsymbol{d}_u)\, \mathrm{d}V\,,
\end{aligned} \tag{3.49}$$

with the fourth order elasticity tensor in matrix notation denoted by $\underline{\mathbb{C}}$. For convenience the corresponding weighting parameters ω_i are omitted here. Based on this, the discretization of the linearization leads to

$$\begin{aligned}
\Delta_u \delta_u \mathcal{F}^{\text{e}} = \delta \boldsymbol{d}_u^T\, \boldsymbol{k}_{uu}^{\text{e}}\, \Delta \boldsymbol{d}_u \quad &\Rightarrow \quad \boldsymbol{k}_{uu}^{\text{e}} = \int_{\mathcal{B}} \mathbb{B}^T\, \mathbb{B}\, \mathrm{d}V\,, \\
\Delta_\sigma \delta_u \mathcal{F}^{\text{e}} = \delta \boldsymbol{d}_u^T\, \boldsymbol{k}_{u\sigma}^{\text{e}}\, \Delta \boldsymbol{d}_\sigma \quad &\Rightarrow \quad \boldsymbol{k}_{u\sigma}^{\text{e}} = -\int_{\mathcal{B}} \mathbb{B}^T\, \underline{\mathbb{C}}^T\, \mathbb{S}\, \mathrm{d}V\,, \\
\Delta_u \delta_\sigma \mathcal{F}^{\text{e}} = \delta \boldsymbol{d}_\sigma^T\, \boldsymbol{k}_{\sigma u}^{\text{e}}\, \Delta \boldsymbol{d}_u \quad &\Rightarrow \quad \boldsymbol{k}_{\sigma u}^{\text{e}} = -\int_{\mathcal{B}} \mathbb{S}^T\, \underline{\mathbb{C}}\, \mathbb{B}\, \mathrm{d}V\,, \\
\Delta_\sigma \delta_\sigma \mathcal{F}^{\text{e}} = \delta \boldsymbol{d}_\sigma^T\, \boldsymbol{k}_{\sigma\sigma}^{\text{e}}\, \Delta \boldsymbol{d}_\sigma \quad &\Rightarrow \quad \boldsymbol{k}_{\sigma\sigma}^{\text{e}} = \int_{\mathcal{B}} \mathbb{S}'^T\, \mathbb{S}'\, \mathrm{d}V + \int_{\mathcal{B}} \mathbb{S}^T\, \mathbb{S}\, \mathrm{d}V\,,
\end{aligned} \tag{3.50}$$

and the resulting local system of equations for a typical LS element reads

$$\underbrace{\begin{bmatrix} \boldsymbol{k}_{uu}^{\text{e}} & \boldsymbol{k}_{u\sigma}^{\text{e}} \\ \boldsymbol{k}_{\sigma u}^{\text{e}} & \boldsymbol{k}_{\sigma\sigma}^{\text{e}} \end{bmatrix}}_{\boldsymbol{k}^{\text{e}}} \underbrace{\begin{bmatrix} \Delta \boldsymbol{d}_u \\ \Delta \boldsymbol{d}_\sigma \end{bmatrix}}_{\Delta \boldsymbol{d}^{\text{e}}} = - \underbrace{\begin{bmatrix} \boldsymbol{r}_u^{\text{e}} \\ \boldsymbol{r}_\sigma^{\text{e}} \end{bmatrix}}_{\boldsymbol{r}^{\text{e}}}\,. \tag{3.51}$$

This system is constructed on element level, based on the first variation $\delta_{\mathcal{U}} \mathcal{F}$ and linearized first variation $\Delta_{\mathcal{U}} \delta_{\mathcal{U}} \mathcal{F}$ of the problem, and solved applying the standard Newton-Raphson

method. The global stiffness matrix $\boldsymbol{K}$ and global residual vector $\boldsymbol{R}$, determined by assembling over all elements in $\mathcal{B}_h$, are

$$\boldsymbol{K} = \mathop{\mathsf{A}}_{\mathrm{e}=1}^{n_{ele}} \boldsymbol{k}^{\mathrm{e}} \quad \text{and} \quad \boldsymbol{R} = \mathop{\mathsf{A}}_{\mathrm{e}=1}^{n_{ele}} \boldsymbol{r}^{\mathrm{e}}, \tag{3.52}$$

and thus the system of equations can be given by

$$\delta \boldsymbol{D}^T (\boldsymbol{K} \Delta \boldsymbol{D} + \boldsymbol{R}) = \boldsymbol{0} \quad \Rightarrow \quad \Delta \boldsymbol{D} = -\boldsymbol{K}^{-1} \boldsymbol{R}, \tag{3.53}$$

with $\delta \boldsymbol{D}$ and $\Delta \boldsymbol{D}$ as virtual and incremental vector of unknowns. For the determination of the nodal degrees of freedom $\boldsymbol{D}_{n+1} = \boldsymbol{D}_n + \Delta \boldsymbol{D}$ the system $\Delta \boldsymbol{D} = -\boldsymbol{K}^{-1} \boldsymbol{R}$ is solved and an update of $\boldsymbol{D}$ is performed until $\boldsymbol{R} \leq tol$, i.e., the global residual vector is smaller or equal to a predefined tolerance, and global convergence is reached. Furthermore, depending on the chosen continuity of the related unknown field quantities an elimination of local unknowns can be performed on the element level, cf., e.g., Arnold et al. [8] and Stenberg [224]. The element stiffness matrix $\boldsymbol{k}^{\mathrm{e}}$ and the associated element right hand side vector $\boldsymbol{r}^{\mathrm{e}}$ are presented for the discussed formulations if necessary.

3.3 Conforming finite element approximation

For the choice of the function spaces, various approaches have been introduced over the years, which can be roughly divided into conforming and non-conforming discretization. Here, the terms conforming and non-conforming refer to the relation between the discrete and the real problem. If $\mathcal{V}_h \not\subset \mathcal{V}$, i.e., the finite element space $\mathcal{V}_h$ is not a subspace of the required solution space $\mathcal{V}$, in which the continuous problem is defined, one speaks of non-conforming approximations. In addition, this definition results in the fact, that for a problem defined in $\mathcal{H}^1(\mathcal{B})$, a non-conforming function space is not located in the Sobolev space $\mathcal{H}^1(\mathcal{B})$ and, e.g., only in $\mathcal{L}^2(\mathcal{B})$. For conforming elements it holds that $\mathcal{V}_h \subset \mathcal{V}$. A general introduction of properties and relations of function spaces is given in Chapter 3.1. Subsequently, the different approximation functions and related finite elements are introduced and further their construction is briefly presented. The consideration is limited to conforming approximations in the Sobolev spaces $\mathcal{W}^{1,p}(\mathcal{B})$ and $\mathcal{W}^q(\mathrm{div}, \mathcal{B})$, which however contain a large range of the standard approximation functions.

One of the best known conforming elements is the $\mathcal{P}_1$ element, which is a triangular element with linear approximation functions of Lagrange type and goes back to Courant [82]. Additionally, the quadratic triangular element is first introduced by Fraeijs De Veubeke [101], cf. Zienkiewicz [244]. A general overview of a wide range of finite elements is given by Kirby et al. [131] and, e.g., the monographs Boffi et al. [49], Brezzi and Fortin [56]. Furthermore, conforming elements in $\mathcal{W}^{1,p}(\mathcal{B})$ are presented in Zienkiewicz et al. [250], Chen [74] and Boffi et al. [49], beside others.

For the conforming approximation of unknown field variables in $\mathcal{W}^q(\mathrm{div}, \mathcal{B})$, various suitable choices of approximation functions are available. In general, these are vector-valued approaches such as Raviart-Thomas ($\mathcal{RT}$), Brezzi-Douglas-Marini ($\mathcal{BDM}$), Brezzi-Douglas-Fortin-Marini ($\mathcal{BDFM}$) and Arnold-Boffi-Falk ($\mathcal{ABF}$) functions, among others, see Raviart and Thomas [188], Brezzi et al. [57], Brezzi et al. [59] and Arnold et al. [8]. The $\mathcal{RT}$ function space was first introduced by Raviart and Thomas [189] for two dimensional elements and extended

by NÉDÉLEC [170] into the three dimensional framework. A variation of these elements is given by the $\mathcal{BDM}$ elements, proposed by BREZZI ET AL. [57] for $d = 2$ and BREZZI ET AL. [58] for $d = 3$. These spaces include the Raviart-Thomas and Nédélec spaces within their definition, see NÉDÉLEC [170; 171]. A modification of the $\mathcal{BDM}$ elements is introduced by BREZZI ET AL. [59] yielding the $\mathcal{BDFM}$ element approach. Additionally, ARNOLD ET AL. [8] propose a finite element space which provides optimal order approximation in $\mathcal{H}(\mathrm{div}, \mathcal{B})$ for quadrilaterals, denoted as $\mathcal{ABF}$ elements. Further discussions on these spaces and approaches in $\mathcal{W}^q(\mathrm{div}, \mathcal{B})$ are given in, e.g., BREZZI AND FORTIN [56]. Furthermore, overviews of conforming and non-conforming finite element approximations are presented in, e.g., KIRBY ET AL. [131], ROGNES ET AL. [193] and BOFFI ET AL. [49]. A short overview of non-conforming approaches is given below, for more details see, e.g., BRENNER AND SCOTT [53], KIRBY ET AL. [131], CHEN [74], BOFFI ET AL. [49] and BREZZI AND FORTIN [56]. In the next section the $\mathcal{RT}$ and $\mathcal{BDM}$ elements are introduced on triangular and quadrilateral domains and additionally the $\mathcal{RT}$ space is discussed on tetrahedral elements.
Some well-known non-conforming finite elements are the Crouzeix-Raviart element, referred as the non-conforming $\mathcal{P}_1$ element, and the Rannacher-Turek element on quadrilaterals, cf. BRENNER [52], CROUZEIX AND RAVIART [83] and RANNACHER AND TUREK [187]. For the Crouzeix-Raviart element the interpolation sites are not located at the vertices of the triangle like in the conforming $\mathcal{P}_1$ element, but at the centers of the three edges. Therefore, the continuity is solely controlled at one point of the edge and is discontinuous in the vertices of the related edge. The application of non-conforming approximations on quadrilaterals is, e.g., performed by RANNACHER AND TUREK [187], HENNART ET AL. [108], MATTHIES [160] and KÖSTER ET AL. [140]. Therein, RANNACHER AND TUREK [187] have presented four variants of non-conforming ansatz spaces, one of these corresponds to the first-order element of HENNART ET AL. [108]. Furthermore, inf-sup stability of non-conforming elements is investigated by MATTHIES [160]. In KÖSTER ET AL. [140] also higher order variants, which allow optimal error estimations and are based on area moments assigned to $(n-1)$-dimensional surfaces, and bubble functions assigned to single cells, are presented. For completeness, the utilization of non-conforming finite element approaches simultaneously leads to a violation of the Céa-Lemma, respectively forces a generalization of the requirements.
It has to be mentioned, that based on the given definition of non-conforming finite elements, discontinuous approaches can be also seen as non-conforming. Since, e.g., in the case of a discontinuous displacement element, the degrees of freedom only lie within the element and no global continuity is required by these elements, which can be overcome by hybrid FEM formulations, see, e.g., ROBERTS AND THOMAS [192], CAREY AND ODEN [70], ATLURI ET AL. [16], ATLURI ET AL. [15] and BREZZI AND FORTIN [56]. The idea of hybrid elements is presented in the course of this work, see Chapter 6.

3.3.1 The $\mathcal{W}^{1,p}(\mathcal{B})$-conforming $\mathcal{P}_k$ and $\mathcal{Q}_k$ elements

The conforming approximation functions are introduced based on the approach of reference elements in the parameter space $(\xi, \eta)^T$ and $(\xi, \eta, \zeta)^T$, exemplarily depicted for a triangular and quadrilateral element domain in Figure 3.1. These approximation functions are transferred into the physical space $(x, y)^T$ and $(x, y, z)^T$ by means of a transformation depending on the structure of the approximated field variable. However, this approach

can be avoided by a direct construction of shape functions in the physical space, which is discussed for straight-edged element shapes hereafter.

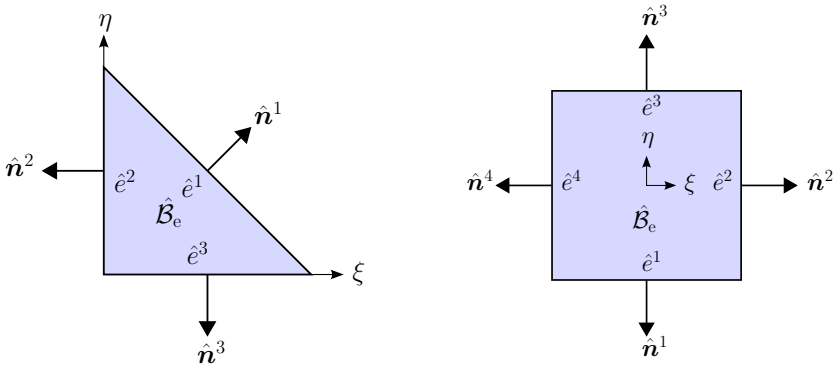

Figure 3.1: Reference elements given by the unit triangle and the unit quadrilateral.

The Lagrange type approximation functions are piecewise defined polynomials of order k, e.g., a polynomial of order $k \in \mathbb{R}^2$ on a triangular element domain has exactly $(k+1)(k+2)/2$ sampling points and in general the same number of degrees of freedom in each dimension d. Here, only complete polynomial functions in $\mathcal{P}_k$ and $\mathcal{Q}_k$ are considered for the approximation, where $\mathcal{P}$ denotes triangular and $\mathcal{Q}$ quadrilateral based domains in $d = 2, 3$. The spaces of polynomials are defined for triangles and tetrahedrals by

$$[\mathcal{P}_k]^2 = \sum_{\substack{i,j\geq 0 \\ i+j\leq k}} a_{ij}\, \xi^i\, \eta^j \quad \text{and} \quad [\mathcal{P}_k]^3 = \sum_{\substack{i,j,p\geq 0 \\ i+j+p\leq k}} a_{ijp}\, \xi^i\, \eta^j\, \zeta^p\,, \tag{3.54}$$

and for quadrilaterals and hexahedrals by

$$[\mathcal{Q}_k]^2 = \sum_{0\leq i,j\leq k} a_{ij}\, \xi^i\, \eta^j \quad \text{and} \quad [\mathcal{Q}_k]^3 = \sum_{0\leq i,j,p\leq k} a_{ijp}\, \xi^i\, \eta^j\, \zeta^p\,. \tag{3.55}$$

The underlying polynomial for the $[\mathcal{P}_k]^d$ and $[\mathcal{Q}_k]^d$ can be also given with respect to Pascal's triangle, describing the monomials for functions in $d = 2$ and by a straightforward extension for $d = 3$, see, e.g., Zienkiewicz et al. [250]. However, beside the here considered standard Lagrange functions with complete polynomials, there are functions based on a reduced polynomial space as, e.g., the so-called Serendipity elements on quadrilaterals, cf., e.g., Zienkiewicz et al. [250]. The choice of complete polynomials up to order k is based on reasons of convergence, see, e.g., Zienkiewicz and Taylor [246] and Wriggers [236]. For simplicity only two dimensional $[\mathcal{P}_k]^2$ and $[\mathcal{Q}_k]^2$ are depicted in Figure 3.2 and 3.3, which can be easily extended to the three dimensional setup, see Zienkiewicz et al. [250], Kirby et al. [131], Wriggers [236].

The sampling points $\hat{P}^j$ are numbered counterclockwise. Furthermore, the dimensions of $[\mathcal{P}_k]^d$ and $[\mathcal{Q}_k]^d$ space, cf. Brezzi and Fortin [56] and Kirby et al. [131], are given by

$$\dim([\mathcal{P}_k]^d) = \begin{cases} \frac{1}{2}(k+1)(k+2)\,, & \text{for } d = 2 \\ \frac{1}{6}(k+1)(k+2)(k+3)\,, & \text{for } d = 3 \end{cases}, \tag{3.56}$$

$$\dim([\mathcal{Q}_k]^d) = \begin{cases} (k+1)(k+1)\,, & \text{for } d = 2 \\ (k+1)(k+1)(k+1)\,, & \text{for } d = 3 \end{cases}, \tag{3.57}$$

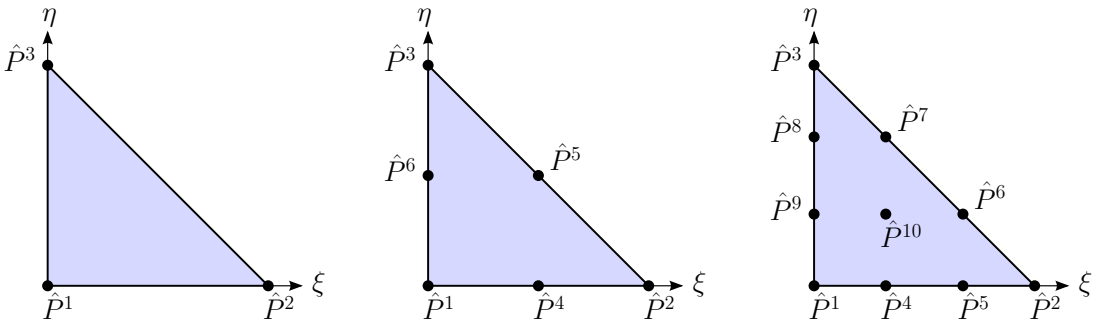

Figure 3.2: $[\mathcal{P}_k]^2$ elements with $k = 1, 2, 3$

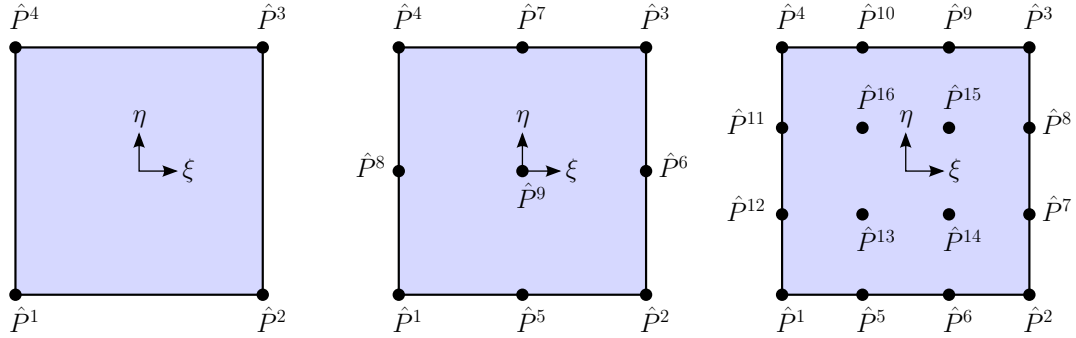

Figure 3.3: $[\mathcal{Q}_k]^2$ elements with $k = 1, 2, 3$

and listed in Table 3.1 for $d = 2, 3$ and $k = 1, 2, 3$.

Table 3.1: Dimensions of $[\mathcal{P}_k]^d$ and $[\mathcal{Q}_k]^d$ spaces for $d = 2, 3$

	$\dim([\mathcal{P}_k]^2)$	$\dim([\mathcal{Q}_k]^2)$	$\dim([\mathcal{P}_k]^3)$	$\dim([\mathcal{Q}_k]^3)$
$k = 1$	3	4	4	8
$k = 2$	6	9	10	27
$k = 3$	10	16	20	64

Evaluation of approximation functions within the space $\mathcal{P}_k$
The evaluation of approximation functions $\hat{N}^j$ at each node j, either for $[\mathcal{P}_k]^d$ or $[\mathcal{Q}_k]^d$ elements, can be performed by solving a system of equations. This system of equations is determined based on the corresponding complete polynomials (3.54), (3.55) and the coordinates of the sampling points and solved with respect to the condition

$$N^j(\xi^i, \eta^i) = \begin{cases} 1\,, & \text{for } j = i \\ 0\,, & \text{for } j \neq i \end{cases} . \tag{3.58}$$

The lowest order functions on a triangular element, cf., e.g., Zienkiewicz et al. [250] chapter 6, are determined by

$$L_a(x, y) = \frac{1}{2\Delta}(a_a + b_a\, x + c_a\, y) = \frac{\Delta_a}{\Delta}\,, \quad \text{with} \quad 2\Delta_a = a_a + b_a\, x + c_a\, y \tag{3.59}$$

with the coefficients a_a, b_a, c_a for $a = 1, 2, 3$ based on the coordinates x_a, y_a of the vertices of a three-noded triangular element, i.e.,

$$a_a = x_{a+1}\, y_{a+2} - x_{a+2}\, y_{a+1}\,, \quad b_a = y_{a+1} - y_{a+2} \quad \text{and} \quad c_a = x_{a+2} - x_{a+1}\,, \tag{3.60}$$

defined by cyclic interchange of the subscripts $1, 2, 3$. The area of the triangular domain is $\Delta = 1/2 \sum_a x_a\, b_a$. As a geometrical interpretation Δ_a is twice the area of a triangle defined through two points of the considered triangle and a point (x, y) inside the triangular domain. The shape functions for the three-noded triangle are $N^j = L_a$. For further insides and a detailed description of the construction, cf., e.g., Zienkiewicz et al. [250], Zienkiewicz and Taylor [246]. The resulting functions for $[\mathcal{P}_1]^2$, in parameter space $\boldsymbol{\xi}$ by interchanging $\boldsymbol{x}$ with $\boldsymbol{\xi}$ in (3.59), (3.60), are given by $N^1 = L_1 = 1-\xi-\eta$, $N^2 = L_2 = \xi$ and $N^3 = L_3 = \eta$ and for $[\mathcal{P}_2]^2$, below.

$$N^j = \begin{cases} (2L_j - 1)L_j\,, & \text{for } j = 1, 2, 3 \\ 4L_1 L_2\,, & \text{for } j = 4 \\ 4L_2 L_3\,, & \text{for } j = 5 \\ 4L_3 L_1\,, & \text{for } j = 6 \end{cases} \tag{3.61}$$

For applications in $d = 3$, the lowest order functions on a tetrahedral element in volume coordinates are

$$L_a(x, y, z) = \frac{1}{6V}(a_a j + b_a\, x + c_a\, y + d_a\, z)\,, \quad \text{for } a = 1, 2, 3, 4\,. \tag{3.62}$$

The volume V and the coefficients a_a, b_a, c_a, d_a of the tetrahedral element are determined by

$$6V = \det \begin{bmatrix} 1 & x_1 & y_1 & z_1 \\ 1 & x_2 & y_2 & z_2 \\ 1 & x_3 & y_3 & z_3 \\ 1 & x_4 & y_4 & z_4 \end{bmatrix}\,, \tag{3.63}$$

and

$$(a, b, c, d)_a = \det \left(\begin{bmatrix} x_2 & y_2 & z_2 \\ x_3 & y_3 & z_3 \\ x_4 & y_4 & z_4 \end{bmatrix}, \begin{bmatrix} y_2 & z_2 & 1 \\ y_3 & z_3 & 1 \\ y_4 & z_4 & 1 \end{bmatrix}, \begin{bmatrix} z_2 & 1 & x_2 \\ z_3 & 1 & x_3 \\ z_4 & 1 & x_4 \end{bmatrix}, \begin{bmatrix} 1 & x_2 & y_2 \\ 1 & x_3 & y_3 \\ 1 & x_4 & y_4 \end{bmatrix} \right)\,, \tag{3.64}$$

with the constants $(a, b, c, d)_a$ with $a = 1, 2, 3, 4$ defined by cyclic interchange of the subscripts in the order 1, 2, 3, 4, cf. Zienkiewicz et al. [250]. The functions for $[\mathcal{P}_1]^3$, in parameter space $\boldsymbol{\xi}$, by replacing $\boldsymbol{x}$ with $\boldsymbol{\xi}$, are $N^1 = L_1 = 1 - \xi - \eta - \zeta$, $N^2 = L_2 = \xi$, $N^3 = L_3 = \eta$ and $N^4 = L_4 = \zeta$ and for $[\mathcal{P}_2]^3$ given below.

$$N^j = \begin{cases} (2L_j - 1)L_j\,, & \text{for } j = 1, 2, 3, 4 & & \\ 4L_2 L_1\,, & \text{for } j = 5 & 4L_3 L_1\,, & \text{for } j = 6 \\ 4L_4 L_1\,, & \text{for } j = 7 & 4L_2 L_3\,, & \text{for } j = 8 \\ 4L_3 L_4\,, & \text{for } j = 9 & 4L_4 L_2\,, & \text{for } j = 10 \end{cases} \tag{3.65}$$

For the evaluation of higher order functions a combinations of the lowest order functions are used. The later approach can be used for a construction of approximation

functions on arbitrary domains directly in the physical space $\boldsymbol{x}$ without any transformation or mapping from the parameter space $\boldsymbol{\xi}$, if the elements in physical space are straight-edged, which holds for higher order functions as well. For a detailed explanation of the derivative of Lagrange functions see Zienkiewicz et al. [250] chapter 6 and Zienkiewicz and Taylor [246] chapter 8. A further approach is given, e.g., in Argyris et al. [4], Taylor [228] and Silvester [209], cf. Zienkiewicz et al. [250].

Evaluation of approximation functions within the space $\mathcal{Q}_k$
The determination of approximation functions in $\mathcal{Q}_k$ can be performed either with respect to a system of equations and (3.58) or based on a combination of one dimensional shape functions with

$$N^j = N^{il} = N^i(\xi)\, N^l(\eta)\,, \tag{3.66}$$

with i and l denoting the column and row number of the considered sampling point j of the domain, which is, e.g., $N^1 = N^{11}$ with $j = 1, i = 1$ and $l = 1$ related to P^1 in Figure 3.3, in terms of an equal number of subdivisions in each direction. The one dimensional polynomial functions $N^j(\xi)$, of degree $k-1$, with $N^j(\xi^j) = 1$ and $N^j(\xi^i) = 0$, are determined by

$$N^j(\xi) = \prod_{\substack{i=1 \\ i \neq j}}^{k} \frac{\xi^i - \xi}{\xi^i - \xi^j}\,. \tag{3.67}$$

The evaluation of (3.66) with (3.67) for $[\mathcal{Q}_1]^2$ yields

$$N^j = \frac{1}{4}(1 + \xi^j\,\xi)(1 + \eta^j\,\eta) \quad \text{for corner nodes } j = 1, 2, 3, 4 \tag{3.68}$$

with ξ^j and η^j denoting the coordinates at the j-th node, see, e.g., Wriggers [236], Zienkiewicz et al. [250]. For a higher order approach of $[\mathcal{Q}_2]^2$ the functions are given by

$$N^j = \begin{cases} \frac{1}{4}\xi\eta(1+\xi^j)(1+\eta^j)\,, & \text{for corner nodes}\,, & j = 1, .., 4\,, \\ \frac{1}{2}\eta(1-\xi^2)(\eta+\eta^j)\,, & \text{for mid nodes with } \xi^j = 0\,, & j = 5, 7\,, \\ \frac{1}{2}\xi(\xi+\xi^j)(1+\eta^2)\,, & \text{for mid nodes with } \eta^j = 0\,, & j = 6, 8\,, \\ (1-\xi^2)(1-\eta^2)\,, & \text{for center nodes}\,, & j = 9\,. \end{cases} \tag{3.69}$$

Analogously to the extension of function evaluation on triangular domains with $k \geq 2$, higher order functions on quadrilaterals can be constructed, cf. Zienkiewicz et al. [250], among others. For the framework of hexahedral domains the basic relation (3.66) is extended by a third one-dimensional Lagrange function leading to

$$N^j = N^{ilm} = N^i(\xi)\, N^l(\eta)\, N^m(\zeta)\,. \tag{3.70}$$

The alternative approach for the evaluation of approximation functions on quadrilateral and hexahedral domains is defined by the construction of a system of equations by means of the function $N^j(\boldsymbol{\xi})$, based on a complete polynomial in the space $\mathcal{Q}_k$ of order k, which is defined by the relations (3.55), and solved regarding the condition (3.58).

3.3.2 The $\mathcal{W}^q(\mathrm{div},\mathcal{B})$-conforming Raviart-Thomas ($\mathcal{RT}_m$) element

The $\mathcal{W}^q(\mathrm{div},\mathcal{B})$-conforming Raviart-Thomas space, see Boffi et al. [49], Brezzi and Fortin [56], can be considered for quantities, which are from a physical point of view normal continuous. Therein, the normal components of the quantities are approximated continuously, whereas the tangential components are unrestricted, cf., e.g., Brezzi and Fortin [56] and Ervin [95]. These quantities are, e.g., the Cauchy stresses $\boldsymbol{\sigma}$ or the magnetic induction $\boldsymbol{B}$. The approximation space is given by $\mathcal{W}^q(\mathrm{div},\mathcal{B})$, where q denotes the corresponding $\mathcal{L}^q(\mathcal{B})$-norm, which has to be satisfied (i.e., for $\boldsymbol{\sigma}$: $\|\boldsymbol{\sigma}\|_{\mathcal{L}^q(\mathcal{B})} < \infty$ and $\|\operatorname{div}\boldsymbol{\sigma}\|_{\mathcal{L}^q(\mathcal{B})} < \infty$). Since the formulations considered are restricted to quantities occurring in quadratic form in $\mathcal{W}^q(\mathrm{div},\mathcal{B})$, a restriction to the Hilbert space $\mathcal{H}(\mathrm{div},\mathcal{B})$ is applied and therefore only square integrable functions are considered with $\mathcal{L}^2(\mathcal{B})$-norm in (3.2). The $\mathcal{RT}_m$ space for $d = 2$ triangular and for $d = 3$ tetrahedral elements, denoted with the upper character $\triangle$, is defined by

$$[\mathcal{RT}_m^{\triangle}]^d = [\mathcal{P}_m]^d \oplus \boldsymbol{\xi}\,\mathcal{P}_m\,, \quad (m \geq 0)\,, \tag{3.71}$$

based on the definition of the space $\mathcal{P}_m$ (3.54). For the application of $\mathcal{RT}_m$ functions on bilinear and trilinear elements, denoted with the upper character $\square$, the $\mathcal{RT}_m$ space is introduced by

$$[\mathcal{RT}_m^{\square}]^d = [\mathcal{Q}_m]^d \oplus \boldsymbol{\xi}\,\mathcal{Q}_m\,, \quad (m \geq 0)\,, \tag{3.72}$$

with $\mathcal{Q}_k$ defined by (3.55), which can be reformulated into

$$[\mathcal{RT}_m^{\square}]^2 = \mathcal{P}_{m+1,m} \times \mathcal{P}_{m,m+1}\,, \quad (m \geq 0) \tag{3.73}$$

for quadrilateral elements with $d = 2$ and the $\mathcal{RT}$ space for hexahedral elements with $d = 3$ is

$$[\mathcal{RT}_m^{\square}]^3 = \mathcal{P}_{m+1,m,m} \times \mathcal{P}_{m,m+1,m} \times \mathcal{P}_{m,m,m+1}\,, \quad (m \geq 0)\,, \tag{3.74}$$

where $\mathcal{P}_{n,o}$ and analogously $\mathcal{P}_{n,o,p}$ define the space of polynomial functions on $\hat{\mathcal{B}}$ of degree at most n in ξ, o in η and p in ζ with some constants $a_{ij}, a_{ijk} \in \mathbb{R}$, which is

$$\mathcal{P}_{n,o} = \sum_{0\leq i,j\leq n,o} a_{ij}\,\xi^i\,\eta^j \quad \text{and} \quad \mathcal{P}_{n,o,p} = \sum_{0\leq i,j,k\leq n,o,p} a_{ijk}\,\xi^i\,\eta^j\,\zeta^k\,. \tag{3.75}$$

Therefore, the $[\mathcal{RT}_m^{\square}]^2$ basis is denoted by the vector fields $(\xi^i\eta^j, 0)$ and $(0, \xi^j\eta^i)$ with $0 \leq i \leq m+1$ and $0 \leq j \leq m$, cf. Arnold et al. [8]. The dimensions of the $\mathcal{RT}_m$ space, cf., e.g., Brezzi and Fortin [56] and Kirby et al. [131], are given for triangular ($d = 2$) and tetrahedral ($d = 3$) elements with

$$\dim([\mathcal{RT}_m^{\triangle}]^d) = \begin{cases} (m+1)(m+3)\,, & \text{for } d = 2\,, \\ \frac{1}{2}(m+1)(m+2)(m+4)\,, & \text{for } d = 3\,, \end{cases} \tag{3.76}$$

and for quadrilateral ($d = 2$) and hexahedral ($d = 3$) element domains by

$$\dim([\mathcal{RT}_m^{\square}]^d) = \begin{cases} 2(m+1)(m+2)\,, & \text{for } d = 2\,, \\ 3(m+1)^2(m+2)\,, & \text{for } d = 3\,. \end{cases} \tag{3.77}$$

Both can be divided into the dimensions of inner and outer sampling points with

$$\dim([\mathcal{RT}_m^{\triangle}]^d) = \begin{cases} d=2: \begin{cases} 3(m+1)\,, & \text{out. dim}\,, \\ m(m+1)\,, & \text{in. dim}\,, \end{cases} \\ d=3: \begin{cases} 2(m+1)(m+2)\,, & \text{out. dim}\,, \\ \frac{1}{2}m(m+1)(m+2)\,, & \text{in. dim}\,, \end{cases} \end{cases} \tag{3.78}$$

and further

$$\dim([\mathcal{RT}_m^{\square}]^d) = \begin{cases} d=2: \begin{cases} 4(m+1)\,, & \text{out. dim}\,, \\ 2m(m+1)\,, & \text{in. dim}\,, \end{cases} \\ d=3: \begin{cases} 6(m+1)^2\,, & \text{out. dim}\,, \\ 3m(m+1)^2\,, & \text{in. dim}\,. \end{cases} \end{cases} \tag{3.79}$$

The resulting number of sampling points and consequently the number of degrees of freedom in each dimension are exemplarily listed in Table 3.2. In addition, the resulting element topologies for $\mathcal{RT}_m$ with $m = 0, 1, 2$ are illustrated in Figure 3.4 and 3.5, for $d = 2$ on triangle and quadrilateral domains.

Table 3.2: Dimensions of $\mathcal{RT}_m$ spaces for $d = 2, 3$

	$\dim([\mathcal{RT}_m^{\triangle}]^2)$	$\dim([\mathcal{RT}_m^{\triangle}]^3)$	$\dim([\mathcal{RT}_m^{\square}]^2)$	$\dim([\mathcal{RT}_m^{\square}]^3)$
$m=0$	3	4	4	6
$m=1$	$8\,(6+2)$	$15\,(12+3)$	$12\,(8+4)$	$36\,(24+12)$
$m=2$	$15\,(9+6)$	$36\,(24+12)$	$24\,(12+12)$	$108\,(54+54)$

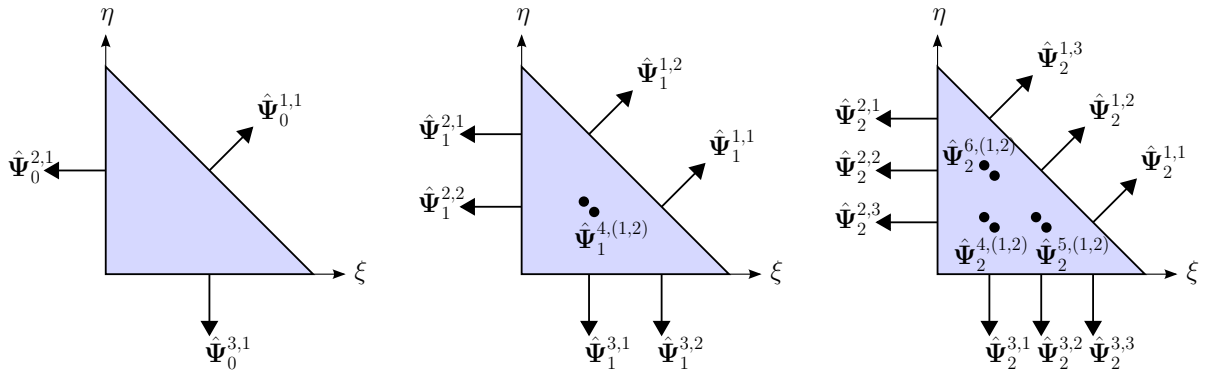

Figure 3.4: $[\mathcal{RT}_m^{\triangle}]^2$ elements with $m = 0, 1, 2$

The vector-valued Raviart-Thomas functions $\boldsymbol{\Psi}_m^{j,i}$, with j denoting the associated edge e^j or face f^j, i the node number on that edge or face with $i = 1, .., m+1$ and m the approximation order, are determined by solving a system of equations, which is constructed by evaluation of the inner and outer moments. These outer moments, evaluated for the edge degrees of freedom, are defined by

$$\int_{e^j} (\hat{\boldsymbol{v}}_m \cdot \hat{\boldsymbol{n}}^j)\, \hat{p}_m \,\mathrm{d}s\,, \quad \forall\, \hat{p}_m \in \mathcal{P}_m(e^j)\,, \text{for each edge } e^j\,, \tag{3.80}$$

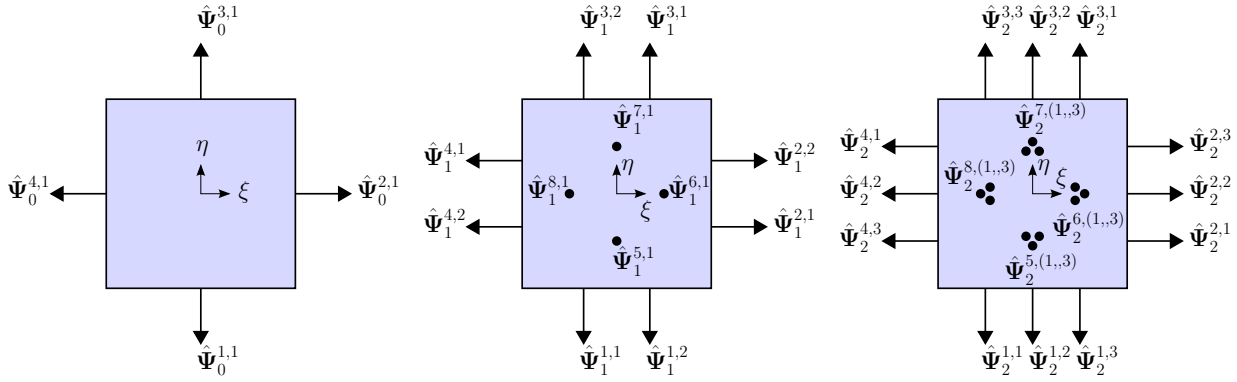

Figure 3.5: $[\mathcal{RT}_m^{\square}]^2$ elements with $m = 0, 1, 2$

and the inner moments for the internal degrees of freedom are

$$\int_K \hat{\boldsymbol{v}}_m \cdot \hat{\boldsymbol{p}}_{m-1} \, \mathrm{d}a \,, \quad \forall \, \hat{\boldsymbol{p}}_{m-1} \in [\mathcal{P}_{m-1}]^2 \,, \text{for } m \geq 1 \,. \tag{3.81}$$

Analogously, the degrees of freedom on the faces ($d = 3$) are obtained by

$$\int_{f^j} (\hat{\boldsymbol{v}}_m \cdot \hat{\boldsymbol{n}}^j) \, \hat{p}_m \, \mathrm{d}a \,, \quad \forall \, \hat{p}_m \in \mathcal{P}_m(f^j) \,, \text{for each face } f^j \,, \tag{3.82}$$

and for the internal degrees of freedom with

$$\int_T \hat{\boldsymbol{v}}_m \cdot \hat{\boldsymbol{p}}_{m-1} \, \mathrm{d}v \,, \quad \forall \, \hat{\boldsymbol{p}}_{m-1} \in [\mathcal{P}_{m-1}]^3 \,, \text{for } m \geq 1 \,, \tag{3.83}$$

cf., e.g., Brezzi and Fortin [56], Boffi et al. [49]. Here, $\hat{\boldsymbol{n}}^j$ is the outward normal vector on the associated edge or face on the unit reference element, $\hat{p}_m$ and $\hat{\boldsymbol{p}}_{m-1}$ are scalar and vectorial functions of order m and $m-1$ at the corresponding interpolation site depending on the related edge and sampling point, see Appendix 8.1.2. These functions have to be chosen linear independent. For the functions $\hat{p}_m$ and $\hat{\boldsymbol{p}}_{m-1}$ on $[\mathcal{RT}_m]^2$ one dimensional Lagrange functions on the associated edge, related to the $[\mathcal{RT}_m]^2$ nodes on that edge, are used here. Analogously, two dimensional Lagrange functions on the associated faces are considered for $\hat{p}_m$ and $\hat{\boldsymbol{p}}_{m-1}$ on $[\mathcal{RT}_m]^3$. A requirement, which has to be fulfilled by the Raviart-Thomas basis functions, is that the sum of $\mathcal{RT}_m$ functions $\boldsymbol{\Psi}_m^{j,i}$ related to one edge or face j, multiplied with the corresponding outward normal and considering the associated edge relation (see Appendix 8.1.2), has to be equal to one on that edge and 0 on all other edges, which is

$$\boldsymbol{n}^l \cdot \sum_i \boldsymbol{\Psi}_m^{j,i} = \begin{cases} 1 \,, & \text{for } l = j \\ 0 \,, & \text{for } l \neq j \end{cases} \,. \tag{3.84}$$

The solution of the system of equations yields the linear independent vectorial basis functions for the inner and outer degrees of freedom at the j-th edge of the reference element, denoted by $\boldsymbol{\Psi}_m^{j,i}(\boldsymbol{\xi})$, cf. Ciarlet and Lions [76]. These vectorial basis functions have to be transformed from the parameter space $(\xi, \eta)^T$ to the physical space $(x, y)^T$. This is performed for vector-valued functions by using a contra- or covariant Piola transformation, which is discussed later on. The basic assumptions for the evaluation of $\mathcal{H}(\mathrm{div}, \mathcal{B})$-conforming functions as outer and inner moments are briefly presented in Appendix 8.1.2.

There are different possibilities for the construction of $\mathcal{RT}_m$ functions. An alternative procedure, avoiding the application of the Piola transformation for vector-valued quantities, is the construction of $\mathcal{H}(\mathrm{div}, \mathcal{B})$-conforming $\mathcal{RT}$ functions directly in the physical space $\boldsymbol{x} = (x, y)^T$ and $\boldsymbol{x} = (x, y, z)^T$, respectively. This procedure is performed, here exemplarily for triangular and tetrahedral elements, based on the construction of lowest order functions with $m = 0$, cf., e.g., Bahriawati and Carstensen [22]. The extension to higher order $\mathcal{RT}_m$ elements with $m \geq 1$ is done by means of the lowest order approximation functions and additional $\mathcal{P}_m$ Lagrange functions. Following Bahriawati and Carstensen [22], the $\mathcal{RT}_0$ functions are determined by

$$\boldsymbol{\Psi}_0^{j,1}(\boldsymbol{x}) = \frac{|e^j|}{2|T|}(\boldsymbol{x} - P^j) \quad \text{for } j = 1, 2, 3 \text{ and } \boldsymbol{x} \in T\,, \tag{3.85}$$

with the length of the j-th edge $|e^j|$, T as the area of the triangle and P^j is the vertex opposite to the edge e^j. The extension to the three dimensional framework is given straightforward by

$$\boldsymbol{\Psi}_0^{j,1}(\boldsymbol{x}) = \frac{|f^j|}{3|V|}(\boldsymbol{x} - P^j) \quad \text{for } j = 1, 2, 3, 4 \text{ and } \boldsymbol{x} \in V\,, \tag{3.86}$$

with f^j the area of the j-th face, V as the volume of tetrahedron and P_j as the vertex opposite to the face f^j. For the determination of the shape functions within the parameter space $\boldsymbol{\xi} = (\xi, \eta)^T$ or respectively $\boldsymbol{\xi} = (\xi, \eta, \zeta)^T$ on unit triangular and tetrahedral elements, with known area and volume, the equations can be simplified to

$$\boldsymbol{\Psi}_0^{j,1}(\boldsymbol{x}) = |e^j|(\boldsymbol{x} - P^j) \quad \text{for } j = 1, 2, 3 \text{ and } \boldsymbol{x} \in T\,, \tag{3.87}$$

and

$$\boldsymbol{\Psi}_0^{j,1}(\boldsymbol{x}) = 2|f^j|(\boldsymbol{x} - P^j) \quad \text{for } j = 1, 2, 3, 4 \text{ and } \boldsymbol{x} \in V\,. \tag{3.88}$$

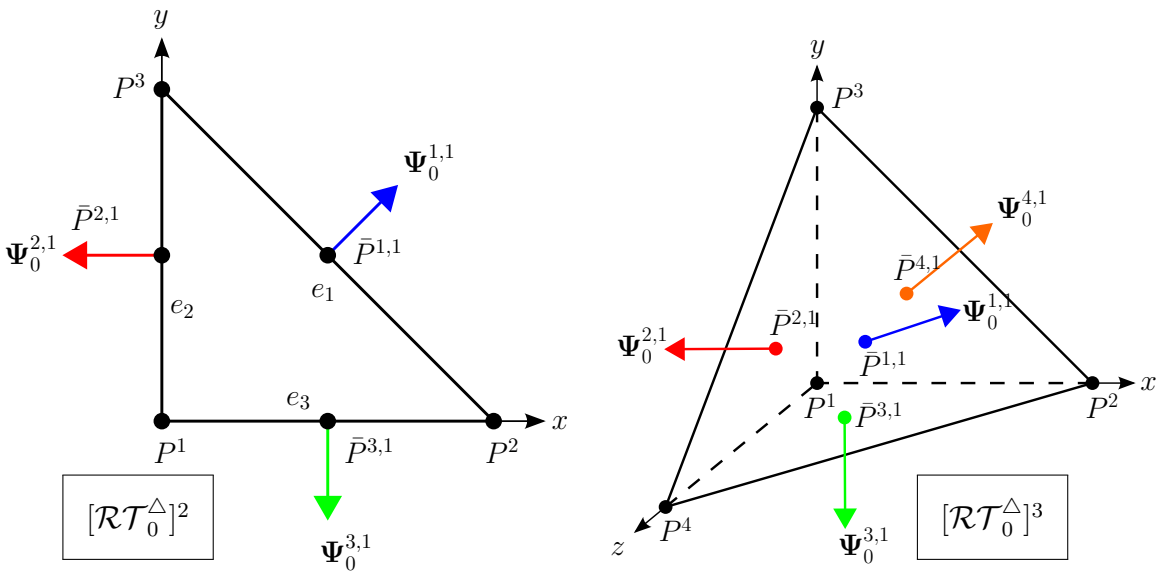

Figure 3.6: $\mathcal{RT}_0$ shape functions on unit triangle and tetrahedral elements in physical space

The fundamental basis for the construction of higher order $\mathcal{H}(\mathrm{div})$-conforming vector-valued Raviart-Thomas ansatz functions is given by the $\mathcal{RT}_0$ functions in (3.85) and

(3.86) and shown in Figure 3.6 for $[\mathcal{RT}_0^{\triangle}]^d$. For a higher order approximation, additional nodes have to be introduced on the edges and faces as well as at the interior of the element domain, which produces new edge and internal degrees of freedom, cf. Table 3.2. As a basis for the construction of $[\mathcal{RT}_1^{\triangle}]^2$ functions, the $[\mathcal{RT}_0^{\triangle}]^2$ basis functions are used. Additionally, linear Lagrange shape functions $\mathcal{P}_1$ are considered, with respect to the two nodes on the related edge $\bar{P}^{j,i}$ and the inner node $\bar{P}^I$. For $[\mathcal{RT}_1^{\triangle}]^2$, $\bar{P}^I$ is located at the centroid. Therefore, three separate triangles are constructed, see top right in Figure 3.7, for which the condition of Lagrange shape functions, with the value 1 at the specific node and 0 at the other two nodes, is fulfilled. This procedure can be extended straightforward for $d = 3$. An illustration of this idea for a $[\mathcal{RT}_m^{\triangle}]^d$ approach is exemplarily depicted in Figure 3.7 for triangular elements up to order $m = 3$ and for tetrahedral elements up to order $m = 1$ in Figure 3.8. The evaluation of edge or face related outer functions is denoted by

$$\boldsymbol{\Psi}_m^{j,i}(\boldsymbol{x}) = \boldsymbol{\Psi}_0^{j,1}(\boldsymbol{x})\, N_m^{j,\bar{P}^{j,i}}(\boldsymbol{x}) \quad \text{for } \boldsymbol{x} \in \mathbb{R}^2 \text{ and } \boldsymbol{x} \in \mathbb{R}^3\,, \tag{3.89}$$

where j is defined by the considered edge or face number e^j or f^j, i is the number of sampling points on each edge or face with $i = 1, .., m+1$ for $d = 2$ and $i = 1, .., 1/2(m+1)(m+2)$ for $d = 3$ and m corresponds to the polynomial degree of the function to be constructed.
Furthermore, for the polynomial order of $m \geq 1$ the inner functions have to be evaluated additionally. Therefore, the Lagrange functions at the corresponding inner nodes $\bar{P}^{I,j-3}$ for $d = 2$ and $\bar{P}^{I,j-4}$ for $d = 3$ are considered, which yields the following relations applicable for the inner functions for $d = 2$

$$\boldsymbol{\Psi}_m^{j,i}(\boldsymbol{x}) = \boldsymbol{\Psi}_0^{i+1,1}(\boldsymbol{x})\, N_m^{i+1,\bar{P}^{I,j-3}}(\boldsymbol{x}) \quad \text{for } \boldsymbol{x} \in \mathbb{R}^2\,, \tag{3.90}$$

and $d = 3$

$$\boldsymbol{\Psi}_m^{j,i}(\boldsymbol{x}) = \boldsymbol{\Psi}_0^{i+1,1}(\boldsymbol{x})\, N_m^{i+1,\bar{P}^{I,j-4}}(\boldsymbol{x}) \quad \text{for } \boldsymbol{x} \in \mathbb{R}^3\,. \tag{3.91}$$

Here, j is the node number of the inner nodes, which is defined for triangular and tetrahedral elements by

$$j = \begin{cases} j = 4, .., 3 + m(m+1)/2\,, & \text{for in. functions } d = 2 \\ j = 5, .., 4 + m(m+1)(m+2)/6\,, & \text{for in. functions } d = 3 \end{cases}\,. \tag{3.92}$$

The construction of the necessary Lagrange shape functions is straightforward, as discussed previously, where the only needed quantities are the nodal coordinates within the element. An example for the evaluation of $[\mathcal{RT}_1^{\triangle}]^2$ based on $[\mathcal{RT}_0^{\triangle}]^2$ functions is performed in Appendix 8.1.2. The choice of Lagrange functions for the evaluation at the inner $\mathcal{RT}$ sampling points is not restricted to the here proposed formulation. Due to the topology of the unit triangle and tetrahedral element lowest order $\mathcal{RT}$ functions of the inclined edge or face are not considered. The presented approach for a direct evaluation of $\mathcal{RT}_m$ approximation functions on arbitrary straight-edged triangular and tetrahedral elements, also holds for the framework of quadrilateral and hexahedral element domains, which will not be presented in detail. This approach is possible, since the properties and direction of the $\mathcal{RT}_m$ function is always determined by the lowest order $\mathcal{RT}$ approach (3.85), (3.86). For higher order functions, only the polynomial degree has to be increased, which is done by the Lagrange functions.

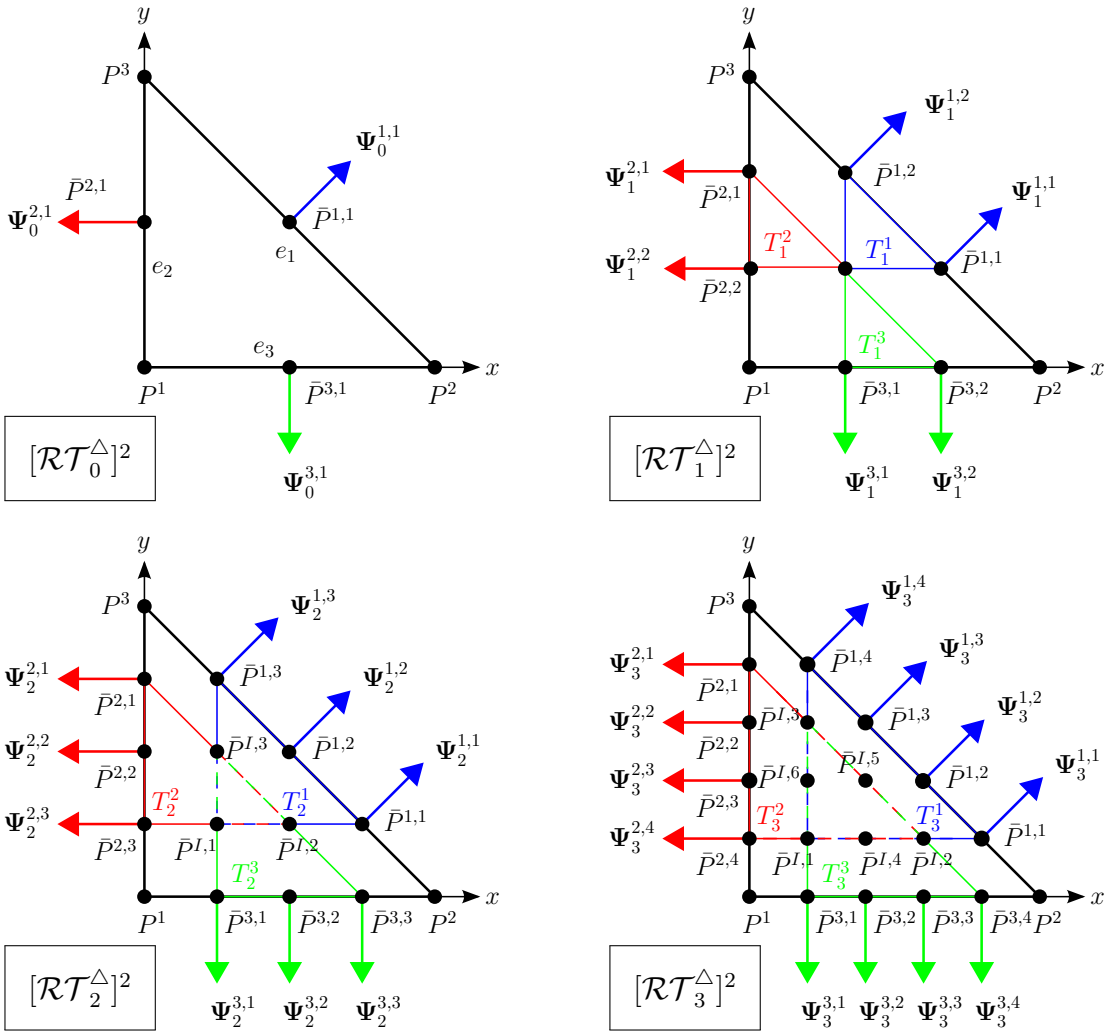

Figure 3.7: Evaluation of $[\mathcal{RT}_m^{\triangle}]^2$, $m = 1, 2, 3$, functions on arbitrary configurations for straight-edged elements, based on $[\mathcal{RT}_0^{\triangle}]^2$ and $[\mathcal{P}_m]^2$ (plots without internal functions).

3.3.3 The $\mathcal{W}^q(\mathrm{div}, \mathcal{B})$-conforming Brezzi-Douglas-Marini ($\mathcal{BDM}_m$) element

The $\mathcal{H}(\mathrm{div}, \mathcal{B})$-conforming Brezzi-Douglas-Marini element is considered for quantities, which are normal continuous, from a physical point of view. Thus the properties correspond to those of the Raviart-Thomas element. Furthermore, both the $\mathcal{BDM}_m$ and $\mathcal{RT}_m$ spaces strictly contain the space $\mathcal{P}_m$ but not the space $\mathcal{P}_{m+1}$. For triangular and tetrahedral elements, with the same approximation order m the space $\mathcal{RT}_m$ contains the space $\mathcal{BDM}_m$ with $\mathcal{BDM}_m \subset \mathcal{RT}_m$, cf. Brezzi and Fortin [56]. The $\mathcal{BDM}$ space is proposed for $d = 2$ elements by Brezzi et al. [57] and extended to $d = 3$ by Brezzi et al. [58]. The $\mathcal{BDM}_m$ space on triangular and tetrahedral elements is defined by

$$[\mathcal{BDM}_m^{\triangle}]^d = [\mathcal{P}_m]^d\,, \quad \text{for } m \geq 1\,. \tag{3.93}$$

This does not hold for quadrilateral elements, see Arnold et al. [8], where the $\mathcal{BDM}_m$ space is the span of $\mathcal{P}_m \times \mathcal{P}_m$ and the two vector fields $\mathrm{curl}(\xi^{m+1}\eta)$ and $\mathrm{curl}(\xi\eta^{m+1})$ defined by

$$[\mathcal{BDM}_m^{\square}]^2 = [\mathcal{P}_m]^2 \oplus \mathrm{curl}(\xi^{m+1}\eta) \oplus \mathrm{curl}(\xi\eta^{m+1})\,, \quad \text{for } m \geq 1\,, \tag{3.94}$$

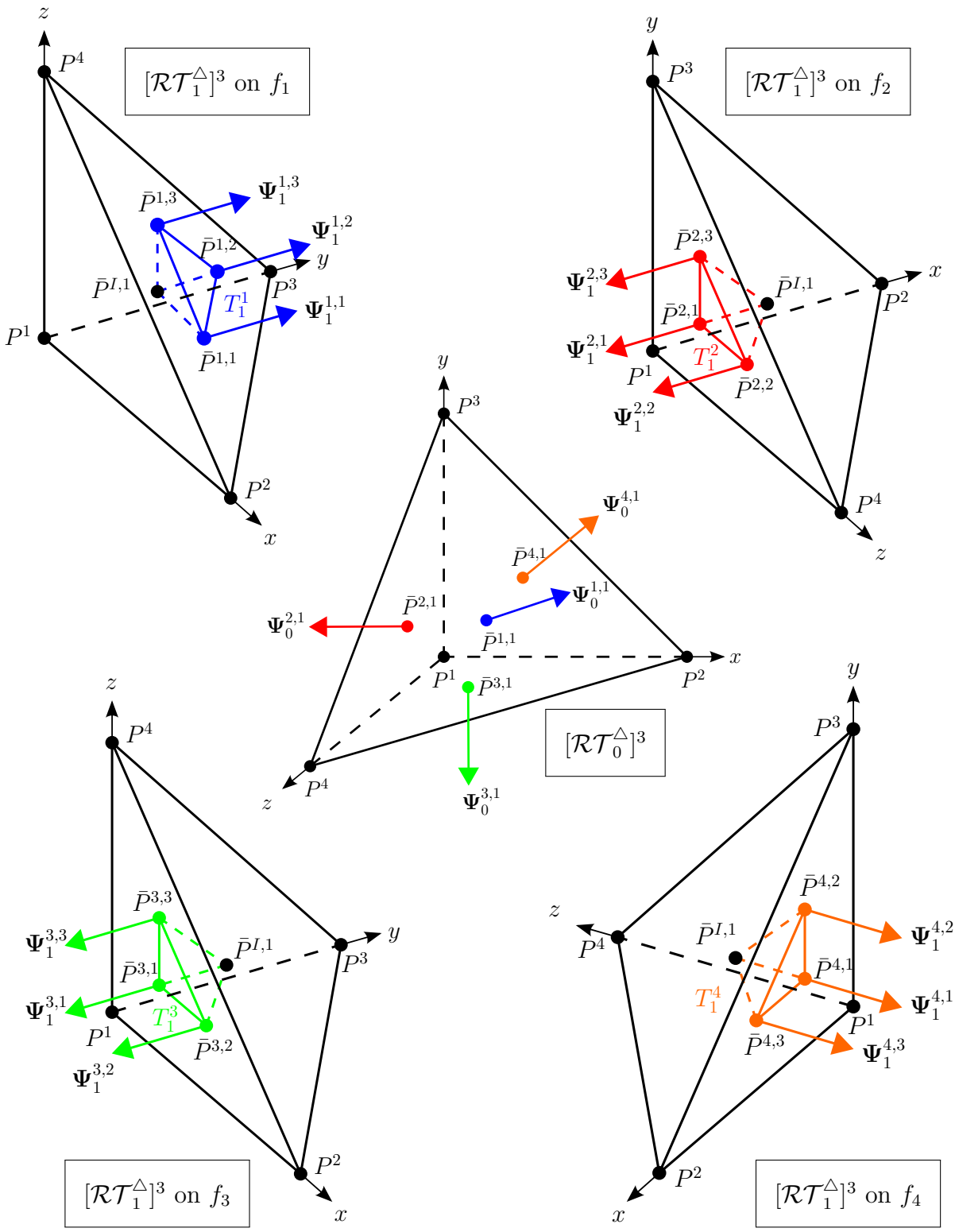

Figure 3.8: Evaluation of $[\mathcal{RT}_1^{\triangle}]^3$ functions on an arbitrary configuration for straight-edged elements, based on $[\mathcal{RT}_0^{\triangle}]^3$ and $[\mathcal{P}_1]^3$ (plots without internal functions).

with $\mathrm{curl}(v(\xi,\eta)) = \left(-\frac{\partial v}{\partial \eta}, \frac{\partial v}{\partial \xi}\right)^T$. For completeness, the $\mathcal{BDM}_m$ space for $m \geq 1$ is defined on hexahedral elements by

$$[\mathcal{BDM}_m^{\square}]^3 = \; [\mathcal{P}_m]^3 \overset{m}{\underset{i=0}{\oplus}} r_i \,\mathrm{curl}\boldsymbol{\chi}_i^r \overset{m}{\underset{i=0}{\oplus}} s_i \,\mathrm{curl}\boldsymbol{\chi}_i^s \overset{m}{\underset{i=0}{\oplus}} t_i \,\mathrm{curl}\boldsymbol{\chi}_i^t \,, \tag{3.95}$$

with $(r_i, s_i, t_i) \in \mathbb{R}^{3(m+1)}$ and the curl operator $\mathrm{curl}(\boldsymbol{v}) = \left(\frac{\partial v_z}{\partial \eta} - \frac{\partial v_y}{\partial \zeta}, \frac{\partial v_x}{\partial \zeta} - \frac{\partial v_z}{\partial \xi}, \frac{\partial v_y}{\partial \xi} - \frac{\partial v_x}{\partial \eta}\right)^T$ applied on the vector functions $\boldsymbol{\chi}_i^r = (0, 0, \xi^{i+1}\eta\zeta^{m-i})$, $\boldsymbol{\chi}_i^s = (\xi^{m-i}\eta^{i+1}\zeta, 0, 0)$ and $\boldsymbol{\chi}_i^t = (0, \xi\eta^{m-i}\zeta^{i+1}, 0)$, cf. Brezzi and Fortin [56].
The dimension of the $\mathcal{BDM}_m$ space, cf., e.g., Boffi et al. [49], Brezzi and Fortin [56] and Kirby et al. [131], are given for triangular ($d = 2$) and tetrahedral ($d = 3$) elements, denoted by the upper character $\triangle$, with

$$\dim([\mathcal{BDM}_m^{\triangle}]^d) = \begin{cases} (m+1)(m+2) = m^2 + 3m + 2\,, & \text{for } d = 2\,, \\ \frac{1}{2}(m+1)(m+2)(m+3)\,, & \text{for } d = 3\,, \end{cases} \tag{3.96}$$

and furthermore for quadrilateral ($d = 2$) and hexahedral ($d = 3$) element domains, denoted by the upper character $\square$, by

$$\dim([\mathcal{BDM}_m^{\square}]^d) = \begin{cases} (m+1)(m+2) + 2 = m^2 + 3m + 4\,, & \text{for } d = 2\,, \\ \frac{1}{2}(m+1)(m+2)(m+3) + 3(m+1)\,, & \text{for } d = 3\,. \end{cases} \tag{3.97}$$

The number of degrees of freedom for $d = 2, 3$ are listed in Table 3.3.

Table 3.3: Dimensions of $\mathcal{BDM}_m$ spaces for $d = 2, 3$

	$\dim([\mathcal{BDM}_m^{\triangle}]^2)$	$\dim([\mathcal{BDM}_m^{\triangle}]^3)$	$\dim([\mathcal{BDM}_m^{\square}]^2)$	$\dim([\mathcal{BDM}_m^{\square}]^3)$
$m = 1$	6	12	8	18
$m = 2$	12	30	14	39
$m = 3$	20	60	22	72

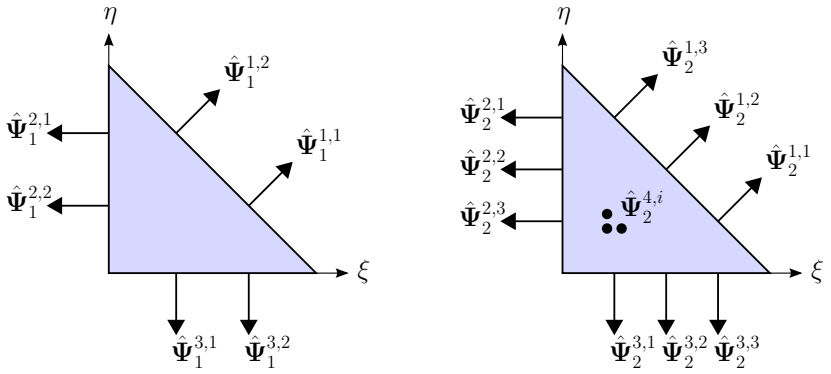

Figure 3.9: $[\mathcal{BDM}_m^{\triangle}]^2$ elements with $m = 1, 2$

However in the proposed work the considered $\mathcal{BDM}_m$ elements are restricted to the two dimensional framework, where the evaluation of the approximation functions are performed with respect to inner and outer moments as in the construction of $\mathcal{RT}_m$ functions. Thus, the evaluation is based on the determination of

$$\int_{e^j} (\hat{\boldsymbol{v}}_m \cdot \hat{\boldsymbol{n}}^j)\, \hat{p}_m \,\mathrm{d}s = 0\,, \quad \forall\, \hat{p}_m \in \mathcal{P}_m(e^j) \text{ for each edge } e^j\,, \tag{3.98}$$

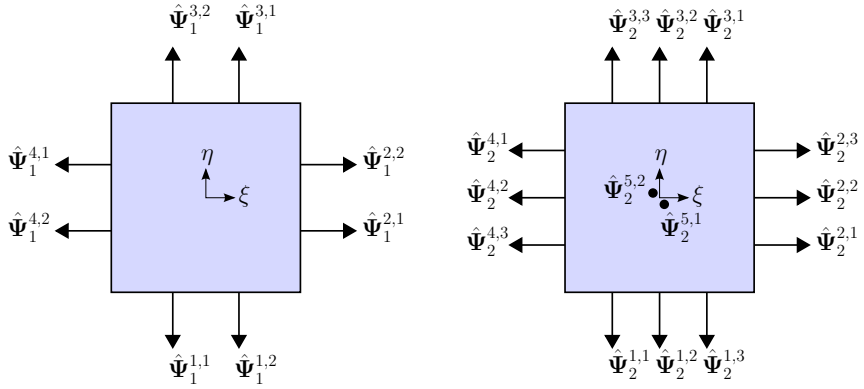

Figure 3.10: $[\mathcal{BDM}_m^{\square}]^2$ elements with $m = 1, 2$

for the outer moments and for the inner moments

$$\int_K \hat{\boldsymbol{v}}_m \cdot \hat{\boldsymbol{p}}_{m-1} \, \mathrm{d}a = 0 \,, \quad \forall \, \hat{\boldsymbol{p}}_{m-1} \in [\mathcal{P}_{m-1}]^2 \,, \text{for } m \geq 1 \,. \tag{3.99}$$

The quantities included $\hat{\boldsymbol{n}}^j$, $\hat{p}_m$ and $\hat{\boldsymbol{p}}_{m-1}$, result from the derivation of $\mathcal{RT}_m$ functions in analogy to the relations (3.80) and (3.81). Furthermore, taking into account the derived outer and inner moments (3.98) and (3.99), a linear system of equations is created for the determination of the coefficients of $\mathcal{BDM}_m$ functions $\boldsymbol{\Psi}_m^{j,i}$, which is solved by the relation to be 1 at the associated node and 0 at all other sampling points. The resulting functions have to fulfill the relation (3.84). The $\mathcal{BDM}_m$ functions are listed for triangular and quadrilateral elements up to order $m = 1, 2$ in the Appendix 8.1.3.

As already mentioned, the here presented spaces $\mathcal{RT}_m$, $\mathcal{BDM}_m$ strictly contain $\mathcal{P}_m$ but do not contain $\mathcal{P}_{m+1}$. This is important for the finite element convergence, which depends on the complete polynomial degree. For triangular elements the relation between the $\mathcal{RT}_m$ and $\mathcal{BDM}_m$ spaces is defined by:

$$\mathcal{RT}_0 \subset \mathcal{BDM}_1 \subset \mathcal{RT}_1 \subset \mathcal{BDM}_2 \subset \mathcal{RT}_2 \,. \tag{3.100}$$

The reduction of the $\mathcal{RT}_m$ space compared to the $\mathcal{BDM}_m$ space of same order m can be seen at the inner degrees of freedom of the related elements. However, for certain problems, especially in elasticity, the space $\mathcal{RT}_m$ is more suited, cf. Brezzi and Fortin [56] for a detailed explanation of the introduced function spaces and their relations.

3.4 Piola transformation and implementation aspects

For the mapping of vector-valued approximation functions between the different configurations, another transformation must be taken into account. Since, the previously introduced mapping φ, is an isomorphic mapping of functions in the finite element spaces $\mathcal{H}^m(\mathcal{B})$ to $\mathcal{H}^m(\hat{\mathcal{B}})$, for some configuration $\hat{\mathcal{B}}$, which does not necessarily guarantee continuity in the normal or tangential direction after the transformation, cf. Boffi et al. [49], Rognes et al. [193] and Ciarlet [78]. However, this continuities are essential for functions in $\mathcal{H}(\mathrm{div}, \mathcal{B})$ and $\mathcal{H}(\mathrm{curl}, \mathcal{B})$. Therefore, so-called Piola transformations have to be

applied. These transformations are denoted by $\varphi^{\mathrm{div}}(\boldsymbol{v})$ and $\varphi^{\mathrm{curl}}(\boldsymbol{v})$ as contravariant and covariant transformations of $\boldsymbol{v}$, defined by

$$\varphi^{\mathrm{div}}(\boldsymbol{v}) = \frac{1}{\det \boldsymbol{J}}\, \boldsymbol{J} \cdot \boldsymbol{v} \quad \text{and} \quad \varphi^{\mathrm{curl}}(\boldsymbol{v}) = \boldsymbol{J}^{-T} \cdot \boldsymbol{v}\,, \tag{3.101}$$

and preserve tangential and normal continuity. The contra- and covariant mappings are isomorphisms of $\mathcal{H}(\mathrm{div}, \mathcal{B})$ onto $\mathcal{H}(\mathrm{div}, \hat{\mathcal{B}})$ and $\mathcal{H}(\mathrm{curl}, \mathcal{B})$ onto $\mathcal{H}(\mathrm{curl}, \hat{\mathcal{B}})$, respectively, cf. Rognes et al. [193]. The transformations can be derived, considering the restrictions, which have to be preserved by the transformation. These are normal continuity with

$$[\![\boldsymbol{v} \cdot \boldsymbol{n}]\!] = 0 \;\Rightarrow (\boldsymbol{v} \cdot \boldsymbol{n})\, \mathrm{d}a = (\hat{\boldsymbol{v}} \cdot \hat{\boldsymbol{n}})\, \mathrm{d}\hat{a} \tag{3.102}$$

and for the covariant transformation tangential continuity

$$[\![\boldsymbol{v} \cdot \boldsymbol{s}]\!] = 0 \;\Rightarrow (\boldsymbol{v} \cdot \boldsymbol{s})\, \mathrm{d}x = (\hat{\boldsymbol{v}} \cdot \hat{\boldsymbol{s}})\, \mathrm{d}\hat{x}\,. \tag{3.103}$$

Here, $\boldsymbol{s}$ denotes the tangent of an edge and $\boldsymbol{J} = \nabla_{\boldsymbol{\xi}} \boldsymbol{x}$, with $\boldsymbol{\xi}$ as the parameter space and $\boldsymbol{x}$ as the physical space. For the contravariant transformation, the mapping of area elements $\mathrm{d}\boldsymbol{a} = \mathrm{cof}\, \boldsymbol{J} \cdot \mathrm{d}\hat{\boldsymbol{a}}$ with $\mathrm{cof}\, \boldsymbol{J} = \det(\boldsymbol{J})\, \boldsymbol{J}^{-T}$ and the relation $\mathrm{d}\boldsymbol{a} = \boldsymbol{n}\, \mathrm{d}a$ are inserted in (3.102), which yields

$$\boldsymbol{v} \cdot \mathrm{d}\boldsymbol{a} = \hat{\boldsymbol{v}} \cdot \mathrm{d}\hat{\boldsymbol{a}} \quad \Rightarrow \quad \boldsymbol{v} = \frac{1}{\det \boldsymbol{J}}\, \boldsymbol{J} \cdot \hat{\boldsymbol{v}}\,. \tag{3.104}$$

Similar to this the covariant transformation is derived, using the mapping of line elements $\mathrm{d}\boldsymbol{x} = \boldsymbol{J} \cdot \mathrm{d}\hat{\boldsymbol{x}}$ and relation $\mathrm{d}\boldsymbol{x} = \boldsymbol{s}\, \mathrm{d}x$, i.e.,

$$\boldsymbol{v} \cdot \mathrm{d}\boldsymbol{x} = \hat{\boldsymbol{v}} \cdot \mathrm{d}\hat{\boldsymbol{x}} \quad \Rightarrow \quad \boldsymbol{v} = \boldsymbol{J}^{-T} \cdot \hat{\boldsymbol{v}}\,. \tag{3.105}$$

This transformations hold for all element geometries, see Boffi et al. [49], Brezzi and Fortin [56] as well as, e.g., Rognes et al. [193] for triangle and tetrahedral elements and, e.g., Arnold et al. [8] for quadrilaterals. As previously presented for $\mathcal{RT}$ functions, this transformations can be avoided by a direct evaluation of functions on the given element domain $\hat{\mathcal{B}}_{\mathrm{e}}$.

For a visualization of the properties of the contra- and covariant Piola transformation an example is depicted in Figure 3.11. Therein, two vectors, $\boldsymbol{v}_n$ in normal and $\boldsymbol{v}_t$ in tangential direction, defined on the edge $P_1 - P_3$ on the triangular element $\mathcal{B}_{\mathrm{e}}$ are mapped onto some elements $\hat{\mathcal{B}}'_{\mathrm{e}}$ and $\hat{\mathcal{B}}''_{\mathrm{e}}$ using the Piola transformations. Here, it can be seen, that the contravariant transformation $\varphi^{\mathrm{div}}(\boldsymbol{v})$ preserves the tangential properties and thus maps tangential vectors to tangential vectors. This results for vector-valued fields in $\mathcal{H}(\mathrm{div}, \mathcal{B})$ to zero normal components on two edges for $d = 2$ and on three faces for $d = 3$, which in consequence yield vector fields only normal to one edge or face. The covariant Piola transformation $\varphi^{\mathrm{curl}}(\boldsymbol{v})$, applied for tangential continuous vector functions in $\mathcal{H}(\mathrm{curl}, \mathcal{B})$, preserves the normal components of vectors, i.e., it maps normal vectors to normal vectors. Based on this property, only tangential components on one edge for $d = 2$ and one surface on $d = 3$ are obtained, since on all other edges or surfaces solely normal components are preserved, cf. Rognes et al. [193].

Furthermore, the mapping of the divergence of a vector field is given by

$$\mathrm{div}\, \boldsymbol{v} = \mathrm{div} \left(\frac{1}{\det \boldsymbol{J}}\, \boldsymbol{J} \cdot \hat{\boldsymbol{v}} \right) = \frac{1}{\det \boldsymbol{J}}\, \mathrm{div}_{\xi}\, \hat{\boldsymbol{v}}\,, \tag{3.106}$$

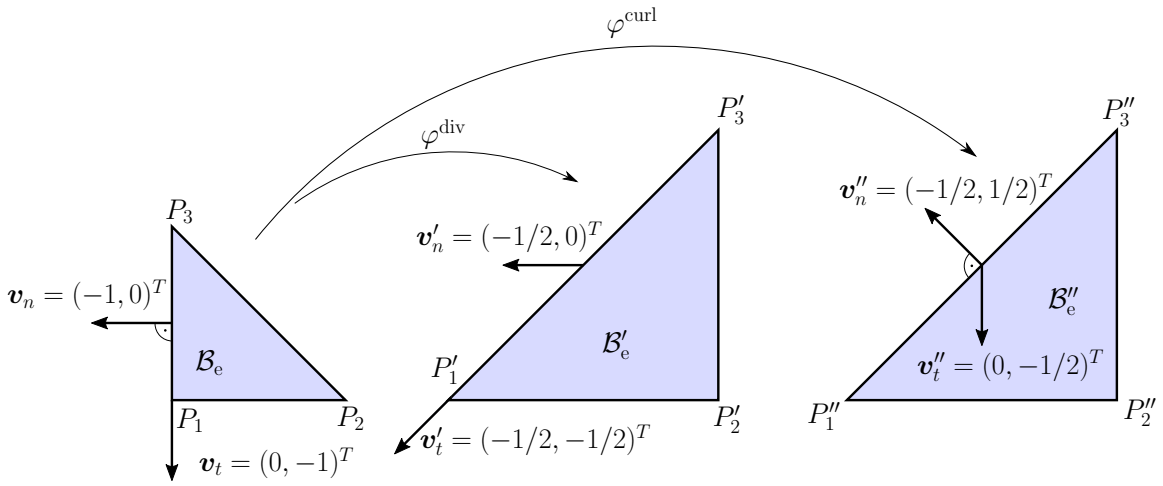

Figure 3.11: Contra- and covariant Piola transformation $\varphi^{\mathrm{div}}(\boldsymbol{v})$ and $\varphi^{\mathrm{curl}}(\boldsymbol{v})$ of two vectors $\boldsymbol{v}_n$ and $\boldsymbol{v}_t$, defined normal and tangential to edge $P_1 - P_3$, onto some triangles $\hat{\mathcal{B}}_{\mathrm{e}}'$ and $\hat{\mathcal{B}}_{\mathrm{e}}''$

with

$$\boldsymbol{J} \cdot \operatorname{div} \hat{\boldsymbol{v}} = \operatorname{div}_{\xi} \hat{\boldsymbol{v}} \quad \text{and} \quad \operatorname{div} \left(\frac{1}{\det \boldsymbol{J}} \boldsymbol{J} \right) = 0 \,, \tag{3.107}$$

where $\operatorname{div}_{\xi}(\boldsymbol{\Upsilon}) = \nabla_{,\xi} \boldsymbol{\Upsilon} : \mathbf{1}$ for a second order tensor $\boldsymbol{\Upsilon}$. The relation for the curl of a vector field can be achieved in a similar manner. In the further course, only the contravariant Piola transformation is applied, since only functions in $\mathcal{H}(\operatorname{div}, \mathcal{B})$ are considered. For the illustration of the contravariant Piola transformation, a $[\mathcal{RT}_0^{\triangle}]^2$ approximation function, see Figure 3.12, with the same node notation as in Figure 3.11, is shown.

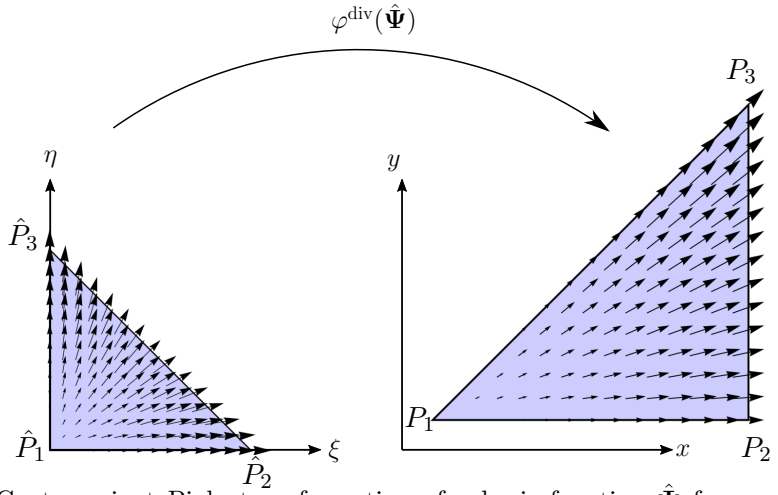

Figure 3.12: Contravariant Piola transformation of a basis function $\hat{\boldsymbol{\Psi}}$ from parameter space to physical space

As mentioned before, the $\mathcal{RT}$ and $\mathcal{BDM}$ functions have to fulfill the condition, that the sum over all nodes i on every edge j, multiplied with the associated outward normal vector, has to be equal to one. For the fulfillment of this relation a normalization by means of the length of the edge might have to be introduced for the functions as well as the divergence of the function. In order to avoid this normalization, the condition can be directly incorporated within the construction of the basis functions, see Steeger [223].

For the implementation of such $\mathcal{H}(\mathrm{div}, \mathcal{B})$ conforming functions, based on the normal direction of the corresponding edge, a consistent positive normal direction has to be defined. The normal directions of two neighboring elements are opposed and a positive direction has to be determined, since only one normal direction can exist at each edge. For the consistent 'positive' normal direction, here defined by positive coordinate direction, the opposite 'negative' normal component is multiplied by a value of -1. This procedure is exemplarily depicted in Figure 3.13.

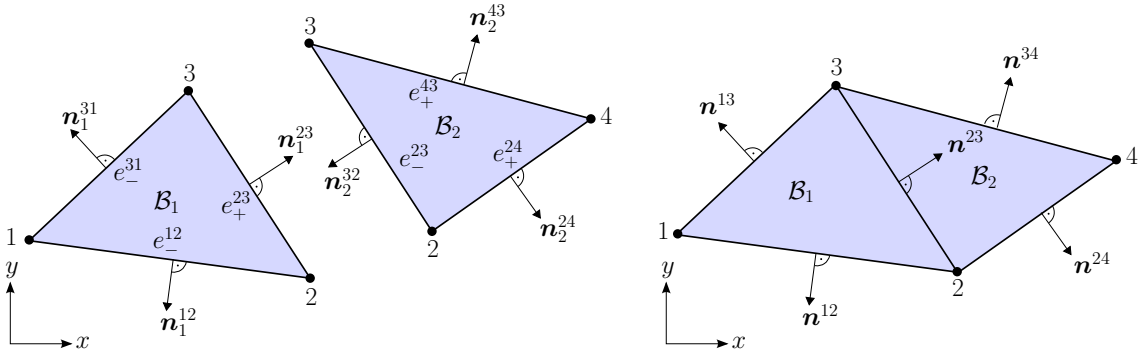

Figure 3.13: Definition of positive flux direction depicted for two elements $\mathcal{B}_1$ and $\mathcal{B}_2$

For the implementation of the presented formulations the representation in terms of the potential energy is considered for simplicity. Based on the used software packages *AceGen* and *AceFEM* (version 6.813 and 7.006), cf., e.g., Korelc [136], Korelc [137], Korelc and Wriggers [138], of *Mathematica* (version 10.2 and 12.0), see Wolfram Research [235] an automatic differentiation approach is considered, which is provided therein. Furthermore, *FEAP* the *Finite Element Analysis Program* (version 8.2), see Taylor [227] is used for some of the FE simulations. The visualizations are performed in *Mathematica*, *AceFEM*, ParaView (version 5.8.0), cf. Ahrens et al. [1], and *Tecplot* 360 (version 14).

3.5 Convergence of finite element formulations

The representation of convergence assumptions and optimal convergence rates of finite element solutions will be considered in the following and is therefore briefly introduced for the applied quantities.
A detailed description of the determination of optimal convergence rates is discussed, e.g., in Brenner and Scott [53], Boffi et al. [49] and Bathe [24]. The determination of the optimal rate of convergence in the theory of elastic problems, can be defined by

$$\|\boldsymbol{u} - \boldsymbol{u}_h\|_{\mathcal{H}^s(\mathcal{B})} \leq c\, h^{m-s}\, |\boldsymbol{u}|_{\mathcal{H}^m(\mathcal{B})} \tag{3.108}$$

with the constant c independent of h and $m = k+1$ depending on k as the degree to which the polynomial is complete, cf. chapter 4.3.5 in Bathe [24]. In general h is chosen as the length of a side of an element or as the diameter of a circle circumscribing the element. Following Brenner and Scott [53], defining $0 \leq s \leq \min\{m, r+1\}$ with the continuity of the finite element solution $\mathcal{C}^r$ for $r \geq 0$. For considering complete polynomials in x and y in $d = 2$ for triangular elements, all possible terms of the form $x^\alpha y^\beta$ are present, with $\alpha + \beta = k$. The degree of a complete polynomial for the displacement approximation is

based on $\mathcal{P}_2$ given with $k = 2$. Here, $s = 1$ due to $\boldsymbol{u} \in \mathcal{H}^1(\mathcal{B})$, i.e.,

$$\|\boldsymbol{u} - \boldsymbol{u}_h\|_{\mathcal{H}^1(\mathcal{B})} \leq c\, h^2\, |\boldsymbol{u}|_{\mathcal{H}^3(\mathcal{B})} \quad \rightarrow \quad \mathcal{O}(h^2)\,. \tag{3.109}$$

For the stress approximation, e.g., based on quadratic Raviart-Thomas functions $\mathcal{RT}_1$ the optimal rate is determined, with $k = 1$ and $\boldsymbol{\sigma} \in \mathcal{H}^m(\mathcal{B})$ and $\operatorname{div} \boldsymbol{\sigma} \in \mathcal{H}^n(\mathcal{B})$, by

$$\begin{aligned} \|\boldsymbol{\sigma} - \boldsymbol{\sigma}_h\|_{\mathcal{H}^0(\mathcal{B})} &\leq c\, h^m\, |\boldsymbol{\sigma}|_{\mathcal{H}^m(\mathcal{B})}\,, \\ \|\operatorname{div}(\boldsymbol{\sigma} - \boldsymbol{\sigma}_h)\|_{\mathcal{H}^0(\mathcal{B})} &\leq c\, h^n\, |\operatorname{div} \boldsymbol{\sigma}|_{\mathcal{H}^n(\mathcal{B})}\,, \end{aligned} \tag{3.110}$$

with $n \leq k + 1$, which yields

$$\begin{aligned} \|\boldsymbol{\sigma} - \boldsymbol{\sigma}_h\|_{\mathcal{H}^0(\mathcal{B})} &\leq c\, h^2\, |\boldsymbol{\sigma}|_{\mathcal{H}^2(\mathcal{B})} \quad \rightarrow \quad \mathcal{O}(h^2)\,, \\ \|\operatorname{div}(\boldsymbol{\sigma} - \boldsymbol{\sigma}_h)\|_{\mathcal{H}^0(\mathcal{B})} &\leq c\, h^2\, |\operatorname{div} \boldsymbol{\sigma}|_{\mathcal{H}^2(\mathcal{B})} \quad \rightarrow \quad \mathcal{O}(h^2)\,. \end{aligned} \tag{3.111}$$

The combination of these estimates, under the assumption of a $\mathcal{RT}_1\mathcal{P}_2$ finite element type, an optimal rate of convergence for the theory of elastic problems of two is expected. The obtained order of convergence for a boundary value problem is crucially influenced by the regularity of the solution of the boundary value problem, i.e., regularity can be reduced by the applied boundary conditions, e.g., by a change from clamped $\boldsymbol{u} = \boldsymbol{0}$ to stress-free conditions $\boldsymbol{\sigma} \cdot \boldsymbol{n} = \boldsymbol{0}$ at a corner point, cf. Rössle [194]. Furthermore, the optimality of the mesh regularity and the used refinement strategy, i.e., regular or adaptive refinement strategies have an influence on the convergence order. It must be noted, that the simple application of the $\mathcal{L}^2(\mathcal{B})$-norm to residual equations, stemming from different continuum equations, does not a priori lead to norm-equivalence. But in the framework of this work, norm-equivalence is not part of the investigated issues, see, e.g., Bochev and Gunzburger [43].
In general, the rate of convergence can be increased by an increasing polynomial order of complete polynomials k, if the solution of the problem is very regular. These assumptions do not hold, if the solution of the problem is irregular, see Carey and Oden [70] and Rössle [194] for a determination of regularity properties of boundary value problems. For such problems, the convergence behavior is unaffected by the polynomial order of the considered functions and only an asymptotic rate of convergence is reached. The theoretical optimal convergence rates only hold for $h_\mathrm{e} \rightarrow 0$.

4 Mixed finite element methods at small strains

For the discussion on mixed FEM, a least-squares formulation for linear elasticity and a primal Hellinger-Reissner formulation, dealing with nonlinear material behavior in terms of small strain elasto-plasticity, are introduced in the following. Here, only stress-displacement LS formulations are discussed.
The presentation of the LSFEM for linear elasticity discusses the challenges of the method, such as the weak performance of low order elements, the influence of weighting factors and the calculation of support reactions. Therefore, two LS formulations are considered, one in analogy to (3.37) and a formulation extended in terms of the balance of angular momentum. The idea is related to an additional control of the stress symmetry within the LSFEM, based on the ideas in Cai and Starke [60] and further developments in Schwarz et al. [207; 208]. The formulations are evaluated and compared for a simple boundary value problem of a cantilever beam.
For a preliminary discussion on plastic constraints and their evaluation by a point- or elementwise enforcement, an elasto-plastic Hellinger-Reissner formulation is discussed for small strains. The publication by Simo et al. [218] provides a basis for this consideration. Furthermore, the study of plasticity for small deformations allows a more detailed consideration of the individual variables.
The main aspects of this section are:

- Presentation of LSFEM for linear elasticity in terms of arising challenges,
- Possible solutions to these challenges through an extended formulation with additional consideration of the stress symmetry, cf. Igelbüscher et al. [120],
- Introduction to elasto-plasticity at small strain utilizing a primal Hellinger-Reissner formulation, cf. Schröder et al. [200],
- Discussion on pointwise enforcement of the plastic constraints: flow rule, hardening law and consistency condition, based on Simo et al. [218].

The results presented below have already been published in Igelbüscher et al. [120] and Schröder et al. [200], therein, further numerical examples are given.

4.1 Mixed least-squares finite element method for linear elasticity

In order to present challenges in the LSFEM, two formulations are investigated which differ in the requirement of the stress symmetry condition, cf. Igelbüscher et al. [120]. Therefore, an extension of the LS functional by an additional control of the stress symmetry condition is performed, see Cai and Starke [60], which is still considered as a weak enforcement of stress symmetry. Furthermore, an exact enforcement of the stress symmetry can be performed, cf. Gopalakrishnan and Guzmán [104] and Kober and Starke [135], among others. Additionally, the weighting of the functional terms is discussed and possible weighting approaches are presented, e.g., a scale independent formulation similar to Bell and Surana [26]. The topic of weighting parameters is presented in several numerical studies, e.g., for the Stokes equation in Deang and Gunzburger [89], Proot and Gerritsma [184] and for solid mechanics

in Schwarz et al. [207; 208] and Schröder et al. [199], among others. Nevertheless, it is still an open topic within the LSFEM.
The element formulations used here are based on the approximations $\boldsymbol{u} \in \mathcal{H}^1(\mathcal{B})$ and a conforming stress approximation with $\boldsymbol{\sigma} \in \mathcal{H}(\mathrm{div}, \mathcal{B})$. For this, different element orders and ansatz functions are chosen, i.e., Lagrange type functions, Raviart-Thomas and Brezzi-Douglas-Marini functions, see Chapter 3.3 and, e.g., Raviart and Thomas [189], Brezzi et al. [57] and Brezzi and Fortin [56].

4.2 Classical stress-displacement least-squares formulation

A mixed stress-displacement LS formulation for linear elasticity is already introduced in Chapter 3.2.4, see, e.g., Cai and Starke [60] and Cai and Starke [61]. This linear elastic LS formulation (3.37) consists of the balance of linear momentum and the constitutive equation and is given by

$$\mathcal{F}(\boldsymbol{\sigma}, \boldsymbol{u}) \;=\; \frac{1}{2}\Big(\Big\| \omega_1(\mathrm{div}\,\boldsymbol{\sigma} + \boldsymbol{f}) \Big\|^2_{\mathcal{L}^2(\mathcal{B})} + \Big\| \omega_2(\boldsymbol{\sigma} - \mathbb{C} : \nabla^s \boldsymbol{u}) \Big\|^2_{\mathcal{L}^2(\mathcal{B})} \Big) \,. \tag{4.1}$$

A general construction approach of the formulation and some general properties of the method are previously discussed. Furthermore, the corresponding weak forms and linearizations are presented in (3.32) and (3.40).
The solution of the problem is sought with respect to appropriate solution spaces. Here, $(\boldsymbol{\sigma}, \boldsymbol{u}) \in \mathcal{S}^m \times \mathcal{V}^k$ are chosen as continuous function spaces with

$$\begin{aligned} \mathcal{S}^m &= \{ \boldsymbol{\sigma} \in [\mathcal{H}(\mathrm{div}, \mathcal{B}_\mathrm{e})]^{d\times d} : \boldsymbol{\sigma}|_{\mathcal{B}_\mathrm{e}} \in [\mathcal{RT}_m(\mathcal{B}_\mathrm{e})]^{d\times d} \,, \forall\, \mathcal{B}_\mathrm{e} \in \mathcal{B} \} \,, \\ \mathcal{V}^k &= \{ \boldsymbol{u} \in [\mathcal{H}^1(\mathcal{B}_\mathrm{e})]^{d} : \boldsymbol{u}|_{\mathcal{B}_\mathrm{e}} \in [\mathcal{P}_k(\mathcal{B}_\mathrm{e})]^{d} \,, \forall\, \mathcal{B}_\mathrm{e} \in \mathcal{B} \} \,, \end{aligned} \tag{4.2}$$

i.e., Lagrange type functions, $\mathcal{P}_k$ of order $k \geq 1$, are chosen for the function space $\mathcal{V}^k$ and Raviart-Thomas functions, $\mathcal{RT}_m$ of degree $m \geq 0$, are introduced for the space $\mathcal{S}^m$. That means, $\boldsymbol{u} \in \mathcal{H}^1(\mathcal{B})$ and $\boldsymbol{\sigma} \in \mathcal{H}(\mathrm{div}, \mathcal{B})$, based on the assumption for the more general Sobolev spaces $\mathcal{W}^{1,p}(\mathcal{B})$ and $\mathcal{W}^q(\mathrm{div}, \mathcal{B})$ with $p = q = 2$ for linear elasticity.
The presented LS formulation leads, using the defined function spaces, only to a weak enforcement of the stress symmetry condition $\boldsymbol{\sigma} = \boldsymbol{\sigma}^T$, since the balance of angular momentum is only enforced in a weak sense, i.e.,

$$\|\boldsymbol{\sigma} - \boldsymbol{\sigma}^T\|^2_{\mathcal{L}^2(\mathcal{B})} \leq c \|\boldsymbol{\sigma} - \partial_{\boldsymbol{\varepsilon}} \psi(\boldsymbol{\varepsilon})\|^2_{\mathcal{L}^2(\mathcal{B})} = c \|\boldsymbol{\sigma} - \mathbb{C} : \boldsymbol{\varepsilon}\|^2_{\mathcal{L}^2(\mathcal{B})} \,, \tag{4.3}$$

in terms of the constitutive relation with the free energy function $\psi(\boldsymbol{\varepsilon}) = \frac{1}{2}\boldsymbol{\varepsilon} : \mathbb{C} : \boldsymbol{\varepsilon}$ and c as a positive constant, cf. Cai and Starke [61]. Furthermore, the applied $\mathcal{RT}$ functions lead to a not a priori fulfillment of the stress symmetry condition, which is described in, e.g., Boffi et al. [48] and Cockburn et al. [80].
A fulfillment of the stress symmetry in a strong sense can be obtained if it is incorporated within the solution space. Therefore, a possible solution for a strong fulfillment of $\boldsymbol{\sigma} = \boldsymbol{\sigma}^T$ is to choose a different approximation for the stresses, which directly provides a symmetric stress tensor. The exact enforcement of the stress symmetry condition is performed, e.g., in Gopalakrishnan and Guzmán [104] for a family of mixed methods and in Kober and Starke [135] for a Hellinger-Reissner formulation.

In this section, an additional control of the stress symmetry condition, as, e.g., suggested by SCHWARZ ET AL. [207], is performed by an extension of (4.1) with respect to the symmetry condition $\boldsymbol{\sigma} = \boldsymbol{\sigma}^T$, see Chapter 4.3. This extension is discussed in several publications, as, e.g., in CAI AND STARKE [60] for linear elasticity and for finite strain elasticity in SCHWARZ ET AL. [208], and is applied here, in terms of the complete balance of angular momentum, to improve formulation (4.1). However, an explicit consideration of $\boldsymbol{\sigma} - \boldsymbol{\sigma}^T = \mathbf{0}$ in the system of equations, still fulfills the constraint in a weak sense, cf. CAI AND STARKE [61]. Nevertheless, it is fulfilled in the limit case $h_\mathrm{e} \to 0$, where h_e denotes the characteristic finite element size (diameter). It has to be mentioned that from the continuum mechanical point of view the balance of angular momentum is ensured by the symmetry of the Cauchy stress tensor, if additionally the balance of linear momentum is exactly fulfilled, i.e., $\operatorname{div} \boldsymbol{\sigma} = -\boldsymbol{f}$.

Furthermore, another challenge in the LSFEM is the recalculation of support reactions, i.e., forces and moments, which is of crucial interest from an engineering point of view. For an illustration of this, the simple example of a clamped cantilever beam with dimensions 5×1 mm is investigated, see Figure 4.1 and cf. IGELBÜSCHER ET AL. [120].
Here, the left edge of the boundary value problem is clamped and a traction boundary condition of $\boldsymbol{\sigma} \cdot \boldsymbol{n} = (0, 0.1)^T \,\mathrm{kN/mm^2}$ is applied on the right side. The example is investigated by the LS formulation (4.1) and the results for the support reactions (A_H, A_V, M_A) are compared to a linear displacement element ($\mathcal{P}_1$) and the analytical solution with $\mathrm{A}_H = 0\,\mathrm{kN}$, $\mathrm{A}_V = 0.1\,\mathrm{kN}$, $\mathrm{M}_A = 0.5\,\mathrm{kNmm}$. The weights ω_i for the LS formulation are chosen with $\omega_i = \alpha_i/\mu$ for $i = 1, 2$, where α_i denote dimensionless weighting factors (i.e., unit 1).
The calculation rules for the reaction forces of the pure displacement formulation are given by

$$\mathrm{A}_H = \sum_{I \in \partial\mathcal{B}_u} F_x^I \,, \quad \mathrm{A}_V = \sum_{I \in \partial\mathcal{B}_u} F_y^I \quad \text{and} \quad \mathrm{M}_A = \sum_{I \in \partial\mathcal{B}_u} F_x^I \cdot y^I \,, \tag{4.4}$$

where $I \in \partial\mathcal{B}_u$ denotes all nodes at the clamped edge and F^I are nodal forces taken from the right hand side vector for the displacement element. Furthermore, M_A is determined by F^I on $\partial\mathcal{B}_u$ in horizontal direction multiplied by the nodal distance in y-direction to the origin (0,0) of each point I. The support reactions for the LSFEM are determined in terms of resulting tractions evaluated at the left face ($\partial\mathcal{B}_u$) and the associated moment by means of the resulting horizontal force A_H at the boundary $\partial\mathcal{B}_u$, i.e.,

$$\mathrm{A}_H = \int_{\partial\mathcal{B}_u} \sigma_{11} \,\mathrm{d}y \,, \quad \mathrm{A}_V = \int_{\partial\mathcal{B}_u} \sigma_{21} \,\mathrm{d}y \quad \text{and} \quad \mathrm{M}_A = \int_{\partial\mathcal{B}_u} \sigma_{11} \cdot y \,\mathrm{d}y \,. \tag{4.5}$$

For the applied weighting parameters, a numerical study is performed, choosing a decreasing value for α_2. Obviously, the convergence of A_H is completely satisfying. However, the LS formulation (4.1) is unable to reproduce the correct solution of the moment M_A, with respect to $\boldsymbol{x} = (0, 0)$. Furthermore, only a weighting with $\alpha_2 \leq 0.1$ leads to the expected solution for A_V, where for $\alpha_2 \geq 0.5$ only insufficient results are obtained. The pure displacement formulation yields an explicit fulfillment of all support reactions, cf. Figure 4.1. Nevertheless, an improved convergence behavior of the LS formulation for reaction forces and moments related to the chosen α_2 can be observed up to a certain level. Especially in the convergence of the resulting moment, a limit for the underlying setup is visualized,

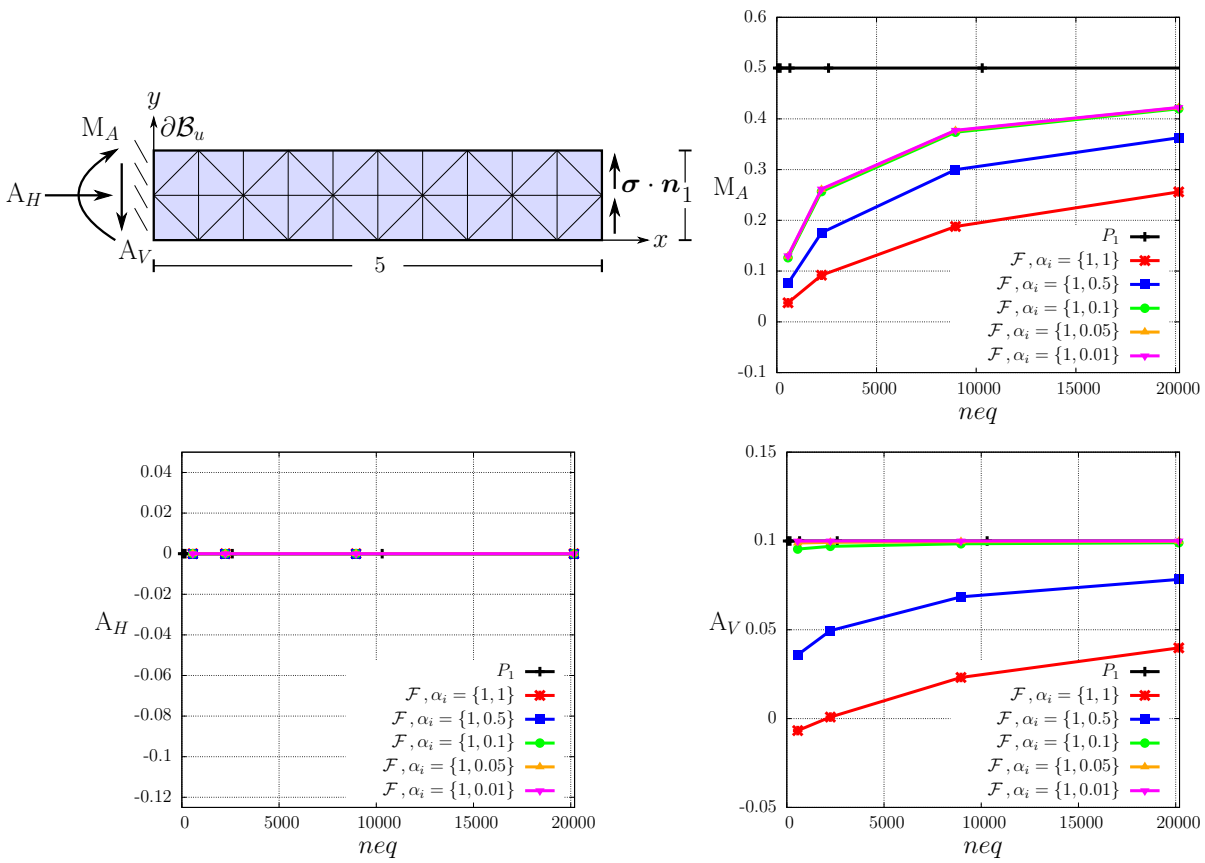

Figure 4.1: Clamped cantilever: setup with exemplary mesh and convergence of A_H, A_V, and M_A vs. the number of equations (*neq*) for the LS functional $\mathcal{F}$ using $\mathcal{RT}_1\mathcal{P}_2$ elements ($E = 70\,\mathrm{kN/mm^2}, \mu = 26.12\,\mathrm{kN/mm^2}$), taken from Igelbüscher et al. [120]

where a decreasing α_2 does not lead to any improvement of the resulting moment. The presented calculations are performed using a $\mathcal{RT}_1\mathcal{P}_2$ element type.
From an engineering point of view, the insufficient solution quality, especially for the moment M_A, is crucial, since these quantities are considered as the foundation for the design of structural components. As a consequence, the fulfillment of the balance of linear momentum (vanishing resultant forces) and the balance of angular momentum (vanishing resultant moment) have to be improved for applications in structural analysis. Therefore, the focus in the following chapter lies on an improvement of the convergence properties of the formulation for support reactions, extending the functional by a stress symmetry condition. Further, a weighting parameter setup is applied, in order to obtain a formulation which is independent of units. These investigations are discussed in the next subsection.

4.3 LSFEM with explicit inclusion of the balance of angular momentum

For an improvement of the results in Figure 4.1, the LS formulation (4.1) is extended. In order to explicitly include $\boldsymbol{\sigma} = \boldsymbol{\sigma}^T$ in the given functional (4.1), the balance of angular momentum is considered as a symmetric stress control, see Chapter 2.3.3. It has to be mentioned again that the fulfillment of the balance of angular momentum is already included in the formulation, from a continuum mechanical point of view, since the balance of linear momentum is enforced and the constitutive equation weakly enforce the stress

symmetry condition. The balance of angular momentum reads

$$\int_{\mathcal{B}} (\boldsymbol{x} - \boldsymbol{x}_0) \times \boldsymbol{f} \, \mathrm{d}V + \int_{\partial\mathcal{B}} (\boldsymbol{x} - \boldsymbol{x}_0) \times (\boldsymbol{\sigma} \cdot \boldsymbol{n}) \, \mathrm{d}A = \boldsymbol{0} \,, \tag{4.6}$$

by neglecting accelerations and applying Cauchy's theorem ($\boldsymbol{t} = \boldsymbol{\sigma} \cdot \boldsymbol{n}$). Furthermore, considering $\nabla(\boldsymbol{x} - \boldsymbol{x}_0) = \boldsymbol{1}$ and the Gauss theorem, (4.6) is reformulated to

$$\boldsymbol{0} = \int_{\mathcal{B}} ((\boldsymbol{x} - \boldsymbol{x}_0) \times (\operatorname{div} \boldsymbol{\sigma} + \boldsymbol{f}) + \operatorname{axl}(\boldsymbol{\sigma})) \, \mathrm{d}V \quad \text{with} \quad \operatorname{axl}(\boldsymbol{\sigma}) := \begin{pmatrix} \sigma_{32} - \sigma_{23} \\ \sigma_{13} - \sigma_{31} \\ \sigma_{21} - \sigma_{12} \end{pmatrix} . \tag{4.7}$$

Therefore, it is composed of $\boldsymbol{\sigma} = \boldsymbol{\sigma}^T$ and the cross product of the balance of linear momentum ($\operatorname{div} \boldsymbol{\sigma} + \boldsymbol{f}$) with the related distance to a fixed reference point $\boldsymbol{x}_0$. Consequently, adding $(4.7)_1$ to the functional (4.1), yields the extended functional $\mathcal{F}^\star(\boldsymbol{\sigma}, \boldsymbol{u})$, i.e.,

$$\begin{aligned} \mathcal{F}^\star(\boldsymbol{\sigma}, \boldsymbol{u}) &= \frac{1}{2} \Big(\Big\| \omega_1^\star (\operatorname{div} \boldsymbol{\sigma} + \boldsymbol{f}) \Big\|^2_{\mathcal{L}^2(\mathcal{B})} + \Big\| \omega_2^\star (\boldsymbol{\sigma} - \mathbb{C} : \nabla^s \boldsymbol{u}) \Big\|^2_{\mathcal{L}^2(\mathcal{B})} \\ &+ \Big\| \omega_3^\star ((\boldsymbol{x} - \boldsymbol{x}_0) \times (\operatorname{div} \boldsymbol{\sigma} + \boldsymbol{f}) + \operatorname{axl}(\boldsymbol{\sigma})) \Big\|^2_{\mathcal{L}^2(\mathcal{B})} \Big) \,. \end{aligned} \tag{4.8}$$

In order to solve the minimization problem, with $\delta_{\boldsymbol{\sigma},\boldsymbol{u}} \mathcal{F}^\star(\boldsymbol{\sigma}, \boldsymbol{u}, \delta\boldsymbol{\sigma}, \delta\boldsymbol{u}) = 0$, the first variations of (4.8), considering (3.36), are determined by

$$\begin{aligned} \delta_{\boldsymbol{u}} \mathcal{F}^\star &= -\int_{\mathcal{B}} (\mathbb{C} : \nabla^s \delta\boldsymbol{u}) : (\boldsymbol{\sigma} - \mathbb{C} : \nabla^s \boldsymbol{u}) \, \mathrm{d}V \,, \\ \delta_{\boldsymbol{\sigma}} \mathcal{F}^\star &= \int_{\mathcal{B}} \operatorname{div} \delta\boldsymbol{\sigma} \cdot (\operatorname{div} \boldsymbol{\sigma} + \boldsymbol{f}) \, \mathrm{d}V + \int_{\mathcal{B}} \delta\boldsymbol{\sigma} : (\mathbb{C} : \nabla^s \boldsymbol{u}) \, \mathrm{d}V \\ &+ \int_{\mathcal{B}} ((\boldsymbol{x} - \boldsymbol{x}_0) \times \operatorname{div} \delta\boldsymbol{\sigma} + \operatorname{axl}(\delta\boldsymbol{\sigma})) \cdot ((\boldsymbol{x} - \boldsymbol{x}_0) \times \operatorname{div} \boldsymbol{\sigma} + \operatorname{axl}(\boldsymbol{\sigma})) \, \mathrm{d}V \,. \end{aligned} \tag{4.9}$$

For notational simplicity, the weighting parameters $\omega_i^\star$ are omitted. In order to apply the Newton-Raphson method, the linearization is necessary, utilizing (3.39), yields

$$\begin{aligned} \Delta\delta_{\boldsymbol{u}} \mathcal{F}^\star &= \int_{\mathcal{B}} (\mathbb{C} : \nabla^s \delta\boldsymbol{u}) : (\mathbb{C} : \nabla^s \Delta\boldsymbol{u}) \, \mathrm{d}V - \int_{\mathcal{B}} \mathbb{C} : \nabla^s \delta\boldsymbol{u} : \Delta\boldsymbol{\sigma} \, \mathrm{d}V \,, \\ \Delta\delta_{\boldsymbol{\sigma}} \mathcal{F}^\star &= \int_{\mathcal{B}} \operatorname{div} \delta\boldsymbol{\sigma} \cdot \operatorname{div} \Delta\boldsymbol{\sigma} \, \mathrm{d}V + \int_{\mathcal{B}} \delta\boldsymbol{\sigma} : \Delta\boldsymbol{\sigma} \, \mathrm{d}V \\ &+ \int_{\mathcal{B}} ((\boldsymbol{x} - \boldsymbol{x}_0) \times \operatorname{div} \delta\boldsymbol{\sigma} + \operatorname{axl}(\delta\boldsymbol{\sigma})) \cdot ((\boldsymbol{x} - \boldsymbol{x}_0) \times \operatorname{div} \Delta\boldsymbol{\sigma} + \operatorname{axl}(\Delta\boldsymbol{\sigma})) \, \mathrm{d}V \\ &- \int_{\mathcal{B}} \delta\boldsymbol{\sigma} : \mathbb{C} : \nabla^s \Delta\boldsymbol{u} \, \mathrm{d}V \,. \end{aligned} \tag{4.10}$$

In addition to the extension of the LS formulation, an approach for a scale independent formulation, similar to Bell and Surana [26], which uses dimensionless variables, is performed. Therefore, a weighting of the residuals is introduced by means of the Lamé constant μ and a characteristic length $\tilde{l}$. The weighting factors $\omega_i^\star$ for (4.8) are chosen to be of the form

$$\omega_1^\star = \frac{\alpha_1^\star}{\mu} \, \tilde{l} \,, \quad \omega_2^\star = \frac{\alpha_2^\star}{\mu} \quad \text{and} \quad \omega_3^\star = \frac{\alpha_3^\star}{\mu} \,. \tag{4.11}$$

Here, $\alpha_i^\star$ denote dimensionless weighting factors (i.e., unit 1). The weights $\omega_i^\star$ lead to a scale independent functional, multiplying each functional term with the inverse unit, i.e., a dimensionless formulation is obtained. In order to achieve this, the parameter $\tilde{l}$ is necessary due to the unit of the balance of linear momentum given by, e.g., kN/mm^3, where the unit of μ is kN/mm^2. However, a reasonable choice for $\tilde{l}$ is obligatory and possible measures are, e.g., length, height or the square root of the area of the boundary value problem.

4.4 Clamped cantilever beam example for small strain elasticity

The proposed formulation (4.8) is analyzed for the clamped cantilever beam example, see Chapter 4.1, to illustrated the improvement, especially for the result of M_A, compared to the results for $\mathcal{F}$ in (4.1), see Figure 4.1. Analogously, the left face is clamped, a load of $\boldsymbol{\sigma} \cdot \boldsymbol{n} = (0, 0.1)^T$ kN/mm^2 is applied on the right face and a $\mathcal{RT}_1\mathcal{P}_2$ element type is considered. The parameter setup $\alpha_i^\star$ are chosen in accordance with the previous analysis with a decreasing $\alpha_2^\star$ from 1 to 0.01 and further the characteristic length $\tilde{l}$ is chosen as the square root of the area of the boundary value problem.
The results for the extended LS functional (4.8) are depicted in Figure 4.2. Therein, it is shown that a sufficient solution is reached for all support reactions A_H, A_V and M_A. Here, especially the strong improvement for the determination of the support reaction of the moment M_A for all weighting setups as well as an improvement for the vertical support reaction A_V compared to the results obtained based on formulation (4.1) is clearly visible. The convergence of the horizontal support reaction A_H illustrate a deviation in comparison with the results in Figure 4.1, but for $\alpha_2^\star \leq 0.1$ the expected solution is obtained. For weights $\alpha_2^\star \leq 0.1$ all support reactions lead to satisfying solutions for moderate mesh densities. Thus, for further applications of the LSFEM, especially if the representation of reaction forces is included, an extended formulation with an additional control of the stress symmetry has to be chosen. Furthermore, a balanced weighting parameter setup must be regarded, since the influence of weights on the solution accuracy is crucial. Although the stress symmetry is indirectly included in formulation (4.1), it is shown that an additional consideration as presented in the extended LS formulation in (4.8) provides an improvement in the element performance. This approach is therefore considered in the following LS formulations, especially because no additional degrees of freedom need to be introduced for an improved solution.

In order to show that the presented behavior is similar for elements with higher polynomial degrees and not restricted to triangular elements, further element combinations are considered. Figure 4.3 illustrates a direct comparison of the convergence of the equilibrium of moments for the LS functionals (4.1) and (4.8) with respect to different finite elements, applying $\mathcal{BDM}_1\mathcal{Q}_2$, $\mathcal{RT}_1\mathcal{Q}_2$ and $\mathcal{RT}_2\mathcal{P}_3$ elements. The analyzed elements show the improvement within the convergence of the moment M_A for $\mathcal{F}^\star$. For the formulation $\mathcal{F}$ no improvement for the choice of different polynomial types can be observed. The extended functional (4.8) illustrates conformity with the analytical solution for a weighting $\alpha_2^\star \leq 0.1$, which also holds for the fulfillment of A_H and A_V. For completeness, the convergence of the reaction forces A_H and A_V are depicted in Appendix 8.2 in Figure 8.1 and 8.2.

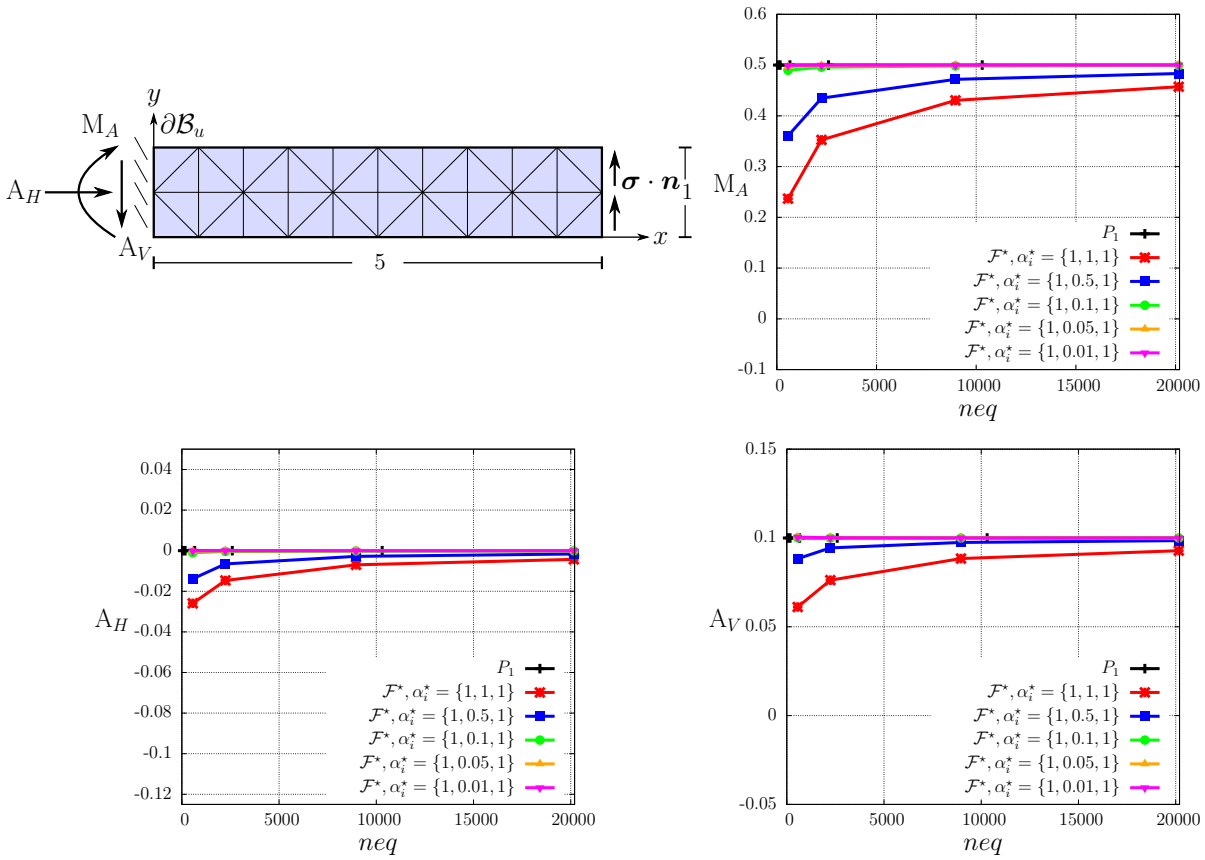

Figure 4.2: Clamped cantilever: setup with exemplary mesh and convergence of A_H, A_V, and M_A vs. number of equations (*neq*) for the LS functional $\mathcal{F}^\star$ using $\mathcal{RT}_1\mathcal{P}_2$ elements ($E = 70\,\mathrm{kN/mm^2}, \mu = 26.12\,\mathrm{kN/mm^2}$), taken from Igelbüscher et al. [120]

Furthermore, the introduction of the balance of angular momentum leads, beside a stronger fulfillment of the equilibrium of moments, simultaneously to a fulfillment of stress symmetry. This is illustrated with the development of stress symmetry by $\int_\mathcal{B} \sigma_{12} - \sigma_{21}\,\mathrm{d}V$ in Figure 4.4. Here, the improvement for $\mathcal{F}^\star$ is clearly visible. Nevertheless, all formulations provide a symmetric stress tensor for $h_\mathrm{e} \to 0$. This is due to the weak enforcement of stress symmetry in the constitutive equation, cf. (4.3) and the not a priori fulfillment of $\boldsymbol{\sigma} = \boldsymbol{\sigma}^T$ by the stress approximation with $\mathcal{RT}$ and $\mathcal{BDM}$ functions. It has to be noted that the weightings $\alpha_2 \leq 0.1$ in $\mathcal{F}$ lead to a slightly increase of the unsymmetry in $\boldsymbol{\sigma}$, which is in contrast to the influence of weightings for $\mathcal{F}^\star$, cf. Figure 4.4. This is reasonable, since the stress symmetry in $\mathcal{F}$ is controlled by the constitutive law and thus a weighting $\alpha_2 < 1$ lead to a weaker enforcement. Consequently, at least an extended approach for the LSFEM combined with an appropriate weighting strategy yields to a sufficient representation of support reactions and is in line with the demanded stress symmetry condition. The crucial influence of weights, as a disadvantage within the LSFEM, must be carefully considered in further applications. Therefore, all applied weightings are explicitly mentioned and their choice is based on numerical studies, see, e.g., Schwarz et al. [207; 208]. An investigation of the formulation with explicit consideration of balance of angular momentum (4.8) for further boundary value problems is proposed in Igelbüscher et al. [120].

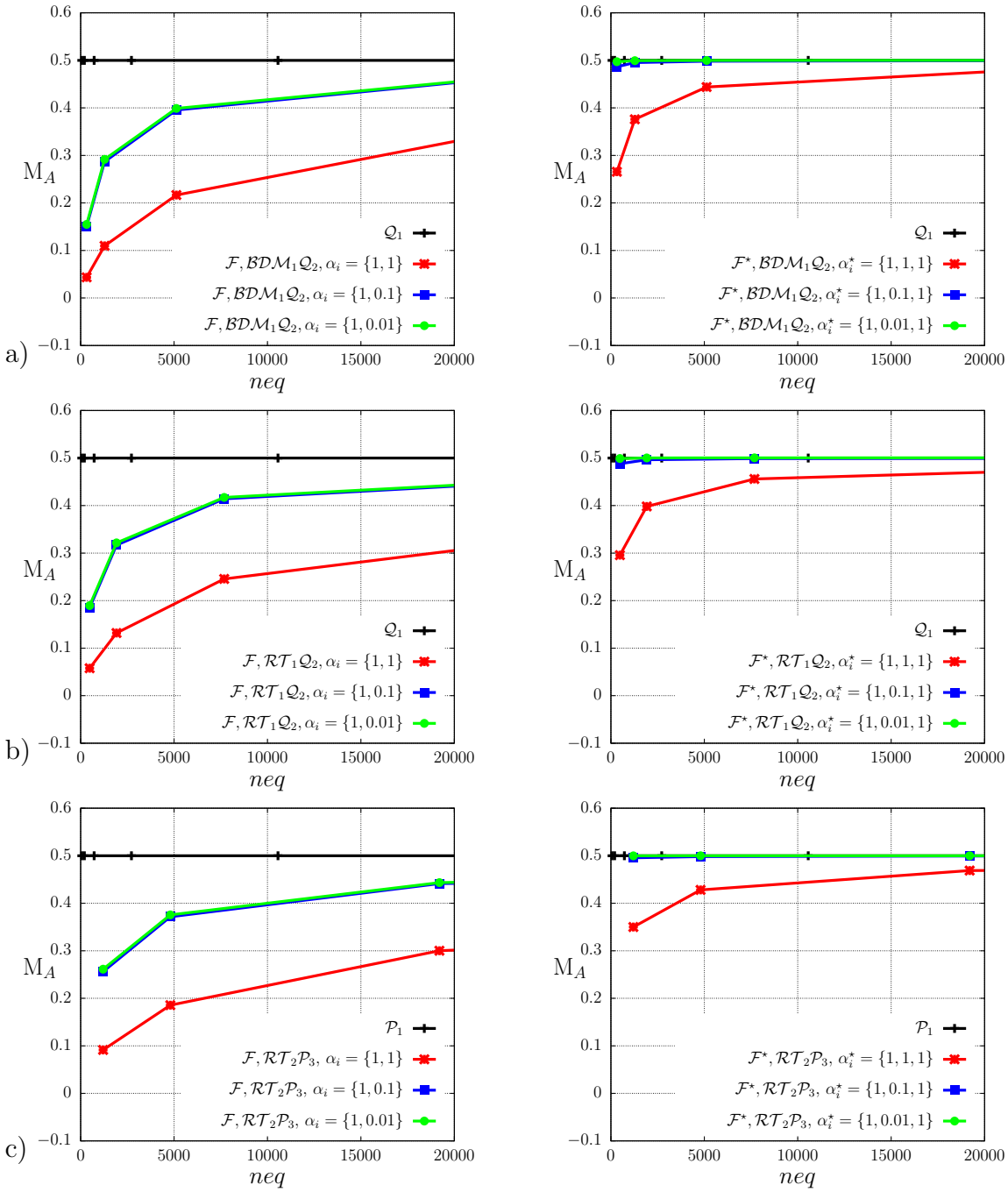

Figure 4.3: Clamped cantilever: Results for the fulfillment of moment M_A for $\mathcal{F}$ (left) and $\mathcal{F}^\star$ (right), considering a) $\mathcal{BDM}_1\mathcal{Q}_2$, b) $\mathcal{RT}_1\mathcal{Q}_2$ and c) $\mathcal{RT}_2\mathcal{P}_3$ elements

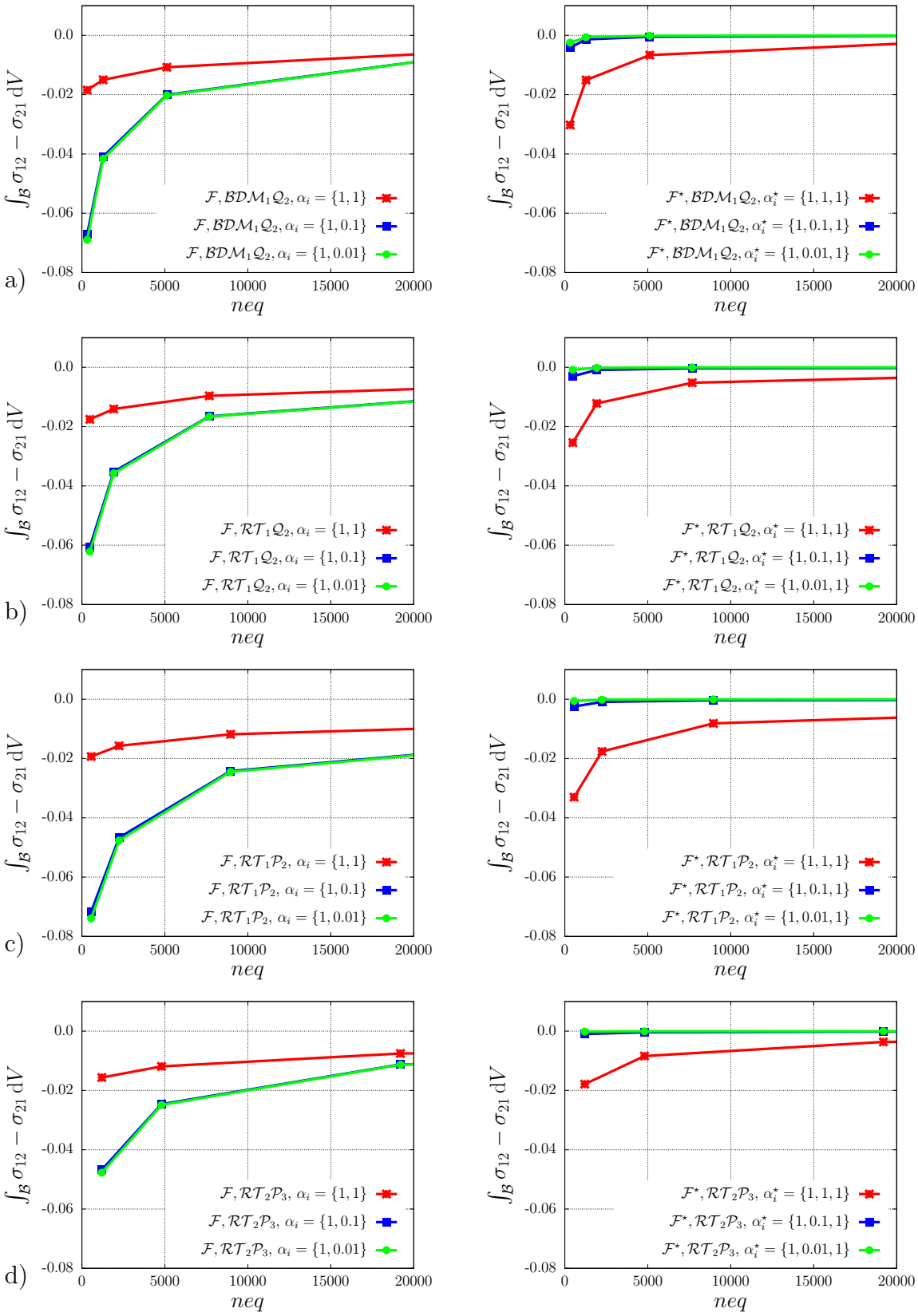

Figure 4.4: Clamped cantilever: Results for the stress symmetry condition for $\mathcal{F}$ (left) and $\mathcal{F}^\star$ (right), considering a) $\mathcal{BDM}_1\mathcal{Q}_2$, b) $\mathcal{RT}_1\mathcal{Q}_2$, c) $\mathcal{RT}_1\mathcal{P}_2$ and d) $\mathcal{RT}_2\mathcal{P}_3$ elements

4.5 Mixed Hellinger-Reissner principle for elasto-plasticity at small strains

For the application of elasto-plasticity within mixed finite element formulations, a small strain model is considered in the following. The continuum mechanical foundations and the algorithmic treatment of the presented formulation is presented in Chapter 2.5.2. The focus lies on the variational formulation with a pointwise enforcement of the flow rule, the hardening law and the consistency condition, cf. SCHRÖDER ET AL. [200]. This is in contrast to the approach by SIMO ET AL. [218], where the authors postulate that the flow rule can no longer be evaluated independently at each Gauss point. The presented formulation is closely related to SIMO ET AL. [218]. The results presented below are published in SCHRÖDER ET AL. [200], in which further numerical examples are discussed.

4.6 Formulation of elasto-plastic Hellinger-Reissner principle

The following set up is based on a primal Hellinger-Reissner formulation (3.27). The formulation with $\boldsymbol{u} \in \mathcal{H}^1(\mathcal{B})$ and $\boldsymbol{\sigma} \in \mathcal{L}^2(\mathcal{B})$ lead directly to an application of discontinuous stress approximation, applied with the 5-parameter ansatz of PIAN AND SUMIHARA [178]. This stress approximation is also investigated for nonlinear problems by PILTNER [180] and an extension to the three dimensional case is given in PIAN AND TONG [179]. For the framework of elasto-plasticity at small strains, the additive split of the total strains $\boldsymbol{\varepsilon}$ is introduced. Furthermore, in Chapter 2.5.2 it is shown that the stress is a function of the elastic strains. Based on this relation, the free energy function is reformulated into an elastic part $\psi^e(\boldsymbol{\varepsilon}^e) = \psi^e(\boldsymbol{\varepsilon} - \boldsymbol{\varepsilon}^p) = \frac{1}{2}(\boldsymbol{\varepsilon} - \boldsymbol{\varepsilon}^p) : \mathbb{C} : (\boldsymbol{\varepsilon} - \boldsymbol{\varepsilon}^p)$ and a plastic part with respect to the internal variable α, i.e., $\psi^p(\alpha) = \frac{1}{2} h\, \alpha^2$, which holds for the simple case of isotropic linear hardening. The introduction of $\boldsymbol{\sigma}$ as an additional independent variable, applying a Legendre transformation for ψ^e, yields $\psi^e(\boldsymbol{\varepsilon} - \boldsymbol{\varepsilon}^p) = \boldsymbol{\sigma} : (\boldsymbol{\varepsilon} - \boldsymbol{\varepsilon}^p) - \chi(\boldsymbol{\sigma})$ with the complementary stored energy function $\chi(\boldsymbol{\sigma}) = \frac{1}{2}\boldsymbol{\sigma} : \mathbb{C}^{-1} : \boldsymbol{\sigma}$. By substitution of these functions in (3.27), the elasto-plastic primal Hellinger-Reissner potential Π^{epHR} is obtained, i.e.,

$$\Pi^{\mathrm{epHR}}(\boldsymbol{\sigma}, \boldsymbol{u}) = \int_{\mathcal{B}} (\boldsymbol{\sigma} : (\boldsymbol{\varepsilon} - \boldsymbol{\varepsilon}^p) - \chi(\boldsymbol{\sigma}) + \psi^p(\alpha)) \, \mathrm{d}V - \int_{\mathcal{B}} \boldsymbol{f} \cdot \boldsymbol{u} \, \mathrm{d}V - \int_{\partial \mathcal{B}_N} \boldsymbol{t} \cdot \boldsymbol{u} \, \mathrm{d}A \,. \tag{4.12}$$

In order to solve for the stationary point of the potential, the weak forms $\mathcal{G}_u$ and $\mathcal{G}_\sigma$, with respect to the virtual displacements $\delta\boldsymbol{u}$ and virtual stresses $\delta\boldsymbol{\sigma}$, are determined by

$$\begin{aligned} \mathcal{G}_u &:= \delta_{\boldsymbol{u}} \Pi^{\mathrm{epHR}} = \int_{\mathcal{B}} \nabla^s \delta\boldsymbol{u} : \boldsymbol{\sigma} \, \mathrm{d}V - \int_{\mathcal{B}} \delta\boldsymbol{u} \cdot \boldsymbol{f} \, \mathrm{d}V - \int_{\partial \mathcal{B}_N} \delta\boldsymbol{u} \cdot \boldsymbol{t} \, \mathrm{d}A \,, \\ \mathcal{G}_\sigma &:= \delta_{\boldsymbol{\sigma}} \Pi^{\mathrm{epHR}} = \int_{\mathcal{B}} (\delta\boldsymbol{\sigma} : (\boldsymbol{\varepsilon} - \boldsymbol{\varepsilon}^p) - \delta\boldsymbol{\sigma} : \partial_{\boldsymbol{\sigma}} \chi(\boldsymbol{\sigma})) \, \mathrm{d}V \,. \end{aligned} \tag{4.13}$$

The solution is sought by finding $(\boldsymbol{u}, \boldsymbol{\sigma}) \in \mathcal{V} \times \bar{\mathcal{S}}$ such that $\mathcal{G}_{\boldsymbol{u}} = 0 \; \forall \, \delta\boldsymbol{u} \in \mathcal{V}$ and $\mathcal{G}_{\boldsymbol{\sigma}} = 0 \; \forall \, \delta\boldsymbol{\sigma} \in \bar{\mathcal{S}}$ with the approximation spaces $\mathcal{V} := \mathcal{H}^1(\mathcal{B})$ and $\bar{\mathcal{S}} := \mathcal{L}^2(\mathcal{B})$, defined by

$$\begin{aligned} \mathcal{V}^k &:= \{\boldsymbol{u} \in [\mathcal{H}^1(\mathcal{B})]^d : \boldsymbol{u}|_{\mathcal{B}_e} \in [\mathcal{Q}_k(\mathcal{B}_e)]^d, \, \forall \, \mathcal{B}_e \in \mathcal{B}\} \subset \mathcal{V} \,, \\ \bar{\mathcal{S}} &:= \{\boldsymbol{\sigma} \in [\mathcal{L}^2(\mathcal{B})]^{d \times d}_{\mathrm{sym}} : \boldsymbol{\sigma}|_{\mathcal{B}_e} \in [\mathcal{PS}(\mathcal{B}_e)]^{d \times d}, \, \forall \, \mathcal{B}_e \in \mathcal{B}\} \,. \end{aligned} \tag{4.14}$$

Here, an element combination $\mathcal{Q}_1\mathcal{PS}$ with $k = 1$ is considered, where $\mathcal{Q}_k$ denote Lagrange shape functions on quadrilaterals and $\mathcal{PS}$ is the 5-parameter stress approximation by

Pian and Sumihara [178]. The advantages of this approach are characterized by a remarkable insensitivity to mesh distortion, locking free behavior for plane strain quasi-incompressible elasticity and superconvergent results for bending dominated problems, see, e.g., Pian and Sumihara [178], Simo et al. [218] and Chun et al. [75]. The stability of the chosen finite element combination with respect to the LBB conditions is investigated, e.g., in Yu et al. [243] and Li et al. [151].

The associated Euler-Lagrange equations, extracted from $\mathcal{G}_u = 0$ and $\mathcal{G}_\sigma = 0$, follow directly from a straight-forward reformulation of the weak forms, i.e.,

$$\begin{aligned} \mathcal{G}_u &= -\int_{\mathcal{B}} \delta\boldsymbol{u} \cdot (\operatorname{div}\boldsymbol{\sigma} + \boldsymbol{f})\,\mathrm{d}V = \boldsymbol{0} \qquad \rightarrow \quad \operatorname{div}\boldsymbol{\sigma} + \boldsymbol{f} = 0\,, \\ \mathcal{G}_\sigma &= \int_{\mathcal{B}} \delta\boldsymbol{\sigma} : (\boldsymbol{\varepsilon} - \boldsymbol{\varepsilon}^p - \partial_{\boldsymbol{\sigma}}\chi(\boldsymbol{\sigma}))\,\mathrm{d}V = 0 \quad \rightarrow \quad \boldsymbol{\varepsilon} - \boldsymbol{\varepsilon}^p = \partial_{\boldsymbol{\sigma}}\chi(\boldsymbol{\sigma})\,. \end{aligned} \tag{4.15}$$

The thermodynamic consistent formulation based on the dissipation inequality (2.59) has to be reformulated, cf. (2.60), based on the introduced free energy function $\psi^e(\boldsymbol{\varepsilon} - \boldsymbol{\varepsilon}^p)$, such that

$$\begin{aligned} \mathcal{D} &= \boldsymbol{\sigma} : \dot{\boldsymbol{\varepsilon}} - \{\dot{\boldsymbol{\sigma}} : (\boldsymbol{\varepsilon} - \boldsymbol{\varepsilon}^p) + \boldsymbol{\sigma} : (\dot{\boldsymbol{\varepsilon}} - \dot{\boldsymbol{\varepsilon}}^p) - \partial_{\boldsymbol{\sigma}}\chi(\boldsymbol{\sigma}) : \dot{\boldsymbol{\sigma}} + \partial_\alpha\psi^p\,\dot{\alpha}\} \\ &= \boldsymbol{\sigma} : \dot{\boldsymbol{\varepsilon}}^p + \dot{\boldsymbol{\sigma}} : (\partial_{\boldsymbol{\sigma}}\chi(\boldsymbol{\sigma}) - (\boldsymbol{\varepsilon} - \boldsymbol{\varepsilon}^p)) + \beta\,\dot{\alpha} \\ &= \boldsymbol{\sigma} : \dot{\boldsymbol{\varepsilon}}^p + \dot{\boldsymbol{\sigma}} : (\partial_{\boldsymbol{\sigma}}\chi(\boldsymbol{\sigma}) - \boldsymbol{\varepsilon}^e) + \beta\,\dot{\alpha}\,. \end{aligned} \tag{4.16}$$

By substituting of the Euler-Lagrange equation $(4.15)_2$ in (4.16), the reduced dissipation inequality is obtained by $\mathcal{D}_{\mathrm{red}} = \boldsymbol{\sigma} : \dot{\boldsymbol{\varepsilon}}^p + \beta\,\dot{\alpha} \geq 0$, cf. (2.60). Obviously, the term $\partial_{\boldsymbol{\sigma}}\chi(\boldsymbol{\sigma})$ characterizes the elastic strains $\boldsymbol{\varepsilon}^e$ with $\boldsymbol{\varepsilon}^e = \mathbb{C}^{-1} : \boldsymbol{\sigma}$, see $(4.15)_2$. The linearization of $\mathcal{G}_u$ and $\mathcal{G}_\sigma$ yields

$$\begin{aligned} \Delta\mathcal{G}_u &= \int_{\mathcal{B}} \nabla^s\delta\boldsymbol{u} : \Delta\boldsymbol{\sigma}\,\mathrm{d}V\,, \\ \Delta\mathcal{G}_\sigma &= \int_{\mathcal{B}} \delta\boldsymbol{\sigma} : (\Delta\boldsymbol{\varepsilon} - \Delta\boldsymbol{\varepsilon}^p - \partial^2_{\boldsymbol{\sigma}\boldsymbol{\sigma}}\chi(\boldsymbol{\sigma}) : \Delta\boldsymbol{\sigma})\,\mathrm{d}V\,, \end{aligned} \tag{4.17}$$

with $\partial^2_{\boldsymbol{\sigma}\boldsymbol{\sigma}}\chi(\boldsymbol{\sigma}) : \Delta\boldsymbol{\sigma} = \mathbb{C}^{-1} : \Delta\boldsymbol{\sigma} = \Delta\boldsymbol{\varepsilon}^e(\boldsymbol{\sigma})$. The term $\Delta\boldsymbol{\varepsilon}^p$ denotes the linearization of $\boldsymbol{\varepsilon}^p$ with respect to the stresses, cf. (2.66), i.e.,

$$\Delta\boldsymbol{\varepsilon}^p = \Delta(\boldsymbol{\varepsilon}^p_n + \Delta_t\gamma\,\boldsymbol{n}) = \Delta(\Delta_t\gamma)\,\boldsymbol{n} + \Delta_t\gamma\,\Delta\boldsymbol{n}\,. \tag{4.18}$$

For notational simplicity, only the index n is explicitly denoted, where the index $n+1$ is omitted here for the obvious terms, cf. Schröder et al. [200]. The linear increment of the time integrated plastic multiplier $\Delta_t\gamma$ is obtained by

$$\Delta(\Delta_t\gamma) = \frac{3\Delta\Phi^{\mathrm{trial}}}{2\,h} = \frac{3}{2\,h}\boldsymbol{n} : \Delta\boldsymbol{\sigma}\,, \tag{4.19}$$

which holds for linear isotropic hardening. Furthermore, the linearization of the outward normal on the deviatoric stress plane $\boldsymbol{n}$ yields

$$\Delta\boldsymbol{n} = -\frac{1}{\|\operatorname{dev}\boldsymbol{\sigma}\|}(\boldsymbol{n}\otimes\boldsymbol{n} - \mathbb{P}) : \Delta\boldsymbol{\sigma}\,, \tag{4.20}$$

where $\mathbb{P} = \mathbb{I} - \frac{1}{3}\mathbf{1} \otimes \mathbf{1}$, with $\mathbb{I} = \frac{1}{2}(\delta_{ik}\,\delta_{jl} + \delta_{il}\,\delta_{jk})$, is the fourth-order deviatoric projection tensor. Thereby, $\mathbb{P}$ extracts the deviatoric part of a second-order tensor, e.g., $\operatorname{dev}\boldsymbol{\sigma} = \mathbb{P} : \boldsymbol{\sigma}$. The linearization of the plastic strains is given by

$$\Delta\boldsymbol{\varepsilon}^p = \underbrace{\left(\left(\frac{3}{2\,h} - \frac{\Delta_t\gamma}{\|\operatorname{dev}\boldsymbol{\sigma}\|}\right)\boldsymbol{n}\otimes\boldsymbol{n} + \frac{\Delta_t\gamma}{\|\operatorname{dev}\boldsymbol{\sigma}\|}\mathbb{P}\right)}_{:=\,\boldsymbol{\Xi}} : \Delta\boldsymbol{\sigma}\,, \tag{4.21}$$

see, e.g., Schröder et al. [198]. Thus, the expression for the linearization of $(4.17)_2$ gives

$$\Delta\mathcal{G}_\sigma = \int_{\mathcal{B}} \delta\boldsymbol{\sigma} : (\Delta\boldsymbol{\varepsilon} - \mathbb{D}^{ep} : \Delta\boldsymbol{\sigma})\,\mathrm{d}V \quad \text{with} \quad \mathbb{D}^{ep} := \boldsymbol{\Xi} + \partial^2_{\boldsymbol{\sigma}\boldsymbol{\sigma}}\chi(\boldsymbol{\sigma}) = \boldsymbol{\Xi} + \mathbb{C}^{-1}\,, \tag{4.22}$$

where $\mathbb{D}^{ep}$ is the algorithmic consistent fourth-order inverse elasto-plastic material tangent.

4.7 Discretization and static condensation of Hellinger-Reissner formulation

The discretization of the elasto-plastic Hellinger-Reissner formulation, with respect to the stresses, displacements and related fields, is considered, cf. Chapter 3.2.7, with

$$\boldsymbol{\sigma} = \bar{\mathbb{S}}\,\boldsymbol{d}_\sigma\,, \quad \boldsymbol{u} = \mathbb{N}\,\boldsymbol{d}_u \quad \text{and} \quad \boldsymbol{\varepsilon} = \mathbb{B}\,\boldsymbol{d}_u\,. \tag{4.23}$$

The approximation matrix considering the stress approach by Pian and Sumihara [178] for two dimensions regarding plane stress conditions $\bar{\mathbb{S}}$ is declared in the Appendix 8.1.1. In the discretization, the index e denotes values for a single element and not an elastic material state. The discrete weak forms $\mathcal{G}_u^h = \sum_{\mathrm{e}} \mathcal{G}_u^{\mathrm{e}}$ and $\mathcal{G}_\sigma^h = \sum_{\mathrm{e}} \mathcal{G}_\sigma^{\mathrm{e}}$ for a typical element with domain $\mathcal{B}_{\mathrm{e}}$ appear as

$$\begin{aligned}
\mathcal{G}_u^{\mathrm{e}} &= \delta\boldsymbol{d}_u^T\,\boldsymbol{r}_u^{\mathrm{e}} = \delta\boldsymbol{d}_u^T\Big(\int_{\mathcal{B}_{\mathrm{e}}} \mathbb{B}^T\,\bar{\mathbb{S}}\,\boldsymbol{d}_\sigma\;\mathrm{d}V - \int_{\mathcal{B}_{\mathrm{e}}} \mathbb{N}^T\,\boldsymbol{f}\;\mathrm{d}V - \int_{\partial\mathcal{B}_{\mathrm{e,t}}} \mathbb{N}^T\boldsymbol{t}\;\mathrm{d}A\Big)\,,\\
\mathcal{G}_\sigma^{\mathrm{e}} &= \delta\boldsymbol{d}_\sigma^T\,\boldsymbol{r}_\sigma^{\mathrm{e}} = \delta\boldsymbol{d}_\sigma^T\int_{\mathcal{B}_{\mathrm{e}}} \bar{\mathbb{S}}^T(\mathbb{B}\,\boldsymbol{d}_u - \boldsymbol{\varepsilon}^p - \underline{\mathbb{C}}^{-1}\,\bar{\mathbb{S}}\,\boldsymbol{d}_\sigma)\,\mathrm{d}V\,.
\end{aligned} \tag{4.24}$$

The discretized linearizations are

$$\begin{aligned}
\Delta\mathcal{G}_u^{\mathrm{e}} &= \delta\boldsymbol{d}_u^T\,\boldsymbol{k}_{u\sigma}^{\mathrm{e}}\,\Delta\boldsymbol{d}_\sigma &&= \delta\boldsymbol{d}_u^T\int_{\mathcal{B}_{\mathrm{e}}} \mathbb{B}^T\,\bar{\mathbb{S}}\,\mathrm{d}V\Delta\boldsymbol{d}_\sigma\,,\\
\Delta\mathcal{G}_\sigma^{\mathrm{e}} &= \delta\boldsymbol{d}_\sigma^T\,(\boldsymbol{k}_{\sigma u}^{\mathrm{e}}\,\Delta\boldsymbol{d}_u - \boldsymbol{k}_{\sigma\sigma}^{\mathrm{e}}\,\Delta\boldsymbol{d}_\sigma) &&= \delta\boldsymbol{d}_\sigma^T\Big(\int_{\mathcal{B}_{\mathrm{e}}} \bar{\mathbb{S}}^T\,\mathbb{B}\,\mathrm{d}V\Delta\boldsymbol{d}_u - \int_{\mathcal{B}_{\mathrm{e}}} \bar{\mathbb{S}}^T\,\underline{\mathbb{D}}^{ep}\,\bar{\mathbb{S}}\,\mathrm{d}V\Delta\boldsymbol{d}_\sigma\Big)\,,
\end{aligned} \tag{4.25}$$

with $\underline{\mathbb{C}}$ and $\underline{\mathbb{D}}^{ep}$ as the matrix notation of the associated tensor. Consequently, the resulting system of equations reads

$$\overset{num_{ele}}{\underset{e\,=\,1}{\mathbf{A}}}\left[\begin{array}{c}\delta\boldsymbol{d}_\sigma\\ \delta\boldsymbol{d}_u\end{array}\right]^T\left(\left[\begin{array}{cc}-\boldsymbol{k}_{\sigma\sigma}^{\mathrm{e}} & \boldsymbol{k}_{\sigma u}^{\mathrm{e}}\\ \boldsymbol{k}_{u\sigma}^{\mathrm{e}} & \mathbf{0}\end{array}\right]\left[\begin{array}{c}\Delta\boldsymbol{d}_\sigma\\ \Delta\boldsymbol{d}_u\end{array}\right] + \left[\begin{array}{c}\boldsymbol{r}_\sigma^{\mathrm{e}}\\ \boldsymbol{r}_u^{\mathrm{e}}\end{array}\right]\right) = 0\,. \tag{4.26}$$

Obviously, zero entries on the main diagonal, reveals the underlying saddle point structure of the system. In the presented case, the system can be reduced due to the stress

approximation $\boldsymbol{\sigma} \in \mathcal{L}^2(\mathcal{B})$, i.e., no global continuity is required for the stresses and $\boldsymbol{d}_\sigma$ can be solved on each element separately with respect to the displacements. Therefore, the system of equations (4.26) is solved for the stresses $\Delta\boldsymbol{d}_\sigma$ in the first equation and introduced in the second equation, cf. SCHRÖDER ET AL. [200]. The degrees of freedom for the increment of the stresses in terms of the displacements are

$$\Delta\boldsymbol{d}_\sigma = \underbrace{\boldsymbol{k}_{\sigma\sigma}^{\mathrm{e}\,-1}\,\boldsymbol{r}_\sigma^{\mathrm{e}}}_{\bar{\boldsymbol{r}}_\sigma} + \underbrace{\boldsymbol{k}_{\sigma\sigma}^{\mathrm{e}\,-1}\,\boldsymbol{k}_{\sigma u}^{\mathrm{e}}}_{\bar{\boldsymbol{k}}_\sigma}\,\Delta\boldsymbol{d}_u = \bar{\boldsymbol{r}}_\sigma + \bar{\boldsymbol{k}}_\sigma\,\Delta\boldsymbol{d}_u\,, \tag{4.27}$$

and the reduced form of (4.26) is given by

$$\delta\boldsymbol{d}_u^T(\underbrace{\boldsymbol{r}_u^{\mathrm{e}} + \boldsymbol{k}_{u\sigma}^{\mathrm{e}}\,\boldsymbol{k}_{\sigma\sigma}^{\mathrm{e}\,-1}\,\boldsymbol{r}_\sigma^{\mathrm{e}}}_{\boldsymbol{r}_{\mathrm{red}}^{\mathrm{e}}} + \underbrace{\boldsymbol{k}_{u\sigma}^{\mathrm{e}}\,\boldsymbol{k}_{\sigma\sigma}^{\mathrm{e}\,-1}\,\boldsymbol{k}_{\sigma u}^{\mathrm{e}}}_{\boldsymbol{k}_{\mathrm{red}}^{\mathrm{e}}}\Delta\boldsymbol{d}_u) = \boldsymbol{0}\,. \tag{4.28}$$

The static condensation reduces the system to a pure displacement based formulation. However, the discontinuous stress approximation allows for a static condensation, only if the inverse of $\boldsymbol{k}_{\sigma\sigma}^{\mathrm{e}}$ exists. Assembling over the number of finite elements num_{ele} leads to the global system of equations

$$\mathop{\mathsf{A}}_{\mathrm{e}\,=\,1}^{num_{ele}} \delta\boldsymbol{d}_u^T(\boldsymbol{r}_{\mathrm{red}}^{\mathrm{e}} + \boldsymbol{k}_{\mathrm{red}}^{\mathrm{e}}\,\Delta\boldsymbol{d}_u) = \delta\boldsymbol{D}^T(\boldsymbol{R}_{\mathrm{red}} + \boldsymbol{K}_{\mathrm{red}}\,\Delta\boldsymbol{D}) = \boldsymbol{0}\,, \tag{4.29}$$

cf. Chapter 3.2.7 and therefore the nodal displacements can be computed by $\Delta\boldsymbol{D} = -\boldsymbol{K}_{\mathrm{red}}^{-1}\,\boldsymbol{R}_{\mathrm{red}}$. The algorithmic treatment for the implementation of the derived formulation for small strain elasto-plasticity using plane stress condition is summarized in Table 4.1.

4.8 Extension of a perforated plate - plane stress formulation

The following example presents the possibility and comparability to enforce the flow rule pointwise instead of an elementwise enforcement as postulated in SIMO ET AL. [218]. In order to show this, the proposed formulation, denoted further by $\mathrm{HR}^{\mathrm{ep}}$, is compared to the element formulation presented in SIMO ET AL. [218], denoted by $\overline{\mathrm{HR}}^{\mathrm{ep}}$, see SCHRÖDER ET AL. [200]. The validation is completed by an additional comparison to a linear displacement formulation ($\mathcal{Q}_1$). All element formulations are considered with plane stress condition, which follows directly for the mixed formulation by application of the Pian-Sumihara stress approximation, see PIAN AND SUMIHARA [178].
For completeness, the results for the proposed formulation are compared with the one presented in SIMO ET AL. [218] on the same boundary value problem due to performance and accuracy. The considered academic example is a perforated plate problem, where the units are defined in {force} and {length}, see SIMO ET AL. [218]. As mentioned before, the following Figures and Tables were originally published in SCHRÖDER ET AL. [200].
The perforated plate problem is reduced to one quarter of the plate with corresponding boundary conditions based on the symmetry of the problem. The boundary value problem is loaded by a displacement controlled boundary condition on the upper edge of the plate, depicted in Figure 4.5 together with the material setup.

For the comparison of the three finite element formulations ($\mathrm{HR}^{\mathrm{ep}}$, $\overline{\mathrm{HR}}^{\mathrm{ep}}$, $\mathcal{Q}_1$) a load-displacement curve is shown in Figure 4.6. The load is determined by the nodal reactions

Table 4.1: Algorithmic treatment for the presented elasto-plastic Hellinger-Reissner formulation (Variables without indices are given at iteration $k+1$ and time t_{n+1})

(1) Update of the displacements (Newton iteration k+1)

Read from history: $\boldsymbol{\varepsilon}_n^p, \alpha_n, \sigma_{33,n}, \boldsymbol{d}_{\sigma,n}^{(k)}, \bar{\boldsymbol{r}}_\sigma^{(k)}$ and $\bar{\boldsymbol{k}}_\sigma^{(k)}$

$\boldsymbol{d}_u = \boldsymbol{d}_{u,n}^{(k)} + \Delta\boldsymbol{d}_u$ and $\boldsymbol{d}_\sigma = \boldsymbol{d}_{\sigma,n}^{(k)} + \Delta\boldsymbol{d}_\sigma$ with $\Delta\boldsymbol{d}_\sigma = \bar{\boldsymbol{r}}_\sigma^{(k)} + \bar{\boldsymbol{k}}_\sigma^{(k)}\Delta\boldsymbol{d}_u$

GAUSS LOOP (2) - (4)

(2) Compute stresses at each Gauss point with $\boldsymbol{\sigma} = \bar{\mathbb{S}}\,\boldsymbol{d}_\sigma$

(3) IF plane stress condition THEN

$\Phi^{\text{trial}} = \|\operatorname{dev}\boldsymbol{\sigma}_{n+1}\| - \sqrt{\frac{2}{3}}(y_0 + h\,\alpha_n)$

IF $\Phi^{\text{trial}} \leq 0$: $\boldsymbol{\varepsilon}^p = \boldsymbol{\varepsilon}_n^p$ and $\alpha = \alpha_n$

ELSE IF $\Phi^{\text{trial}} > 0$: $\Delta_t\gamma = \frac{3\Phi^{\text{trial}}}{2h}, \boldsymbol{\varepsilon}^p = \boldsymbol{\varepsilon}_n^p + \Delta_t\gamma\,\boldsymbol{n}$ and $\alpha = \alpha_n + \sqrt{\frac{2}{3}}\,\Delta_t\gamma$

ELSE IF plane strain condition THEN GO TO Table 4.6

(4) Determine element matrices and vectors $\boldsymbol{k}_{\sigma\sigma}^{\text{e}}$, $\boldsymbol{k}_{\sigma u}^{\text{e}}$ and $\boldsymbol{r}_\sigma^{\text{e}}$

(5) Calculate vector and matrix for local stress computation $\bar{\boldsymbol{r}}_\sigma$ and $\bar{\boldsymbol{k}}_\sigma$

(6) Determine right hand side vector and element stiffness matrix $\boldsymbol{r}_{\text{red}}^{\text{e}}$ and $\boldsymbol{k}_{\text{red}}^{\text{e}}$

(7) Write to history: $\boldsymbol{\varepsilon}^p, \alpha, \sigma_{33}, \boldsymbol{d}_\sigma, \bar{\boldsymbol{r}}_\sigma$ and $\bar{\boldsymbol{k}}_\sigma$

(8) Assembling, see equation (4.29), and solving the system of equations

Setup of BVP

Left edge	$u_x = 0\,\{\text{length}\}$
Lower edge	$u_y = 0\,\{\text{length}\}$
Upper edge	$\boldsymbol{u} = (0, 6.15)^T\,\{\text{length}\}$
Young's modulus	$E = 70\,\{\text{force}\}/\{\text{length}\}^2$
Poisson's ratio	$\nu = 0.2$
Yield stress	$y_0 = 0.243\,\{\text{force}\}/\{\text{length}\}^2$
Hardening modulus	$h = 0.2\,\{\text{force}\}/\{\text{length}\}^2$

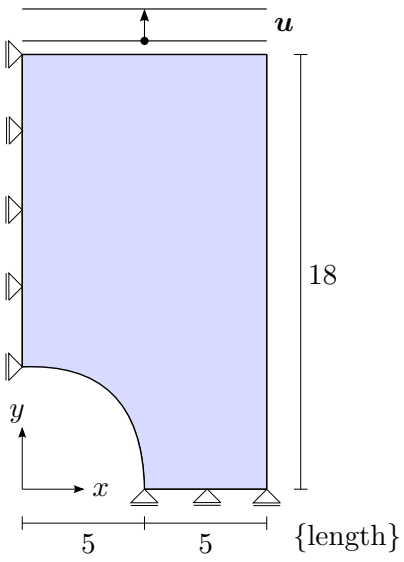

Figure 4.5: Geometrical and material setup of the perforated plate problem

at the upper edge $y = 18$. The results are obtained on finite element meshes with 72 and 722 elements depicted within the numerical results.
For both Hellinger-Reissner formulations, the results in Figure 4.6 are in accordance. In contrast to that, the displacement formulation lead for both mesh densities to deviations

in the load-displacement curve. The results for $\mathrm{HR}^{\mathrm{ep}}$ and $\overline{\mathrm{HR}}^{\mathrm{ep}}$ illustrates that the point- and elementwise enforcement of the return mapping algorithm lead to similar results for the underlying Hellinger-Reissner formulations and therefore to the assumption that both approaches are applicable for mixed formulations. Additionally, the distribution of the equivalent plastic strains represented by α are depicted in Figure 4.7, which give almost identical results for the investigated elements. Here, the proposed $\mathrm{HR}^{\mathrm{ep}}$ formulation is compared to a linear displacement element $\mathcal{Q}_1$ and a mixed displacement-pressure element $\mathcal{Q}_1\mathcal{P}_0$ with linear displacement and constant pressure approximation.

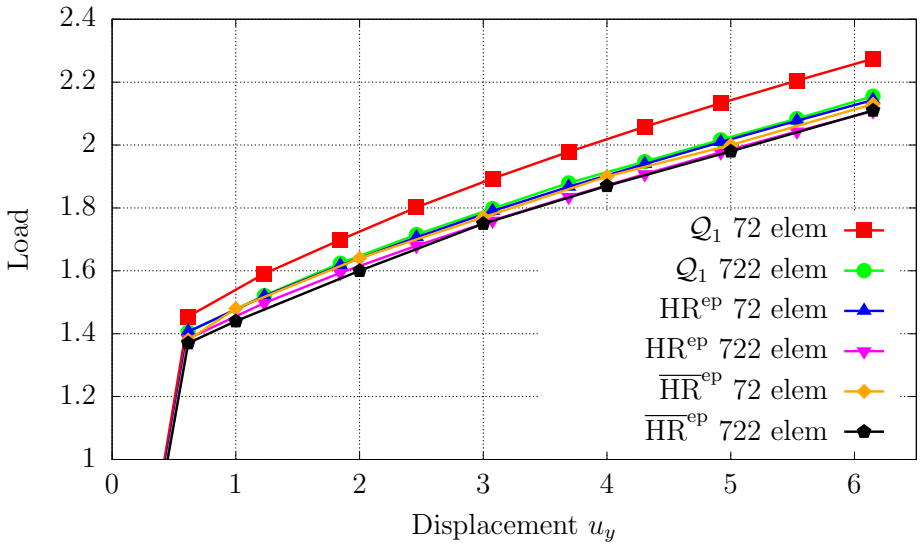

Figure 4.6: Load-displacement curves, cf. Simo et al. [218] and Schröder et al. [200]

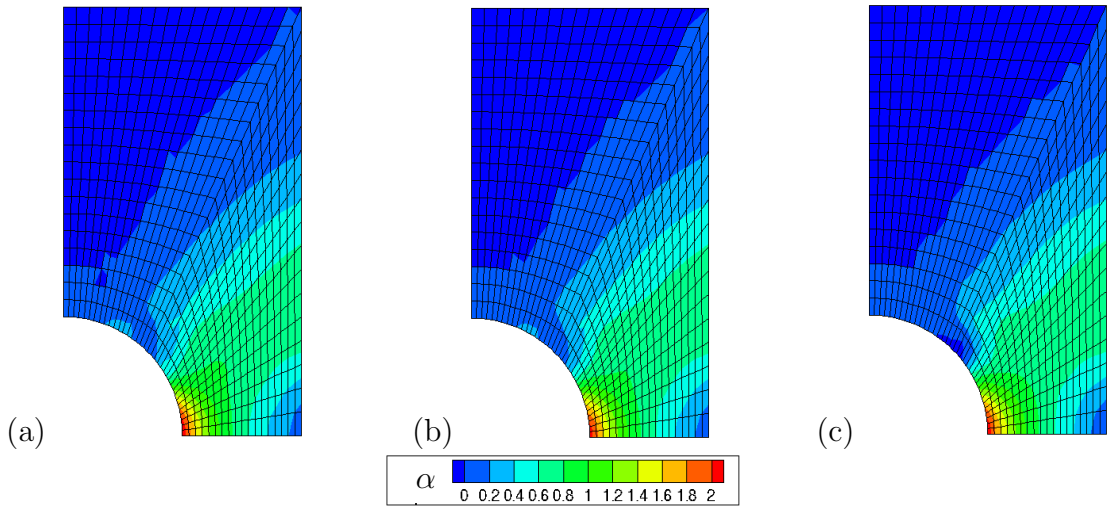

Figure 4.7: Distribution of α for (a) the $\mathcal{Q}_1$, (b) the $\mathcal{Q}_1\mathcal{P}_0$ and (c) the $\mathrm{HR}^{\mathrm{ep}}$ element on the undeformed 722 element mesh for a u_y displacement of 6.15, cf. Schröder et al. [200]

For a complete comparison with the results in Simo et al. [218], the evolution of the plastic zone within the plate and the convergence of the energy norm for the global Newton iteration are presented. The plastic zone for linear isotropic hardening, following

Simo et al. [218], is defined by

$$\tilde{\phi} := \| \operatorname{dev} \boldsymbol{\sigma} \| / \sqrt{\tfrac{2}{3}}\, y_0 \,. \tag{4.30}$$

This leads to a definition of three areas, i.e., a purely elastic region ($\tilde{\phi} < 0.9$), an elasto-plastic transition zone ($0.9 \leq \tilde{\phi} < 1.0$), in which plastic deformations will occur under continuous loading, and a plastic region ($\tilde{\phi} \geq 1.0$). The evolution of the plastic zone, as an indicator for plastic strains, is depicted in Figure 4.8 and 4.9 for $\mathrm{HR}^{\mathrm{ep}}$ on a 72 and 722 element mesh. Based on the problem, the initial and maximum plastic strains occur at the stress concentration of the perforated plate, which is located at the right corner of the circular arc (at $\boldsymbol{x} = (5, 0)^T$), cf. Figure 4.7. The distribution of the plastic zone yields satisfying results, which are in accordance with the results for the $\overline{\mathrm{HR}}^{\mathrm{ep}}$ element given in Simo et al. [218].
Furthermore, the convergence of the Newton-Raphson scheme for the proposed $\mathrm{HR}^{\mathrm{ep}}$ formulation, in Table 4.2 and 4.3, is compared to the one of the $\overline{\mathrm{HR}}^{\mathrm{ep}}$ element of Simo et al. [218], given in Table 4.4 and 4.5, using the same load steps.

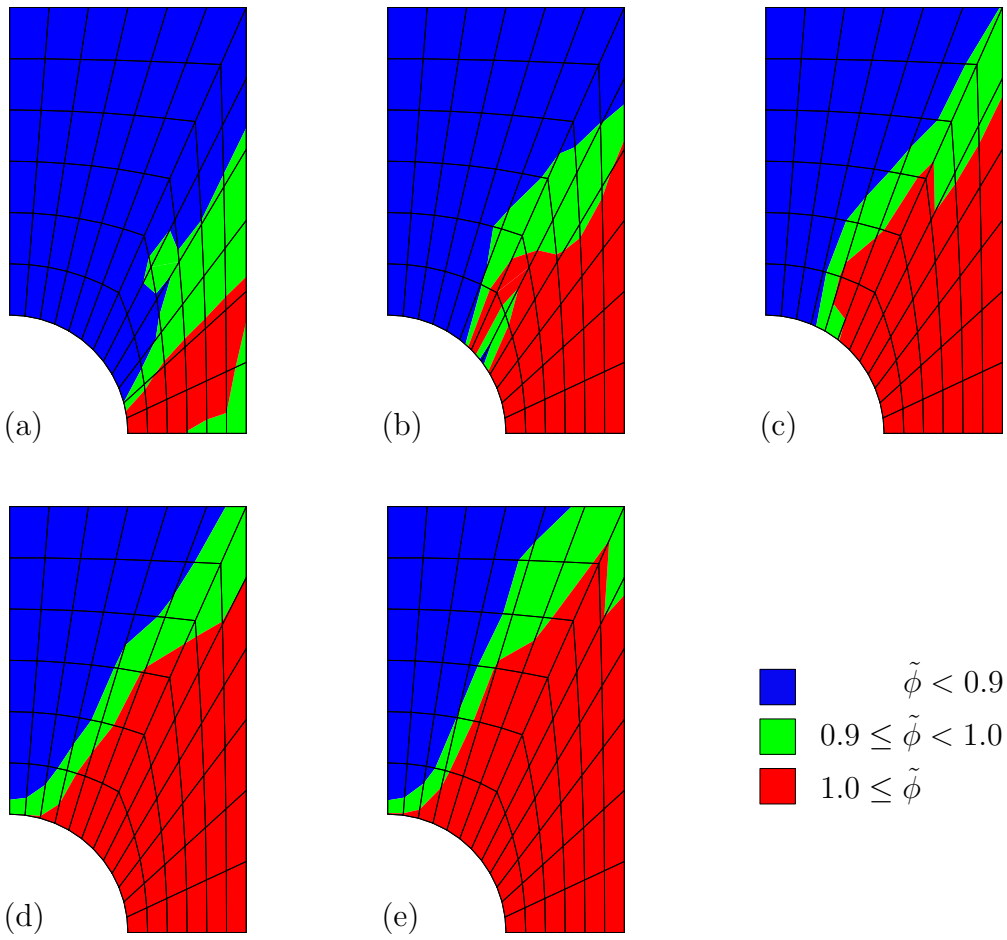

Figure 4.8: Distribution of $\tilde{\phi}$ for the $\mathrm{HR}^{\mathrm{ep}}$ on the undeformed 72 element mesh for a u_y displacement of (a) 0.15, (b) 1.65, (c) 3.15, (d) 4.65 and (e) 6.15, cf. Schröder et al. [200]

The given results in Table 4.2 to 4.5 show a satisfying performance due to the fact that quadratic convergence is attained only for energy norms below 10^{-6} caused by the radius

Table 4.2: Convergence of relative residual norm in the Newton-Raphson iteration for $\mathrm{HR}^{\mathrm{ep}}$ with 72 element mesh, cf. Schröder et al. [200]

	Load step			
	1	5	10	17
Iteration	($u_y = 0.03$)	($u_y = 0.15$)	($u_y = 2.65$)	($u_y = 6.15$)
1	1.0000 E+00	1.0000 E+00	1.0000 E+00	1.0000 E+00
2	4.3560 E-03	6.7304 E-03	1.2833 E-03	6.0352 E-04
3	2.1955 E-02	1.4551 E-02	5.8301 E-03	1.2810 E-03
4	2.6966 E-02	2.0175 E-03	4.4649 E-04	6.9739 E-04
5	1.2170 E-03	5.1973 E-06	8.5537 E-04	2.0760 E-05
6	1.2706 E-03	8.4837 E-10	6.4444 E-06	5.0264 E-08
7	9.5159 E-06	3.2705 E-15	1.8075 E-09	9.6836 E-13
8	8.7670 E-09	-	2.1193 E-15	-
9	1.2305 E-15	-	-	-

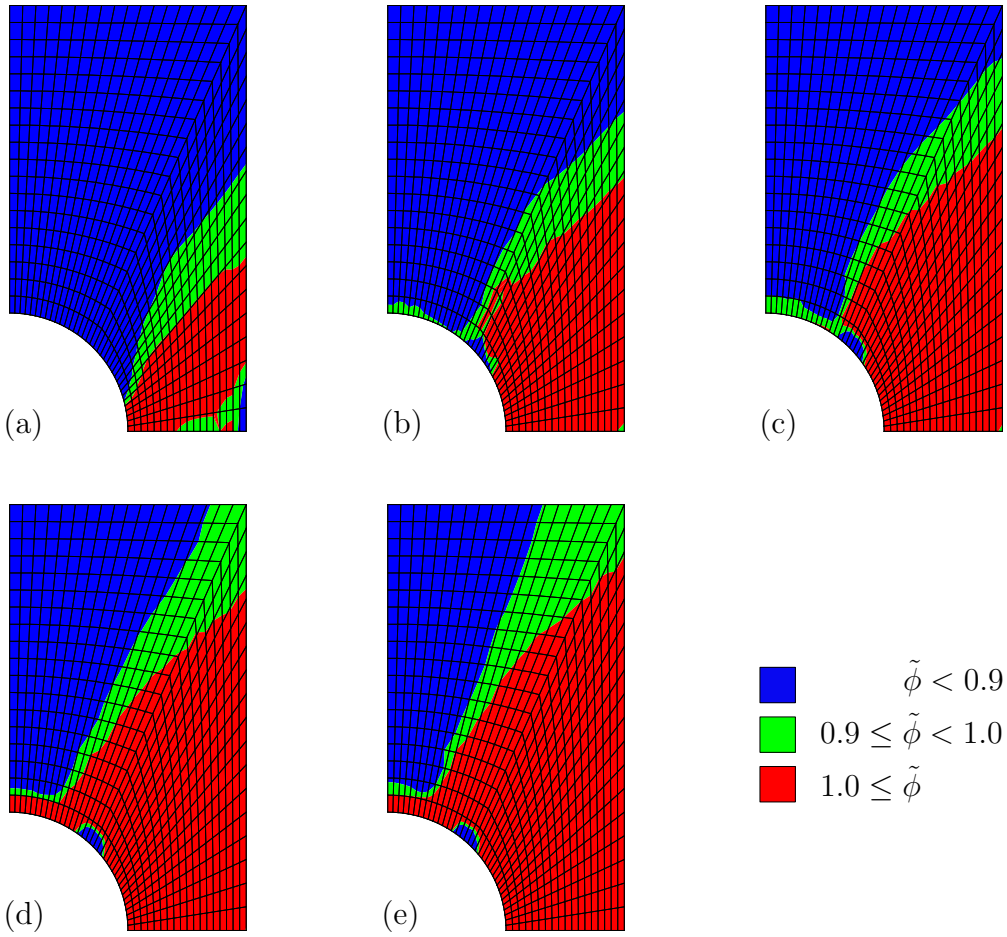

Figure 4.9: Distribution of $\tilde{\phi}$ for the $\mathrm{HR}^{\mathrm{ep}}$ on the undeformed 722 element mesh for a u_y displacement of (a) 0.15, (b) 1.65, (c) 3.15, (d) 4.65 and (e) 6.15, cf. Schröder et al. [200]

of convergence. A further aspect is the slight degradation of the rate of convergence for more refined meshes. This degradation is shown for the mixed formulation in Table 4.3, where, e.g., for load step 10, the Newton method needs 11 iterations. The same effect is

Table 4.3: Convergence of relative residual norm in the Newton-Raphson iteration for HR^{ep} with 722 element mesh, cf. SCHRÖDER ET AL. [200]

	Load step			
	1	5	10	17
Iteration	($u_y = 0.03$)	($u_y = 0.15$)	($u_y = 2.65$)	($u_y = 6.15$)
1	1.0000 E+00	1.0000 E+00	1.0000 E+00	1.0000 E+00
2	1.1914 E-03	2.4627 E-03	1.0090 E-03	2.3216 E-04
3	4.5942 E-02	1.1869 E-02	4.0853 E-03	9.3445 E-04
4	1.6117 E-03	6.8015 E-04	1.2712 E-03	6.9568 E-04
5	3.1768 E-04	1.0278 E-03	9.0929 E-04	1.8675 E-04
6	2.5042 E-06	1.6548 E-05	1.3427 E-04	3.9894 E-05
7	2.4724 E-08	9.5113 E-08	9.4389 E-05	6.9197 E-06
8	1.8996 E-14	9.7087 E-14	5.6719 E-06	1.1346 E-05
9	-	-	6.7623 E-06	7.6111 E-09
10	-	-	3.3072 E-09	2.4700 E-13
11	-	-	8.0553 E-15	-

shown in Table 4.5 for the formulation of SIMO ET AL. [218], where load step 10 needs 10 Newton iterations.
It has to be noted that the global effort for all depicted element formulations is similar. In the proposed HR^{ep} formulation, a small increase in the effort on a local level has to be mentioned due to the computation of the inverse matrix, which is however insignificant.

Table 4.4: Convergence of relative residual norm in the Newton-Raphson iteration for $\overline{HR}^{ep}$ with 72 element mesh, taken from SIMO ET AL. [218]

	Load step			
	1	5	10	17
Iteration	($u_y = 0.03$)	($u_y = 0.15$)	($u_y = 2.65$)	($u_y = 6.15$)
1	0.264 E+00	0.288 E+00	0.800 E+02	0.779 E+02
2	0.222 E-04	0.164 E-04	0.970 E-03	0.196 E-03
3	0.260 E-04	0.165 E-06	0.797 E-04	0.139 E-05
4	0.332 E-08	0.645 E-11	0.755 E-06	0.278 E-09
5	0.228 E-14	0.956 E-20	0.222 E-09	0.210 E-16
6	0.172 E-26	0.116 E-29	0.320 E-16	0.564 E-27

Based on the investigated HR formulation, Remark 2.1(2) in SIMO ET AL. [218] cannot be confirmed. It claims that a pointwise enforcement of the flow rule, hardening law and consistency condition recovers the displacement model. In the work of SIMO ET AL. [218], the hardening law and consistency condition are enforced pointwise whereas the flow rule is fulfilled in a weak sense over the element domain. The results, e.g., shown in Figure 4.6, illustrate that HR^{ep} does not coincide with the displacement model.

4.9 Hellinger-Reissner formulation with plane strain condition

In addition to the plane stress formulation described in the previous subsection, the performance of a plane strain algorithm is analyzed on the example of a plate with a circular

Table 4.5: Convergence of relative residual norm in the Newton-Raphson iteration for $\overline{\text{HR}}^{\text{ep}}$ with 722 element mesh, taken from SIMO ET AL. [218]

	Load step			
	1	5	10	17
Iteration	($u_y = 0.03$)	($u_y = 0.15$)	($u_y = 2.65$)	($u_y = 6.15$)
1	0.897 E+00	0.921 E+00	0.256 E+03	0.245 E+03
2	0.220 E-04	0.217 E-04	0.831 E-03	0.185 E-03
3	0.175 E-05	0.196 E-05	0.683 E-02	0.156 E-04
4	0.449 E-07	0.883 E-07	0.753 E-04	0.189 E-05
5	0.320 E-13	0.719 E-10	0.871 E-05	0.951 E-07
6	0.559 E-23	0.125 E-15	0.275 E-06	0.375 E-11
7	-	0.483 E-27	0.176 E-07	0.210 E-18
8	-	-	0.192 E-11	0.164 E-25
9	-	-	0.578 E-19	-
10	-	-	0.255 E-26	-

elastic inclusion. The plane strain condition is enforced by an incremental algorithmic treatment, see, e.g., DE BORST [85] and KLINKEL AND GOVINDJEE [134]. For a plane strain setup, the requirements are $\varepsilon_{13} = \varepsilon_{23} = \varepsilon_{33} = 0$, which results in general in a non-zero value for σ_{33}. In order to derive the associated algorithmic treatment, a vector representation of the incremental elasto-plastic constitutive equation is considered by

$$\Delta\underline{\boldsymbol{\varepsilon}} = \underline{\mathbb{D}}^{ep}\Delta\underline{\boldsymbol{\sigma}} \quad \Rightarrow \quad \begin{pmatrix} \Delta\boldsymbol{\varepsilon}_m \\ \Delta\varepsilon_z \end{pmatrix} = \begin{pmatrix} \mathbb{D}^{ep}_{mm} & \mathbb{D}^{ep}_{mz} \\ \mathbb{D}^{ep}_{zm} & \mathbb{D}^{ep}_{zz} \end{pmatrix} \begin{pmatrix} \Delta\boldsymbol{\sigma}_m \\ \Delta\sigma_z \end{pmatrix}, \tag{4.31}$$

with the matrices $\mathbb{D}^{ep}_{mm} \in \mathbb{R}^{3\times3}$, $\mathbb{D}^{ep}_{mz} \in \mathbb{R}^{3\times1}$, $\mathbb{D}^{ep}_{zm} \in \mathbb{R}^{1\times3}$ and $\mathbb{D}^{ep}_{zz}$ as a scalar value. Furthermore, the strains $\boldsymbol{\varepsilon}_m$, ε_z and the stresses $\boldsymbol{\sigma}_m$, σ_z are defined by

$$\boldsymbol{\varepsilon}_m = (\varepsilon_{11}, \varepsilon_{22}, 2\varepsilon_{12})^T\,, \quad \varepsilon_z = (\varepsilon_{33}) = 0\,, \quad \boldsymbol{\sigma}_m = (\sigma_{11}, \sigma_{22}, \sigma_{12})^T \text{ and } \sigma_z = (\sigma_{33})\,. \tag{4.32}$$

For the development of a local plane strain algorithm, it has to be ensured that $\varepsilon_z = 0$ enforced by the corresponding stress σ_z. Based on the vector representation (4.31), the strain $\varepsilon_z^{(i+1)} = \varepsilon_z^{(i)} + \Delta\varepsilon_z$ is expressed by

$$\varepsilon_z^{(i+1)} = \varepsilon_z^{(i)} + \mathbb{D}^{ep}_{zz}\,\Delta\sigma_z \stackrel{!}{=} 0 \quad \Rightarrow \quad \Delta\sigma_z = -\mathbb{D}^{ep\,-1}_{zz}\,\varepsilon_z^{(i)}\,, \tag{4.33}$$

with the incremental stress update scheme by $\sigma_z^{(i+1)} = \sigma_z^{(i)} + \Delta\sigma_z$. For quadratic convergence of the Newton-Raphson scheme, a modification of the elasto-plastic tangent modulus is necessary. The material tangent is still depending on the full stress state $\boldsymbol{\sigma}$, since only a reduction of the strain and stress tensor to $\boldsymbol{\varepsilon}_m$ and $\boldsymbol{\sigma}_m$ is performed. Thus, a condensed material tangent has to be determined with respect to the plane strain condition. The relation $(4.31)_2$ ($\Delta\varepsilon_z = \mathbb{D}^{ep}_{zm}\,\Delta\boldsymbol{\sigma}_m + \mathbb{D}^{ep}_{zz}\,\Delta\sigma_z$) is solved, with $\Delta\varepsilon_z = 0$, which yields

$$\Delta\sigma_z = -\mathbb{D}^{ep\,-1}_{zz}\,\mathbb{D}^{ep}_{zm}\,\Delta\boldsymbol{\sigma}_m\,. \tag{4.34}$$

Substituting the latter expression into $(4.31)_1$, the term $\Delta\boldsymbol{\varepsilon}_m = \mathbb{D}^{ep}_{mm}\Delta\boldsymbol{\sigma}_m + \mathbb{D}^{ep}_{mz}\Delta\sigma_z$ provides the elasto-plastic material tangent for the plane strain setup $\mathbb{D}^{ep}_{\text{mod}}$:

$$\Delta\boldsymbol{\varepsilon}_m = \mathbb{D}^{ep}_{\text{mod}}\,\Delta\boldsymbol{\sigma}_m \quad \text{with} \quad \mathbb{D}^{ep}_{\text{mod}} = [\mathbb{D}^{ep}_{mm} - \mathbb{D}^{ep}_{mz}\,\mathbb{D}^{ep\,-1}_{zz}\,\mathbb{D}^{ep}_{zm}]\,. \tag{4.35}$$

The algorithmic treatment of the local plane strain algorithm is illustrated in Table 4.6 and can be directly included in the mixed HR^{ep} formulation presented in Table 4.1.

Table 4.6: Algorithmic treatment for local enforcement of plane strain condition

(1) Read from history $\sigma_{33} = \sigma_{33,\,n}$

Initialize $tol = 10^{-8}$

(2) Compute elastic and plastic strains

$$\boldsymbol{\sigma} = \begin{bmatrix} \sigma_{11} & \sigma_{12} & 0 \\ \sigma_{21} & \sigma_{22} & 0 \\ 0 & 0 & \sigma_{33} \end{bmatrix} \text{ with } \sigma_{21} = \sigma_{12}$$

$\boldsymbol{\varepsilon}^e = \mathbb{C}^{-1}\boldsymbol{\sigma}$

IF $\Phi^{\text{trial}} \leq 0$ THEN

$\boldsymbol{\varepsilon}^p = \boldsymbol{\varepsilon}^p_n$ and $\alpha = \alpha_n$

ELSE IF $\Phi^{\text{trial}} > 0$ THEN

$\Delta_t\gamma = \frac{3\Phi^{\text{trial}}}{2h}, \boldsymbol{\varepsilon}^p = \boldsymbol{\varepsilon}^p_n + \Delta_t\gamma\,\boldsymbol{n}$ and $\alpha = \alpha_n + \sqrt{\frac{2}{3}}\Delta_t\gamma$

END IF

$\varepsilon_{33} = \varepsilon^e_{33} + \varepsilon^p_{33}$

(3) Algorithmic consistent tangent

$$\mathbb{D}^{ep} = \mathbb{C}^{-1} + \partial_{\boldsymbol{\sigma}}\boldsymbol{\varepsilon}^p = \mathbb{C}^{-1} + \left(\frac{3}{2\,h} - \frac{\Delta_t\gamma}{\|\operatorname{dev}\boldsymbol{\sigma}\|}\right)\boldsymbol{n}\otimes\boldsymbol{n} + \frac{\Delta_t\gamma}{\|\operatorname{dev}\boldsymbol{\sigma}\|}\mathbb{P}$$

(4) Check for plane strain condition:

IF $|\varepsilon_{33}| < tol$ THEN GO TO (5)

ELSE IF $\sigma_{33} = \sigma_{33} + \Delta\sigma_{33}$ with $\Delta\sigma_{33} = \varepsilon_{33}/\mathbb{D}^{ep}_{3333}$ THEN GO TO (2)

(5) Plane strain modification for material tangent $\mathbb{D}^{ep}$

$$\mathbb{D}^{ep}_{\text{mod}} = \mathbb{D}^{ep}_{mm} - \mathbb{D}^{ep}_{mz}\,\mathbb{D}^{ep\,-1}_{zz}\,\mathbb{D}^{ep}_{zm}$$

Write in history σ_{33} and continue with Table 4.1

4.10 Elongation of a plate with circular inclusion - plane strain formulation

For the validation of the presented plane strain algorithm, the example of a rectangular domain with an elastic circular inclusion is considered, loaded by a displacement controlled boundary condition to a maximum of $u_y = 0.1\,\text{mm}$. The boundary value problem and the material setup are presented in Figure 4.10. The considered finite element meshes are depicted within the numerical results.

The performance of the plane strain setup of the HR^{ep} element is compared to a $\mathcal{Q}_1$ and a mixed $\mathcal{Q}_1\mathcal{P}_0$ formulation utilizing plane strain condition. In Figure 4.11, a load-displacement curve is shown, determined with the nodal reactions at the upper edge $y = 10\,\text{mm}$ for a mesh with 252 elements. The results for the evaluated elements yield almost the same behavior, where an insignificant increase of the load above a displacement of $u_y = 0.07\,\text{mm}$ is visible for the $\mathcal{Q}_1$ element.

Setup of BVP

Left edge	$u_x = 0$
Lower edge	$u_y = 0$
Upper edge	$\boldsymbol{u} = (0, 0.1)^T$ mm
Young's modulus	$E_1 = 206$ GPa
	$E_2 = 412$ GPa
Poisson's ratio	$\nu = 0.3$
Yield stress	$y_{01} = 1.0$ GPa
	$y_{02} \to \infty$
Hardening modulus	$h = 0.01$ GPa

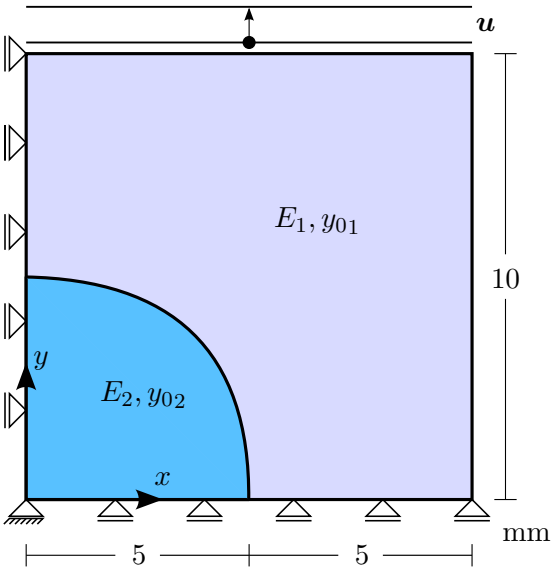

Figure 4.10: Geometrical and material setup for the plate with elastic circular inclusion

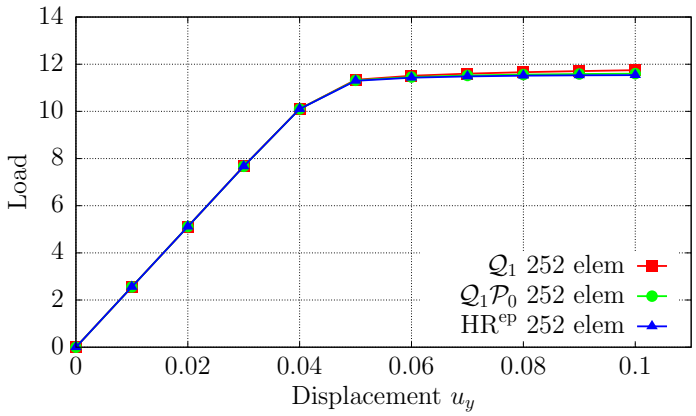

Figure 4.11: Load-displacement curves for a discretization with 252 elements for the $\mathcal{Q}_1$, $\mathcal{Q}_1\mathcal{P}_0$ and the proposed HR^{ep} element formulations, cf. Schröder et al. [200]

Additionally, equivalent plastic strains for a displacement of $u_y = 0.05\,\text{mm}$ are displayed in Figure 4.12. The material response of the circular inclusion is purely elastic and the plastic strains are concentrated above the purely elastic inclusion. The maximum amount of plastic strains occur above the top of the circular inclusion, $\boldsymbol{x} = (0, 5)^T$, which is given as the intersection of the elastic and elasto-plastic material. All element formulations yield a similar distribution for α. For completeness, the stress σ_{33} and the plastic strains ε^p_{33} are depicted in Figure 4.13 and 4.14. The illustration of the plastic strain ε^p_{33} represent that the plane strain enforcement still yield a plastic strain $\varepsilon^p_{33} \neq 0$. As a consequence of this and since the stress is a function of $\boldsymbol{\varepsilon}^e$, an elastic strain value $\varepsilon^e_{33} \neq 0$ must occur, which arises in opposite direction and results in a plane strain setup for the total strains. The distribution of the field quantities for the displacement and mixed displacement-pressure formulation are in accordance with the Hellinger-Reissner approach.

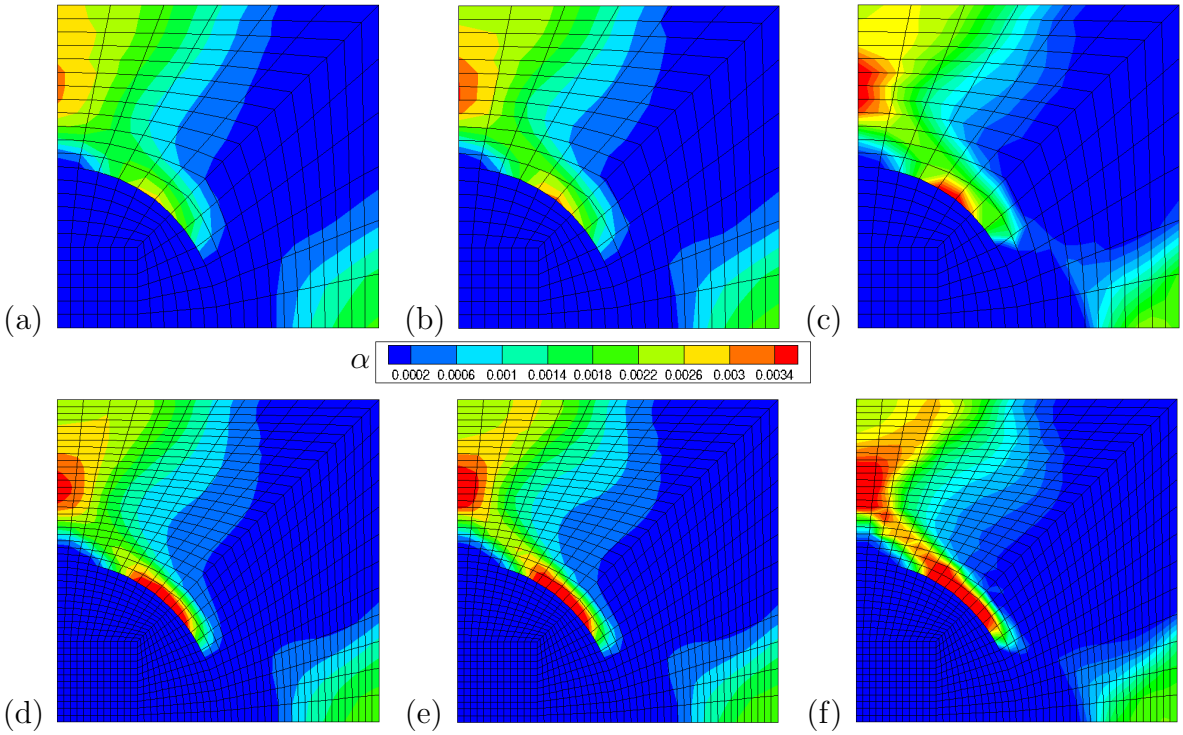

Figure 4.12: Distribution of α for $\mathcal{Q}_1$ (a), (d), $\mathcal{Q}_1\mathcal{P}_0$ (b), (e) and HR$^{\text{ep}}$ (c), (f) at $u_y = 0.05\,\text{mm}$ for a mesh with 252 (top) and 1008 elements (bottom), cf. Schröder et al. [200]

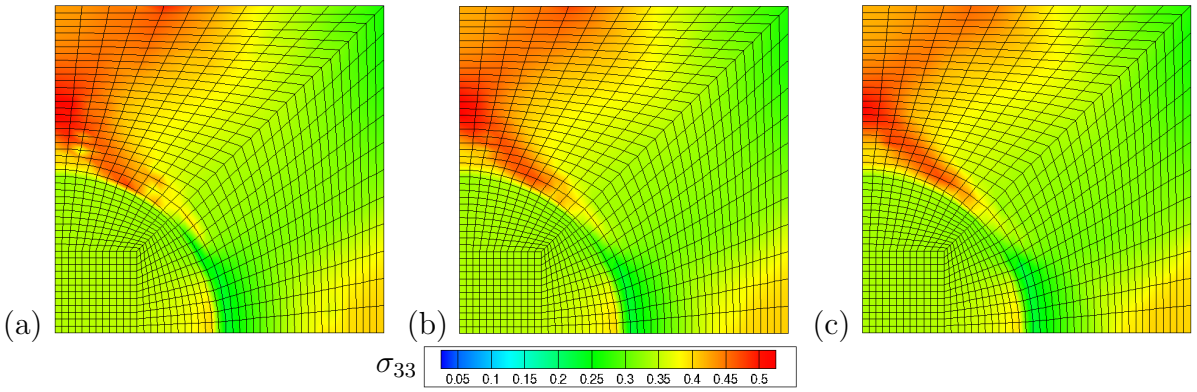

Figure 4.13: Distribution of σ_{33} for $\mathcal{Q}_1$ (a), $\mathcal{Q}_1\mathcal{P}_0$ (b) and HR$^{\text{ep}}$ (c) formulation on the 1008 element mesh at $u_y = 0.05\,\text{mm}$, cf. Schröder et al. [200]

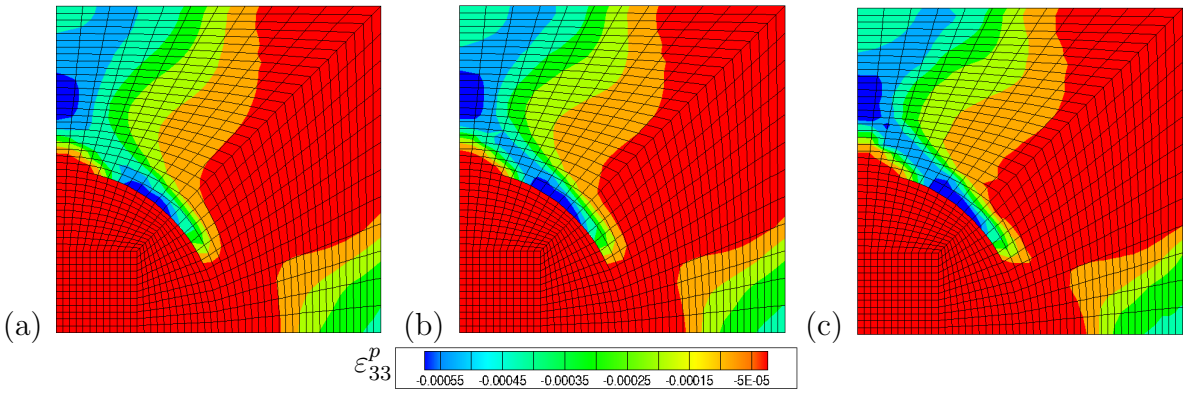

Figure 4.14: Distribution of ε^p_{33} for $\mathcal{Q}_1$ (a), $\mathcal{Q}_1\mathcal{P}_0$ (b) and HR$^{\text{ep}}$ (c) formulation on the 1008 element mesh at $u_y = 0.05\,\text{mm}$, cf. Schröder et al. [200]

5 Mixed finite element formulations at finite strains

The description of materials can often only be inadequately represented with the help of the theory of small deformations, since materials often undergo large deformations. This behavior usually cannot be represented by linear elasticity. For a generally valid representation of material properties, finite elastic deformations are considered in the following, which are in general characterized by a nonlinear stress-strain relation. It should be noted, that the St. Venant Kirchhoff material represent a special case which is based on a linear stress-strain relation and can therefore only be used for certain applications. The theory of large deformations is also denoted as hyperelasticity and is valid for rubber, steel and aluminum, among others. For finite elasticity, there are a number of different material laws. A detailed description on finite elasticity is given in Ogden [174] and Ciarlet [78]. For investigating finite deformations, the laws for material modeling, listed in Chapter 2.4, have to be considered.
A first inside of least-squares finite element formulations for hyperelastic material behavior is analyzed, cf., e.g., Manteuffel et al. [158], Schwarz [203], Müller et al. [167], Steeger [223] and Schwarz et al. [208]. Therefore, a Neo-Hookean free energy function (2.57) is considered, see Ogden [174] and Wriggers [236], given in terms of the left Cauchy-Green deformation tensor $\boldsymbol{B} = \boldsymbol{F} \cdot \boldsymbol{F}^T$. The resulting LS formulation is analyzed, with respect to finite element performance and the weighting of functional parts, based on the insights in Chapter 4.1, for plane strain and plane stress conditions. Beside the extended formulation, with additional control of the stress symmetry condition, a further modification of the classical LS approach is presented, replacing the first variation by a modified weak form, which is characterized by the antisymmetric displacement gradient in the test space, cf. Schwarz et al. [205], Starke et al. [221] for linear elasticity, Schwarz et al. [208] for hyperelasticity and Igelbüscher et al. [119] for finite J_2-plasticity. The same Neo-Hookean energy function (2.57) is further used as a foundation for finite J_2-plasticity. Therefore, the hyperelastic LS formulation is extended in terms of the multiplicative decomposition of the deformation gradient $\boldsymbol{F} = \boldsymbol{F}^e \cdot \boldsymbol{F}^p$, introduced by Lee and Liu [145] and Lee [148] and motivated by micromechanic effects in crystal plasticity, see, e.g., Hill [114], Asaro [14] and the reference given in Chapter 2.5.3. Furthermore, the drawbacks of LSFEM for the application to rate-independent plasticity formulations are addressed separately. Here, the main aspects of the investigation are:

- Analysis of the hyperelastic LS formulation in terms of finite element performance and weighting parameters,
- Development and validation of a plane stress formulation in the framework of an automated differentiation procedure,
- Discussion on remarks on the LSFEM for hyperelastic material setups,
- Extension of the LS formulation to finite J_2-plasticity,
- Discussion on shortcomings and limitations of LSFEM for elasto-plasticity.

The following results and analyses have already been published in Schwarz et al. [208] and Igelbüscher et al. [119; 121].

5.1 Least-squares formulation at finite elastic deformations

As in the case of linear elasticity, finite elastic deformations can be characterized by a set of equations defined by

$$\begin{aligned} \operatorname{Div} \boldsymbol{P} &= -\boldsymbol{f} && \text{on } \mathcal{B}\,, \\ \boldsymbol{\tau} &= 2\,\partial_{\boldsymbol{B}}\psi(\boldsymbol{B})\cdot\boldsymbol{B} && \text{on } \mathcal{B}\,, \\ \boldsymbol{F} &= \boldsymbol{1} + \nabla\boldsymbol{u} && \text{on } \mathcal{B}\,, \\ \boldsymbol{\tau} &= \boldsymbol{\tau}^T && \text{on } \mathcal{B}\,, \\ \boldsymbol{P}\cdot\boldsymbol{N} &= \bar{\boldsymbol{T}} && \text{on } \partial\mathcal{B}_N\,, \\ \boldsymbol{u} &= \bar{\boldsymbol{u}} && \text{on } \partial\mathcal{B}_D\,. \end{aligned} \tag{5.1}$$

Analogously to (3.17), this system is given by the balance of linear momentum, constitutive equation with

$$\psi(\boldsymbol{B}) = \psi^{\text{iso}}_{\text{NH}}(\boldsymbol{B}) = \frac{\lambda}{4}(I_3(\boldsymbol{B})-1) + \frac{\mu}{2}(I_1(\boldsymbol{B})-3) - \left(\frac{\lambda}{2}+\mu\right)\ln\sqrt{I_3(\boldsymbol{B})}\,, \tag{5.2}$$

see (2.57), compatibility condition of the strains, balance of angular momentum and corresponding boundary conditions with the boundary traction and displacement ($\bar{\boldsymbol{T}}$, $\bar{\boldsymbol{u}}$) defined on the reference configuration. Here, the system is formulated in terms of the Piola-Kirchhoff stresses $\boldsymbol{\tau} = \boldsymbol{P}\cdot\boldsymbol{F}^T$, with the material relation defined in terms of $\boldsymbol{B}$, see (2.79). Since the LSFEM is here only applied to first-order systems, the balance of linear momentum is considered with respect to the first Piola Kirchhoff stresses $\boldsymbol{P}$. Nevertheless, a representation with $\operatorname{Div}(\boldsymbol{\tau}\cdot\boldsymbol{F}^{-T}) = -\boldsymbol{f}$ on $\mathcal{B}$ is possible as well and denotes a second-order system that can be solved using $\mathcal{C}^1$-continuous functions.
The constitutive equation can also be formulated in the first Piola-Kirchhoff stresses $\boldsymbol{P}$ with $\boldsymbol{P} = \partial_{\boldsymbol{F}}\psi(\boldsymbol{F})$, with the free energy function per reference volume. Here, a formulation in Kirchhoff stresses $\boldsymbol{\tau}$, cf. (2.79), as a symmetric stress measure is considered, which can directly be reformulated in terms of any symmetric stress measure, e.g., the second Piola-Kirchhoff stresses $\boldsymbol{S} = \boldsymbol{F}^{-1}\cdot\boldsymbol{P}$ with $\boldsymbol{S} = \boldsymbol{S}^T$.
The LS functional, as a first-order system of differential equations, is constructed with respect to the squared $\mathcal{L}^2(\mathcal{B})$-norm and (3.35), in terms of the balance of linear momentum, the constitutive relation and stress symmetry condition, i.e.,

$$\begin{aligned} \mathcal{F}^{\text{hyp}}(\boldsymbol{P},\boldsymbol{u}) \;=\; & \frac{1}{2}\Big(\Big\| \omega_1 \underbrace{\Big(\operatorname{Div}\boldsymbol{P} + \boldsymbol{f}\Big)}_{\mathcal{R}^{\text{hyp}}_1} \Big\|^2_{\mathcal{L}^2(\mathcal{B})} + \Big\| \omega_2 \underbrace{\Big(\boldsymbol{P}\cdot\boldsymbol{F}^T - 2\,\frac{\partial\psi(\boldsymbol{B})}{\partial\boldsymbol{B}}\cdot\boldsymbol{B}\Big)}_{\mathcal{R}^{\text{hyp}}_2} \Big\|^2_{\mathcal{L}^2(\mathcal{B})} \\ & + \Big\| \omega_3 \underbrace{\Big(\boldsymbol{P}\cdot\boldsymbol{F}^T - \boldsymbol{F}\cdot\boldsymbol{P}^T\Big)}_{\mathcal{R}^{\text{hyp}}_3} \Big\|^2_{\mathcal{L}^2(\mathcal{B})} \Big)\,, \end{aligned} \tag{5.3}$$

which is discussed in Schwarz et al. [208] based on logarithmic deformation measures for a free energy function in principal stretches, cf. Simo [212]. For convenience, the single residual equations are denoted as $\mathcal{R}^{\text{hyp}}_i$.
For the solution of the nonlinear problem, the condition $\delta_{\boldsymbol{P},\boldsymbol{u}}\mathcal{F}^{\text{hyp}}(\boldsymbol{P},\boldsymbol{u},\delta\boldsymbol{P},\delta\boldsymbol{u}) = 0$ is

considered. In order to solve this, the first variations of $\mathcal{F}^{\text{hyp}}$, with respect to $\boldsymbol{P}$ and $\boldsymbol{u}$ and for notational simplicity without the associated weightings ω_i, are determined by

$$\begin{aligned}
\delta_{\boldsymbol{P}}\mathcal{F}^{\text{hyp}} &= \int_{\mathcal{B}} \operatorname{Div}\delta\boldsymbol{P}\cdot(\operatorname{Div}\boldsymbol{P}+\boldsymbol{f})\,\mathrm{d}V \\
&+ \int_{\mathcal{B}} \Big(\delta\boldsymbol{P}\cdot\boldsymbol{F}^T\Big) : \Big(\boldsymbol{P}\cdot\boldsymbol{F}^T - 2\,\frac{\partial\psi(\boldsymbol{B})}{\partial\boldsymbol{B}}\cdot\boldsymbol{B}\Big)\,\mathrm{d}V \\
&+ \int_{\mathcal{B}} \Big(\delta\boldsymbol{P}\cdot\boldsymbol{F}^T - \boldsymbol{F}\cdot\delta\boldsymbol{P}^T\Big) : \Big(\boldsymbol{P}\cdot\boldsymbol{F}^T - \boldsymbol{F}\cdot\boldsymbol{P}^T\Big)\,\mathrm{d}V\,, \\
\delta_{\boldsymbol{u}}\mathcal{F}^{\text{hyp}} &= \int_{\mathcal{B}} \Big(\boldsymbol{P}\cdot\delta\boldsymbol{F}^T - 2\Big[\delta_{\boldsymbol{u}}\Big(\frac{\partial\psi(\boldsymbol{B})}{\partial\boldsymbol{B}}\cdot\boldsymbol{B}\Big)\Big]\Big) : \Big(\boldsymbol{P}\cdot\boldsymbol{F}^T - 2\,\frac{\partial\psi(\boldsymbol{B})}{\partial\boldsymbol{B}}\cdot\boldsymbol{B}\Big)\,\mathrm{d}V \\
&+ \int_{\mathcal{B}} \Big(\boldsymbol{P}\cdot\delta\boldsymbol{F}^T - \delta\boldsymbol{F}\cdot\boldsymbol{P}^T\Big) : \Big(\boldsymbol{P}\cdot\boldsymbol{F}^T - \boldsymbol{F}\cdot\boldsymbol{P}^T\Big)\,\mathrm{d}V\,.
\end{aligned} \tag{5.4}$$

For the given problem (5.4) the solution is sought by find $(\boldsymbol{u},\boldsymbol{P}) \in \mathcal{V}\times\mathcal{S}$ such that $\delta_{\boldsymbol{u}}\mathcal{F}^{\text{hyp}} = 0 \;\forall\; \delta\boldsymbol{u}\in\mathcal{V}$ and $\delta_{\boldsymbol{P}}\mathcal{F}^{\text{hyp}} = 0 \;\forall\; \delta\boldsymbol{P}\in\mathcal{S}$ with $\mathcal{V} := \mathcal{W}^{1,p}(\mathcal{B})$ and $\mathcal{S} := \mathcal{W}^{q}(\operatorname{div},\mathcal{B})$, see (3.5) and (3.6).

For the case of linear elasticity the approximation variables $\boldsymbol{u}$ and $\boldsymbol{\sigma}$ occur up to quadratic order. Therefore, the Sobolev space $\mathcal{W}^{1,p}$ is chosen with $p=2$, which represents the Hilbert space $\mathcal{H}^1(\mathcal{B})$. However, in hyperelastic formulations the arising order of the displacement gradient is not directly obvious, but has to be considered at least by $p\geq 2$. In consequence the Hilbert space $\mathcal{H}^1(\mathcal{B})$ is not the natural choice. For a correct representation the Sobolev space $\mathcal{W}^{1,p}$ is denoted as the function space for the displacement at finite strains. The conforming approximation functions are still chosen to be piecewise continuous polynomial functions of Lagrange type. These functions are given in $\mathcal{W}^{1,p}$ and hold for $p\geq 2$, even for $p=\infty$ and are therefore $\mathcal{L}^\infty$ integrable. The same holds for the stress variable, which occur in general only up to quadratic order and thus can be represented by the Sobolev space $\mathcal{H}(\operatorname{div},\mathcal{B})$. For a consistent presentation the function space for the stress approximation is denoted further by $\mathcal{W}^{q}(\operatorname{div},\mathcal{B})$, which is represented by Raviart-Thomas functions.

In order to apply the Newton-Raphson method to solve the nonlinear problem at hand, the linearization of (5.4) has to be computed, which reads

$$\begin{aligned}
\Delta\delta_{\boldsymbol{P}}\mathcal{F}^{\text{hyp}} &= \int_{\mathcal{B}} \operatorname{Div}\delta\boldsymbol{P}\cdot\operatorname{Div}\Delta\boldsymbol{P}\,\mathrm{d}V \\
&+ \int_{\mathcal{B}} \Big(\delta\boldsymbol{P}\cdot\Delta\boldsymbol{F}^T\Big) : \Big(\boldsymbol{P}\cdot\boldsymbol{F}^T - 2\,\frac{\partial\psi(\boldsymbol{B})}{\partial\boldsymbol{B}}\cdot\boldsymbol{B}\Big)\,\mathrm{d}V \\
&+ \int_{\mathcal{B}} \Big(\delta\boldsymbol{P}\cdot\boldsymbol{F}^T\Big) : \Big(\boldsymbol{P}\cdot\Delta\boldsymbol{F}^T - 2\Big[\Delta_{\boldsymbol{u}}\Big(\frac{\partial\psi(\boldsymbol{B})}{\partial\boldsymbol{B}}\cdot\boldsymbol{B}\Big)\Big]\Big)\,\mathrm{d}V \\
&+ \int_{\mathcal{B}} \Big(\delta\boldsymbol{P}\cdot\boldsymbol{F}^T\Big) : \Big(\Delta\boldsymbol{P}\cdot\boldsymbol{F}^T\Big)\,\mathrm{d}V \\
&+ \int_{\mathcal{B}} \Big(\delta\boldsymbol{P}\cdot\Delta\boldsymbol{F}^T - \Delta\boldsymbol{F}\cdot\delta\boldsymbol{P}^T\Big) : \Big(\boldsymbol{P}\cdot\boldsymbol{F}^T - \boldsymbol{F}\cdot\boldsymbol{P}^T\Big)\,\mathrm{d}V \\
&+ \int_{\mathcal{B}} \Big(\delta\boldsymbol{P}\cdot\boldsymbol{F}^T - \boldsymbol{F}\cdot\delta\boldsymbol{P}^T\Big) : \Big(\boldsymbol{P}\cdot\Delta\boldsymbol{F}^T - \Delta\boldsymbol{F}\cdot\boldsymbol{P}^T\Big)\,\mathrm{d}V \\
&+ \int_{\mathcal{B}} \Big(\delta\boldsymbol{P}\cdot\boldsymbol{F}^T - \boldsymbol{F}\cdot\delta\boldsymbol{P}^T\Big) : \Big(\Delta\boldsymbol{P}\cdot\boldsymbol{F}^T - \boldsymbol{F}\cdot\Delta\boldsymbol{P}^T\Big)\,\mathrm{d}V\,,
\end{aligned} \tag{5.5}$$

and

$$
\begin{aligned}
\Delta\delta_{\boldsymbol{u}}\mathcal{F}^{\text{hyp}} &= \int_{\mathcal{B}} \Big(\Delta\boldsymbol{P}\cdot\delta\boldsymbol{F}^T\Big) : \Big(\boldsymbol{P}\cdot\boldsymbol{F}^T - 2\,\frac{\partial\psi(\boldsymbol{B})}{\partial\boldsymbol{B}}\cdot\boldsymbol{B}\Big)\,\mathrm{d}V \\
&+ \int_{\mathcal{B}} \Big(\boldsymbol{P}\cdot\delta\boldsymbol{F}^T\Big) : (\Delta\boldsymbol{P}\cdot\boldsymbol{F}^T)\,\mathrm{d}V \\
&- \int_{\mathcal{B}} 2\Big[\Delta_{\boldsymbol{u}}\Big(\delta_{\boldsymbol{u}}\Big(\frac{\partial\psi(\boldsymbol{B})}{\partial\boldsymbol{B}}\cdot\boldsymbol{B}\Big)\Big)\Big] : \Big(\boldsymbol{P}\cdot\boldsymbol{F}^T - 2\,\frac{\partial\psi(\boldsymbol{B})}{\partial\boldsymbol{B}}\cdot\boldsymbol{B}\Big)\,\mathrm{d}V \\
&+ \int_{\mathcal{B}} \Big(\boldsymbol{P}\cdot\delta\boldsymbol{F}^T - 2\Big[\delta_{\boldsymbol{u}}\Big(\frac{\partial\psi(\boldsymbol{B})}{\partial\boldsymbol{B}}\cdot\boldsymbol{B}\Big)\Big]\Big) : \Big(\boldsymbol{P}\cdot\Delta\boldsymbol{F}^T - 2\Big[\Delta_{\boldsymbol{u}}\Big(\frac{\partial\psi(\boldsymbol{B})}{\partial\boldsymbol{B}}\cdot\boldsymbol{B}\Big)\Big]\Big)\,\mathrm{d}V \\
&+ \int_{\mathcal{B}} \Big(\boldsymbol{P}\cdot\delta\boldsymbol{F}^T - \delta\boldsymbol{F}\cdot\boldsymbol{P}^T\Big) : \Big(\boldsymbol{P}\cdot\Delta\boldsymbol{F}^T - \Delta\boldsymbol{F}\cdot\boldsymbol{P}^T\Big)\,\mathrm{d}V \\
&+ \int_{\mathcal{B}} \Big(\Delta\boldsymbol{P}\cdot\delta\boldsymbol{F}^T - \delta\boldsymbol{F}\cdot\Delta\boldsymbol{P}^T\Big) : \Big(\boldsymbol{P}\cdot\boldsymbol{F}^T - \boldsymbol{F}\cdot\boldsymbol{P}^T\Big)\,\mathrm{d}V \\
&+ \int_{\mathcal{B}} \Big(\boldsymbol{P}\cdot\delta\boldsymbol{F}^T - \delta\boldsymbol{F}\cdot\boldsymbol{P}^T\Big) : \Big(\boldsymbol{P}\cdot\boldsymbol{F}^T - \boldsymbol{F}\cdot\boldsymbol{P}^T\Big)\,\mathrm{d}V\,,
\end{aligned}
\tag{5.6}
$$

where the applied abbreviations, are given by

$$
\begin{aligned}
\delta_{\boldsymbol{u}}\Big(\frac{\partial\psi(\boldsymbol{B})}{\partial\boldsymbol{B}}\cdot\boldsymbol{B}\Big) &= \Big(\frac{\partial^2\psi(\boldsymbol{B})}{\partial\boldsymbol{B}\partial\boldsymbol{B}}\cdot\delta\boldsymbol{B}\Big)\cdot\boldsymbol{B} + \frac{\partial\psi(\boldsymbol{B})}{\partial\boldsymbol{B}}\cdot\delta\boldsymbol{B}\,, \\
\Delta_{\boldsymbol{u}}\Big(\frac{\partial\psi(\boldsymbol{B})}{\partial\boldsymbol{B}}\cdot\boldsymbol{B}\Big) &= \Big(\frac{\partial^2\psi(\boldsymbol{B})}{\partial\boldsymbol{B}\partial\boldsymbol{B}}\cdot\Delta\boldsymbol{B}\Big)\cdot\boldsymbol{B} + \frac{\partial\psi(\boldsymbol{B})}{\partial\boldsymbol{B}}\cdot\Delta\boldsymbol{B}\,, \\
\Delta_{\boldsymbol{u}}\Big(\delta_{\boldsymbol{u}}\Big(\frac{\partial\psi(\boldsymbol{B})}{\partial\boldsymbol{B}}\cdot\boldsymbol{B}\Big)\Big) &= \Big(\Big(\frac{\partial^3\psi(\boldsymbol{B})}{\partial\boldsymbol{B}\partial\boldsymbol{B}\partial\boldsymbol{B}}\cdot\Delta\boldsymbol{B}\Big)\cdot\delta\boldsymbol{B} + \frac{\partial^2\psi(\boldsymbol{B})}{\partial\boldsymbol{B}\partial\boldsymbol{B}}\cdot\Delta\delta\boldsymbol{B}\Big)\cdot\boldsymbol{B} \\
&+ \Big(\frac{\partial^2\psi(\boldsymbol{B})}{\partial\boldsymbol{B}\partial\boldsymbol{B}}\cdot\delta\boldsymbol{B}\Big)\cdot\Delta\boldsymbol{B} \\
&+ \Big(\Big(\frac{\partial\psi(\boldsymbol{B})}{\partial\boldsymbol{B}\partial\boldsymbol{B}}\cdot\Delta\boldsymbol{B}\Big)\cdot\delta\boldsymbol{B} + \frac{\partial\psi(\boldsymbol{B})}{\partial\boldsymbol{B}}\cdot\Delta\delta\boldsymbol{B}\Big)\,.
\end{aligned}
\tag{5.7}
$$

For completeness, the variations and linearizations of $\boldsymbol{B}$, with $\delta\boldsymbol{B}$, $\Delta\boldsymbol{B}$ and $\Delta\delta\boldsymbol{B}$, are given by $\delta\boldsymbol{B} = \delta\boldsymbol{F}\cdot\boldsymbol{F}^T + \boldsymbol{F}\cdot\delta\boldsymbol{F}^T$, $\Delta\boldsymbol{B} = \Delta\boldsymbol{F}\cdot\boldsymbol{F}^T + \boldsymbol{F}\cdot\Delta\boldsymbol{F}^T$ and $\Delta\delta\boldsymbol{B} = \delta\boldsymbol{F}\cdot\Delta\boldsymbol{F}^T + \Delta\boldsymbol{F}\cdot\delta\boldsymbol{F}^T$. The analytically derived linearized equations can also be established numerically by an automated differentiation approach, cf. Korelc [136] and Korelc and Wriggers [138]. For the implementation of the given hyperelastic least-squares formulation an automated differentiation scheme is applied in *Mathematica* utilizing the packages *AceGen* and *AceFEM*.

Note that an important point for the determination of stability points is the different approaches by the mixed LS formulation and mixed formulations leading to saddle point problems, e.g., HR and HW formulations. In mixed HR and HW formulations, the stability point is determined by a sign change of the smallest positive eigenvalue, cf., e.g., Schröder et al. [201]. This is not possible with classical LSFEM, because the system is positive (semi-) definite and thus no sign change can be analyzed in the range of eigenvalues. Therefore, stability points in LS formulations have to be determined by a minimum eigenvalue. The problem here is that an occurring stability point in mixed formulations with saddle point structure is always recognizable by the existing sign change. For LS formulations this is only recognizable for sufficiently small loading steps, since

the eigenvalue spectrum appears unchanged again after reaching the critical loading. This problem has already been discussed in, e.g., MÜLLER ET AL. [167], MÜLLER [165] and STEEGER [223].

5.2 Cantilever beam example at finite elasticity

The numerical analysis of the presented LSFEM for hyperelasticity (5.3) is performed on the example of a clamped cantilever beam with dimensions $10 \times 1\,\text{mm}$, see Figure 5.1. The Lamé parameters λ and μ in $\psi_{\text{NH}}^{\text{iso}}(\boldsymbol{B})$ are determined based on E and ν by $\lambda = E\nu/((1+\nu)(1-2\nu))$ and $\mu = E/(2+2\nu)$. The boundary value problem is clamped on the left side, loaded on the right edge with $\boldsymbol{P}\cdot\boldsymbol{N} = (0, 0.1)^T\,\text{kN/mm}^2$ and all other edges are stress-free ($\boldsymbol{P}\cdot\boldsymbol{N} = (0,0)^T\,\text{kN/mm}^2$).

Setup of BVP

Left edge:	$\boldsymbol{u} = (0,0)^T\,\text{mm}$	Young's mod.:	$E = 200\,\text{kN/mm}^2$
Right edge:	$\boldsymbol{P}\cdot\boldsymbol{N} = (0,0.1)^T\,\text{kN/mm}^2$	Poisson's ratio:	$\nu = 0.35$

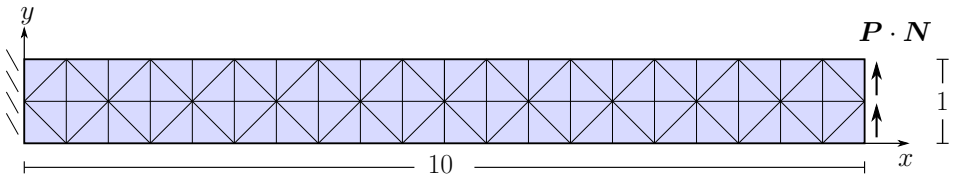

Figure 5.1: Cantilever beam example for hyperelasticity

For the given problem the solution quality, based on the polynomial order and the setup of weighting parameters is discussed as a basic for the extension to finite plasticity. The influence of functional weighting and polynomial order on the solution quality is already shown for small deformations in Chapter 4.1 and further, e.g., in SCHWARZ ET AL. [204] and SCHRÖDER ET AL. [199] for compressible and quasi-incompressible elasticity, in SCHWARZ ET AL. [207] for static and dynamic problems for quasi-incompressible behavior as well as for hyperelasticity in SCHWARZ ET AL. [208]. Here, the method is analyzed based on different weighting parameter setups, by varying choices for ω_3, and for different polynomial orders $\mathcal{RT}_m\mathcal{P}_k$ with $m \geq 0$ and $k = m+1$. The balancing of the polynomial orders for displacement and stress approximation are chosen to give an optimal convergence order for the LS functional, at least from a theoretical point of view, cf. Chapter 3.5. As mentioned before, optimal convergence order can only be achieved for regular problems, cf. RÖSSLE [194].
The chosen approximations are given by linear to cubic functions for $\boldsymbol{u}$ and $\boldsymbol{P}$. Here, both fields are approximated by the same order of complete polynomials with $\mathcal{RT}_m\mathcal{P}_k$ elements of order $m = 0, 1, 2$ and $k = 1, 2, 3$. In Figure 5.2 the results for a displacement convergence of the top corner node $(10, 1)$ in y-direction and the convergence of the presented LS functional $\mathcal{F}$ (5.3) are displayed. The displacement convergence of the LSFEM is compared to a quadratic displacement element $\mathcal{P}_2$.
For all considered LS elements $\mathcal{RT}_m\mathcal{P}_k$ a satisfying solution is achievable, at least for weighting factors $\omega_3 \geq 5/\mu$. The special weighting of the stress symmetry condition lead to an improvement, especially for the lowest order element $\mathcal{RT}_0\mathcal{P}_1$. The poor performance

of lowest order elements is already mentioned as a disadvantages of LSFEM. This is especially illustrated for the $\mathcal{RT}_0\mathcal{P}_1$ using $\omega_3 = 0$ in Figure 5.2, which gives a formulation only with respect to the balance of momentum and constitutive equation. This behavior can also be seen in the convergence of the functional. Here only for mesh levels with $neq > 80000$ a decrease of the error can be observed. At least for an increasing factor ω_3 the convergences for displacements and LS functional are improved. Furthermore, the $\mathcal{RT}_0\mathcal{P}_1$ element leads for the extended LS formulation, i.e., $\omega_3 > 1/\mu$, a sufficient error convergence at least for refined mesh levels. This shows that even for a simple problem, the consideration of weightings is essential for solution quality and convergence behavior.

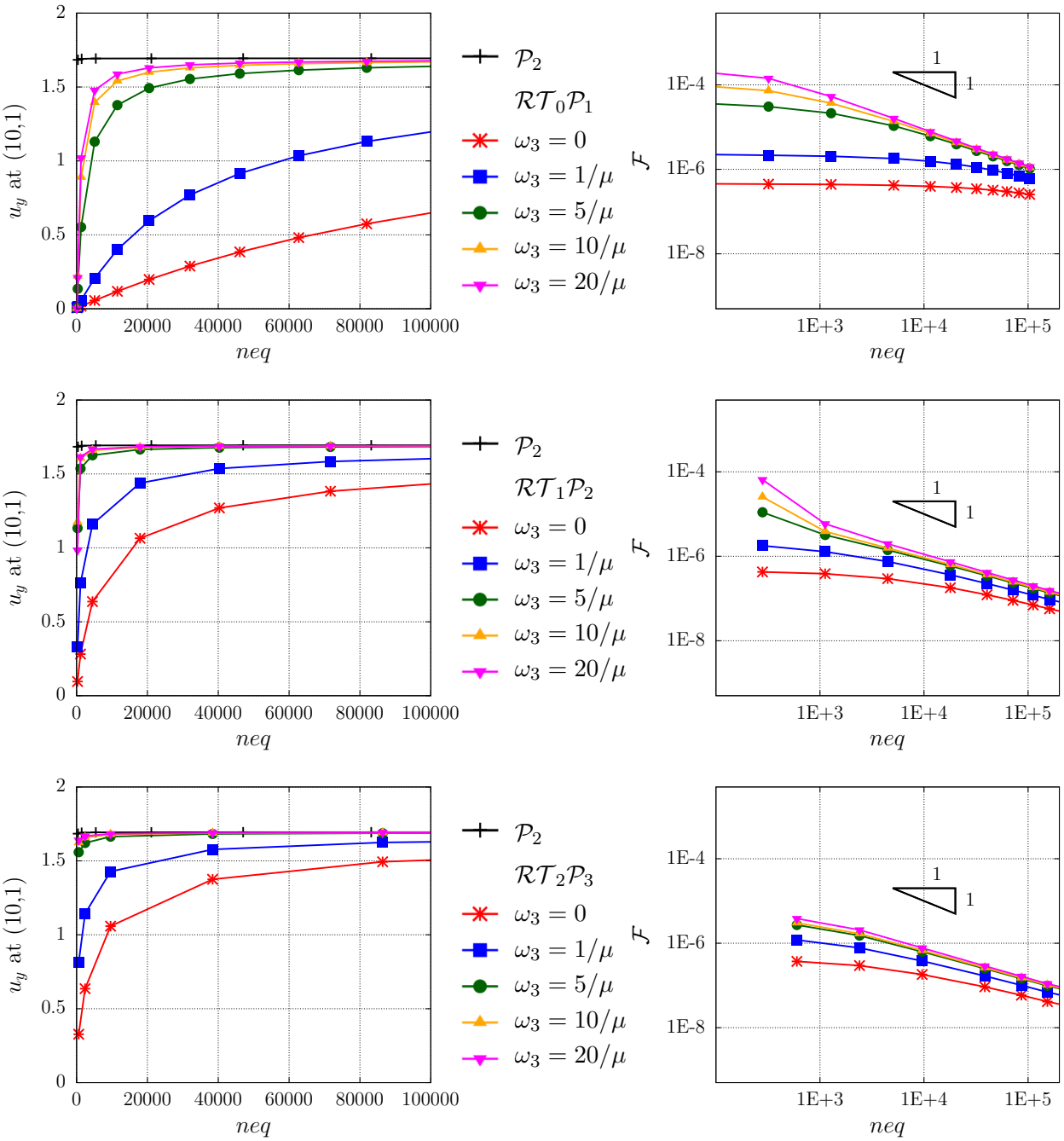

Figure 5.2: Convergence of u_y-displacement (left) and LS functional $\mathcal{F}$ for varying weights ω_3 and different $\mathcal{RT}_m\mathcal{P}_k$ elements ($m = 0, 1, 2$; $k = 1, 2, 3$) under plane strain condition

However, the crucial impact of the weights for the stress symmetry condition is reduced by elements with higher polynomial orders, i.e., $m \geq 1$ and $k \geq 2$. Nevertheless, these elements also show a poorer functional convergence for $\omega_3 = 0$, which also holds for $\omega_3 = 1/\mu$ at coarse mesh densities. For the weights $\omega_3 > 10/\mu$ no improvement for the displacement and functional convergence is reached. Nevertheless, also for higher polynomial orders a weighting is unavoidable. This impression is further verified by the functional convergence on the right side of Figure 5.2. Therein, the convergence of $\mathcal{F}$ with $\omega_3 = 0$ is clearly reduced, especially for the low order element. An increasing convergence is reached with respect to the mesh level and the choice of $\omega_3 \geq 1/\mu$ up to a limitation, which is based on the underlying boundary value problem and regular mesh refinement.
Furthermore, the fulfillment of symmetric stress measures is demonstrated for the Kirchhoff stresses. Therefore, the non-symmetric stresses are determined by $\tau_{\text{asym}} = \int_{\mathcal{B}} \tau_{12} - \tau_{21} \, \mathrm{d}V$. The results are given in Figure 5.3 for $\omega_3 = 0$ and $\omega_3 = 10/\mu$. It can be seen directly that the balance of angular momentum is not sufficiently fulfilled for any element combination applying $\omega_3 = 0$, even for mesh levels with $neq \geq 50000$. For $\omega_3 = 10/\mu$ all elements show a satisfying solution already for mesh levels $neq < 20000$. The performance of the presented formulation yield to similar behavior for all analyzed values. Based on these results, an extended formulation with additional weighting on the stress symmetry condition is preferable, especially for low order elements. Furthermore, elements with higher polynomial order are recommended, i.e., $m \geq 1$ and $k \geq 2$.

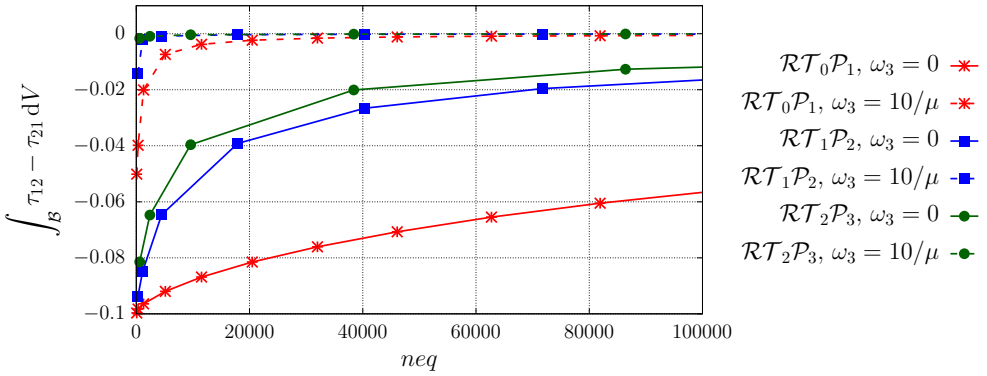

Figure 5.3: Evolution of τ_{asym} for $\omega_3 = 0, 10/\mu$ for $\mathcal{RT}_m\mathcal{P}_k$ $(m = 0, 1, 2;\ k = 1, 2, 3)$

A similar approach as in the small strain case for the parameter $\omega_2 \leq 1$, cf. Chapter 4.1, is applied to the unsatisfying solutions of the $\mathcal{RT}_0\mathcal{P}_1$ and $\mathcal{RT}_1\mathcal{P}_2$ elements with $\omega_3 = 0, 1/\mu$, see Figure 5.4 and 5.5. Here, the choice of $\omega_2 < 1$ directly yield an improvement for the results, if the extended formulation is used. For $\omega_3 = 0$ an additional weighting of the constitutive equation leads to no improvement in the convergence of the functional or the displacement convergence. From a continuum mechanical point of view, the stronger fulfillment of the balance of angular momentum (e.g. $\boldsymbol{\tau} = \boldsymbol{\tau}^T$) in consequence yields to a stronger fulfillment of the balance of linear momentum. Furthermore, the improved stress symmetry enforcement is depicted for the analyzed weighting setup in Figure 5.6. Therein, the fulfillment of $\boldsymbol{\tau} = \boldsymbol{\tau}^T$ is unaffected and only by considering the extended LS formulation the results are strongly improved. The weighting of the constitutive equation with a parameter $\omega_2 < 1$ yield to a stronger enforcement of the balance of linear momentum under consideration of an extended LS formulation. Further ideas on this are presented in Müller et al. [167], by a weighting of the balance of linear momentum or a scaling of the boundary value problem to a smaller length scale, in order to improve the fulfillment of the momentum balance by regarding the dimension of the boundary value problem.

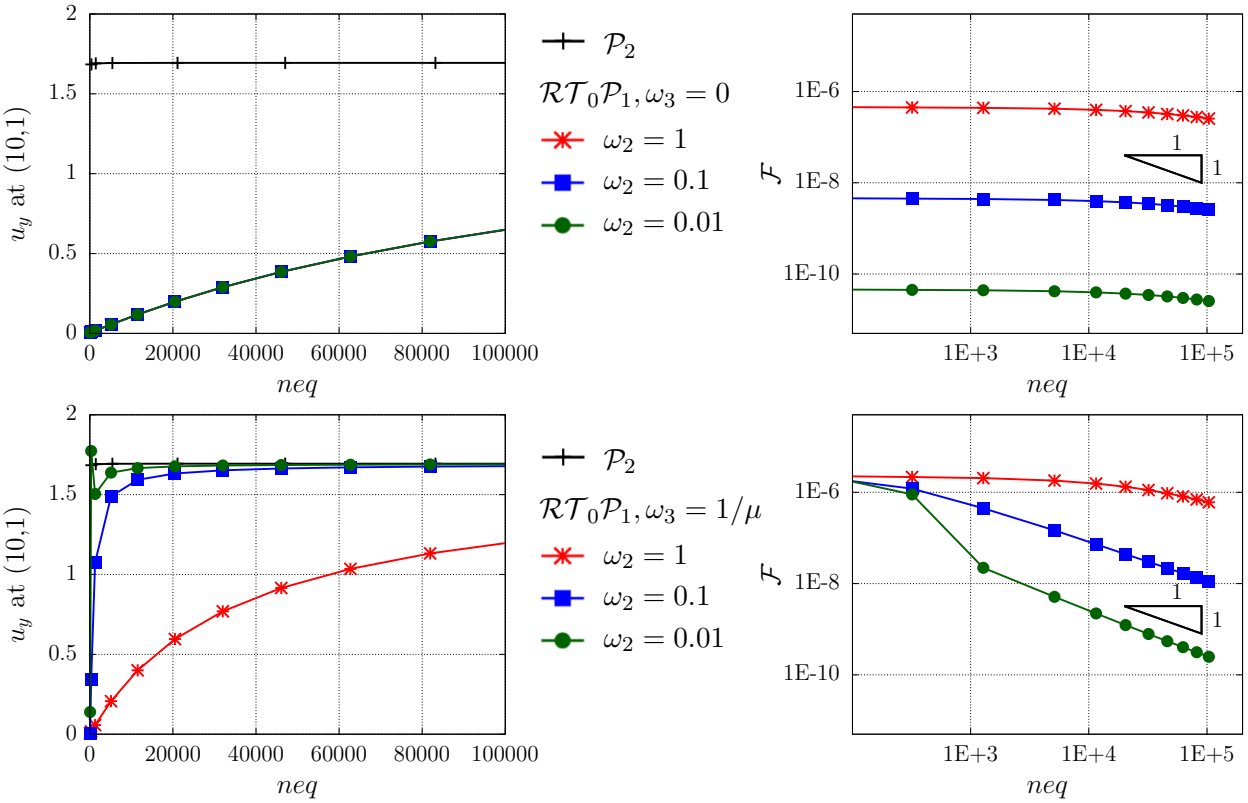

Figure 5.4: Convergence of u_y-displacement (left) and $\mathcal{F}$ (right) with $\omega_3 = 0$ (top) and $\omega_3 = 1/\mu$ (bottom) for $\omega_2 \leq 1$ for a $\mathcal{RT}_0\mathcal{P}_1$ element

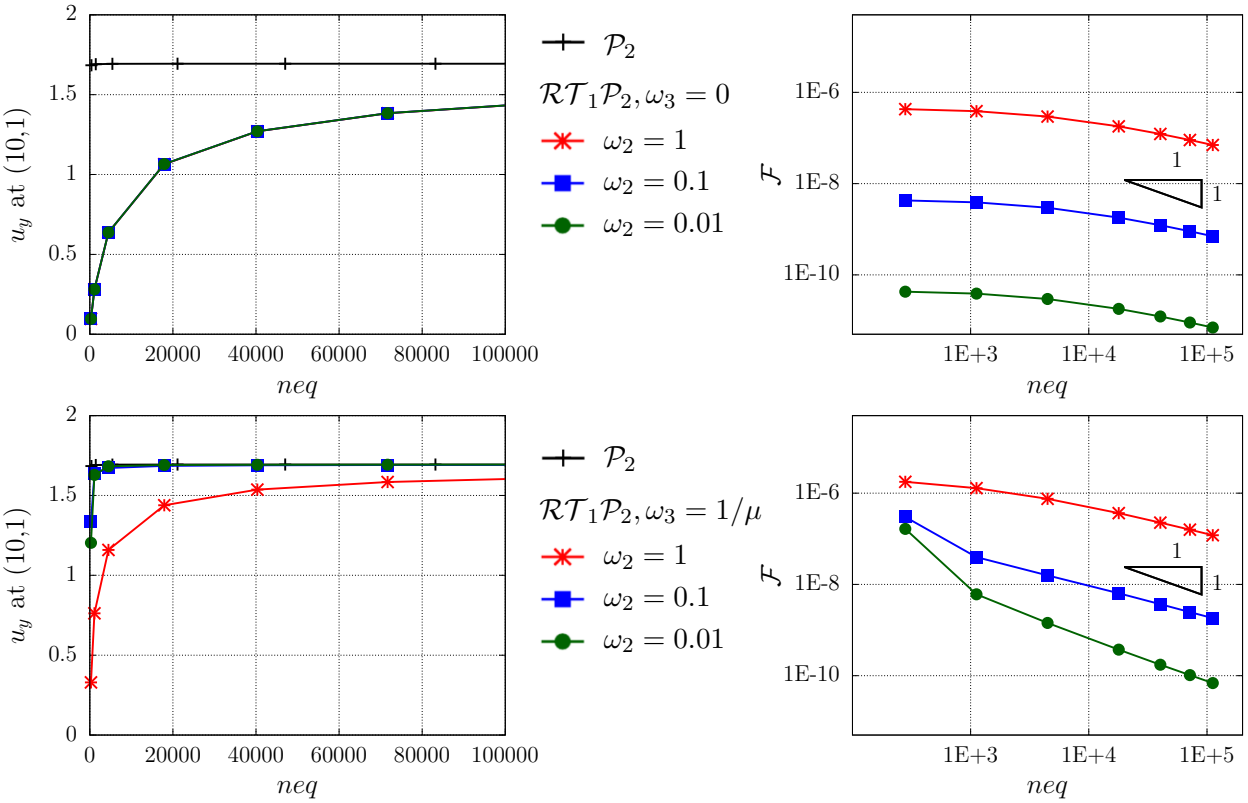

Figure 5.5: Convergence of u_y-displacement (left) and $\mathcal{F}$ (right) with $\omega_3 = 0$ (top) and $\omega_3 = 1/\mu$ (bottom) for $\omega_2 \leq 1$ for a $\mathcal{RT}_1\mathcal{P}_2$ element

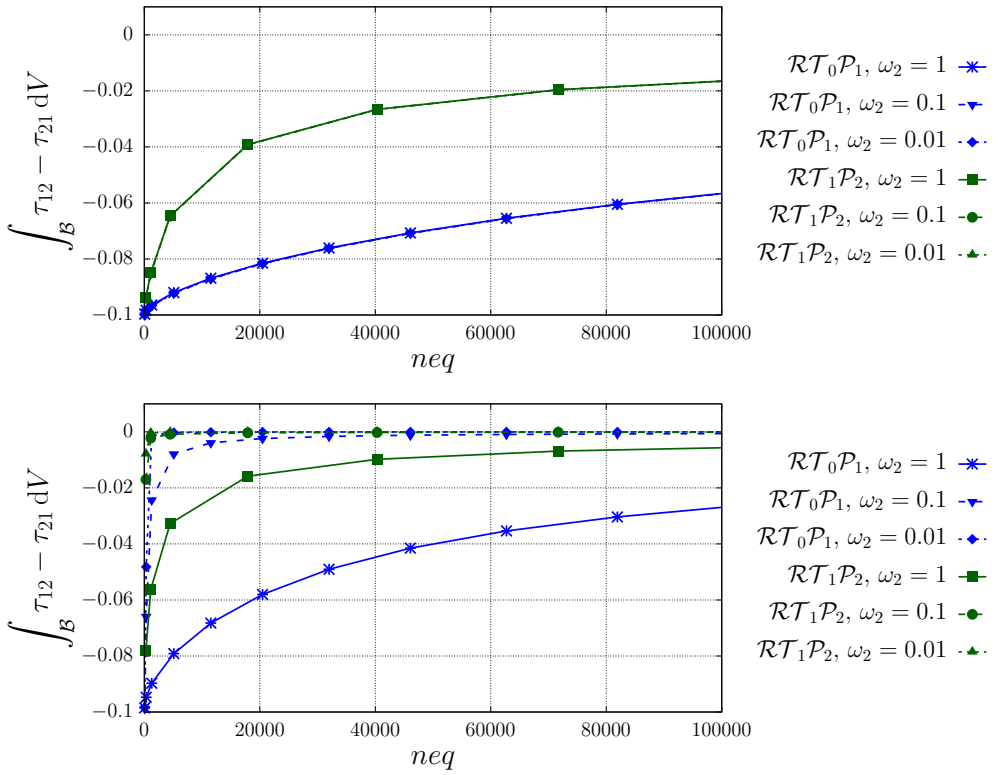

Figure 5.6: Convergence of τ_{asym} for $\mathcal{RT}_m\mathcal{P}_k$ with $\omega_3 = 0$ (top) and $\omega_3 = 1/\mu$ (bottom)

5.3 Hyperelastic least-squares formulation under plane stress condition

Furthermore, an incremental algorithmic treatment for the plane stress condition is analyzed, following the approach in De Borst [85] and Klinkel and Govindjee [134]. For the work conjugate pair $(\boldsymbol{P}, \boldsymbol{F})$, see (2.46), the relation $\boldsymbol{P} = \partial\psi/\partial\boldsymbol{F}$ holds and follows with respect to the Clausius-Duhem inequality. Since an incremental algorithmic treatment is applied for the nonlinear process, the stress-strain relation has to be linearized. This yields

$$\Delta\boldsymbol{P} = \bar{\mathbb{D}} : \Delta\boldsymbol{F} \quad \text{with} \quad \bar{\mathbb{D}} = \frac{\partial^2\psi}{\partial\boldsymbol{F}\partial\boldsymbol{F}}\,, \tag{5.8}$$

with the material tangent modulus $\bar{\mathbb{D}}$. The modification of the stress quantity, by enforcing $P_{33} = 0$, implies a simultaneous modification of the stress-strain relation and the material tangent moduli for the plane stress case, see Klinkel and Govindjee [134] for a detailed description and Chapter 4.9 for a similar approach. The iteration procedure is being applied on $F_z = F_{33}$ to guarantee $P_z = P_{33} \overset{!}{=} 0$ with a vector representation of the incremental constitutive equation. A Taylor series expansion for the enforced stress quantity P_z, neglecting higher order terms, leads

$$P_z^{(i+1)} = P_z^{(i)} + \frac{\partial P_z^{(i)}}{\partial F_z^{(i)}}\,\Delta F_z \overset{!}{=} 0 \quad \Rightarrow \quad \Delta F_z = -\left(\frac{\partial P_z^{(i)}}{\partial F_z^{(i)}}\right)^{-1} P_z^{(i)} = -\bar{\mathbb{D}}_{zz}^{(i)-1}\, P_z^{(i)}\,, \tag{5.9}$$

with i as the number of local iterations. The necessary modification of the tangent modulus can be determined following the approach of an incremental vector representation as proposed in Klinkel and Govindjee [134] and applied for small strain elasto-plasticity in Chapter 4.9. Since the formulation is implemented in *Mathematica* using the *AceGen* and *AceFEM* package, an automated differentiation approach is applied, cf., e.g.,

Korelc [136; 137] and Korelc and Wriggers [138]. For the modification of the material tangent, the dependence of the variables to be deduced must be stored, which are here given with respect to the deformation gradient $\boldsymbol{F}$. This dependence results in the associated tangent modulus and gives the related first variation and linearization by automated differentiation. The algorithmic procedure is shown schematically in Table 5.1. Here, the stresses $\boldsymbol{P}$ are determined based on the smmetric stress tensor $\boldsymbol{\tau}$ with $\boldsymbol{P} = 2\,\partial_{\boldsymbol{B}}\psi(\boldsymbol{B}) \cdot \boldsymbol{B} \cdot \boldsymbol{F}^{-T}$.

Table 5.1: Algorithmic treatment for a hyperelastic, plane stress LS element

ELEMENT LOOP

(1) Update displacements and stresses (Newton iteration k+1)

$\boldsymbol{d}_u = \boldsymbol{d}_{u,n}^{(k)} + \Delta\boldsymbol{d}_u$, $\boldsymbol{d}_\sigma = \boldsymbol{d}_{\sigma,n}^{(k)} + \Delta\boldsymbol{d}_\sigma$

INTEGRATION LOOP

(2) Compute stresses $\boldsymbol{P}$ and displacements $\boldsymbol{u}$ at each Gauss Point:

$\boldsymbol{P} = \mathbb{S}\,\boldsymbol{d}_\sigma$ and $\boldsymbol{u} = \mathbb{N}_u\,\boldsymbol{d}_u$ and read from history: ∇u_{33}

CONSTITUTIVE LOOP

SUBITERATION (i as local iteration number)

(.1) Compute $\boldsymbol{F} = \boldsymbol{I} + \nabla\boldsymbol{u}$ and $\boldsymbol{B} = \boldsymbol{F} \cdot \boldsymbol{F}^T$

$\boldsymbol{P} = 2\,\partial_{\boldsymbol{B}}\psi(\boldsymbol{B}) \cdot \boldsymbol{B} \cdot \boldsymbol{F}^{-T}$

(.2) If $|P_z^{(i)}| \leq tol$ Exit SUBITERATION

(.3) If $n_{\text{iter}} > n_{\max}$ Then stop iteration

(.4) Update: $F_z^{(i+1)} = F_z^{(i)} - \bar{\mathbb{D}}_{zz}^{(i)-1}\, P_z^{(i)}$ with $\bar{\mathbb{D}}_{zz}^{(i)} = \partial P_z^{(i)} / \partial F_z^{(i)}$

(3) Save to history: $\nabla u_{33} = F_z - 1$

(4) Compute single functional parts and exit CONSTITUTIVE LOOP

(5) Determine and export right hand side and element stiffness matrix

5.4 Numerical validation of the plane stress subiteration

For the validation of the plane stress algorithm at finite elasticity the well-known Cook's membrane problem is analyzed, see Cook [81]. The problem is characterized by a clamped left side and a constant shear load $\boldsymbol{P} \cdot \boldsymbol{N} = (0, 20)^T$ N/mm^2 on the right side, see Figure 5.7. The material setup and boundary conditions are taken from the benchmark collection of Schröder et al. [202].

The results for the displacement convergence u_y at the node $(48, 60)$ for the hyperelastic LS elements $\mathcal{RT}_m\mathcal{P}_k$ for varying polynomial degrees m and k under plane stress conditions are compared to a quadratic displacement element $\mathcal{P}_2$, see Figure 5.8. Here, the weighting setups are given with $\omega_i = \{1, 1/\mu, 0\}$ and $\omega_i = \{1, 1/\mu, 10/\mu\}$ to illustrate the dependence of the solution accuracy on the weights. Both weighting setups converge to the reference solution, but only the extended formulation (i.e., $\omega_3 \neq 0$) yield satisfying results, at least for higher order elements, and the weak performance of the lowest order elements is clearly visible. Additionally $\mathcal{RT}_0\mathcal{P}_2$ and $\mathcal{RT}_1\mathcal{P}_3$ elements are chosen, which do not provide an optimal convergence rate. For both elements the chosen order of the stress approximation limits the theoretically possible convergence rate. Nevertheless, since the

System setup:			
Left edge:	$\boldsymbol{u}$	$=$	$(0,0)^T$ mm
Right edge:	$\boldsymbol{P}\cdot\boldsymbol{N}$	$=$	$(0,20)^T$ N/mm^2
Young's modulus:	E	$=$	500 N/mm^2
Poisson's ratio:	ν	$=$	0.35
Lamé's parameter:	λ	$=$	432.099 N/mm^2
	μ	$=$	185.185 N/mm^2

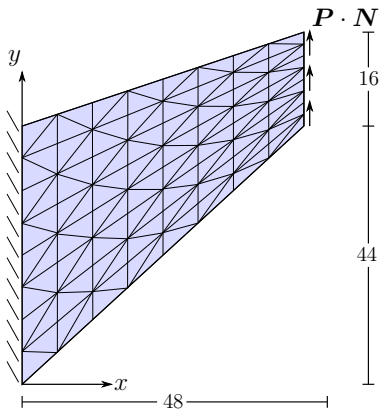

Figure 5.7: Material parameters, boundary conditions and geometry of Cook's membrane

optimal convergence rate can only be obtained for regular problems and the Cook's membrane is known to be a non-regular problem, the choice of $\mathcal{RT}_0\mathcal{P}_2$ and $\mathcal{RT}_1\mathcal{P}_3$ does not affect the achievable rates for this problem. However, in general, this must be taken into account when choosing the polynomial degree of the elements. The application of these two elements is motivated only by an improvement of the convergence in the displacement quantities, which is shown in Figure 5.8.

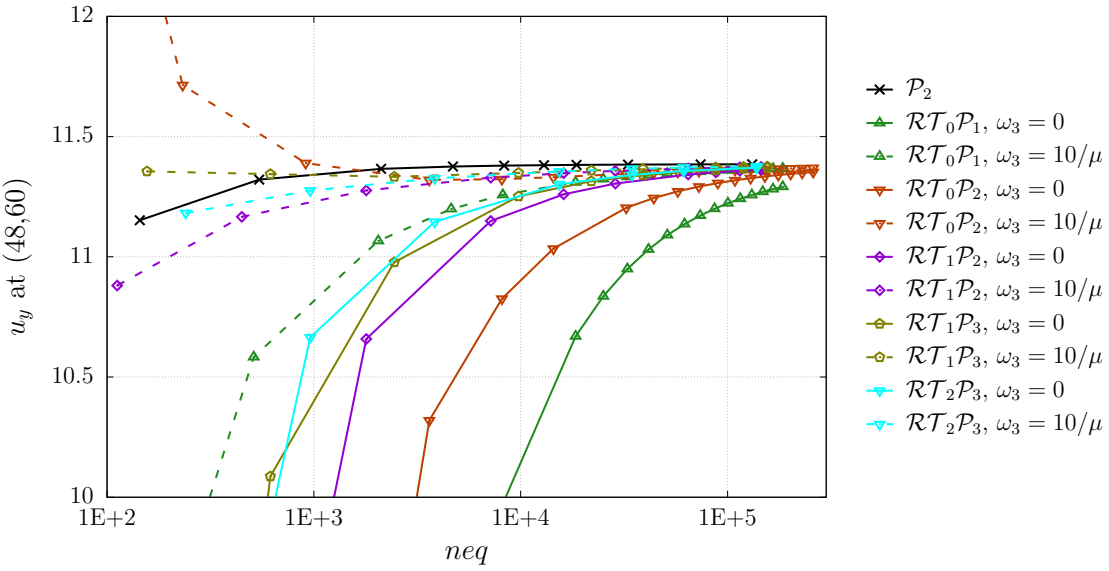

Figure 5.8: Displacement convergence u_y at (48,60) with $\omega_3 = 0, 10/\mu$

Furthermore, the convergence of the LS functional (5.3) is depicted in Figure 5.9. Therein, all element formulations yield to quite similar convergence rates of approximately $0.7-0.8$ independent of the polynomial order, see Table 5.2, 5.3 and 5.4. These results do not correspond to the theoretically possible convergence order, see Chapter 3.5, which can be estimated by the chosen polynomial degree and in dependence of the solution regularity. The limitation of the convergence order is given by the considered boundary value problem, where the solution of the continuous problem is less regular based on the geometry and the applied boundary conditions, cf. Rössle [194]. For a more regular problem, related to the Cook's membrane, the load application and the angle between Dirichlet and Neumann boundaries have to be changed, which is investigated by, e.g., Kober and Starke [135] and Bertrand et al. [35]. The application of adaptive mesh refinement, which avoid unnecessary refinements in terms of the functional error, would also yield a limitation in

the rates, since the problem description itself limit the rates.

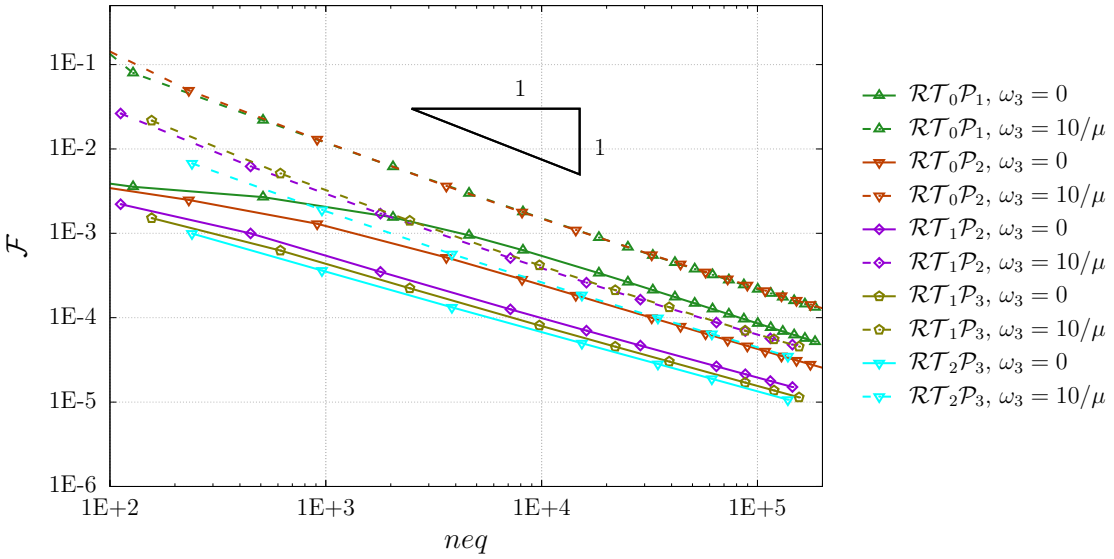

Figure 5.9: $\mathcal{F}^{\text{hyp}}$ convergence for $\mathcal{RT}_m\mathcal{P}_k$ with $m = 0, 1, 2$, $k = 1, 2, 3$ and $\omega_3 = 0, 10/\mu$

Furthermore, the resulting values for the u_y displacement at $(48, 60)$, the functional $\mathcal{F}$, the balance of linear momentum and the stress symmetry ($|\boldsymbol{\tau}_{\text{as}}| = \int_{\mathcal{B}} |\tau_{12} - \tau_{21}| \, \mathrm{d}V$) are listed in Table 5.2, 5.3 and 5.4 for some of the applied elements. The values show that solely the convergence of the complete functional is unaffected by the raising polynomial degree, as denoted previously. For the other terms, higher accuracies are achieved with increasing element order. Here, the reference solution $u_{y,\text{ref}}$ is taken from SCHRÖDER ET AL. [202] with $u_{y,\text{ref}} = 11.381135\,\text{mm}$.

Table 5.2: Results for Cook's membrane with classical LS formulation using a $\mathcal{RT}_0\mathcal{P}_1$

$\mathcal{RT}_0\mathcal{P}_1$	neq	$\lvert u_y - u_{y,\text{ref}}\rvert$	$\mathcal{F}$	(order)	$\lVert \operatorname{Div} \boldsymbol{P}\rVert_{\mathcal{L}^2(\mathcal{B})}$	$\lvert\boldsymbol{\tau}_{\text{as}}\rvert$
$\omega_3 = 0$	32	9.4848 E-0	4.6649 E-3	(-)	2.1489 E-5	1.9766 E+1
	128	8.7602 E-0	3.5652 E-3	(0.1939)	1.4050 E-5	1.7594 E+1
	512	6.8585 E-0	2.6865 E-3	(0.2041)	8.0209 E-6	1.3868 E+1
	2048	3.7435 E-0	1.5458 E-3	(0.3987)	2.6995 E-6	8.1529 E-0
	8192	1.3991 E-0	6.2996 E-4	(0.6475)	1.0519 E-6	3.4036 E-0
$\omega_3 = 10/\mu$	32	3.9281 E-0	2.6583 E-1	(-)	2.2688 E-2	4.2602 E-0
	128	1.9284 E-0	7.9375 E-2	(0.8719)	1.9983 E-3	1.1303 E-0
	512	7.9850 E-1	2.1868 E-2	(0.9299)	1.7132 E-4	2.9969 E-1
	2048	3.1519 E-1	6.1433 E-3	(0.9159)	1.7608 E-5	8.3419 E-2
	8192	1.2359 E-1	1.7954 E-3	(0.8874)	5.1561 E-6	2.4719 E-2

It might not be practical to apply higher order elements to all kind of problems, if only the convergence of the functional is analyzed, because the rate is by far not optimal for most of the cases, since often non-regular problems are discussed. Furthermore, higher order elements are more time consuming in the computation due to the increasing number of equations. Nevertheless, from an engineering point of view, also values at particular points are of special interest, e.g., for the dimensioning of structural components. The results for higher order elements are often more accurate for coarse meshes and the influence of weights is reduced, see Figure 5.2 and 5.10.

Table 5.3: Results for Cook's membrane with classical LS formulation using a $\mathcal{RT}_1\mathcal{P}_2$

$\mathcal{RT}_1\mathcal{P}_2$	*neq*	$\lvert u_y - u_{y,\mathrm{ref}}\rvert$	$\mathcal{F}$	(order)	$\lVert \mathrm{Div}\, \boldsymbol{P}\rVert_{\mathcal{L}^2(\mathcal{B})}$	$\lvert \boldsymbol{\tau}_{\mathrm{as}}\rvert$
$\omega_3 = 0$	112	5.8407 E-0	2.2112 E-3	(-)	7.6084 E-6	1.2906 E+1
	448	2.3588 E-0	9.9732 E-4	(0.5743)	2.4649 E-6	6.5023 E-0
	1792	7.2274 E-1	3.4936 E-4	(0.7567)	4.3532 E-7	2.4397 E-0
	7168	2.3201 E-1	1.2566 E-4	(0.7376)	6.8761 E-8	9.0464 E-1
	28672	7.6368 E-2	4.6753 E-5	(0.7132)	2.3103 E-8	3.4099 E-1
$\omega_3 = 10/\mu$	112	5.0048 E-1	2.6312 E-2	(-)	4.2386 E-4	4.2342 E-1
	448	2.1477 E-1	6.2176 E-3	(1.0406)	2.9828 E-5	9.5475 E-2
	1792	1.0520 E-1	1.7117 E-3	(0.9305)	3.0381 E-6	2.6394 E-2
	7168	5.1841 E-2	5.1009 E-4	(0.8733)	4.1417 E-7	8.2169 E-3
	28672	2.3695 E-2	1.6398 E-4	(0.8186)	1.4246 E-7	2.8280 E-3

Table 5.4: Results for Cook's membrane with classical LS formulation using a $\mathcal{RT}_2\mathcal{P}_3$

$\mathcal{RT}_2\mathcal{P}_3$	*neq*	$\lvert u_y - u_{y,\mathrm{ref}}\rvert$	$\mathcal{F}$	(order)	$\lVert \mathrm{Div}\, \boldsymbol{P}\rVert_{\mathcal{L}^2(\mathcal{B})}$	$\lvert \boldsymbol{\tau}_{\mathrm{as}}\rvert$
$\omega_3 = 0$	240	2.2692 E-0	9.9405 E-4	(-)	2.6839 E-6	6.5322 E-0
	960	7.1623 E-1	3.6277 E-4	(0.7271)	4.8462 E-7	2.5085 E-0
	3840	2.3544 E-1	1.3279 E-4	(0.7249)	7.7649 E-8	9.4239 E-1
	15360	7.8967 E-2	4.9879 E-5	(0.7063)	1.1883 E-8	3.5524 E-1
	61440	2.4256 E-2	1.8906 E-5	(0.6998)	3.8898 E-9	1.3251 E-1
$\omega_3 = 10/\mu$	240	1.9914 E-1	6.7589 E-3	(-)	4.3167 E-5	9.6731 E-2
	960	1.0544 E-1	1.8976 E-3	(0.9163)	4.4147 E-6	2.8197 E-2
	3840	5.5051 E-2	5.6736 E-4	(0.8709)	5.8971 E-7	9.0387 E-3
	15360	2.5693 E-2	1.8539 E-4	(0.8068)	9.3682 E-8	3.1300 E-3
	61440	9.7979 E-3	6.4289 E-5	(0.7639)	3.2202 E-8	1.1163 E-3

For completeness and further investigations, the cantilever beam example in Figure 5.1 is also considered under plane stress condition exemplarily for the $\mathcal{RT}_0\mathcal{P}_1$ element, see Figure 5.10. The depicted results for the convergence of the functional and the displacement u_y at the particular point $(10, 1)$ are in accordance with the plane strain case and confirm these results. In contrast to the additional weighting with $\omega_2 < 1$ for the plane strain case, see Figure 5.4 and 5.5, a further approach is presented to improve the solution accuracy and functional convergence, especially for the lowest order elements.

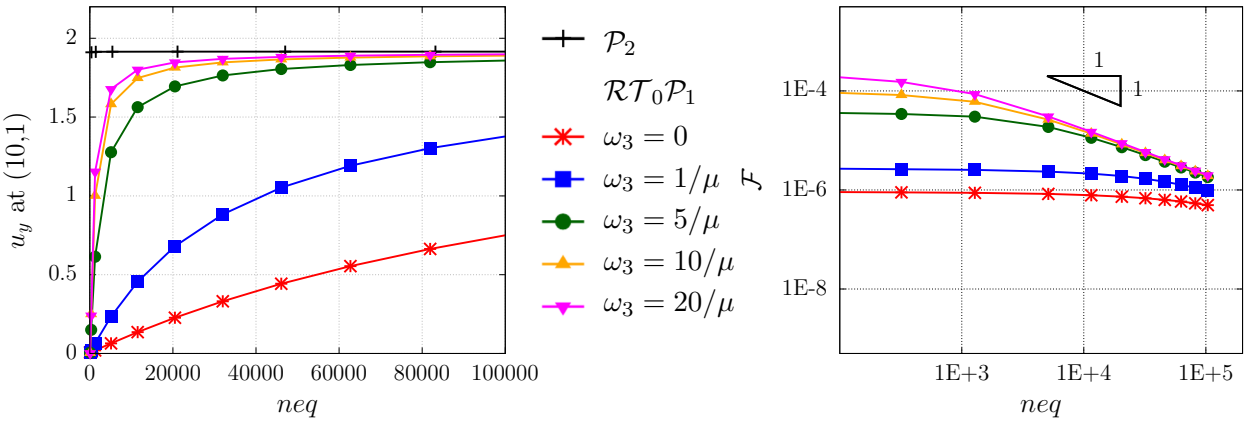

Figure 5.10: Convergence of u_y-displacement (left) and LS functional $\mathcal{F}$ (right) for $\mathcal{RT}_0\mathcal{P}_1$ with varying ω_3 under plane stress condition

5.5 Asymmetric least-squares formulation for finite elasticity

As already discussed for the small strain framework, the classical least-squares formulation with a stress approximation using Raviart-Thomas functions can be improved with respect to the fulfillment of the balance of angular momentum. This formulations are denoted by extended formulations and are characterized by the extension of the functional by an additional mathematically redundant residual equation, see (4.3), while maintaining the classical LS approach. In addition to an extended functional in (4.8) and (5.3), an approach based on the idea of a so-called modified first variation is applied, cf. SCHWARZ ET AL. [205], STARKE ET AL. [221] for linear elasticity, SCHWARZ ET AL. [208] for hyperelasticity and IGELBÜSCHER ET AL. [119] for finite plasticity.
The resulting modified first variation is denoted by $\delta_{\boldsymbol{P},\boldsymbol{u}}\mathcal{G}(\boldsymbol{P},\boldsymbol{u})$ and motivated by a scalar multiplication of a symmetric stress measure $\boldsymbol{\Sigma}_{\mathrm{sym}}$ and an asymmetric defined tensor function $\boldsymbol{H}_{\mathrm{as}}(\delta\boldsymbol{u})$ in terms of the displacement test function. Therefore, the modification, denoted by $\delta_{\boldsymbol{u}}\tilde{\mathcal{G}}$, is only introduced in the first variation with respect to the displacement field $(5.4)_1$ and yield the modified first variations

$$\delta_{\boldsymbol{u}}\mathcal{G} := \delta_{\boldsymbol{u}}\mathcal{F}^{\mathrm{hyp}} + \delta_{\boldsymbol{u}}\tilde{\mathcal{G}}(\boldsymbol{H}_{\mathrm{as}}(\delta\boldsymbol{u}),\boldsymbol{\Sigma}_{\mathrm{sym}}) \quad \text{and} \quad \delta_{\boldsymbol{P}}\mathcal{G} := \delta_{\boldsymbol{P}}\mathcal{F}^{\mathrm{hyp}}\,. \tag{5.10}$$

A suitable approach for $\boldsymbol{\Sigma}_{\mathrm{sym}}$ is any symmetric stress measure, here, e.g., the Kirchhoff stress $\boldsymbol{\tau} = \boldsymbol{P}\cdot\boldsymbol{F}^T$ is considered. The tensor function $\boldsymbol{H}_{\mathrm{as}}(\delta\boldsymbol{u})$ is chosen as the antisymmetric gradient of the displacement test functions with respect to the actual configuration with

$$\nabla^{\mathrm{as}}_{,x}(\delta\boldsymbol{u}) = \frac{1}{2}\left(\nabla_{,x}(\delta\boldsymbol{u}) - (\nabla_{,x}(\delta\boldsymbol{u}))^T\right)\,. \tag{5.11}$$

The resulting modified first variation $\delta_{\boldsymbol{u}}\mathcal{G}$ of formulation (5.3), introducing $\delta_{\boldsymbol{u}}\tilde{\mathcal{G}}$, yields

$$\delta_{\boldsymbol{u}}\mathcal{G} = \delta_{\boldsymbol{u}}\mathcal{F}^{\mathrm{hyp}} \underbrace{- \int_{\mathcal{B}} \nabla^{\mathrm{as}}_{,x}(\delta\boldsymbol{u}) : \frac{1}{\mu}\left(\boldsymbol{P}\cdot\boldsymbol{F}^T - 2\frac{\partial\psi}{\partial\boldsymbol{B}}\cdot\boldsymbol{B}\right)\mathrm{d}V}_{\delta_{\boldsymbol{u}}\tilde{\mathcal{G}}} \quad \text{and} \quad \delta_{\boldsymbol{P}}\mathcal{G} := \delta_{\boldsymbol{P}}\mathcal{F}^{\mathrm{hyp}}\,. \tag{5.12}$$

Here, the factor $1/\mu$ is considered as a physical weighting parameter. It has to be mentioned that this approach not result in a classical LSFEM, since the resulting system of equation is unsymmetric based on the introduced modified first variation only for the displacement field. However, for a decreasing characteristic element length $h_{\mathrm{e}} \to 0$ it holds $\boldsymbol{P}\cdot\boldsymbol{F}^T = \boldsymbol{F}\cdot\boldsymbol{P}^T$ and thus the modification results to zero, which gives the classical LSFEM approach with $\delta_{\boldsymbol{u}}\mathcal{G} = \delta_{\boldsymbol{u}}\mathcal{F}$. This approach additionally controls the fulfillment of the balance of angular momentum, similar to the extended LS approach, which lead simultaneously to an improved convergence of the balance of linear momentum, as shown in SCHWARZ ET AL. [205] and STARKE ET AL. [221].
Obviously, the modified formulation lead to a non-symmetric system, because the modification is only applied to the first variation with respect to the displacement field, which yields for the system matrices $\boldsymbol{k}_{uP} \neq \boldsymbol{k}_{Pu}^T$. Thus preconditioner have to be used in order to apply iterative solvers to the system, see, e.g., FABER ET AL. [97], ARNOLD ET AL. [7] and HIPTMAIR AND XU [115]. The resulting unsymmetric system does not necessarily lead to a deviation from positive definiteness, since a real square matrix $\boldsymbol{A}$, which is not necessarily symmetric, is positive definite if its symmetric part $\boldsymbol{A}_s = 1/2(\boldsymbol{A}+\boldsymbol{A}^T)$ is positive definite. Applying this assumption, the positive definiteness can be still fulfilled for the

symmetric part of the resulting system matrix and thus also the asymmetric formulation can be positive definite. Furthermore, the system leads to a fully occupied matrix system and therefore the stability requirements of saddle point problems must not be taken into account. The well-posedness of the approach is discussed in STARKE ET AL. [221] for linear elasticity.

5.6 Numerical validation of the asymmetric least-squares formulation

In the following, the modified LS formulation is investigated for the previous boundary value problems to obtain a direct comparability. The results for the modified approach applied to the Cook's membrane problem, with the setup given in Figure 5.7, are shown in Figure 5.11. Here, satisfying solution depending on the number of equations is reached for all $\mathcal{RT}_m\mathcal{P}_k$ elements. The modified formulation yields, especially for the lowest order element with $\omega_3 = 0$ a significant improvement. However, the comparison of the classical and modified LS approach for a $\mathcal{RT}_0\mathcal{P}_1$ with $\omega = 10/\mu$ show no further improvement within the displacement convergence. This behavior is obviously given for all comparisons of classical and modified formulations, where for $\omega_3 = 0$ an improvement is obtained and for $\omega_3 = 10/\mu$ the results are quite unaffected by the additional modification, see Figure 5.8. Therefore, it seem to be sufficient to apply either the extended formulation with proper weights for ω_3 or the modified formulation in order to achieve reliable and efficient formulations.
The convergences of the modified LS functionals in Figure 5.12 show no improvement and thus confirm the previous statement regarding the limitation of the convergence order based on the boundary value problem. Each functional converge with the order of $\approx 0.7 - 0.8$ as it is presented in Table 5.5, 5.6 and 5.7 and the same holds for the $\mathcal{RT}_0\mathcal{P}_2$ and $\mathcal{RT}_1\mathcal{P}_3$ elements. Based on the non-regular problem description, cf. RÖSSLE [194].

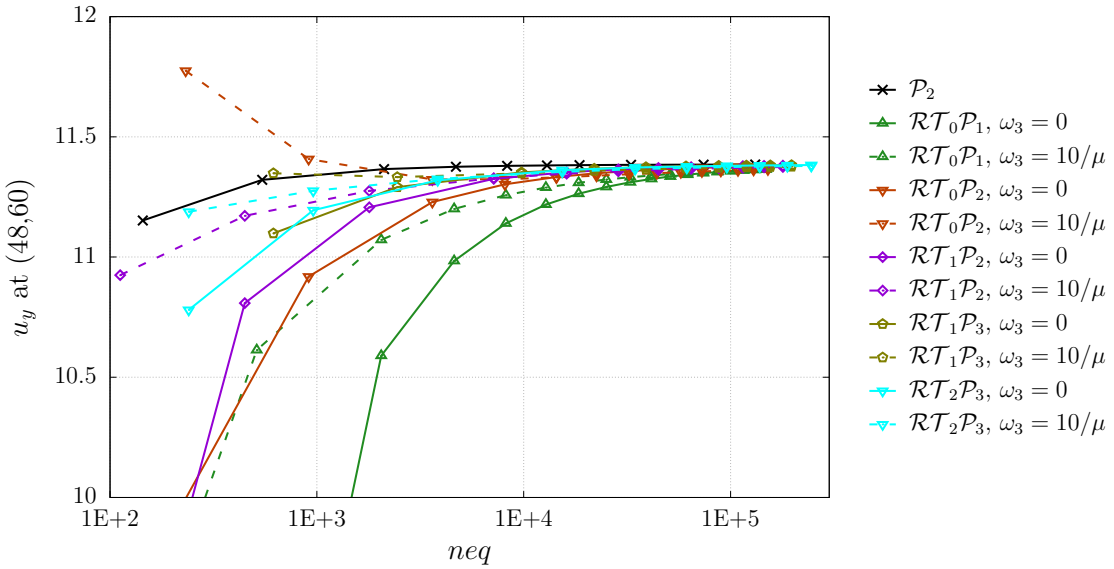

Figure 5.11: Displacement convergence u_y at (48,60) with $\omega_3 = 0, 10/\mu$

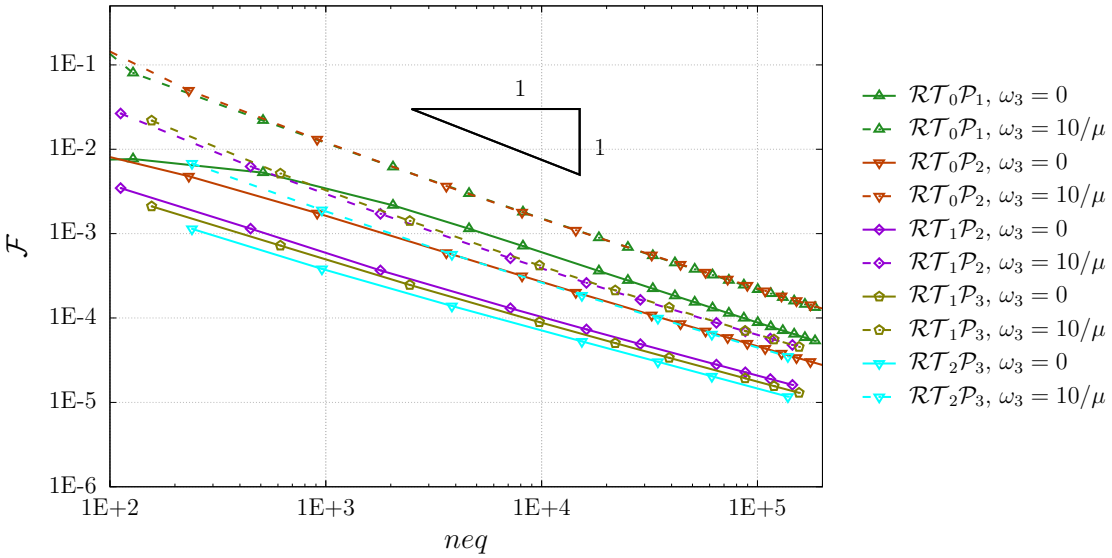

Figure 5.12: Convergence of modified LS functional for the Cook's membrane using $\mathcal{RT}_m\mathcal{P}_k$ elements with $m = 0, 1, 2$, $k = 1, 2, 3$ and $\omega_3 = 0, 10/\mu$

Table 5.5: Results for Cook's membrane with modified LS formulation using a $\mathcal{RT}_0\mathcal{P}_1$

$\mathcal{RT}_0\mathcal{P}_1$	neq	$\lvert u_y - u_{y,\mathrm{ref}}\rvert$	$\mathcal{F}$	(order)	$\lVert \mathrm{Div}\, \boldsymbol{P}\rVert_{\mathcal{L}^2(\mathcal{B})}$	$\lvert \boldsymbol{\tau}_{\mathrm{as}}\rvert$
$\omega_3 = 0$	32	7.8987 E-0	7.2522 E-3	(-)	1.6628 E-5	1.6662 E+1
	128	5.2813 E-0	7.6660 E-3	(0.0401)	6.7330 E-6	1.1667 E+1
	512	2.3612 E-0	5.2789 E-3	(0.2691)	1.5964 E-6	5.8396 E-0
	2048	7.9181 E-1	2.1664 E-3	(0.6425)	2.7301 E-7	2.3031 E-0
	8192	2.4131 E-1	7.1116 E-4	(0.8035)	4.4526 E-8	8.4577 E-1
$\omega_3 = 10/\mu$	32	3.6093 E-0	2.6867 E-1	(-)	2.2612 E-2	4.2258 E-0
	128	1.8195 E-0	8.0042 E-2	(0.8735)	1.9471 E-3	1.1122 E-0
	512	7.6817 E-1	2.1967 E-2	(0.9327)	1.6491 E-4	2.9391 E-1
	2048	3.0951 E-1	6.1593 E-3	(0.9173)	1.7002 E-5	8.1819 E-2
	8192	1.2355 E-1	1.7983 E-3	(0.8881)	2.1836 E-6	2.4288 E-2

Table 5.6: Results for Cook's membrane with modified LS formulation using a $\mathcal{RT}_1\mathcal{P}_2$

$\mathcal{RT}_1\mathcal{P}_2$	neq	$\lvert u_y - u_{y,\mathrm{ref}}\rvert$	$\mathcal{F}$	(order)	$\lVert \mathrm{Div}\, \boldsymbol{P}\rVert_{\mathcal{L}^2(\mathcal{B})}$	$\lvert \boldsymbol{\tau}_{\mathrm{as}}\rvert$
$\omega_3 = 0$	112	1.9455 E-0	3.4633 E-3	(-)	1.7854 E-6	5.3965 E-0
	448	5.7299 E-1	1.1462 E-3	(0.7976)	4.7030 E-7	2.2379 E-0
	1792	1.7424 E-1	3.6701 E-4	(0.8215)	8.2703 E-8	8.7115 E-1
	7168	5.5736 E-2	1.3051 E-4	(0.7458)	1.3647 E-8	3.4369 E-1
	28672	1.6799 E-2	4.8994 E-5	(0.7068)	2.2661 E-9	1.3757 E-1
$\omega_3 = 10/\mu$	112	4.5642 E-1	2.6517 E-2	(-)	4.1512 E-4	4.1499 E-1
	448	2.0977 E-1	6.2509 E-3	(1.0424)	2.9331 E-5	9.3479 E-2
	1792	1.0612 E-1	1.7180 E-3	(0.9317)	2.9942 E-6	2.5890 E-2
	7168	5.3220 E-2	5.1147 E-4	(0.8740)	4.0896 E-7	8.0842 E-3
	28672	2.4624 E-2	1.6427 E-4	(0.8193)	6.7851 E-8	2.7911 E-3

For completeness, the example of the cantilever beam, Figure 5.1, is analyzed for the plane stress case under consideration of the modified LS formulation. The results show for all investigated elements that the influence of weighting factors ω_3 is significantly

Table 5.7: Results for Cook's membrane with modified LS formulation using a $\mathcal{RT}_2\mathcal{P}_3$

$\mathcal{RT}_2\mathcal{P}_3$	*neq*	$\lvert u_y - u_{y,\mathrm{ref}}\rvert$	$\mathcal{F}$	(order)	$\lVert \operatorname{Div} \boldsymbol{P}\rVert_{\mathcal{L}^2(\mathcal{B})}$	$\lvert \boldsymbol{\tau}_{\mathrm{as}}\rvert$
$\omega_3 = 0$	240	6.0086 E-1	1.1404 E-3	(-)	6.0329 E-7	2.4356 E-0
	960	1.8635 E-1	3.8241 E-4	(0.7882)	1.0284 E-7	9.5589 E-1
	3840	6.1647 E-2	1.3885 E-4	(0.7308)	1.6865 E-8	3.7852 E-1
	15360	1.9468 E-2	5.2823 E-5	(0.6972)	2.8006 E-9	1.5167 E-1
	61440	4.2097 E-3	2.0428 E-5	(0.6853)	4.6948 E-10	6.1170 E-2
$\omega_3 = 10/\mu$	240	1.9295 E-1	6.7983 E-3	(-)	4.2523 E-5	9.4615 E-2
	960	1.0557 E-1	1.9046 E-3	(0.9178)	4.3591 E-6	2.7672 E-2
	3840	5.6125 E-2	5.6887 E-4	(0.8717)	5.8292 E-7	8.8999 E-3
	15360	2.6510 E-2	1.8572 E-4	(0.8075)	9.2849 E-8	3.0925 E-3
	61440	1.0288 E-2	6.4361 E-5	(0.7645)	1.4786 E-8	1.1060 E-3

reduced or non-existent, see Figure 5.13. This is in clear contrast to the results under plane strain and plane stress conditions for the classical LS approach in Figure 5.2 and 5.10. The functional convergences of the classical and modified LS approach are depicted in Figure 5.13 (right). Here, both formulations show the same convergence properties for finer meshes ($h_{\mathrm{e}} \to 0$) with different weights. A clear difference is perceptible for the $\mathcal{RT}_0\mathcal{P}_1$ element. It can be seen already for coarse meshes that for the plane stress case the modified formulations with $\omega_3 = 0$ directly yield the same behavior as the formulations with $\omega_3 > 1/\mu$, see Figure 5.13 (top). This behavior occurs for a $\mathcal{RT}_0\mathcal{P}_1$ element for the classical formulations only for weights with $\omega_3 \geq 10/\mu$, cf. Figure 5.2 and 5.10. Therefore, an additional weighting with $\omega_2 \leq 1$, as shown in Figure 5.4 and 5.5 is unnecessary for the modified formulation. These findings are taken into account for the extension of the formulation to finite plasticity.

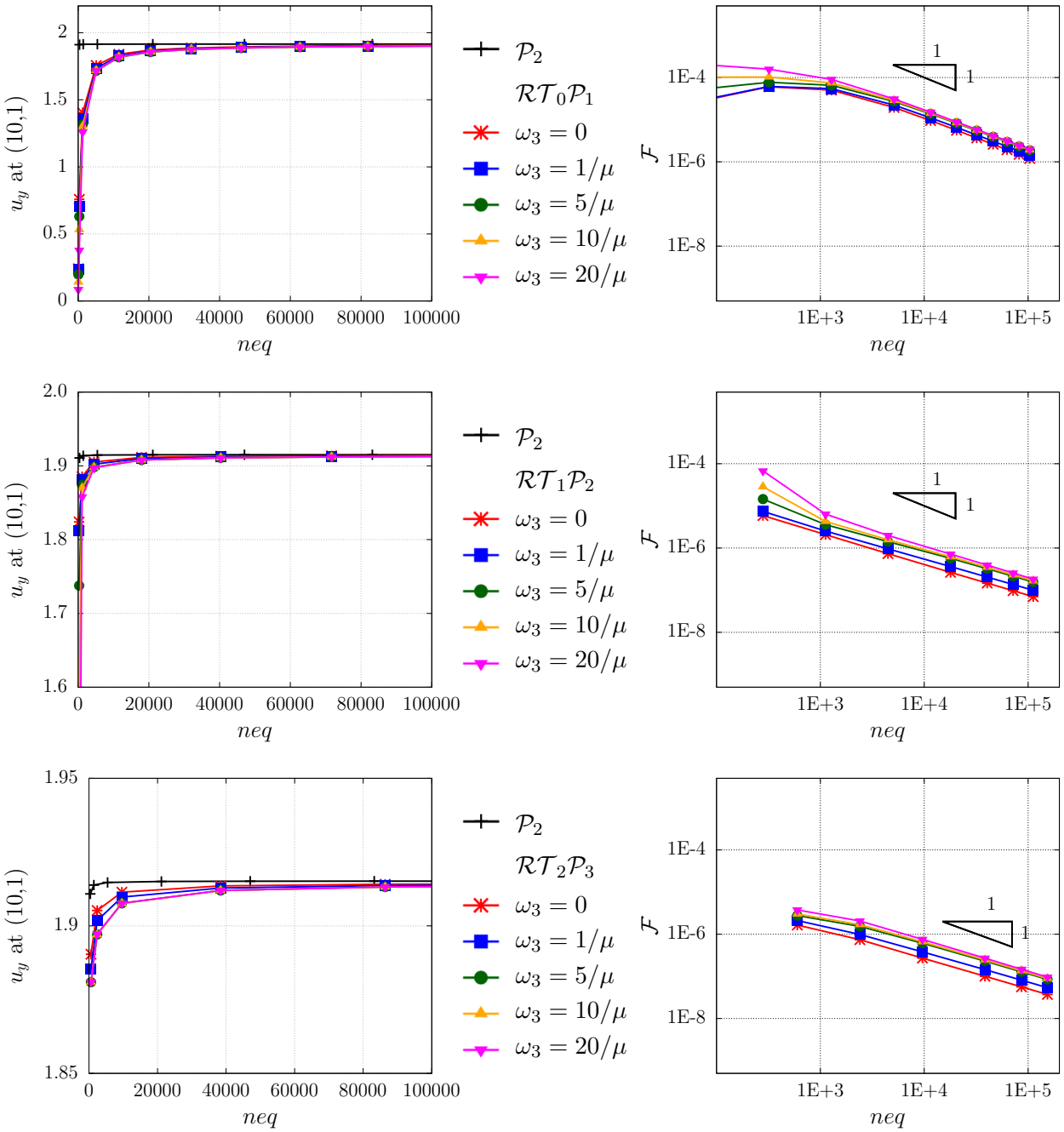

Figure 5.13: Cantilever beam convergence of u_y-displacement (left) and LS functional $\mathcal{F}$ for varying weights ω_3 and different $\mathcal{RT}_m\mathcal{P}_k$ elements ($m = 0, 1, 2$; $k = 1, 2, 3$) for the modified formulation

5.7 Least-squares formulation for rate-independent finite J_2-plasticity

The previous findings for the LSFEM at finite elasticity are extended to the field of rate-independent finite J_2-plasticity. Here, the continuum mechanical relations presented in Chapter 2.5.3 are taken into account as a foundation for the discussion. The theory of plasticity has been analyzed in detail over the past decades and is presented in several monographs, see, e.g., the textbooks of Hill [113], Lubliner [154], Maugin [161] and Han and Reddy [105]. Furthermore, the following presentations are mainly based on the literature of Simo [210; 211; 212; 213], Simo and Miehe [215], Weber and Anand [232], Eterovic and Bathe [96], Simo and Hughes [214] and de Souza Neto et al. [86], to which a great impact must be attributed.
For the framework of elasto-plasticity, the approximation of the stress values are an important aspect, since the stresses determine the evolution of plastic material response. Therefore, a direct approximation of the stresses as an unknown variable, by applying mixed methods, seems to be promising for modeling plastic material behavior. The results presented below for finite J_2-plasticity are originally published in Igelbüscher et al. [119; 121]. Furthermore, an analyses for LSFEM at small strain plasticity is given in Kwon et al. [143], Starke [219; 220], Kubitz [142] and Schwarz [203]. Some of these publications illustrate a drawback for the application of the LSFEM at rate-independent plasticity. The problem becomes visible in the solution of the system of equations, e.g., through oscillations in the application of the standard Newton-Raphson method and thus none or only inaccurate solutions are obtained. This effect is due to the non-smooth material law in elasto-plasticity, occurring at the transition from purely elastic to elasto-plastic material behavior. Therefore, the resulting functional includes kink-like points, which lead in consequence to discontinuities within the first variation. For visualizations of the oscillatory effects, see the works of Kubitz [142] and Schwarz [203]. In Kubitz [142] a smoothing algorithm is presented and in Starke [220] a generalized Newton approach is used for the efficient solution of the elasto-plastic problem as a nonlinear and non-smooth algebraic problem. Furthermore, adaptive refinement strategies are applied in Starke [219; 220] and Kwon et al. [143] introduce elasto-plasticity for a meshfree least-squares method.
For the mixed Hellinger-Reissner formulation the described drawback does not occur, since the weak form remains unchanged for elasticity and plasticity, and a straightforward approach lead a consistent system, see Chapter 4.5. Furthermore, a LS formulation for rate-dependent plasticity solve the issue by the nature of the formulation which allows overstresses and therefore, the transition of elastic and plastic material results not in such kink-like points, cf. Schwarz et al. [204].
The described disadvantage is here solved by the construction of a continuous first variation in terms of a modification. Therefore, the formulation (5.3) is taken into account as a basis. For the elastic material description a hyperelastic isotropic Neo-Hookean material, cf. (2.57), is considered with the elastic free energy $\psi_{\mathrm{NH}}^{e,\mathrm{iso}}(\boldsymbol{B}^e)$ as

$$\psi_{\mathrm{NH}}^{e,\mathrm{iso}}(\boldsymbol{B}^e) := \frac{\lambda}{4}\left(I_3(\boldsymbol{B}^e) - 1\right) + \frac{\mu}{2}(I_1(\boldsymbol{B}^e) - 3) - \left(\frac{\lambda}{2} + \mu\right) \ln\sqrt{I_3(\boldsymbol{B}^e)}\,, \tag{5.13}$$

in dependence of the elastic left Cauchy-Green deformation tensor $\boldsymbol{B}^e$. Note that it is defined by means of the multiplicative decomposition of the deformation gradient $\boldsymbol{F} = \boldsymbol{F}^e \cdot \boldsymbol{F}^p$ and given through the relation of $\boldsymbol{B}^e = \boldsymbol{F}^e \cdot \boldsymbol{F}^{e\,T} = \boldsymbol{F} \cdot \boldsymbol{C}^{p\,-1} \cdot \boldsymbol{F}^T$ with

$\boldsymbol{C}^{p-1} = \boldsymbol{F}^{p-1} \cdot \boldsymbol{F}^{p-T}$, see Chapter 2.5.3. The difference to (5.3) is given by the deformation tensor $\boldsymbol{B}^e$, which is no longer a pure displacement related variable as in $\boldsymbol{B} = \boldsymbol{F} \cdot \boldsymbol{F}^T$, since it is dependent on the plastic deformation tensor $\boldsymbol{C}^{p-1}$ and therefore, also on the stress tensor $\boldsymbol{P}$. The investigated material law is determined by the symmetric Kirchhoff stresses $\boldsymbol{\tau}$ with $\boldsymbol{\tau} = 2\,\partial_{\boldsymbol{B}^e}\psi^{e,\mathrm{iso}}_{\mathrm{NH}}(\boldsymbol{B}^e) \cdot \boldsymbol{B}^e$, see (2.79). Consequently, the elasto-plastic mixed LS functional $\mathcal{F}^{\mathrm{ep}}(\boldsymbol{P}, \boldsymbol{u})$, with $\psi = \psi^{e,\mathrm{iso}}_{\mathrm{NH}}(\boldsymbol{B}^e)$, cf. Igelbüscher et al. [119; 121], is defined by

$$\begin{aligned} \mathcal{F}^{\mathrm{ep}}(\boldsymbol{P}, \boldsymbol{u}) &= \frac{1}{2}\Big(\Big\| \omega_1 \underbrace{(\operatorname{Div} \boldsymbol{P} + \boldsymbol{f})}_{\mathcal{R}^{\mathrm{ep}}_1} \Big\|^2_{\mathcal{L}^2(\mathcal{B})} + \Big\| \omega_2 \underbrace{\Big(\boldsymbol{P} \cdot \boldsymbol{F}^T - 2\,\frac{\partial \psi}{\partial \boldsymbol{B}^e} \cdot \boldsymbol{B}^e \Big)}_{\mathcal{R}^{\mathrm{ep}}_2} \Big\|^2_{\mathcal{L}^2(\mathcal{B})} \\ &+ \Big\| \omega_3 \underbrace{(\boldsymbol{P} \cdot \boldsymbol{F}^T - \boldsymbol{F} \cdot \boldsymbol{P}^T)}_{\mathcal{R}^{\mathrm{ep}}_3} \Big\|^2_{\mathcal{L}^2(\mathcal{B})} \Big) . \end{aligned} \tag{5.14}$$

For reasons of simplicity, the weighting factors of the respective residual equations are omitted in the following, but are still relevant for the performance and accuracy of the formulation. The nonlinear minimization problem is solved utilizing $\delta_{\boldsymbol{P},\boldsymbol{u}}\mathcal{F}^{\mathrm{ep}}(\boldsymbol{P}, \boldsymbol{u}, \delta\boldsymbol{P}, \delta\boldsymbol{u}) = 0$. Therefore, the associated first variations of $\mathcal{F}^{\mathrm{ep}}$ with respect to $\boldsymbol{P}$ and $\boldsymbol{u}$ read

$$\begin{aligned} \delta_{\boldsymbol{P}}\mathcal{F}^{\mathrm{ep}} &= \int_{\mathcal{B}} \operatorname{Div} \delta\boldsymbol{P} \cdot (\operatorname{Div} \boldsymbol{P} + \boldsymbol{f})\, \mathrm{d}V \\ &+ \int_{\mathcal{B}} \Big(\delta\boldsymbol{P} \cdot \boldsymbol{F}^T - 2 \Big[\delta_{\boldsymbol{P}} \Big(\frac{\partial \psi}{\partial \boldsymbol{B}^e} \cdot \boldsymbol{B}^e \Big) \Big] \Big) : \Big(\boldsymbol{P} \cdot \boldsymbol{F}^T - 2\,\frac{\partial \psi}{\partial \boldsymbol{B}^e} \cdot \boldsymbol{B}^e \Big)\, \mathrm{d}V \\ &+ \int_{\mathcal{B}} (\delta\boldsymbol{P} \cdot \boldsymbol{F}^T - \boldsymbol{F} \cdot \delta\boldsymbol{P}^T) : (\boldsymbol{P} \cdot \boldsymbol{F}^T - \boldsymbol{F} \cdot \boldsymbol{P}^T)\, \mathrm{d}V , \\ \delta_{\boldsymbol{u}}\mathcal{F}^{\mathrm{ep}} &= \int_{\mathcal{B}} \Big(\boldsymbol{P} \cdot \delta\boldsymbol{F}^T - 2 \Big[\delta_{\boldsymbol{u}} \Big(\frac{\partial \psi}{\partial \boldsymbol{B}^e} \cdot \boldsymbol{B}^e \Big) \Big] \Big) : \Big(\boldsymbol{P} \cdot \boldsymbol{F}^T - 2\,\frac{\partial \psi}{\partial \boldsymbol{B}^e} \cdot \boldsymbol{B}^e \Big)\, \mathrm{d}V \\ &+ \int_{\mathcal{B}} (\boldsymbol{P} \cdot \delta\boldsymbol{F}^T - \delta\boldsymbol{F} \cdot \boldsymbol{P}^T) : (\boldsymbol{P} \cdot \boldsymbol{F}^T - \boldsymbol{F} \cdot \boldsymbol{P}^T)\, \mathrm{d}V . \end{aligned} \tag{5.15}$$

Based on the properties of the given formulation (5.15) the solution is sought by find $(\boldsymbol{u}, \boldsymbol{P}) \in \mathcal{V} \times \mathcal{S}$ such that $\delta_{\boldsymbol{u}}\mathcal{F}^{\mathrm{ep}} = 0 \;\forall\; \delta\boldsymbol{u} \in \mathcal{V}$ and $\delta_{\boldsymbol{P}}\mathcal{F}^{\mathrm{ep}} = 0 \;\forall\; \delta\boldsymbol{P} \in \mathcal{S}$, where the function spaces are given by $\mathcal{V} := \mathcal{W}^{1,p}(\mathcal{B})$ and $\mathcal{S} := \mathcal{W}^{q}(\mathrm{div}, \mathcal{B})$, see (3.5) and (3.6).
The before mentioned drawback arising by the straightforward application of a mixed LS formulation for rate-independent elasto-plasticity becomes visible in (5.15) compared to (5.4). It is based on the non-smoothness of the constitutive relation, occurring at the transition from purely elastic to elasto-plastic material behavior, which can lead to problems within the minimization scheme, e.g., with the standard Newton-Raphson method, cf. Schwarz [203] and Igelbüscher et al. [119]. The non-smooth relation could lead to kink-like points in the functional and furthermore to a discontinuous first variation. For guaranteeing a continuous first variation and overcome the resulting discontinuity, an unsymmetric formulation is constructed, which leaves the underlying system of differential equations unchanged. In order to ensure continuity, either if pure elasticity or plasticity occurs in the formulation, a modification of the plastic deformation tensor $\boldsymbol{C}^{p-1}$ within the stress and displacement test space is introduced. This is done based on the consideration at the transition from elastic to elasto-plastic material reactions. For convenience the

plastic right Cauchy-Green deformation tensor with respect to the implicit exponential time integration, cf. Weber and Anand [232] and Eterovic and Bathe [96], is here presented again with

$$\boldsymbol{C}^{p\,-1} = \boldsymbol{F}^{-1} \cdot \exp\Big[-2\,\Delta_t\gamma\,\boldsymbol{n}\Big] \cdot \boldsymbol{F} \cdot \boldsymbol{C}_n^{p\,-1}\,,$$

as given in (2.86) and derived in Chapter 2.5.3. Thus, $\boldsymbol{B}^e$ can be defined as

$$\boldsymbol{B}^e = \boldsymbol{F} \cdot \boldsymbol{C}^{p-1} \cdot \boldsymbol{F}^T = \boldsymbol{F} \cdot \Big(\boldsymbol{F}^{-1} \cdot \exp\Big[-2\,\Delta_t\gamma\,\boldsymbol{n}\Big] \cdot \boldsymbol{F} \cdot \boldsymbol{C}_n^{p\,-1}\Big) \cdot \boldsymbol{F}^T\,, \tag{5.16}$$

where $\Delta_t\gamma$ and $\boldsymbol{n} = \partial_{\boldsymbol{\tau}}\Phi(\boldsymbol{\tau}, \alpha)$ are stress dependent variables. The discontinuity within the first variation originates in the constitutive relation, in the variation of the plastic strains depending on the Kirchhoff stresses $\boldsymbol{\tau}$ defined in (2.79). Thus the critical point is defined by $\boldsymbol{B}^e$ as a pure displacement function $\tilde{\boldsymbol{B}}^e(\boldsymbol{u})$ and a function of displacements and stresses $\boldsymbol{B}^e(\boldsymbol{P}, \boldsymbol{u})$. For an obvious illustration of this statement, a case distinction is performed, where $\lim\limits_{\Phi\,\to\,0^-}$ describes an elastic material state with $\Phi < 0$ and $\lim\limits_{\Phi\,\to\,0^+}$ an elasto-plastic material state in which the yield surface is exceeded. The elastic left Cauchy-Green tensor for the purely elastic case is further denoted by $\tilde{\boldsymbol{B}}^e$, i.e.,

$$\boldsymbol{B}^e = \boldsymbol{F} \cdot \boldsymbol{C}_n^{p-1} \cdot \boldsymbol{F}^T := \tilde{\boldsymbol{B}}^e(\boldsymbol{u}) \quad \text{for} \quad \lim_{\Phi\,\to\,0^-}\,, \tag{5.17}$$

which is solely a function of the displacement field $\boldsymbol{u}$, since $\boldsymbol{C}_n^{p\,-1}$ consists of previously calculated (history) values and thus, is considered as a constant parameter within the derivatives of $\boldsymbol{B}^e$ with respect to $\boldsymbol{P}$. For arising plasticity $\boldsymbol{B}^e$ is defined by

$$\boldsymbol{B}^e = \boldsymbol{F} \cdot \boldsymbol{C}_{n+1}^{p-1} \cdot \boldsymbol{F}^T \quad \text{for} \quad \lim_{\Phi\,\to\,0^+}\,. \tag{5.18}$$

Here, the index $n+1$ is explicitly given for $\boldsymbol{C}^{p-1}$ in order to emphasize the difference to (5.17) and the dependence on $\boldsymbol{u}$ and $\boldsymbol{P}$. Nevertheless, all variables without index are defined at the current time step $n+1$. The resulting case distinction for the first variation of the constitutive relation $\delta\mathcal{R}_2^{\text{ep}}$, cf. (5.14), at the elasto-plastic transition based on (5.17) and (5.18) yields

$$\underbrace{\Big(\delta_{\boldsymbol{P},\boldsymbol{u}}\boldsymbol{\tau} - 2\Big[\delta_{\boldsymbol{u}}\Big(\frac{\partial\psi}{\partial\tilde{\boldsymbol{B}}^e}\cdot\tilde{\boldsymbol{B}}^e\Big)\Big]\Big)}_{\text{elastic step; } \lim\limits_{\Phi\,\to\,0^-}} \neq \underbrace{\Big(\delta_{\boldsymbol{P},\boldsymbol{u}}\boldsymbol{\tau} - 2\Big[\delta_{\boldsymbol{P},\boldsymbol{u}}\Big(\frac{\partial\psi}{\partial\boldsymbol{B}^e}\cdot\boldsymbol{B}^e\Big)\Big]\Big)}_{\text{elasto-plastic step; } \lim\limits_{\Phi\,\to\,0^+}}\,, \tag{5.19}$$

with the abbreviation $\delta_{\boldsymbol{P},\boldsymbol{u}}\boldsymbol{\tau} = \delta\boldsymbol{P}\cdot\boldsymbol{F}^T + \boldsymbol{P}\cdot\delta\boldsymbol{F}^T$. Obviously, $\delta_{\boldsymbol{P},\boldsymbol{u}}\boldsymbol{\tau}$ is the same for both cases. The modification of the test spaces is performed based on the approach for the small strain theory, see Schwarz [203] and Igelbüscher et al. [119]. The extension of this approach to finite strain formulations results in a neglection of the variation of the plastic right Cauchy-Green tensor $\delta_{\boldsymbol{u}}\boldsymbol{C}^{p\,-1}$ and $\delta_{\boldsymbol{P}}\boldsymbol{C}^{p\,-1}$. The idea leaves the underlying system of equations unchanged, as the modification is applied exclusively to the first variation. This yields a so-called modified first variation ($\delta_{\boldsymbol{u}}\hat{\mathcal{G}}^{\text{ep}}$ and $\delta_{\boldsymbol{P}}\hat{\mathcal{G}}^{\text{ep}}$) of the least-squares functional

(5.14), i.e.,

$$\begin{aligned}
\delta_{\boldsymbol{u}}\hat{\mathcal{G}}^{\mathrm{ep}} &= \int_{\mathcal{B}} \Big(\boldsymbol{P}\cdot\delta\boldsymbol{F}^T - 2\Big[\delta_{\boldsymbol{u}}\Big(\frac{\partial\psi}{\partial\tilde{\boldsymbol{B}}^e}\cdot\tilde{\boldsymbol{B}}^e\Big)\Big]\Big) : \Big(\boldsymbol{P}\cdot\boldsymbol{F}^T - 2\frac{\partial\psi}{\partial\boldsymbol{B}^e}\cdot\boldsymbol{B}^e\Big)\,\mathrm{d}V \\
&+ \int_{\mathcal{B}} (\boldsymbol{P}\cdot\delta\boldsymbol{F}^T - \delta\boldsymbol{F}\cdot\boldsymbol{P}^T) : (\boldsymbol{P}\cdot\boldsymbol{F}^T - \boldsymbol{F}\cdot\boldsymbol{P}^T)\,\mathrm{d}V\,, \\
\delta_{\boldsymbol{P}}\hat{\mathcal{G}}^{\mathrm{ep}} &= \int_{\mathcal{B}} \mathrm{Div}\,\delta\boldsymbol{P}\cdot(\mathrm{Div}\,\boldsymbol{P}+\boldsymbol{f})\,\mathrm{d}V + \int_{\mathcal{B}} \Big(\delta\boldsymbol{P}\cdot\boldsymbol{F}^T\Big) : \Big(\boldsymbol{P}\cdot\boldsymbol{F}^T - 2\frac{\partial\psi}{\partial\boldsymbol{B}^e}\cdot\boldsymbol{B}^e\Big)\,\mathrm{d}V \\
&+ \int_{\mathcal{B}} (\delta\boldsymbol{P}\cdot\boldsymbol{F}^T - \boldsymbol{F}\cdot\delta\boldsymbol{P}^T) : (\boldsymbol{P}\cdot\boldsymbol{F}^T - \boldsymbol{F}\cdot\boldsymbol{P}^T)\,\mathrm{d}V\,,
\end{aligned} \tag{5.20}$$

which are continuous for elastic ($\lim_{\Phi\to 0^-}$) and plastic ($\lim_{\Phi\to 0^+}$) loading.

Note that the advantage of symmetric system matrices is no longer valid due to the modification in the weak form in (5.20). This is analogously to the modified LS formulation presented in (5.12), which is shown to lead improved solution accuracy, see Chapter 5.6. Furthermore, the modified LS approach is shown to be well posed for the small strain framework in Schwarz et al. [205] and Starke et al. [221]. Since the underlying formulations already yields an unsymmetric system, the modified LS formulation (5.12) is additionally applied to (5.20), i.e.,

$$\delta_{\boldsymbol{u}}\mathcal{G}^{\mathrm{ep}} = \delta_{\boldsymbol{u}}\hat{\mathcal{G}}^{\mathrm{ep}} - \int_{\mathcal{B}} \nabla^{as}_{,x}(\delta\boldsymbol{u}) : \frac{1}{\mu}\Big(\boldsymbol{P}\cdot\boldsymbol{F}^T - 2\frac{\partial\psi}{\partial\boldsymbol{B}^e}\cdot\boldsymbol{B}^e\Big)\,\mathrm{d}V \quad\text{and}\quad \delta_{\boldsymbol{P}}\mathcal{G}^{\mathrm{ep}} := \delta_{\boldsymbol{P}}\hat{\mathcal{G}}^{\mathrm{ep}}\,. \tag{5.21}$$

The modified first variation in terms of the asymmetric defined tensor function (5.12) and the applied modification for ensuring continuous first variations (5.20) lead the linearized forms $\Delta\delta_{\boldsymbol{u}}\mathcal{G}^{\mathrm{ep}}$ and $\Delta\delta_{\boldsymbol{P}}\mathcal{G}^{\mathrm{ep}}$ with

$$\begin{aligned}
\Delta\delta_{\boldsymbol{u}}\mathcal{G}^{\mathrm{ep}} &= \int_{\mathcal{B}} \Big(\boldsymbol{P}\cdot\delta\boldsymbol{F}^T - 2\Big[\delta_{\boldsymbol{u}}\Big(\frac{\partial\psi}{\partial\tilde{\boldsymbol{B}}^e}\cdot\tilde{\boldsymbol{B}}^e\Big)\Big]\Big) : \Big(\boldsymbol{P}\cdot\Delta\boldsymbol{F}^T - 2\Big[\Delta_{\boldsymbol{u}}\Big(\frac{\partial\psi}{\partial\boldsymbol{B}^e}\cdot\boldsymbol{B}^e\Big)\Big]\Big)\,\mathrm{d}V \\
&+ \int_{\mathcal{B}} \Big(\boldsymbol{P}\cdot\Delta\delta\boldsymbol{F}^T - 2\Big[\Delta_{\boldsymbol{u}}\Big[\delta_{\boldsymbol{u}}\Big(\frac{\partial\psi}{\partial\tilde{\boldsymbol{B}}^e}\cdot\tilde{\boldsymbol{B}}^e\Big)\Big]\Big]\Big) : \Big(\boldsymbol{P}\cdot\delta\boldsymbol{F}^T - 2\Big[\delta_{\boldsymbol{u}}\Big(\frac{\partial\psi}{\partial\boldsymbol{B}^e}\cdot\boldsymbol{B}^e\Big)\Big]\Big)\,\mathrm{d}V \\
&+ \int_{\mathcal{B}} (\boldsymbol{P}\cdot\delta\boldsymbol{F}^T - \delta\boldsymbol{F}\cdot\boldsymbol{P}^T) : (\boldsymbol{P}\cdot\Delta\boldsymbol{F}^T - \Delta\boldsymbol{F}\cdot\boldsymbol{P}^T)\,\mathrm{d}V \\
&- \int_{\mathcal{B}} \nabla^{as}_{,x}(\delta\boldsymbol{u}) : \frac{1}{\mu}\Big(\boldsymbol{P}\cdot\Delta\boldsymbol{F}^T - 2\Big[\Delta_{\boldsymbol{u}}\Big(\frac{\partial\psi}{\partial\boldsymbol{B}^e}\cdot\boldsymbol{B}^e\Big)\Big]\Big)\,\mathrm{d}V \\
&+ \int_{\mathcal{B}} \Big(\boldsymbol{P}\cdot\delta\boldsymbol{F}^T - 2\Big[\delta_{\boldsymbol{u}}\Big(\frac{\partial\psi}{\partial\tilde{\boldsymbol{B}}^e}\cdot\tilde{\boldsymbol{B}}^e\Big)\Big]\Big) : \Big(\Delta\boldsymbol{P}\cdot\boldsymbol{F}^T - 2\Big[\Delta_{\boldsymbol{P}}\Big(\frac{\partial\psi}{\partial\boldsymbol{B}^e}\cdot\boldsymbol{B}^e\Big)\Big]\Big)\,\mathrm{d}V \\
&+ \int_{\mathcal{B}} \Big(\Delta\boldsymbol{P}\cdot\delta\boldsymbol{F}^T\Big) : \Big(\boldsymbol{P}\cdot\boldsymbol{F}^T - 2\,\frac{\partial\psi}{\partial\boldsymbol{B}^e}\cdot\boldsymbol{B}^e\Big)\,\mathrm{d}V \\
&+ \int_{\mathcal{B}} (\boldsymbol{P}\cdot\delta\boldsymbol{F}^T - \delta\boldsymbol{F}\cdot\boldsymbol{P}^T) : (\Delta\boldsymbol{P}\cdot\boldsymbol{F}^T - \boldsymbol{F}\cdot\Delta\boldsymbol{P}^T)\,\mathrm{d}V \\
&+ \int_{\mathcal{B}} (\Delta\boldsymbol{P}\cdot\delta\boldsymbol{F}^T - \delta\boldsymbol{F}\cdot\Delta\boldsymbol{P}^T) : (\boldsymbol{P}\cdot\boldsymbol{F}^T - \boldsymbol{F}\cdot\boldsymbol{P}^T)\,\mathrm{d}V \\
&- \int_{\mathcal{B}} \nabla^{as}_{,x}(\delta\boldsymbol{u}) : \frac{1}{\mu}\Big(\Delta\boldsymbol{P}\cdot\boldsymbol{F}^T - 2\Big[\Delta_{\boldsymbol{P}}\Big(\frac{\partial\psi}{\partial\boldsymbol{B}^e}\cdot\boldsymbol{B}^e\Big)\Big]\Big)\,\mathrm{d}V
\end{aligned} \tag{5.22}$$

and

$$
\begin{aligned}
\Delta\delta_{\boldsymbol{P}}\mathcal{G}^{\mathrm{ep}} \;=\; & \int_{\mathcal{B}} \operatorname{Div}\delta\boldsymbol{P}\cdot\operatorname{Div}\Delta\boldsymbol{P}\,\mathrm{d}V \\
+\; & \int_{\mathcal{B}} \Big(\delta\boldsymbol{P}\cdot\boldsymbol{F}^{T}\Big) : \Big(\boldsymbol{P}\cdot\Delta\boldsymbol{F}^{T} - 2\Big[\Delta_{\boldsymbol{u}}\Big(\frac{\partial\psi}{\partial\boldsymbol{B}^{e}}\cdot\boldsymbol{B}^{e}\Big]\Big)\,\mathrm{d}V \\
+\; & \int_{\mathcal{B}} \Big(\delta\boldsymbol{P}\cdot\Delta\boldsymbol{F}^{T}\Big) : \Big(\boldsymbol{P}\cdot\boldsymbol{F}^{T} - 2\frac{\partial\psi}{\partial\boldsymbol{B}^{e}}\cdot\boldsymbol{B}^{e}\Big)\,\mathrm{d}V \\
+\; & \int_{\mathcal{B}} (\delta\boldsymbol{P}\cdot\boldsymbol{F}^{T} - \boldsymbol{F}\cdot\delta\boldsymbol{P}^{T}) : (\boldsymbol{P}\cdot\Delta\boldsymbol{F}^{T} - \Delta\boldsymbol{F}\cdot\boldsymbol{P}^{T})\,\mathrm{d}V \\
+\; & \int_{\mathcal{B}} (\delta\boldsymbol{P}\cdot\Delta\boldsymbol{F}^{T} - \Delta\boldsymbol{F}\cdot\delta\boldsymbol{P}^{T}) : (\boldsymbol{P}\cdot\boldsymbol{F}^{T} - \boldsymbol{F}\cdot\boldsymbol{P}^{T})\,\mathrm{d}V \\
+\; & \int_{\mathcal{B}} \Big(\delta\boldsymbol{P}\cdot\boldsymbol{F}^{T}\Big) : \Big(\Delta\boldsymbol{P}\cdot\boldsymbol{F}^{T} - 2\Big[\Delta_{\boldsymbol{P}}\Big(\frac{\partial\psi}{\partial\boldsymbol{B}^{e}}\cdot\boldsymbol{B}^{e}\Big)\Big]\Big)\,\mathrm{d}V \\
+\; & \int_{\mathcal{B}} (\delta\boldsymbol{P}\cdot\boldsymbol{F}^{T} - \boldsymbol{F}\cdot\delta\boldsymbol{P}^{T}) : (\Delta\boldsymbol{P}\cdot\boldsymbol{F}^{T} - \boldsymbol{F}\cdot\Delta\boldsymbol{P}^{T})\,\mathrm{d}V
\end{aligned}
\tag{5.23}
$$

The modified variations are only part of the linearization $\Delta\delta_{\boldsymbol{u}}\mathcal{G}^{\mathrm{ep}}$. Thus, the unsymmetric system is caused by $\boldsymbol{k}^{\mathrm{e}}_{uP} \neq \boldsymbol{k}^{\mathrm{e}\,T}_{Pu}$. For a decreasing characteristic element length $h_{\mathrm{e}} \to 0$, the constitutive relation is fulfilled and expression $\delta\tilde{\mathcal{G}}(\boldsymbol{H}_{\mathrm{as}}(\delta\boldsymbol{u}), \boldsymbol{\Sigma}_{\mathrm{sym}})$ vanishes and yield $\delta_{\boldsymbol{u}}\mathcal{G}^{\mathrm{ep}} = \delta_{\boldsymbol{u}}\hat{\mathcal{G}}^{\mathrm{ep}}$. However, since the modification with respect to the arising plasticity is unaffected by decreasing mesh levels, the formulation is still unsymmetric and $\boldsymbol{k}^{\mathrm{e}}_{uP} \neq \boldsymbol{k}^{\mathrm{e}\,T}_{Pu}$. Therefore, the proposed modified elasto-plastic LS formulation is no longer a classical LSFEM in terms of the inherent symmetry properties of the resulting matrices.
The algorithmic treatment of the presented LS formulation at finite J_2-plasticity is listed in Table 5.8.

For a reduction of the dimension of the proposed LS formulation from $d = 3$ to $d = 2$ plane stress condition is considered, cf. Chapter 5.3. The assumption of plane stress is preferable due to the analyzed plastic material behavior, in which the complete stress tensor, as the norm of the deviatoric part, has to be considered in order to determine plastic deformations. The plane stress constraint simplify the application, since the stresses in $x - y$ plane are approximated and in z-direction equal to 0. Nevertheless, this requires a subiteration procedure for the strains in z-direction. These are computed analogously to the hyperelastic framework, summarized in 5.1. Therefore, the algorithmic treatment listed in Table 5.8 is modified by introducing the iteration in Table 5.1 previously to the determination of the plastic state, i.e., before step (4) in Table 5.8. The representation of the finite plastic deformations by means of problems in $d = 2$, reduces the required degrees of freedom by a large margin. However, in the following the applications are first validated in $d = 3$.

Table 5.8: Algorithmic treatment for a 3D finite elasto-plastic LS element

ELEMENT LOOP

(1) Update displacements and stresses (Newton iteration k+1)

$\boldsymbol{d} = \boldsymbol{d}_{u,\,n}^{(k)} + \Delta\boldsymbol{d}_u$, $\boldsymbol{d}_\sigma = \boldsymbol{d}_{\sigma,\,n}^{(k)} + \Delta\boldsymbol{d}_\sigma$

INTEGRATION LOOP

(2) Compute stresses $\boldsymbol{P}$ and displacements $\boldsymbol{u}$ at each Gauss Point:

$\boldsymbol{P} = \mathbb{S}\,\boldsymbol{d}_\sigma$ and $\boldsymbol{u} = \mathbb{N}_u\,\boldsymbol{d}_u$

Read from History: $\boldsymbol{C}_n^{p\,-1}$, α_n and state_n

CONSTITUTIVE LOOP

(3) Check plastic state of previous step:

If $\text{state}_n = 0 \;\Rightarrow\; \boldsymbol{C}_i^{p\,-1} = \boldsymbol{I}$; Else $\text{state}_n > 0 \;\Rightarrow\; \boldsymbol{C}_i^{p\,-1} = \boldsymbol{C}_n^{p\,-1}$

(4) Check for plastic state in the actual step:

Call SUBITERATION in Table 5.9

If $\Phi > tol$, compute $\boldsymbol{n} = \partial_\tau \Phi$ and $\boldsymbol{M} := \exp\big[-2\,\gamma_{n+1}\,\boldsymbol{n}\big]$

Update history $\boldsymbol{C}_{n+1}^{p\,-1} = \boldsymbol{F}^{-1}\cdot\boldsymbol{M}\cdot\boldsymbol{F}\cdot\boldsymbol{C}_i^{p\,-1}$ and $\alpha_{n+1} = \alpha_n + \sqrt{\frac{2}{3}}\,\gamma_{n+1}$

Else $\Phi \le tol$, update history $\boldsymbol{C}_{n+1}^{p\,-1} = \boldsymbol{C}_n^{p\,-1}$ and $\alpha_{n+1} = \alpha_n$

(5) Compute stresses $\boldsymbol{\tau}(\boldsymbol{B}^e)$:

$\boldsymbol{\tau}(\boldsymbol{B}^e) = 2\,\partial_{\boldsymbol{B}^e}\psi(\boldsymbol{B}^e)\cdot\boldsymbol{B}^e$ with $\boldsymbol{B}^e := \boldsymbol{F}\cdot\boldsymbol{C}_{n+1}^{p\,-1}\cdot\boldsymbol{F}^T$

(6) Compute single functional parts and exit CONSTITUTIVE LOOP

(7) Determine and export right hand side and element stiffness matrix

In Chapter 2.5.2 and 2.5.3 a yield criterion in terms of isotropic linear hardening is considered. For the application of exponential hardening the von Mises yield criterion is defined by

$$\Phi(\boldsymbol{\tau},\alpha) = \|\operatorname{dev}\boldsymbol{\tau}\| - \sqrt{\tfrac{2}{3}}\Big(y_0 + h\,\alpha + (y_\infty - y_0)(1-\exp[-\eta\,\alpha])\Big)\,, \tag{5.24}$$

where y_∞ denotes the saturation yield stress and η is the exponential hardening modulus. Therefore, a straightforward calculation of the plastic parameter γ, as shown in Chapter 2.5.2, is not valid anymore, since the yield criterion is here an implicit function of α_{n+1} and thus γ_{n+1}. In order to fulfill the exceeded yield criterion ($\Phi \overset{!}{=} 0$) the evaluation of the plastic multiplier γ is performed by means of a subiteration with the iteration index j, analogously to the enforcement of plane stress condition in Chapter 5.3. The basis for this is a Taylor series expansion of the yield criterion Φ_{n+1}, in which higher order terms are neglected, cf., e.g., Klinkel [133]. This results in

$$\Phi_{n+1}^{j+1} = \Phi_{n+1}^{j} + \frac{\partial\Phi_{n+1}^{j}}{\partial\gamma_{n+1}^{j}}\,\Delta\gamma_{n+1}^{j+1} \overset{!}{=} 0 \quad\Rightarrow\quad \Delta\gamma_{n+1}^{j+1} = -\left(\frac{\partial\Phi_{n+1}^{j}}{\partial\gamma_{n+1}^{j}}\right)^{-1}\Phi_{n+1}^{j}\,, \tag{5.25}$$

and is further determined by

$$\Delta\gamma_{n+1}^{j+1} = -\left(\frac{\partial\Phi_{n+1}^{j}}{\partial\alpha_{n+1}^{j}}\,\frac{\partial\alpha_{n+1}^{j}}{\partial\gamma_{n+1}^{j}}\right)^{-1}\Phi_{n+1}^{j} = \frac{3\,\Phi_{n+1}^{j}}{2\,(h+(y_\infty-y_0)(\eta\exp[-\eta\,\alpha_{n+1}^{j}]))} \tag{5.26}$$

with the exponential yield criterion $\Phi(\boldsymbol{\tau},\alpha)$ in (5.24) and the incremental update of the hardening law (2.66), i.e., $\alpha_{n+1}^{j} = \alpha_n^j + \sqrt{\frac{2}{3}}\gamma_{n+1}^{j}$. This follows from the evaluation of the minimization problem with constraint condition in form of a Lagrange functional with respect to the reduced dissipation inequality, see Chapter 2.5.3. The resulting algorithmic treatment within the finite element implementation is listed in Table 5.9. A consistent material tangent is obtained by utilization of automated differentiation and the definitions of the associated dependencies, see, e.g., Korelc [136], Korelc [137] and Korelc and Wriggers [138].

Table 5.9: Algorithmic treatment for the subiteration of the plastic multiplier γ

SUBITERATION (j as local iteration index)

(1) Compute $\alpha_{n+1}^{j} = \alpha_n + \sqrt{\frac{2}{3}}\,\gamma_{n+1}^{j}$ and

$\Phi_{n+1}^{j} = \|\operatorname{dev}\boldsymbol{\tau}_{n+1}\| - \sqrt{\frac{2}{3}}(y_0 + h\,\alpha_{n+1}^{j} + (y_\infty - y_0)(1-\exp[-\eta\,\alpha_{n+1}^{j}]))$

(2) If $\Phi_{n+1}^{j} \leq tol$,

Determine $\dfrac{\partial\gamma_{n+1}^{j}}{\partial\boldsymbol{\tau}_{n+1}} = \left(\dfrac{\partial\Phi_{n+1}^{j}}{\partial\gamma_{n+1}^{j}}\right)^{-1}\dfrac{\partial\Phi_{n+1}^{j}}{\partial\boldsymbol{\tau}_{n+1}}$ and Exit SUBITERATION

(3) If $n_{\text{iter}} > n_{\max}$ Then stop iteration

(4) Update: $\gamma_{n+1}^{j+1} = \gamma_{n+1}^{j} + 3\,\Phi_{n+1}^{j}\big(2\,(h+(y_\infty-y_0)(\eta\exp[-\eta\,\alpha_{n+1}^{j}]))\big)^{-1}$

$j = j+1$ and Go To (1)

5.8 Numerical objectivity test for LSFEM at finite J_2-plasticity

In order to confirm the correct description of superimposed rigid body movements, a numerical objectivity test is performed based on Glaser and Armero [103] and Korelc et al. [139]. Therein, the considered boundary value problem is given by a straight beam ($l = 10$ mm, $b = 1$ mm, $t = 1$ mm) clamped on both ends and on the right end ($z = 0$) a displacement controlled boundary condition $\boldsymbol{u} = (0, 2t, 0)^T$ mm is applied, see Figure 5.14. The remaining faces are stress-free ($\boldsymbol{P}\cdot\boldsymbol{N} = (0,0,0)^T\,\text{kN/mm}^2$). In addition, the prescribed beam is subjected to a superimposed rigid body rotation with an angle of $\vartheta = \pi/10$. The proof of objectivity is validated by constant results for the norm of reaction force in axial and y-shear direction at the clamped end in terms of the superimposed rigid body rotation ϑ, cf. Glaser and Armero [103]. In Glaser and Armero [103] also a non-objective formulation is presented, where the results are crucially depending on the superimposed rotation.

The objectivity test is performed for the proposed modified LS formulations at finite elasticity (5.3) and plasticity (5.14) and the results are given with respect to the rotation angle $\vartheta = \pi/10$, see Figure 5.15(a). Additionally, the geometrical proof is shown in Figure 5.15(b). For both formulations the results fulfill the requirements of objectivity. Here, the weights are $\omega_i = \{1, 1/\mu, 1/\mu\}$. Note that in the case of plasticity it is necessary that the path following procedure follows exactly the prescribed rotation due to the fact that the objectivity of the formulation can be compromised by spurious plastic deformations.

Setup of BVP

Left face	$\boldsymbol{u} = (0, 0, 0)^T$ mm
Right face	$\boldsymbol{u} = (0, 2t, 0)^T$ mm
Young's mod.	$E = 200$ kN/mm^2
Poisson's ratio	$\nu = 0.35$
Yield stress	$y_0 = 6$ kN/mm^2
Hardening mod.	$h = 10$ kN/mm^2

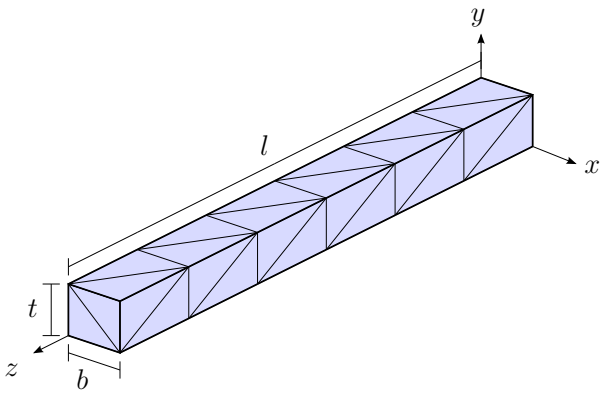

Figure 5.14: Numerical objectivity test for finite elasticity and elasto-plastic LS formulation

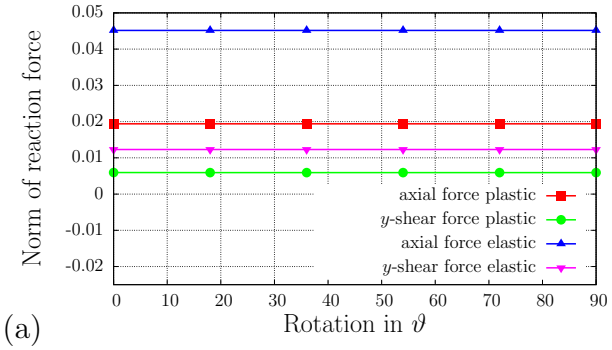

(a)

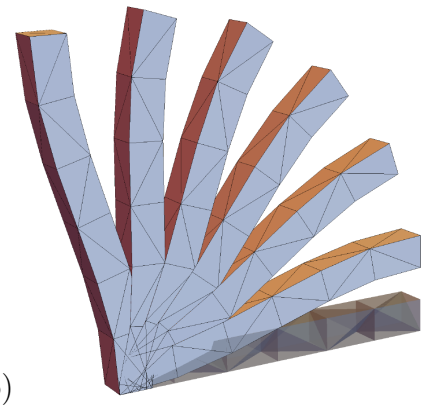

(b)

Figure 5.15: Objectivity proof by (a) norm of reaction forces in axial and y-shear direction and (b) geometrical results with respect to $\vartheta = \pi/10$, cf. Igelbüscher et al. [119]

5.9 Cook's membrane for finite J_2-plasticity

The Cook's membrane example is analyzed at first. In Figure 5.16 the example and the material setup are depicted for two load cases in $d = 3$ with $\boldsymbol{u} = (0, 0, 0)^T$ dm on the left face, the associated load case applied on the right face and all other faces are stress-free. For the first load case a vertical load is considered on the right face with $\boldsymbol{P} \cdot \boldsymbol{N} = (0, 2.5, 0)^T$ MN/dm^2. Additionally, the second setup is loaded in horizontal direction where the stresses are given on the right face by $\boldsymbol{P} \cdot \boldsymbol{N} = (4.5, 0, 0)^T$ MN/dm^2. The crucial dependence of the LSFEM on weighting parameters has already been discussed and is not investigated for the elasto-plastic formulation. The weights are chosen with $\omega_i = \{1, 1/\mu, 10/\mu\}$ for the following examples and thus in line with the insights of Chapter

4.1 and 5.1, see, e.g., SCHWARZ ET AL. [207; 208], SCHRÖDER ET AL. [199]. Here, the numerical results are compared to a quadratic displacement element $\mathcal{P}_2$.

Setup of BVP

Left face	$\boldsymbol{u} = (0,0,0)^T\,\mathrm{dm}$
(a) Right face	$\boldsymbol{P}\cdot\boldsymbol{N} = (4.5,0,0)^T\,\mathrm{MN/dm^2}$
(b) Right face	$\boldsymbol{P}\cdot\boldsymbol{N} = (0,2.5,0)^T\,\mathrm{MN/dm^2}$
Young's mod.	$E = 2069\,\mathrm{MN/dm^2}$
Poisson's ratio	$\nu = 0.29$
Yield stress	$y_0 = 4.5\,\mathrm{MN/dm^2}$
Hardening mod.	$h = 15\,\mathrm{MN/dm^2}$

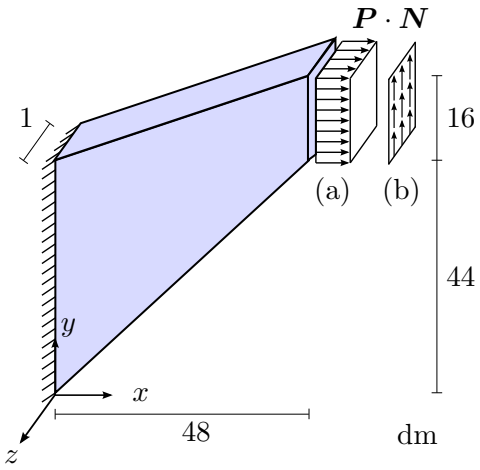

Figure 5.16: Cook's membrane example for finite elasto-plasticity

The modified formulation based on 5.14 is analyzed due to the displacement convergence of the top right corner node $(48, 60, 0)$ for the horizontal and vertical load case, see Figure 5.17. Therein, the number of elements per side is increased in x- and y-direction whereas it is constant in z-direction with 2 elements. The displacement convergence for the here chosen $\mathcal{RT}_0\mathcal{P}_2$ element lead to satisfying solutions compared to the $\mathcal{P}_2$ element, at least for fine mesh densities. The slightly poorer convergence of the LS element is based on the low order interpolation of the stresses by a polynomial order of $m = 0$, which leads to less accurate results in comparison to higher order approaches as shown in Chapter 5.5 and in, e.g., SCHWARZ ET AL. [205; 207; 208]. Furthermore, the distribution of the von Mises stress σ_{vM} and the equivalent plastic strain α are compared for the LS and the pure displacement formulation on the deformed domain, see Figures 5.18, 5.19 for the horizontal load case and Figures 5.20, 5.21 for the vertical load case. Here, the von Mises stress is considered as an indicator for plastic material response and the equivalent plastic strains are chosen as a measure of the plastic deformations which occur. Both formulations yield according results for the considered fields σ_{vM} and α.

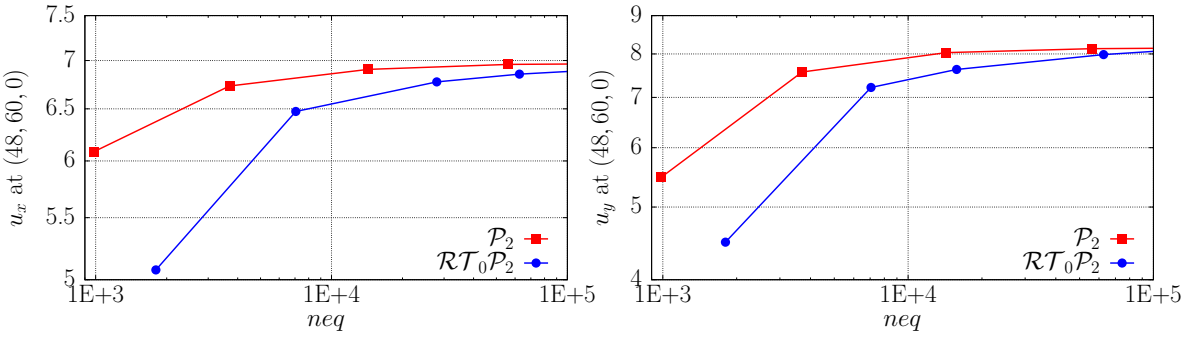

Figure 5.17: Convergence study for Cook's membrane problem with (a) horizontal load case and (b) vertical load case, cf. IGELBÜSCHER ET AL. [119]

For completeness, the convergence of the norm of the right hand side vector is listed in Table 5.10 for the $\mathcal{P}_2$ and $\mathcal{RT}_0\mathcal{P}_2$ elements exemplarily for two mesh levels. Note

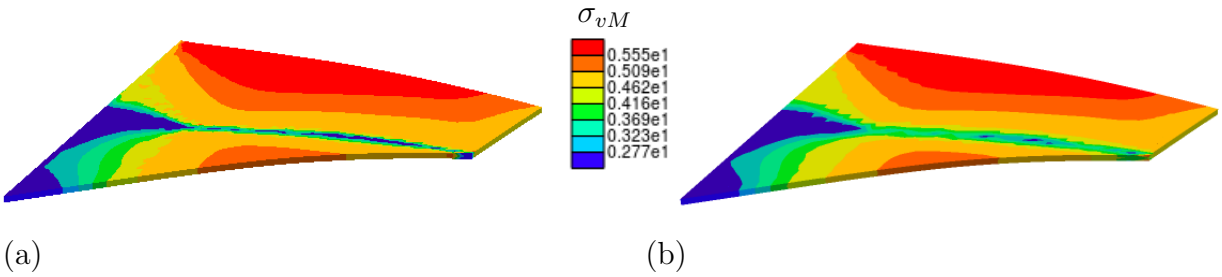

(a) (b)

Figure 5.18: Cook's membrane, horizontal load case: Distribution of σ_{vM} on the deformed body for (a) a $\mathcal{P}_2$ and (b) a $\mathcal{RT}_0\mathcal{P}_2$ element, cf. Igelbüscher et al. [119]

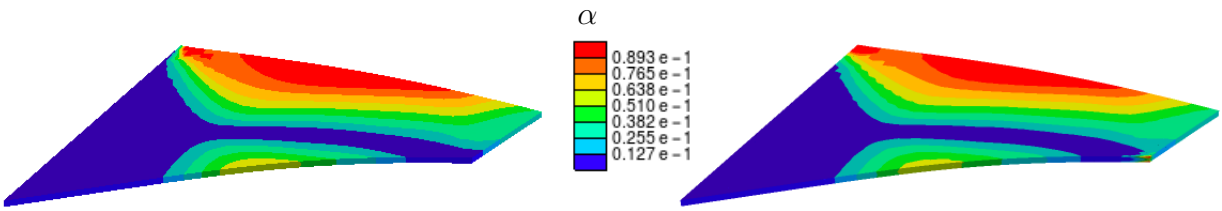

(a) (b)

Figure 5.19: Cook's membrane, horizontal load case: Distribution of α on the deformed body for (a) a $\mathcal{P}_2$ and (b) a $\mathcal{RT}_0\mathcal{P}_2$ element, cf. Igelbüscher et al. [119]

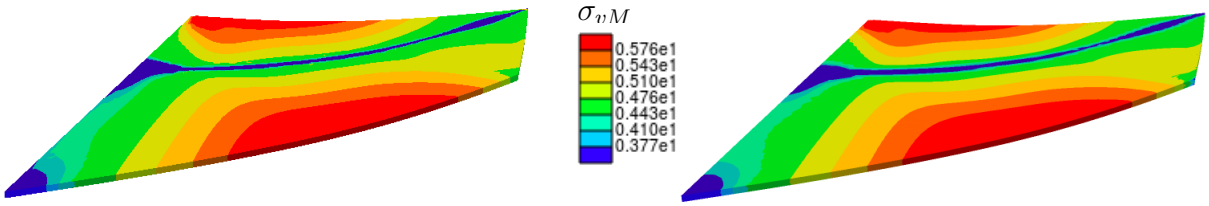

(a) (b)

Figure 5.20: Cook's membrane, vertical load case: Distribution of σ_{vM} on the deformed body for (a) a $\mathcal{P}_2$ and (b) a $\mathcal{RT}_0\mathcal{P}_2$ element, cf. Igelbüscher et al. [119]

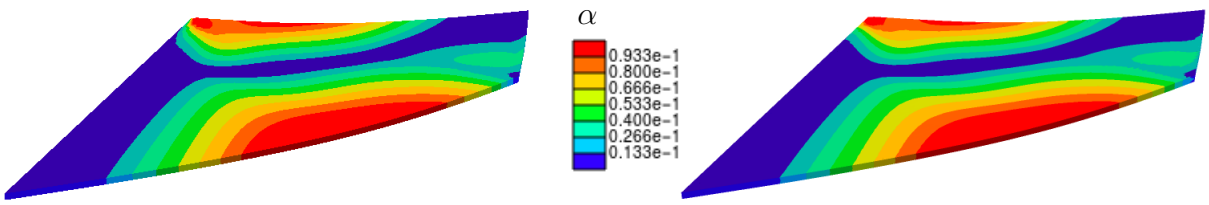

(a) (b)

Figure 5.21: Cook's membrane, vertical load case: Distribution of α on the deformed body for (a) a $\mathcal{P}_2$ and (b) a $\mathcal{RT}_0\mathcal{P}_2$ element, cf. Igelbüscher et al. [119]

that the modified LS formulation at finite J_2-plasticity does not yield to any oscillatory effects in the convergence behavior with the standard Newton-Raphson scheme, which is visualized in Kubitz [142] and Schwarz [203]. The convergence of the norm of the right hand side vector for the $\mathcal{P}_2$ and the $\mathcal{RT}_0\mathcal{P}_2$ elements are quite similar, especially for the finer mesh level. The listed values show quadratic convergence behavior for the last iteration steps, which is satisfying, since quadratic convergence is only attained for energy norms close to the solution caused by the radius of convergence, cf. Braess [50], and only superlinear convergence is to be expected for rate-independent elasto-plasticity, see Sauter and Wieners [196].

Table 5.10: Convergence of the norm of the right hand side vector for the Cook's membrane (Figure 5.16(b)) at final load for different element numbers (nel) with a load step $\Delta t = 0.01$

	$\mathcal{P}_2$		$\mathcal{RT}_0\mathcal{P}_2$	
Iteration	$nel = 160$	$nel = 2560$	$nel = 160$	$nel = 2560$
1	4.5193 E-3	6.2552 E-2	1.2766 E-1	1.3709 E-2
2	3.6627 E-2	1.0561 E+1	7.4056 E-1	3.4898 E-2
3	1.4541 E-6	9.5596 E-2	3.4349 E-1	1.1761 E-2
4	3.5656 E-10	8.3256 E-3	2.2415 E-2	1.2522 E-3
5	-	4.8756 E-6	2.7728 E-5	1.7059 E-7
6	-	1.4522 E-10	3.1099 E-10	2.3540 E-10

5.10 Cook's membrane for finite J_2-plasticity with plane stress iteration

Furthermore, the Cook's membrane is analyzed for $d = 2$, in order to reduced the number of degrees of freedom and illustrate the convergence behavior for elements with higher polynomial orders. Therefore, the local plane stress iteration in Chapter 5.3 is applied to the finite plasticity formulation in Table 5.8. The material parameters and the applied load are listed in Table 5.11 with the weighting setup $\omega_i = \{1, 1/\mu, 10/\mu\}$ for $i = 1, 2, 3$ utilizing the proposed modified LS formulation.

Table 5.11: Material parameters and load for Cook's membrane at $d = 2$

E	μ	y_0	h	y_∞	η	$\boldsymbol{P} \cdot \boldsymbol{N}$
206900 MPa	0.29	450 MPa	1292.4 MPa	715 MPa	16.93	$(0, 350)^T$ MPa

In order to achieve convergent solutions in all fields, the convergence is first of all analyzed in relation to different numbers of load steps. Therefore, in Figure 5.22 the convergence of the displacements u_y at $(48, 60)$ and the von Mises stress σ_{vM} at $(35.2, 44)$ are depicted with respect to the number of load steps. Therein, convergence in terms of the load step is reached for a number of load steps ≥ 1000 and thus a load step of $\Delta t = 0.001$. Furthermore, since the formulation under investigation includes a modified first variation, in Figure 5.23(a) the evolution of the smallest eigenvalue of the global stiffness matrix is depicted, in order to show the positive definiteness of the LS formulation. Here, the system matrix is positive (semi-) definite. The property of positive (semi-) definiteness of the system matrix has already been shown in Müller [165] and Steeger [223] for the calculation of stability points with the LSFEM. As a consequence of the decreasing smallest eigenvalue, the condition number of the solved system increases, see Figure 5.23(b), which has to be taken into account for the evaluation of the results, since a high condition number might lead to reduced convergence and accuracy of an iterative solution process. Nevertheless, high condition numbers can be avoided by application of preconditioners for the system matrix leading to comparable condition numbers as in Galerkin formulations, cf. Bochev and Gunzburger [43].

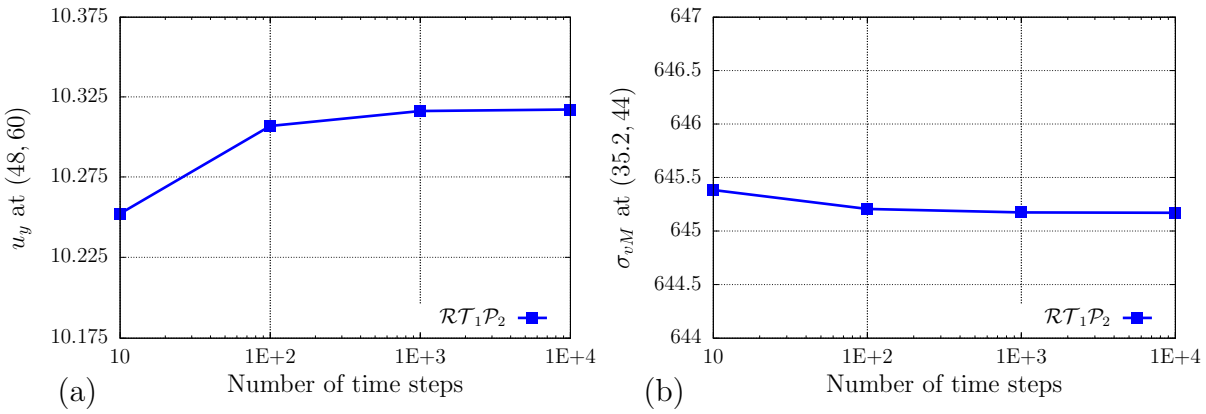

Figure 5.22: Convergence study for applied load steps using $\mathcal{RT}_1\mathcal{P}_2$ for (a) displacement u_y at $(48, 60)$ and (b) von Mises stress σ_{vM} at $(35.2, 44)$

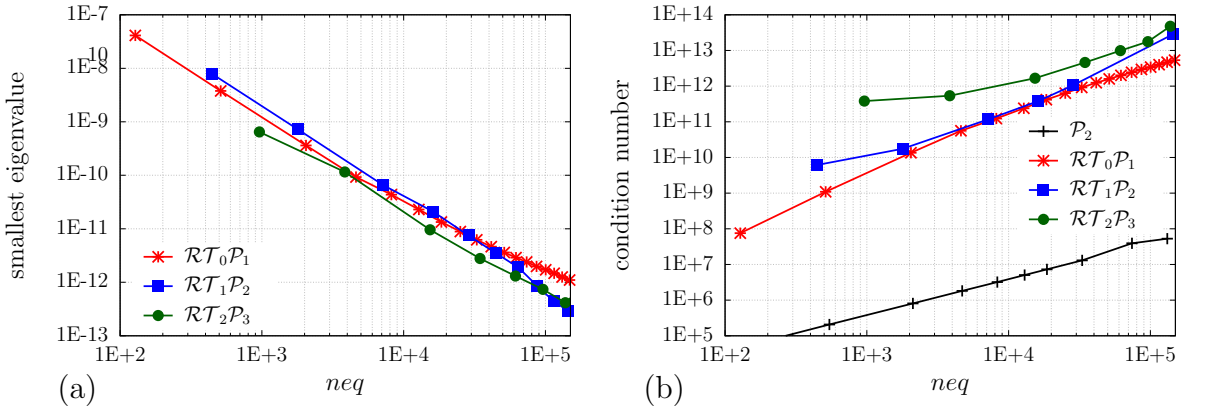

Figure 5.23: Evolution of the smallest eigenvalue (a) and the condition number (b) for the modified LS formulation for an increasing number of elements

Additionally, Figure 5.24(a) shows the convergence of u_y at the particular point $(48, 60)$ and Figure 5.24(b) depicts the convergence of σ_{vM} at the point $(35.2, 44)$, cf. Schröder et al. [202]. The displacement convergence illustrates the expected behavior, compared to the results in Chapter 5.4 and 5.6. Hence, satisfying solutions are obtained for all element orders, depending on the number of equations and the polynomial degree. The comparison of the resulting von Mises stress between the LS formulations and the pure displacement element show that the formulations converge towards slightly different values. For the $\mathcal{P}_2$ element the solution is 642.7013 MPa and for the $\mathcal{RT}_2\mathcal{P}_3$ element at 646.3853 MPa. However, the difference is given by 0.57 % and thus in the range of engineering accuracy.

As a last point the convergence of the modified LS functional is shown in Figure 5.25. Therein, the reduced optimal convergence rates for the Cook's membrane example are shown. In addition to the functional itself, also the single functional parts $\mathcal{F}_i^{\text{ep}}$, in terms of the single residual equations $\mathcal{R}_i^{\text{ep}}$ in (5.14), are illustrated. The restriction of the convergence of the LS functional is clearly given by the constitutive relation in $\mathcal{F}_2^{\text{ep}}$. This results confirm the findings of functional convergence in Figure 5.4, 5.5, wherein the convergence rate are greatly improved by weighting of the constitutive relation with a value of < 1, which yield in consequence to a reduced functional value. Furthermore, the balance of linear momentum is satisfied most effectively for all element types and has

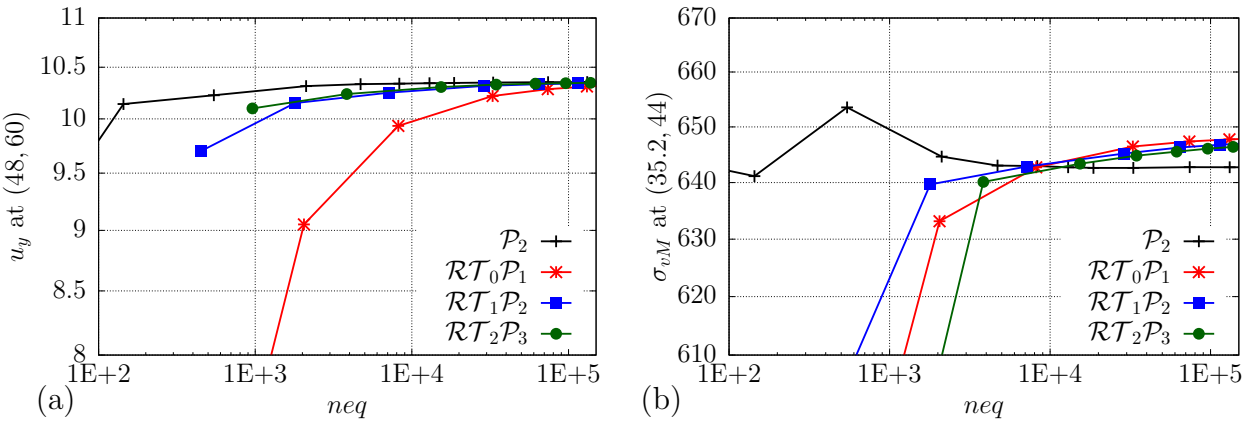

Figure 5.24: Convergence of u_y at (48,60) (a) and σ_{vM} at $(35.2, 44)$ (b) for the Cook's membrane with $\omega_i = \{1, 1/\mu, 10/\mu\}$ for $i = 1, 2, 3$

the least influence on the functional convergence. For a LS functional which is elliptic with respect to some norm on the underlying function spaces, adaptive refinement can be applied. Since the local evaluation of the LS functional provides an a posteriori error estimator, see, e.g., Berndt et al. [31] and Starke [219] for discussions on adaptive refinement in LS formulations for elasticity and elasto-plasticity.

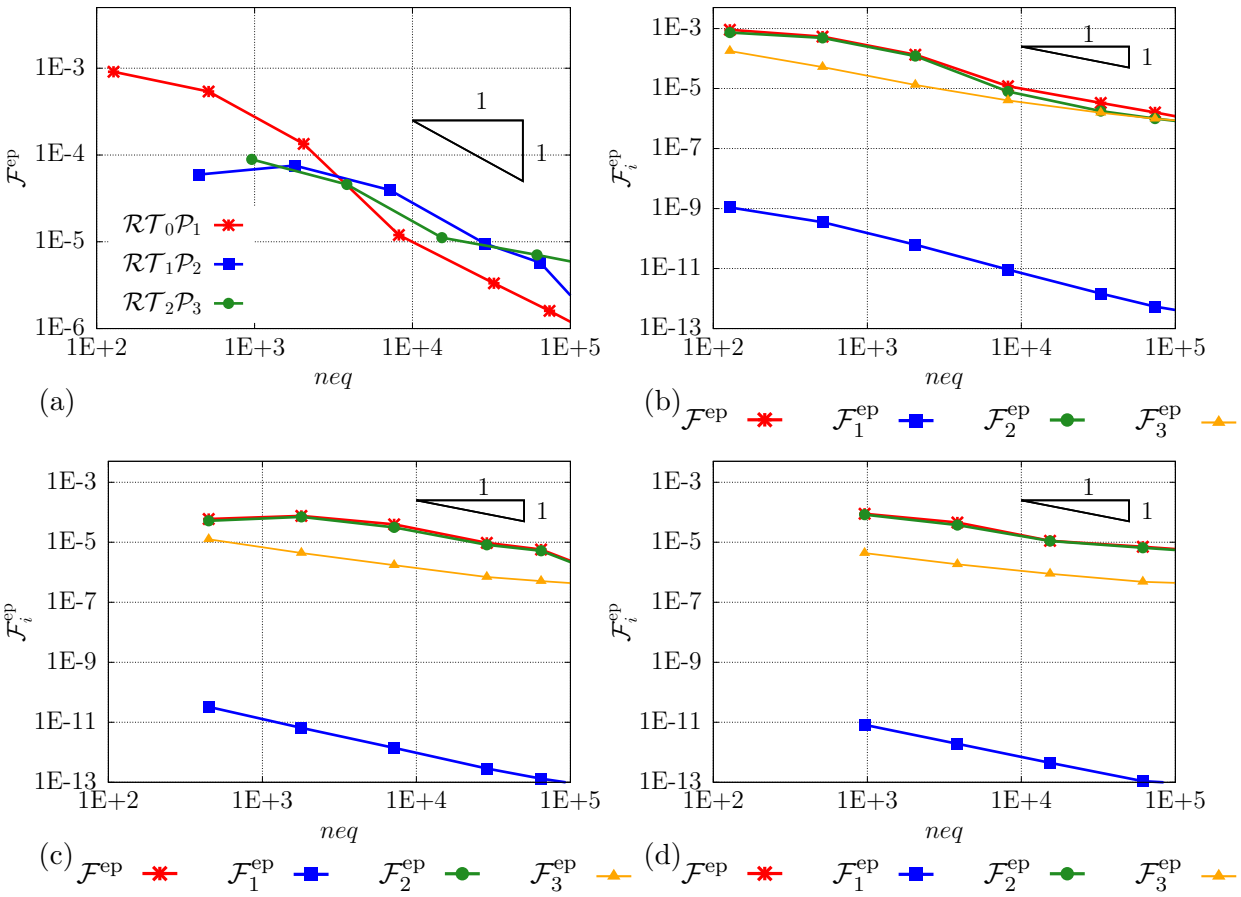

Figure 5.25: Convergence of (a) $\mathcal{F}^{ep}$ for $\mathcal{RT}_m\mathcal{P}_k$ elements and the single functional parts for $\mathcal{RT}_0\mathcal{P}_1$ (b), $\mathcal{RT}_1\mathcal{P}_2$ (c) and $\mathcal{RT}_2\mathcal{P}_3$ (d) with $\omega_i = \{1, 1/\mu, 10/\mu\}$ with $i = 1, 2, 3$

5.11 Plate with circular hole for finite J_2-plasticity

For the analysis of a displacement driven process the perforated plate problem is considered, with the geometry given in Figure 4.5. The material parameters are listed in Table 5.12 and a prescribed displacement boundary condition on the upper edge at $y = 18\,\mathrm{dm}$ of $\boldsymbol{u} = (0, 1.8)^T\,\mathrm{dm}$ is applied. The example is loaded by a load curve which is characterized by $u_y(t)$. For this, the perforated plate is loaded linearly up to a maximum load of $u_y(t = 1.8) = 1.8\,\mathrm{dm}$ and afterwards the applied displacement is reduced linearly back to $u_y(t = 3.6) = 0\,\mathrm{dm}$. The considered load step is chosen with $\Delta t = 0.001$. The analyzed structured meshes consist of a number of elements nel with $nel = \{256, 1024, 4096\}$, where only one mesh with $nel = 4096$ is considered for the $\mathcal{P}_2$ element.

Table 5.12: Material parameters for perforated plate example

E	μ	y_0	h	y_∞	η
$2069\,\mathrm{MN/dm^2}$	0.29	$4.5\,\mathrm{MN/dm^2}$	$12.924\,\mathrm{MN/dm^2}$	$7.15\,\mathrm{MN/dm^2}$	16.93

In Figure 5.26 a load-displacement curve is shown. The load at the bottom edge is determined from the nodal reactions. Here, the vertical reaction force F_y for the $\mathcal{P}_2$ element is determined by the nodal forces taken from the right hand side vector. For the LS formulation the tractions at the lower edge are evaluated, cf. (4.5). The results in Figure 5.26 illustrate the accordance of the investigated elements, using different mesh levels. Therein, the convergence of the $\mathcal{RT}_0\mathcal{P}_1$ element towards the other formulations is visible.

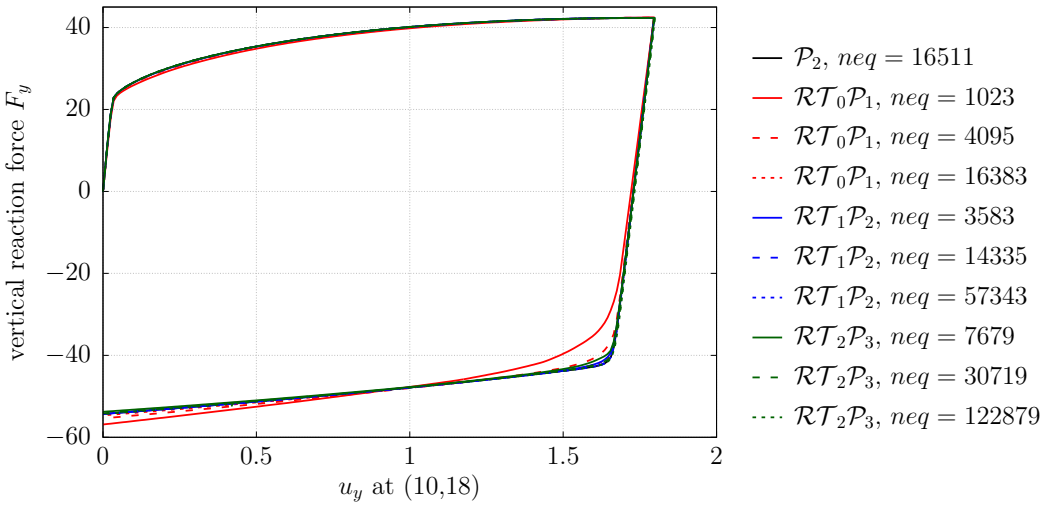

Figure 5.26: Course of vertical reaction force F_y at the bottom edge vs. u_y at (10,18) for $\mathcal{RT}_m\mathcal{P}_k$ for different mesh levels

A similar situation arises from the analysis of the σ_{yy} stress at the particular point $\boldsymbol{x} = (5, 0)$ on the circular section, see Figure 5.27. At this corner point a stress concentration is located due to the load application and hence the highest stress values are to be expected here, which is further illustrated in Figure 5.29. The stress value is plotted against the applied displacement load for the same mesh levels as before. Here, the differences in the performance of the individual LS elements become more obvious. Especially, at the low mesh level with $nel = 256$ the $\mathcal{RT}_m\mathcal{P}_k$ elements are not able to represent at least the correct stress evolution. For higher mesh levels all elements are able to cover a

satisfying solution for the σ_{yy} stress. Since the value of the saturation yield stress is close to the yield stress, the resulting exponential curves are only slightly visible.

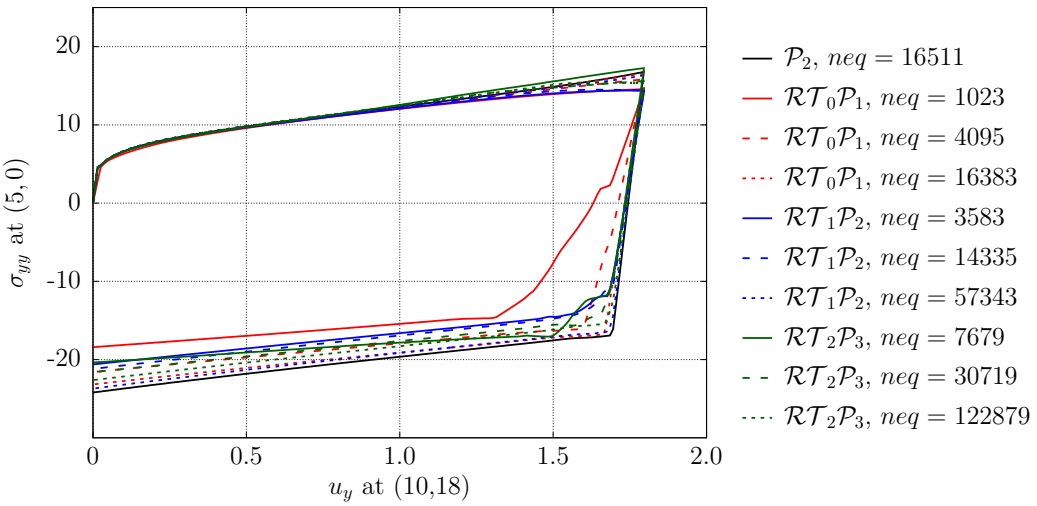

Figure 5.27: Evolution of σ_{yy} stress vs. u_y at (10,18) for $\mathcal{RT}_m\mathcal{P}_k$ for different mesh levels

The plane stress subiteration yields in general to a F_{zz} component of the deformation gradient which differs from 1, since the P_{zz} stress is iteratively solved ($P_{zz} \stackrel{!}{=} 0$). For completeness the resulting F_{zz} values are depicted in Figure 5.28.

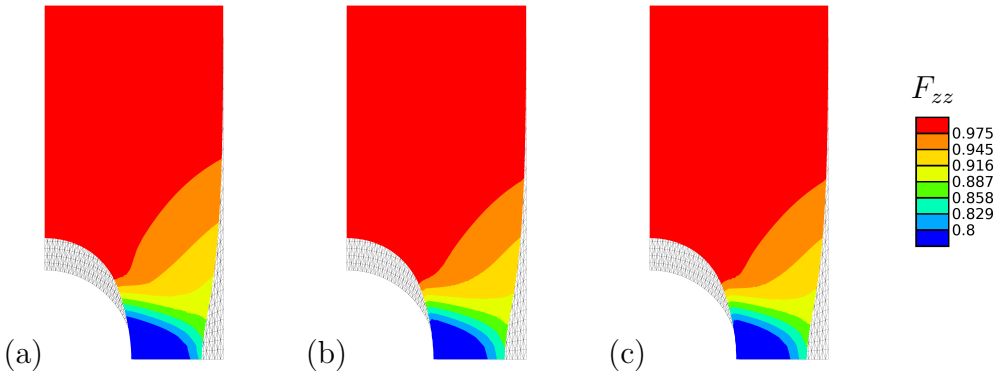

Figure 5.28: Plots of the F_{zz} component for the plane stress subiteration for (a) $\mathcal{P}_2$, (b) $\mathcal{RT}_0\mathcal{P}_1$ and (c) $\mathcal{RT}_1\mathcal{P}_2$ element

Furthermore, occurring plastic material behavior is shown in terms of the distribution of the equivalent plastic strains represented by α and the von Mises stress σ_{vM} in Figure 5.29. Here, the stress and strain courses are illustrated at the maximum displacement load $u_y = 1.8\,\mathrm{dm}$ at $t = 1.8$ and at the end of the loading at $t = 3.6$ with $u_y = 0\,\mathrm{dm}$ on the deformed body using $nel = 4096$. The distribution of σ_{vM} at $t = 3.6$ shows a stress band at the lower right corner of the plate. This is due to the reversal of the loading situation and would continue to grow with sustained loading in the direction. The depicted results show accordance in the distributed fields.

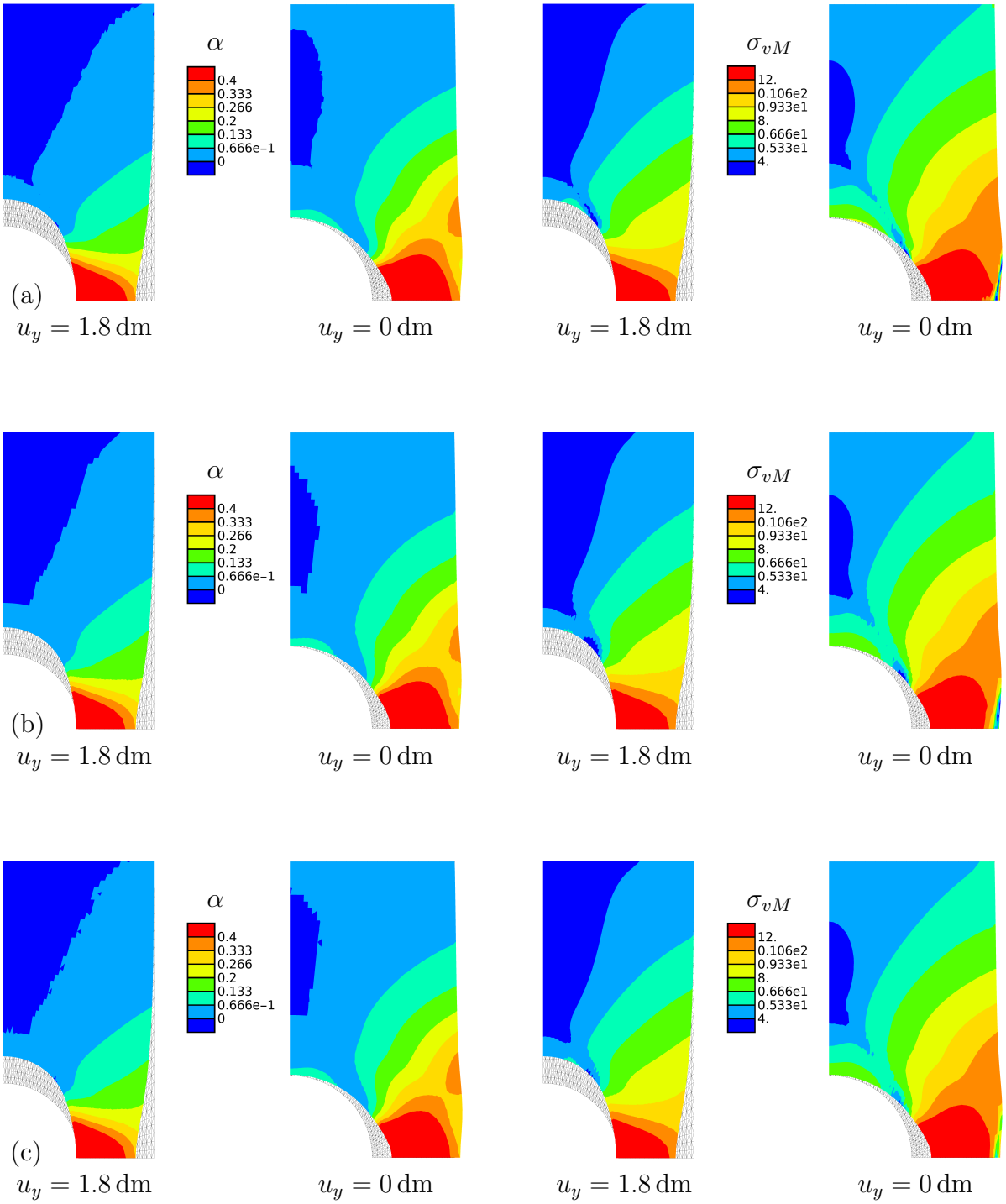

Figure 5.29: Plots of equivalent plastic strains represented by α and von Mises stress σ_{vM} at load level at $t = 1.8$ and $t = 3.6$ for the (a) $\mathcal{P}_2$, (b) $\mathcal{RT}_0\mathcal{P}_1$ and (c) $\mathcal{RT}_1\mathcal{P}_2$ element

6 Hybrid mixed finite element formulations

An additional approach within mixed finite element methods is given by hybrid finite element methods. In conforming finite element formulations, certain continuity requirements at inter-element boundaries have to be fulfilled, which are, e.g., the normal continuity of the traction vector or the continuity of the displacement field. Hybrid finite element formulations are based on the relaxation of these continuity requirements. Therefore, the continuities are introduced by means of constraints on the inter-element boundaries and enforced through the method of Lagrange multipliers, cf. Carey and Oden [70] and Boffi et al. [49]. The basic characteristic of hybrid methods is given by the simultaneous approximation of at least one field defined on the element and a Lagrange multiplier defined on the union of the boundaries of the elements, cf. Roberts and Thomas [192] and Carey and Oden [70]. For a detailed description of the general idea and theoretical assumptions, see, e.g., the publications of Carey and Oden [70], Atluri et al. [15], Roberts and Thomas [192], Brezzi and Fortin [56] and Atluri et al. [16], among others. Further discussions concerning mixed hybrid FEM can be found, e.g., in Pian and Chen [177], Punch and Atluri [185] for hybrid stress elements and an investigation on the existence and stability of general mixed hybrid elements is presented in Xue and Atluri [239; 240].

Generally, the continuity requirements are defined in a variational framework. For the LSFEM, a direct introduction of the relaxed constraint conditions on the inter-element boundaries, in equivalent norms, can be applied, cf. Bensow and Larson [28], Bensow and Larson [29], Ye and Zhang [241]. However, this approach is not considered in the following. Here, an application of a hybrid mixed finite element formulation is discussed, which follows the idea of adding the relaxed continuities in a variational formulation to the classical LS formulation. Therefore, the main aspects are:

- Presentation of preliminaries of hybrid FEM based on a LS formulation with continuous conforming approximation of $\boldsymbol{P}$ and $\boldsymbol{u}$,
- Relaxation of the continuity requirements and their enforcement through Lagrange multipliers on the inter-element and outer boundaries,
- Consideration of the limitation of the formulation and solvability based on the discretization of the resulting formulation,
- Numerical analysis of the discussed formulation for different hybrid stress and displacement approaches as well as comparison to continuous LS formulations.

For convenience, only a formulation with discontinuous stress and displacement approximation is presented in detail. However, the numerical analysis also shows results for formulations where only the stress field is approximated discontinuously. The applied discontinuous approximation of primary variables, as stresses and displacements in the LSFEM, on element level lead to more flexibility, since continuity can be reduced and enforced in a weaker sense. Moreover, it gives the opportunity of a static condensation of these variables and thus a reduction of the overall system size. Thus, the solution time can be reduced, since the effort for solving the system increases unproportional to the number of unknowns, see Braess [50].

6.1 Preliminaries of hybrid finite element formulations

Continuity, in general, is imposed on the interfaces of elements and on the outer boundaries by the chosen approximation spaces. For the previously discussed formulations, only conforming function spaces have been considered, which demand continuity of the displacement field and normal continuity of the stresses. Therefore, displacements $\boldsymbol{u}$ are approximated in $\mathcal{W}^{1,p}(\mathcal{B})$ and stresses $\boldsymbol{P}$ in $\mathcal{W}^{q}(\mathrm{div},\mathcal{B})$ for $2 \leq p,q \leq \infty$. The hybrid FEM utilizes discontinuous functions, without any continuity constraints over the element interfaces. The following suggestions are thus based on the idea of a relaxation of these continuity conditions and their weak enforcement. Therefore, Lagrange multipliers are introduced on inter-element and outer boundaries.

For the analysis of hybrid mixed finite element formulations, the body of interest $\mathcal{B}$ and the boundary $\partial\mathcal{B}$ are further subdivided. The triangulation of the placement $\mathcal{B}$ with finite elements is denoted by $\mathcal{T}$ and $\mathcal{E}$ defines the set of all sides in 2D (faces in 3D), including interior sides of the triangulation. In the following, $\partial\mathcal{T} := \partial\mathcal{T}_N \cup \partial\mathcal{T}_D$ denotes the triangulation of the outer boundary $\partial\mathcal{B}$, where $\partial\mathcal{T}_N$ and $\partial\mathcal{T}_D$ denote the triangulation of the Neumann and Dirichlet boundary. The interior boundaries are defined by $\partial\mathcal{T}_i = \mathcal{E}\backslash\partial\mathcal{T}$, where for completeness $\mathcal{E}\backslash\partial\mathcal{T} \cap \partial\mathcal{T}_N = \emptyset$ as well as $\mathcal{E}\backslash\partial\mathcal{T} \cap \partial\mathcal{T}_D = \emptyset$. Furthermore, two sides of an arbitrary inter-element boundary are denoted by the characters (+) and (-). A first application of a hybrid mixed finite element formulation in terms of a LSFEM is presented in Igelbüscher and Schröder [118] and Schröder and Igelbüscher [197] in the framework of small strain.

6.2 Hybrid finite elements based on a least-squares approach

The basis for the hybrid mixed formulation states the continuous mixed least-squares formulation, i.e.,

$$\begin{aligned} \mathcal{F}^{\mathrm{hyp}}(\boldsymbol{P},\boldsymbol{u}) &= \sum_{K\in\mathcal{T}} \frac{1}{2}\Big(\| \operatorname{Div}\boldsymbol{P} + \boldsymbol{f}\|^2_{\mathcal{L}^2(K)} + \|\boldsymbol{P}\cdot\boldsymbol{F}^T - 2\,\frac{\partial\psi(\boldsymbol{B})}{\partial\boldsymbol{B}}\cdot\boldsymbol{B}\|^2_{\mathcal{L}^2(K)} \\ &+ \|\boldsymbol{P}\cdot\boldsymbol{F}^T - \boldsymbol{F}\cdot\boldsymbol{P}^T\|^2_{\mathcal{L}^2(K)}\Big)\,, \end{aligned} \tag{6.1}$$

omitting the weighting parameters ω_i for convenience, cf. (5.3). The conforming function spaces are given by $\boldsymbol{u} \in \mathcal{W}^{1,p}(\mathcal{T})$ and $\boldsymbol{P} \in \mathcal{W}^{q}(\mathrm{div},\mathcal{T})$ with continuous functions. For the hybrid mixed approach, the continuity of the function spaces for (6.1) is relaxed and the formulation is extended by means of the corresponding continuity conditions enforced by Lagrange multipliers. For this, both primary variables $\boldsymbol{P}$ and $\boldsymbol{u}$ are approximated discontinuously with $\boldsymbol{u} \in \mathcal{L}^2(\mathcal{T})$ and $\boldsymbol{P} \in \mathcal{L}^2(\mathcal{T})$. Thus, the balance of momentum, the material law and the stress symmetry condition in (6.1) are fulfilled on each local element K, but the traction continuity

$$[\![\boldsymbol{P}\cdot\boldsymbol{N}]\!] = (\boldsymbol{P}\cdot\boldsymbol{N})^+ + (\boldsymbol{P}\cdot\boldsymbol{N})^- = \boldsymbol{0} \quad \text{on } \mathcal{E}\,, \tag{6.2}$$

and the displacement compatibility

$$[\![\boldsymbol{u}]\!] = \boldsymbol{u}^+ - \boldsymbol{u}^- = \boldsymbol{0} \quad \text{on } \mathcal{E}\,, \tag{6.3}$$

are not fulfilled directly. Therefore, (6.2) and (6.3) have to be enforced over the boundaries of the local elements in order to achieve the continuity conditions in a weak sense. The consideration and fulfillment of these continuity conditions is discussed in detail, e.g., in Xue and Atluri [239]. The Lagrange multiplier $\boldsymbol{\lambda}$ is applied for the jump of the traction vector $[\![\boldsymbol{P}\cdot\boldsymbol{N}]\!]$ on the inner skeleton $\partial\mathcal{T}_i$ and for the boundary tractions on the outer stress boundary $\partial\mathcal{T}_N$, which is defined by

$$[\![\boldsymbol{P}\cdot\boldsymbol{N}]\!]\cdot\boldsymbol{\lambda}=\boldsymbol{0}\quad\text{on }\partial\mathcal{T}_i\quad\text{and}\quad(\boldsymbol{P}\cdot\boldsymbol{N}-\bar{\boldsymbol{T}})\cdot\boldsymbol{\lambda}=\boldsymbol{0}\quad\text{on }\partial\mathcal{T}_N. \tag{6.4}$$

In a similar manner, the displacement compatibility is introduced with respect to the Lagrange multiplier $\boldsymbol{\mu}$, applied for the jump of the displacement vector $\boldsymbol{u}$ on $\partial\mathcal{T}_i$ and for the boundary displacements on $\partial\mathcal{T}_D$

$$[\![\boldsymbol{u}]\!]\cdot\boldsymbol{\mu}=\boldsymbol{0}\quad\text{on }\partial\mathcal{T}_i\quad\text{and}\quad(\boldsymbol{u}-\bar{\boldsymbol{u}})\cdot\boldsymbol{\mu}=\boldsymbol{0}\quad\text{on }\partial\mathcal{T}_D\,. \tag{6.5}$$

Here, the stress and displacement boundary conditions are denoted by $\bar{\boldsymbol{T}}$ and $\bar{\boldsymbol{u}}$. The setup of equations characterizing the hybrid hyperelastic problem is given by

$$\begin{aligned}
&\operatorname{Div}\boldsymbol{P}=-\boldsymbol{f} && \text{on } K\,,\\
&\boldsymbol{P}\cdot\boldsymbol{F}^T=2\,\partial_B\psi(\boldsymbol{B})\cdot\boldsymbol{B} && \text{on } K\,,\\
&\boldsymbol{P}\cdot\boldsymbol{F}^T=\boldsymbol{F}\cdot\boldsymbol{P}^T && \text{on } K\,,\\
&[\![\boldsymbol{P}\cdot\boldsymbol{N}]\!]\cdot\boldsymbol{\lambda}=\boldsymbol{0} && \text{on } \partial\mathcal{T}_i\,,\\
&(\boldsymbol{P}\cdot\boldsymbol{N}-\bar{\boldsymbol{T}})\cdot\boldsymbol{\lambda}=\boldsymbol{0} && \text{on } \partial\mathcal{T}_N\,,\\
&[\![\boldsymbol{u}]\!]\cdot\boldsymbol{\mu}=\boldsymbol{0} && \text{on } \partial\mathcal{T}_i\,,\\
&(\boldsymbol{u}-\bar{\boldsymbol{u}})\cdot\boldsymbol{\mu}=\boldsymbol{0} && \text{on } \partial\mathcal{T}_D\,.
\end{aligned} \tag{6.6}$$

The resulting hybrid mixed formulation $\mathcal{F}^{\text{hyb}}$ based on a mixed LS approach is given, with respect to (6.1), by

$$\mathcal{F}^{\text{hyb}}(\boldsymbol{P},\boldsymbol{u},\boldsymbol{\lambda},\boldsymbol{\mu})=\mathcal{F}^{\text{hyp}}(\boldsymbol{P},\boldsymbol{u})+\mathcal{F}_t(\boldsymbol{P},\boldsymbol{\lambda})+\mathcal{F}_u(\boldsymbol{u},\boldsymbol{\mu})\,, \tag{6.7}$$

where $\mathcal{F}_t$ and $\mathcal{F}_u$ are the variational formulations enforcing the traction continuity (6.2) and displacement compatibility (6.3) on the inter-element boundaries as well as for the boundary conditions on the outer boundary $\partial\mathcal{T}_D\cup\partial\mathcal{T}_N$. Here, $\mathcal{F}_t$ and $\mathcal{F}_u$ are defined by

$$\begin{aligned}
\mathcal{F}_t(\boldsymbol{P},\boldsymbol{\lambda}) &= \sum_{E\in\partial\mathcal{T}_i}\int_E[\![\boldsymbol{P}\cdot\boldsymbol{N}]\!]\cdot\boldsymbol{\lambda}\,\mathrm{d}A+\sum_{E\in\partial\mathcal{T}_N}\int_E(\boldsymbol{P}\cdot\boldsymbol{N}-\bar{\boldsymbol{T}})\cdot\boldsymbol{\lambda}\,\mathrm{d}A\,,\\
\mathcal{F}_u(\boldsymbol{u},\boldsymbol{\mu}) &= \sum_{E\in\partial\mathcal{T}_i}\int_E[\![\boldsymbol{u}]\!]\cdot\boldsymbol{\mu}\,\mathrm{d}A+\sum_{E\in\partial\mathcal{T}_D}\int_E(\boldsymbol{u}-\bar{\boldsymbol{u}})\cdot\boldsymbol{\mu}\,\mathrm{d}A\,.
\end{aligned} \tag{6.8}$$

Here, the hybrid mixed formulation with regard to discontinuous stresses and displacements is considered below. Nevertheless, a discontinuous approximation of only one of the fields can be achieved in a similar manner.
The approximation $(\boldsymbol{P},\boldsymbol{u},\boldsymbol{\lambda},\boldsymbol{\mu})\in\mathcal{S}^m\times\mathcal{V}^k\times\mathcal{X}^n\times\mathcal{Y}^o$, demands continuity of the

Lagrange multipliers and allows jumps for the stresses and displacements at inter-element boundaries (edges in 2D and faces in 3D). For convenience, the function $\boldsymbol{\lambda}$ on the skeleton is introduced with respect to continuous functions denoted by $\mathcal{C}^0(\partial\mathcal{T})$ on the triangulation of the inter-element boundaries $\partial\mathcal{T}$, cf. , e.g., Boffi et al. [49] and Devloo et al. [91], with

$$\mathcal{X}^{n,con} := \{\boldsymbol{\lambda} \in [\mathcal{C}^0(\partial\mathcal{T})]^d : \boldsymbol{\lambda}|_E \in [\mathcal{P}_n(E)]^d \,, \forall\, E \in \partial\mathcal{T}\}\,. \tag{6.9}$$

The upper character *dis* and *con* clarify the discontinuous and continuous approximation of the function space $\mathcal{X}^n$ of degree $n \geq 0$. The same holds for the approximation of $\boldsymbol{\mu} \in \mathcal{Y}^{o,con}$, i.e.,

$$\mathcal{Y}^{o,con} := \{\boldsymbol{\mu} \in [\mathcal{C}^0(\partial\mathcal{T})]^d : \boldsymbol{\mu}|_E \in [\mathcal{P}_o(E)]^d \,, \forall\, E \in \partial\mathcal{T}\}\,. \tag{6.10}$$

In this work, only $\mathcal{X}^{n,con}$ and $\mathcal{Y}^{o,con}$ are considered for $\boldsymbol{\lambda}$ and $\boldsymbol{\mu}$, i.e., the spaces of piecewise continuous polynomial functions of order $n, o \geq 0$, chosen as Lagrange ansatz functions denoted by $\mathcal{P}_n$ and $\mathcal{P}_o$. Furthermore, the discontinuous function spaces $\mathcal{S}^{m,dis}$ and $\mathcal{V}^{k,dis}$ are specified by

$$\begin{aligned} \mathcal{S}^{m,dis} &:= \{\boldsymbol{P} \in [\mathcal{L}^2(\mathcal{T})]^{d\times d} : \boldsymbol{P}|_K \in [\mathcal{RT}_m(K)]^{d\times d},\, \forall\, K \in \mathcal{T}\} \subseteq [\mathcal{P}_{m+1}(K)]^{d\times d}\,, \\ \mathcal{V}^{k,dis} &:= \{\boldsymbol{u} \in [\mathcal{L}^2(\mathcal{T})]^d : \boldsymbol{u}|_K \in [\mathcal{P}_k(K)]^d,\, \forall\, K \in \mathcal{T}\}\,, \end{aligned} \tag{6.11}$$

where $\mathcal{RT}_m$ denotes Raviart-Thomas functions of m-th order, in the following $\mathrm{d}\mathcal{RT}_m$ emphasizes that the approximation of $\boldsymbol{P} \in [\mathcal{L}^2(\mathcal{T})]^{d\times d}$ with $\boldsymbol{P}|_K \in \mathcal{RT}_m(K)$ is discontinuous. For $\mathcal{V}^{k,dis}$, a discontinuous approximation of $\boldsymbol{u}$ is applied, denoted further by $\mathrm{d}\mathcal{P}_k$, i.e., $\boldsymbol{u} \in [\mathcal{L}^2(\mathcal{T})]^d$ with $\boldsymbol{u}|_K \in \mathcal{P}_k(K)$, where Lagrange ansatz functions of degree k are considered, which are not restricted by any continuity condition between inter-element boundaries. Finally, these choices lead to a finite element type of the form $\mathrm{d}\mathcal{RT}_m\mathrm{d}\mathcal{P}_k\mathcal{P}_n\mathcal{P}_o$. One corresponding element type is exemplarily depicted in Figure 6.1.

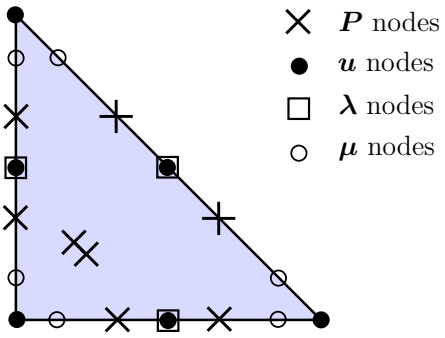

Figure 6.1: Hybrid mixed finite element $\mathrm{d}\mathcal{RT}_1\mathrm{d}\mathcal{P}_2\mathcal{P}_0\mathcal{P}_1$ with edge based degrees of freedom for the Lagrange multipliers $\boldsymbol{\lambda}$ and $\boldsymbol{\mu}$

As previously demonstrated, the construction of $\mathcal{RT}$ functions is more sophisticated than for polynomial functions of Lagrange type. $\mathcal{RT}$ functions are often constructed with respect to inner and outer moments, which is from an engineering point not straightforward. Furthermore, the same holds for the construction of $\mathcal{BDM}$ and $\mathcal{BDFM}$ functions and similar approximation approaches, see Brezzi et al. [57; 59] and Brezzi and Fortin [56]. Therefore, an alternative to the approximation with

$\mathcal{W}^q(\mathrm{div}, \mathcal{B})$ conforming functions is given by a scalar approximation of each component of the stress tensor, where each interpolation site has nine degrees of freedom determining the complete stress tensor. The corresponding finite element spaces, with $\boldsymbol{P} \in \mathcal{W}^{1,p}(K)$ and $\boldsymbol{u} \in \mathcal{W}^{1,p}(\mathcal{B})$ denoted by $\mathcal{S}_P^{m,dis}$ and $\mathcal{V}^{k,con}$ are defined as

$$\begin{aligned} \mathcal{S}_P^{m,dis} &:= \{\boldsymbol{P} \in [\mathcal{L}^2(\mathcal{T})]^{d\times d} : \boldsymbol{P}|_K \in [\mathcal{P}_m(K)]^{d\times d},\, \forall\, K \in \mathcal{T}\}\,, \\ \mathcal{V}^{k,con} &:= \{\boldsymbol{u} \in [\mathcal{C}^0(\mathcal{T})]^{d} : \boldsymbol{u}|_K \in [\mathcal{P}_k(K)]^{d},\, \forall\, K \in \mathcal{T}\}\,. \end{aligned} \tag{6.12}$$

For the sake of completeness the continuous function spaces $\mathcal{S}^{m,con}$ are defined by

$$\begin{aligned} \mathcal{S}^{m,con} &:= \{\boldsymbol{P} \in [\mathcal{C}^0(\mathcal{T})]^{d\times d} : \boldsymbol{P}|_K \in [\mathcal{RT}_m(K)]^{d\times d},\, \forall\, K \in \mathcal{T}\}\,, \\ \mathcal{S}_P^{m,con} &:= \{\boldsymbol{P} \in [\mathcal{C}^0(\mathcal{T})]^{d\times d} : \boldsymbol{P}|_K \in [\mathcal{P}_m(K)]^{d\times d},\, \forall\, K \in \mathcal{T}\}\,. \end{aligned} \tag{6.13}$$

The approximation approach $\boldsymbol{P} \in \mathcal{S}_P^{m,con}$ with $\mathcal{S}_P^{m,con} \subseteq [\mathcal{W}^{1,p}(\mathcal{B})]^{d\times d}$ lead to a drawback, based on the demanded continuity requirements of the stress field and continuity of the function space. The physical constraint is that the stresses are restricted to be normal continuous between two adjacent element edges ($d = 2$) or faces ($d = 3$). However, the stress approximation in $\mathcal{W}^{1,p}(\mathcal{B})$ yields a continuous stress field in all entries, which result into unphysically stress responses at material interfaces. This shortcoming can be solved by introducing a discontinuous stress approximation on element level and enforce only normal continuity of the stresses across the element boundaries. Thus, the restrictions of $\mathcal{W}^{1,p}(\mathcal{B})$ are reduced to $\mathcal{W}^q(\mathrm{div}, \mathcal{B})$. The advantage of utilizing $\boldsymbol{P} \in \mathcal{S}_P^{m,dis}$ is the straightforward application of approximation functions of any polynomial order and dimension. Therefore, finite elements such as $\mathcal{P}_m\mathcal{P}_k$ and $\mathrm{d}\mathcal{P}_m\mathcal{P}_k\mathcal{P}_n$ are also considered in the numerical analysis.

It has to be mentioned that the choice of $(\boldsymbol{P}, \boldsymbol{\lambda}) \in \mathcal{S}^{m,dis} \times \mathcal{Y}^{n,con}$ with $n = m$ for a $\mathrm{d}\mathcal{RT}_m\mathcal{P}_k\mathcal{P}_n$ formulation yields a similar solution as the continuous LS finite element formulation of same order, which is due to the limitation of the finite element solution spaces. A similar restriction is defined by the limitation principle for mixed formulations, which states that: "if the mixed formulation is capable of producing the same approximation of that produced by direct displacement form then it will in fact reproduce that form exactly and give identical and therefore not improved results", cf. Fraeijs De Veubeke [101]. The choice of $\mathcal{Y}^{0,con}$ and $\mathcal{S}^{0,dis}$, covers the properties of the continuous space $\mathcal{W}^q(\mathrm{div}, \mathcal{B})$. Since a constant approximation of the inter-element continuity with a constant stress approximation on the edge is directly obtained by the continuous stress approximation itself. This assumption holds for $m \geq 0$ and $n = m$. The application of this states that a hybrid mixed LS formulation gives identical results as the standard LS formulation if the hybrid mixed form is capable to produce the same approximation as the standard LS formulation with continuous approximation.

The transformation of the mesh structure from a continuous formulation $(\boldsymbol{P}, \boldsymbol{u}) \in \mathcal{S}^{m,con} \times \mathcal{V}^{k,con}$ to a hybrid mixed formulation $(\boldsymbol{P}, \boldsymbol{u}, \boldsymbol{\lambda}, \boldsymbol{\mu}) \in \mathcal{S}^{m,dis} \times \mathcal{V}^{k,dis} \times \mathcal{X}^{n,con} \times \mathcal{Y}^{o,con}$ is depicted in Figure 6.2. Therein, the skeleton, $\partial\mathcal{T} = \sum_i E_i$ with $i = 1, .., 9$, and the local elements K_j are divided, with the continuity conditions related to the skeleton and the primary variables on local element basis. Note that the interface elements E_i are not connected at their outer points and all $\boldsymbol{P}$ and $\boldsymbol{u}$ degrees of freedom are not assembled for the considered $\mathrm{d}\mathcal{RT}_m\mathrm{d}\mathcal{P}_k\mathcal{P}_n\mathcal{P}_o$ element type. For the $\mathrm{d}\mathcal{RT}_m\mathcal{P}_k\mathcal{P}_n$ and $\mathrm{d}\mathcal{P}_m\mathcal{P}_k\mathcal{P}_n$ elements, only the displacement degrees of freedom are assembled.

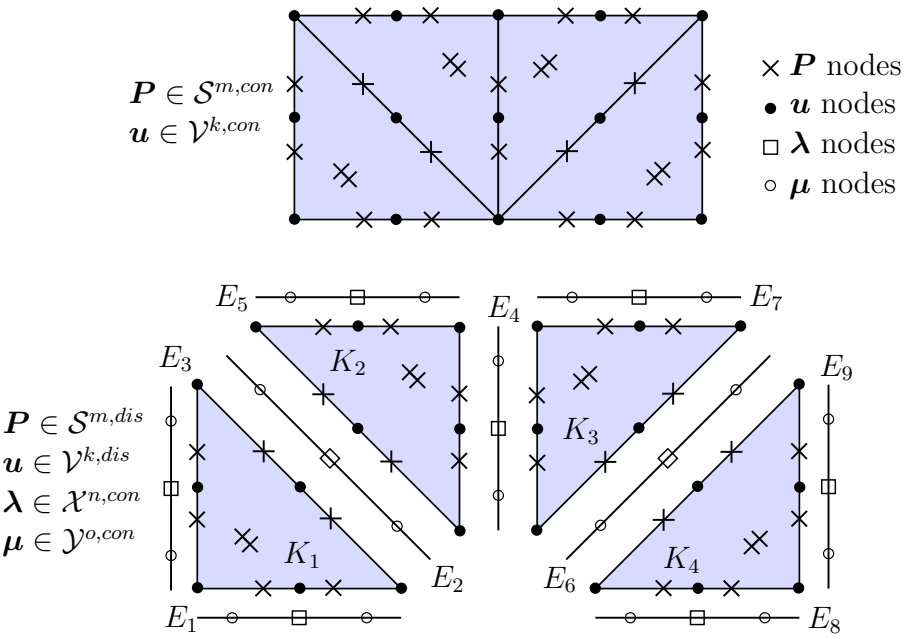

Figure 6.2: Continuous elements $\mathcal{RT}_1\mathcal{P}_2$ (top) and hybrid mixed elements $\mathrm{d}\mathcal{RT}_1\mathrm{d}\mathcal{P}_2\mathcal{P}_0\mathcal{P}_1$, resulting after relaxation of traction and displacement continuity and introduction of Lagrange multipliers on the inter-element boundaries (bottom)

6.3 Weak form and linearization of the hybrid mixed formulation

The derived first variation and linearization is given for a completely discontinuous approximation of the primary variables. Therefore, the first variations of the hybrid mixed formulation $\mathcal{F}^{\mathrm{hyb}}(\boldsymbol{P}, \boldsymbol{u}, \boldsymbol{\lambda}, \boldsymbol{\mu})$ are determined with respect to $\boldsymbol{P}, \boldsymbol{u}, \boldsymbol{\lambda}$ and $\boldsymbol{\mu}$ by

$$
\begin{aligned}
\delta_{\boldsymbol{P}}\mathcal{F}^{\mathrm{hyb}} &= \delta_{\boldsymbol{P}}\mathcal{F}^{\mathrm{hyp}} + \sum_{E \in \partial\mathcal{T}_i \bigcup \partial\mathcal{T}_N} \int_E [\![\delta\boldsymbol{P} \cdot \boldsymbol{N}]\!] \cdot \boldsymbol{\lambda}\, \mathrm{d}A\,, \\
\delta_{\boldsymbol{u}}\mathcal{F}^{\mathrm{hyb}} &= \delta_{\boldsymbol{u}}\mathcal{F}^{\mathrm{hyp}} + \sum_{E \in \partial\mathcal{T}_i \bigcup \partial\mathcal{T}_D} \int_E [\![\delta\boldsymbol{u}]\!] \cdot \boldsymbol{\mu}\, \mathrm{d}A\,, \\
\delta_{\boldsymbol{\lambda}}\mathcal{F}^{\mathrm{hyb}} &= \sum_{E \in \partial\mathcal{T}_i} \int_E \delta\boldsymbol{\lambda} \cdot [\![\boldsymbol{P} \cdot \boldsymbol{N}]\!]\, \mathrm{d}A + \sum_{E \in \partial\mathcal{T}_N} \int_E \delta\boldsymbol{\lambda} \cdot (\boldsymbol{P} \cdot \boldsymbol{N} - \bar{\boldsymbol{T}})\, \mathrm{d}A\,, \\
\delta_{\boldsymbol{\mu}}\mathcal{F}^{\mathrm{hyb}} &= \sum_{E \in \partial\mathcal{T}_i} \int_E \delta\boldsymbol{\mu} \cdot [\![\boldsymbol{u}]\!]\, \mathrm{d}A + \sum_{E \in \partial\mathcal{T}_D} \int_E \delta\boldsymbol{\mu} \cdot (\boldsymbol{u} - \bar{\boldsymbol{u}})\, \mathrm{d}A\,,
\end{aligned}
\tag{6.14}
$$

where the first variations of $\mathcal{F}^{\mathrm{hyp}}$ are abbreviated by $\delta_{\boldsymbol{P}}\mathcal{F}^{\mathrm{hyp}}$ and $\delta_{\boldsymbol{u}}\mathcal{F}^{\mathrm{hyp}}$, see (5.4). Here, the variation of the jump of the traction vector at the skeleton $\partial\mathcal{T}$ and the outer stress boundary is summarized with $\partial\mathcal{T}_i \cup \partial\mathcal{T}_N$ and the jump of the displacement vector at $\partial\mathcal{T}_i$ and the outer displacement boundary by $\partial\mathcal{T}_i \cup \partial\mathcal{T}_D$. The first variation (6.14) is solved by finding $(\boldsymbol{P}, \boldsymbol{u}, \boldsymbol{\lambda}, \boldsymbol{\mu}) \in \mathcal{S}^{m,dis} \times \mathcal{V}^{k,dis} \times \mathcal{X}^{n,con} \times \mathcal{Y}^{o,con}$, see (6.9), (6.10), (6.11) such that $\delta_{\boldsymbol{P},\boldsymbol{u},\boldsymbol{\lambda},\boldsymbol{\mu}}\mathcal{F}^{\mathrm{hyb}} = \boldsymbol{0}\ \forall\, (\delta\boldsymbol{P}, \delta\boldsymbol{u}, \delta\boldsymbol{\lambda}, \delta\boldsymbol{\mu}) \in \mathcal{S}^{m,dis} \times \mathcal{V}^{k,dis} \times \mathcal{X}^{n,con} \times \mathcal{Y}^{o,con}$.

For completeness, the linearization of the mixed hybrid formulation (6.7) reads

$$\begin{aligned}
\Delta\delta_{\boldsymbol{P}}\mathcal{F}^{\mathrm{hyb}} &= \Delta\delta_{\boldsymbol{P}}\mathcal{F}^{\mathrm{hyp}} + \sum_{E\in\partial\mathcal{T}_i\bigcup\partial\mathcal{T}_N}\int_E \delta\boldsymbol{\lambda}\cdot[\![\Delta\boldsymbol{P}\cdot\boldsymbol{N}]\!]\,\mathrm{d}A\,,\\
\Delta\delta_{\boldsymbol{u}}\mathcal{F}^{\mathrm{hyb}} &= \Delta\delta_{\boldsymbol{u}}\mathcal{F}^{\mathrm{hyp}} + \sum_{E\in\partial\mathcal{T}_i\bigcup\partial\mathcal{T}_D}\int_E \delta\boldsymbol{\mu}\cdot[\![\Delta\boldsymbol{u}]\!]\,\mathrm{d}A\,,\\
\Delta\delta_{\boldsymbol{\lambda}}\mathcal{F}^{\mathrm{hyb}} &= \sum_{E\in\partial\mathcal{T}_i\bigcup\partial\mathcal{T}_N}\int_E [\![\delta\boldsymbol{P}\cdot\boldsymbol{N}]\!]\cdot\Delta\boldsymbol{\lambda}\,\mathrm{d}A\,,\\
\Delta\delta_{\boldsymbol{\mu}}\mathcal{F}^{\mathrm{hyb}} &= \sum_{E\in\partial\mathcal{T}_i\bigcup\partial\mathcal{T}_D}\int_E [\![\delta\boldsymbol{u}]\!]\cdot\Delta\boldsymbol{\mu}\,\mathrm{d}A\,,
\end{aligned} \tag{6.15}$$

where, e.g., the sum of all increments with respect to the first variation of the stresses is denoted by

$$\Delta\delta_{\boldsymbol{P}}\mathcal{F}^{\mathrm{hyb}} = \sum_{i=\boldsymbol{P},\boldsymbol{u},\boldsymbol{\lambda},\boldsymbol{\mu}} \Delta_i\delta_{\boldsymbol{P}}\mathcal{F}^{\mathrm{hyb}}\,. \tag{6.16}$$

The abbreviations $\Delta\delta_{\boldsymbol{P}}\mathcal{F}^{\mathrm{hyp}}$ and $\Delta\delta_{\boldsymbol{u}}\mathcal{F}^{\mathrm{hyp}}$ for the linearized hyperelastic LS functional are given in (5.5) and (5.6). The resulting zero matrices are $\Delta_{\boldsymbol{u}}\delta_{\boldsymbol{\lambda}}\mathcal{F}^{\mathrm{hyb}} = \Delta_{\boldsymbol{\lambda}}\delta_{\boldsymbol{u}}\mathcal{F}^{\mathrm{hyb}} = \Delta_{\boldsymbol{\lambda}}\delta_{\boldsymbol{\lambda}}\mathcal{F}^{\mathrm{hyb}} = \boldsymbol{0}$, $\Delta_{\boldsymbol{\mu}}\delta_{\boldsymbol{P}}\mathcal{F}^{\mathrm{hyb}} = \Delta_{\boldsymbol{P}}\delta_{\boldsymbol{\mu}}\mathcal{F}^{\mathrm{hyb}} = \Delta_{\boldsymbol{\mu}}\delta_{\boldsymbol{\mu}}\mathcal{F}^{\mathrm{hyb}} = \boldsymbol{0}$ and $\Delta_{\boldsymbol{\lambda}}\delta_{\boldsymbol{\mu}}\mathcal{F}^{\mathrm{hyb}} = \Delta_{\boldsymbol{\mu}}\delta_{\boldsymbol{\lambda}}\mathcal{F}^{\mathrm{hyb}} = \boldsymbol{0}$, cf. Igelbüscher and Schröder [118] and Schröder and Igelbüscher [197] for a formulation at small strains.

6.4 Discretization and implementation aspects

For the representation of the discretized unknown fields and their variational counterparts in matrix notation denoted by subscript h, the following relations are introduced, $\boldsymbol{\lambda}_h = \mathbb{N}_\lambda\,\boldsymbol{d}_\lambda$, $\delta\boldsymbol{\lambda}_h = \mathbb{N}_\lambda\,\delta\boldsymbol{d}_\lambda$, $\Delta\boldsymbol{\lambda}_h = \mathbb{N}_\lambda\,\Delta\boldsymbol{d}_\lambda$, $\boldsymbol{\mu}_h = \mathbb{N}_\mu\,\boldsymbol{d}_\mu$, $\delta\boldsymbol{\mu}_h = \mathbb{N}_\mu\,\delta\boldsymbol{d}_\mu$, $\Delta\boldsymbol{\mu}_h = \mathbb{N}_\mu\,\Delta\boldsymbol{d}_\mu$. Nodal degrees of freedom for the Lagrange multipliers are denoted by $\boldsymbol{d}_\lambda$ and $\boldsymbol{d}_\mu$, respectively. Furthermore, the matrices $\mathbb{N}_\lambda$ and $\mathbb{N}_\mu$ consist of Lagrange shape functions. The discretization of stresses and displacements is similar to previous cases. The non-vanishing parts of the discrete formulations, for convenience without the corresponding weighting parameters ω_i, are given by

$$\delta_{\boldsymbol{P}}\mathcal{F}_h^{\mathrm{hyb}} = \delta\boldsymbol{d}_P^T\,\boldsymbol{r}_P^{\mathrm{e}}\,,\ \delta_{\boldsymbol{u}}\mathcal{F}_h^{\mathrm{hyb}} = \delta\boldsymbol{d}_u^T\,\boldsymbol{r}_u^{\mathrm{e}}\,,\ \delta_{\boldsymbol{\lambda}}\mathcal{F}_h^{\mathrm{hyb}} = \delta\boldsymbol{d}_\lambda^T\,\boldsymbol{r}_\lambda^{\mathrm{e}} \text{ and } \delta_{\boldsymbol{\mu}}\mathcal{F}_h^{\mathrm{hyb}} = \delta\boldsymbol{d}_\mu^T\,\boldsymbol{r}_\mu^{\mathrm{e}}\,, \tag{6.17}$$

and further

$$\begin{aligned}
\Delta\delta_{\boldsymbol{P}}\mathcal{F}_h^{\mathrm{hyb}} &= \underbrace{\delta\boldsymbol{d}_P^T\,\boldsymbol{k}_{PP}^{\mathrm{e}}\,\Delta\boldsymbol{d}_P}_{\Delta_{\boldsymbol{P}}\delta_{\boldsymbol{P}}\mathcal{F}_h^{\mathrm{hyb}}} + \underbrace{\delta\boldsymbol{d}_P^T\,\boldsymbol{k}_{Pu}^{\mathrm{e}}\,\Delta\boldsymbol{d}_u}_{\Delta_{\boldsymbol{u}}\delta_{\boldsymbol{P}}\mathcal{F}_h^{\mathrm{hyb}}} + \underbrace{\delta\boldsymbol{d}_P^T\,\boldsymbol{k}_{P\lambda}^{\mathrm{e}}\,\Delta\boldsymbol{d}_\lambda}_{\Delta_{\boldsymbol{\lambda}}\delta_{\boldsymbol{P}}\mathcal{F}_h^{\mathrm{hyb}}}\,,\\
\Delta\delta_{\boldsymbol{u}}\mathcal{F}_h^{\mathrm{hyb}} &= \underbrace{\delta\boldsymbol{d}_u^T\,\boldsymbol{k}_{uP}^{\mathrm{e}}\,\Delta\boldsymbol{d}_P}_{\Delta_{\boldsymbol{P}}\delta_{\boldsymbol{u}}\mathcal{F}_h^{\mathrm{hyb}}} + \underbrace{\delta\boldsymbol{d}_u^T\,\boldsymbol{k}_{uu}^{\mathrm{e}}\,\Delta\boldsymbol{d}_u}_{\Delta_{\boldsymbol{u}}\delta_{\boldsymbol{u}}\mathcal{F}_h^{\mathrm{hyb}}} + \underbrace{\delta\boldsymbol{d}_u^T\,\boldsymbol{k}_{u\mu}^{\mathrm{e}}\,\Delta\boldsymbol{d}_\mu}_{\Delta_{\boldsymbol{\mu}}\delta_{\boldsymbol{u}}\mathcal{F}_h^{\mathrm{hyb}}}\,,\\
\Delta\delta_{\boldsymbol{\lambda}}\mathcal{F}_h^{\mathrm{hyb}} &= \underbrace{\delta\boldsymbol{d}_\lambda^T\,\boldsymbol{k}_{\lambda P}^{\mathrm{e}}\,\Delta\boldsymbol{d}_P}_{\Delta_{\boldsymbol{P}}\delta_{\boldsymbol{\lambda}}\mathcal{F}_h^{\mathrm{hyb}}} \qquad \text{and} \qquad \Delta\delta_{\boldsymbol{\mu}}\mathcal{F}_h^{\mathrm{hyb}} = \underbrace{\delta\boldsymbol{d}_\mu^T\,\boldsymbol{k}_{\mu u}^{\mathrm{e}}\,\Delta\boldsymbol{d}_u}_{\Delta_{\boldsymbol{u}}\delta_{\boldsymbol{\mu}}\mathcal{F}_h^{\mathrm{hyb}}}\,.
\end{aligned} \tag{6.18}$$

For convenience, a detailed representation of the discretized form is omitted. The final system of equations for the considered hybrid approach reads

$$\begin{bmatrix} \boldsymbol{k}^{\mathrm{e}}_{PP} & \boldsymbol{k}^{\mathrm{e}}_{Pu} & \boldsymbol{k}^{\mathrm{e}}_{P\lambda} & \mathbf{0} \\ \boldsymbol{k}^{\mathrm{e}}_{uP} & \boldsymbol{k}^{\mathrm{e}}_{uu} & \mathbf{0} & \boldsymbol{k}^{\mathrm{e}}_{u\mu} \\ \boldsymbol{k}^{\mathrm{e}}_{\lambda P} & \mathbf{0} & \mathbf{0} & \mathbf{0} \\ \mathbf{0} & \boldsymbol{k}^{\mathrm{e}}_{\mu u} & \mathbf{0} & \mathbf{0} \end{bmatrix} \begin{bmatrix} \boldsymbol{d}_P \\ \boldsymbol{d}_u \\ \boldsymbol{d}_\lambda \\ \boldsymbol{d}_\mu \end{bmatrix} = - \begin{bmatrix} \boldsymbol{r}^{\mathrm{e}}_P \\ \boldsymbol{r}^{\mathrm{e}}_u \\ \boldsymbol{r}^{\mathrm{e}}_\lambda \\ \boldsymbol{r}^{\mathrm{e}}_\mu \end{bmatrix} \tag{6.19}$$

and can be written in a reduced form as

$$\begin{bmatrix} \mathbb{A} & \mathbb{D}^T \\ \mathbb{D} & \mathbf{0} \end{bmatrix} \begin{bmatrix} \boldsymbol{d}_{P,u} \\ \boldsymbol{d}_{\lambda,\mu} \end{bmatrix} = - \begin{bmatrix} \boldsymbol{r}_{P,u} \\ \boldsymbol{r}_{\lambda,\mu} \end{bmatrix} . \tag{6.20}$$

The resulting system matrix illustrates the typical saddle point structure with

$$\mathbb{A} = \begin{bmatrix} \boldsymbol{k}^{\mathrm{e}}_{PP} & \boldsymbol{k}^{\mathrm{e}}_{Pu} \\ \boldsymbol{k}^{\mathrm{e}}_{uP} & \boldsymbol{k}^{\mathrm{e}}_{uu} \end{bmatrix} , \quad \mathbb{D} = \begin{bmatrix} \boldsymbol{k}^{\mathrm{e}}_{\lambda P} & \mathbf{0} \\ \mathbf{0} & \boldsymbol{k}^{\mathrm{e}}_{\mu u} \end{bmatrix} , \quad \begin{aligned} \boldsymbol{d}_{P,u} &= [\boldsymbol{d}_P, \boldsymbol{d}_u]^T , \quad \boldsymbol{r}^{\mathrm{e}}_{P,u} = [\boldsymbol{r}^{\mathrm{e}}_P, \boldsymbol{r}^{\mathrm{e}}_u]^T , \\ \boldsymbol{d}_{\lambda,\mu} &= [\boldsymbol{d}_\lambda, \boldsymbol{d}_\mu]^T , \quad \boldsymbol{r}^{\mathrm{e}}_{\lambda,\mu} = [\boldsymbol{r}^{\mathrm{e}}_\lambda, \boldsymbol{r}^{\mathrm{e}}_\mu]^T , \end{aligned} \tag{6.21}$$

where $\mathbb{A}$ can be seen as the classical matrix representation of a LS formulation and $\mathbb{D}$ contains the continuity constraints. Obviously, the hybridization of the classical LSFEM leads to a saddle point problem. This is one of the properties of hybrid formulations, cf., e.g., Carey and Oden [70] and Boffi et al. [49]. Consequently, the stability in terms of the chosen finite element approximation must at least be estimated, which is discussed later on.

Due to the discontinuous approximation of at least one field in the hybrid formulation, a static condensation of this quantity can be performed on element level in order to reduce the system size. For a static condensation, e.g., with respect to $\boldsymbol{P}$, it has to be ensured that the corresponding matrix $\boldsymbol{k}^{\mathrm{e}}_{PP}$, see (6.19), is invertible. This is a priori given since the matrices for $\boldsymbol{u}$ and $\boldsymbol{P}$ are constructed based on a squared $\mathcal{L}^2(\mathcal{B})$-norm and therefore inherently fulfill the properties of positive definite and symmetric matrices with respect to corresponding boundary conditions, which guarantee that the inverse of the matrix exists. The condensed system yields the same solution as the complete system, but since the effort for solving the system increases unproportionally to the number of unknowns, it is preferable to solve the reduced system only, cf. Braess [50]. Therefore, an example for a reduced element formulation is given within the numerical analysis in Chapter 6.6.1.

6.5 Remarks on hybrid mixed FEM based on a LS formulation

In the following, some remarks concerning the presented hybrid mixed formulation are discussed. As a first point, the extension of the LS functional (6.1), in terms of the continuity conditions in a variational setup, leads to a loss of at least some of the a priori given advantages of the least-squares method. These are, e.g., the loss of a positive (semi-) definite system matrix and the fact that the formulation itself cannot be applied as a posteriori error estimator. As noted previously, the resulting system matrices reveal the

classical saddle point structure. This observation is crucial, especially for the restriction due to stability conditions. Therefore, the choice of the polynomial order for the Lagrange multipliers in combination with the considered approximation order of displacements and stresses is limited and have to be balanced carefully, see, e.g., Brezzi and Fortin [56], Boffi et al. [49] and Auricchio et al. [17]. It has to be noted that the LSFEM as a classical approach does not require balanced function spaces.
However, in the course of this work, only basic assumptions on the properties of the system are considered, which are necessary but unfortunately not sufficient conditions. The count condition or count criterion, cf. Zienkiewicz et al. [249; 250], yield a first estimate on the stability of the approach. The basic idea is given by restricting the number of constraint variables (in general Lagrange multipliers) in a system by the number of primary variables. Hereby, the non-singularity of the matrices can be ensured in a purely algebraic manner, which can be seen as a first algebraic requirement for stability. In the following, the condition is derived with respect to the system of equations for one typical element and based on the consideration of the rank of the single matrices. For a two and a three field formulation with one and two constraint variables, the conditions are discussed in Zienkiewicz et al. [249; 250]. In analogy to the proposed idea in Zienkiewicz et al. [250], for mixed formulations, the reduced system matrix (6.20) is considered. This results in the estimates:

$$n_{\mathrm{dof},P} \geq n_{\mathrm{dof},\lambda}\,, \quad n_{\mathrm{dof},u} \geq n_{\mathrm{dof},\mu} \quad \text{and thus} \quad n_{\mathrm{dof},P} + n_{\mathrm{dof},u} \geq n_{\mathrm{dof},\lambda} + n_{\mathrm{dof},\mu}\,. \tag{6.22}$$

This states that the number of unknowns of the constraint variables $n_{\mathrm{dof},\lambda} + n_{\mathrm{dof}\mu}$ in $\boldsymbol{d}_{\lambda,\mu}$, i.e., the number of degrees of freedoms of the Lagrange multipliers, have to be smaller than or equal to the number of unknowns $n_{\mathrm{dof},P} + n_{\mathrm{dof},u}$ in $\boldsymbol{d}_{P,u}$ to ensure the necessary but not sufficient criterion for stability. Furthermore, there are similar conditions for primal and dual mixed hybrid methods described in Carey and Oden [70] and Lee [150]. The primal and dual hybrid mixed formulations are defined based on the underlying continuous formulations, cf. Chapter 3.2.2 for the primal and dual Hellinger-Reissner formulations. From this, requirements related to the polynomial degree can be derived, based on the discussion in Carey and Oden [70], chapter 3.4. The transfer of these assumptions, for the here discussed hybrid mixed approach, in a numerical manner, provides

$$k + m > n + 1 \quad \text{or} \quad k + m > n + o\,, \tag{6.23}$$

depending on the considered hybrid formulation with relaxed stress continuity ($\mathrm{d}\mathcal{RT}_m\mathcal{P}_k\mathcal{P}_n$, $\mathrm{d}\mathcal{P}_k\mathcal{P}_k\mathcal{P}_n$) and relaxed stress and displacement continuities ($\mathrm{d}\mathcal{RT}_m\mathrm{d}\mathcal{P}_k\mathcal{P}_n\mathcal{P}_o$).
For $\boldsymbol{\mu} \in \mathcal{Y}^{o,con}$, a further restriction is defined with $o \geq 1$, i.e, at least two interpolation sites have to be given on an edge. This condition has to be applied to the constraint on the inter-element boundaries, in order to circumvent rigid body rotations of the elements. Similar to that, the numerical analysis reveals a limitation on the minimum assumptions of the multiplier $\boldsymbol{\lambda}$. This can be explained by the underlying properties of the LSFEM. If the system of equations of a typical element is considered, without taking into account boundary conditions, zero eigenvalues result in the system. Such values are often declared as rigid body rotations. In order to guarantee a unique solvability of the equation system, the rigid body rotations must be removed, which is generally done by applying corresponding displacement boundary conditions. For the LSFEM, in addition to these rigid body modes, equivalent terms occur related to the stresses, which are referred to as spurious

stress modes in the following. They are removed from the system, analogously to the rigid body rotations, by prescribing corresponding stress boundaries essentially. For the hybrid formulation, based on the LS functional, this results in a minimum requirement for the constraint conditions on the boundary, which restricts the choice of the polynomial order of the multiplier $\boldsymbol{\lambda}$ to $n \geq m-1$. In the numerical analysis of the presented formulations, the assumptions made are taken into account in order to ensure stability, at least through algebraic estimates.

6.6 Numerical analysis for hybrid mixed finite element formulations

For the numerical examples, different finite element types are considered. These are given by continuous LS formulations $\mathcal{RT}_m\mathcal{P}_k$ and $\mathcal{P}_m\mathcal{P}_k$ in order to compare the hybrid and classical LS formulations. Furthermore, discontinuous stress approximations, i.e., $\boldsymbol{P} \in \mathcal{L}^2(\mathcal{T})$, are performed on element level with respect to Raviart-Thomas as well as Lagrange type functions in $\mathcal{S}^{m,dis}$ and $\mathcal{S}_P^{m,dis}$, denoted by $\mathrm{d}\mathcal{RT}_m\mathcal{P}_k\mathcal{P}_n$ and $\mathrm{d}\mathcal{P}_m\mathcal{P}_k\mathcal{P}_n$ elements. Additionally, the discontinuous approach with $(\boldsymbol{P},\boldsymbol{u}) \in \mathcal{S}^{m,dis} \times \mathcal{V}^{k,dis}$ and $(\boldsymbol{\lambda},\boldsymbol{\mu}) \in \mathcal{X}^{n,con} \times \mathcal{Y}^{o,con}$ is given by $\mathrm{d}\mathcal{RT}_m\mathrm{d}\mathcal{P}_k\mathcal{P}_n\mathcal{P}_o$. An overview of the continuous and hybrid finite elements, with their related function spaces, is listed in Table 6.1.

Table 6.1: Overview on LS and hybrid mixed elements with associated function spaces

Element type	Related function spaces
$\mathcal{RT}_m\mathcal{P}_k$	$(\boldsymbol{P},\boldsymbol{u}) \in \mathcal{S}^{m,con} \times \mathcal{V}^{k,con}$; (6.13), (6.12)
$\mathcal{P}_m\mathcal{P}_k$	$(\boldsymbol{P},\boldsymbol{u}) \in \mathcal{S}_P^{m,con} \times \mathcal{V}^{k,con}$; (6.13), (6.12)
$\mathrm{d}\mathcal{RT}_m\mathcal{P}_k\mathcal{P}_n$	$(\boldsymbol{P},\boldsymbol{u},\boldsymbol{\lambda}) \in \mathcal{S}^{m,dis} \times \mathcal{V}^{k,con} \times \mathcal{X}^{n,con}$; (6.11), (6.12), (6.9)
$\mathrm{d}\mathcal{P}_m\mathcal{P}_k\mathcal{P}_n$	$(\boldsymbol{P},\boldsymbol{u},\boldsymbol{\lambda}) \in \mathcal{S}_P^{m,dis} \times \mathcal{V}^{k,con} \times \mathcal{X}^{n,con}$; (6.12), (6.9)
$\mathrm{d}\mathcal{RT}_m\mathrm{d}\mathcal{P}_k\mathcal{P}_n\mathcal{P}_o$	$(\boldsymbol{P},\boldsymbol{u},\boldsymbol{\lambda},\boldsymbol{\mu}) \in \mathcal{S}^{m,dis} \times \mathcal{V}^{k,dis} \times \mathcal{X}^{n,con} \times \mathcal{Y}^{n,con}$; (6.11), (6.9), (6.10)

In the first investigated example, a fully constrained block is subjected to a prescribed body force. The element performance is validated with respect to the convergence rates of the displacements and stresses in associated norms based on an analytical solution of the problem. The second example illustrates the applicability of a stress approximation with Lagrange shape functions. For a continuous LS formulation, this approximation is non-conforming and provides non-physical stress distributions at material interfaces.

6.6.1 Fully constrained block

In order to validate the proposed hybrid mixed formulations, a fully constrained block with a square domain $\mathcal{B} = (-1,1) \times (-1,1)\,\mathrm{mm}$, subjected by a body force, is analyzed. Here, two material setups are considered, given in Figure 6.3 with the corresponding boundary conditions. Furthermore, for a discontinuous displacement approach the multiplier $\boldsymbol{\mu}$ has to be fixed at one point on the inter-element boundary of the four elements in the corners, see the mesh structure in Figure 6.3, to avoid rigid body rotations.

System setup:

$$
\begin{aligned}
\boldsymbol{u} &= (0,0)^T \text{ mm on } \partial\mathcal{T}_D \\
\lambda &= 2 \text{ and } 100 \text{ kN/mm}^2 \\
\mu &= 1 \text{ kN/mm}^2 \\
E &= \tfrac{8}{3} \text{ and } 2.9901 \text{ kN/mm}^2 \\
\nu &= \tfrac{1}{3} \text{ and } 0.49505 \\
\boldsymbol{P} \in \mathcal{S}^{m,d}\colon \boldsymbol{\lambda} &= (0,0)^T \text{ kN/mm}^2 \text{ on } \partial\mathcal{T}_D \\
\boldsymbol{P} \in \mathcal{S}_P^{m,d}\colon \boldsymbol{\lambda} &= (0,0)^T \text{ kN/mm}^2 \text{ on } \partial\mathcal{T}_D
\end{aligned}
$$

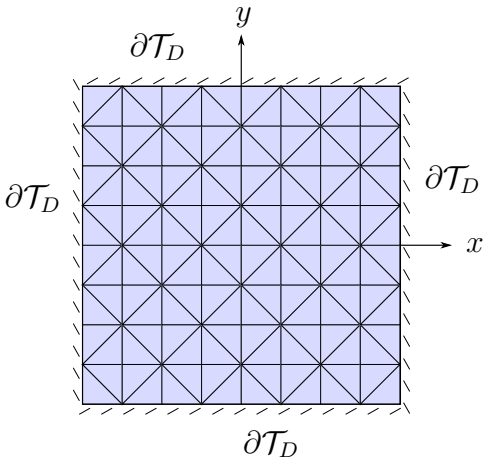

Figure 6.3: Material setup, boundary conditions and geometry of fully constrained block

An analytical solution is considered, i.e.,

$$u_x = \frac{1}{4}\Big((x^2-1)^2(y^2-1)y\Big) \quad \text{and} \quad u_y = \frac{1}{4}\Big((y^2-1)^2(1-x^2)x\Big)\,, \tag{6.24}$$

which is zero on the boundary $\partial\mathcal{T}_D$ and in the center, cf. Auricchio et al. [18]. The corresponding body force is determined by an inverse calculation procedure. Therefore, the balance of momentum is evaluated, in which the stresses $\boldsymbol{P}$ are determined by

$$\boldsymbol{P} = \rho_0 \frac{\partial \psi}{\partial \boldsymbol{F}} = 2\,\rho_0\,\boldsymbol{F}\,\frac{\partial \psi(\boldsymbol{C})}{\partial \boldsymbol{C}} = \boldsymbol{F}\cdot\boldsymbol{S} \quad \text{with} \quad \boldsymbol{S} = \mu(\boldsymbol{1}-\boldsymbol{C}^{-1}) + \frac{\lambda}{2}(I_1(\boldsymbol{C})-1)\boldsymbol{C}^{-1}\,, \tag{6.25}$$

following from $\boldsymbol{S} = 2\,\rho_0\,\partial_C\,\psi(\boldsymbol{C})$ with (2.57). The deformation gradient $\boldsymbol{F}$ is determined with respect to the gradient of the analytical displacement solution (6.24). For completeness, the resulting body force $\boldsymbol{f}$ and stresses $\boldsymbol{P}$ are given in Appendix 8.3.
The convergence of the displacements and stresses is analyzed in the $\mathcal{L}^2(\mathcal{B})$-norm. Here, the natural choice for the displacement convergence would be the $\mathcal{W}^{m,p}(\mathcal{B})$-norm, cf. (3.7), which is for $m = 0$ equivalent to the $\mathcal{L}^p(\mathcal{B})$-norm, see (3.2). This is permissible, since all p-norms are equivalent to each other, i.e., each norm pairing differs by a constant factor, which can be calculated based on the norms themselves, see Bochev and Gunzburger [43]. Consequently, the considered $\mathcal{L}^2(\mathcal{B})$-norms are given by

$$
\begin{aligned}
\|\boldsymbol{u}-\boldsymbol{u}_h\|_{\mathcal{L}^2(\mathcal{B})} &= \left(\int_{\mathcal{B}} (\boldsymbol{u}-\boldsymbol{u}_h)\cdot(\boldsymbol{u}-\boldsymbol{u}_h)\,\mathrm{d}V\right)^{1/2}, \\
\|\boldsymbol{P}-\boldsymbol{P}_h\|_{\mathcal{L}^2(\mathcal{B})} &= \left(\int_{\mathcal{B}} (\boldsymbol{P}-\boldsymbol{P}_h):(\boldsymbol{P}-\boldsymbol{P}_h)\,\mathrm{d}V\right)^{1/2}.
\end{aligned} \tag{6.26}
$$

Here, the analytical solutions are denoted by $\boldsymbol{u}$, $\boldsymbol{P}$ and $\boldsymbol{u}_h$, $\boldsymbol{P}_h$ are the approximated solutions. The order of convergence depends on the polynomial order of the finite element k, the dimension of the problem d, the regularity of the solution and the corresponding norm, cf. Braess [50] §7. This can be concluded by

$$\|\boldsymbol{P}-\boldsymbol{P}_h\|_{\mathcal{L}^2(\mathcal{B})} \leq c\,n_{dof}^{-\frac{k+1}{d}} \quad \text{and} \quad \|\boldsymbol{u}-\boldsymbol{u}_h\|_{\mathcal{L}^2(\mathcal{B})} \leq c\,n_{dof}^{-\frac{k+1}{d}}\,, \tag{6.27}$$

with some positive constant c. This holds for all complete polynomials up to order $k+1$, where the order of convergence is often denoted by $\mathcal{O}(h^{\frac{k+1}{d}})$. The results for the continuous

and discontinuous finite element combinations are illustrated for $\|\boldsymbol{u}-\boldsymbol{u}_h\|_{\mathcal{L}^2(\mathcal{B})}$ in Figure 6.4 and 6.5 as well as in Figure 6.6 and 6.7 for the stress convergence $\|\boldsymbol{P}-\boldsymbol{P}_h\|_{\mathcal{L}^2(\mathcal{B})}$. For the choice of a $\mathcal{W}^{1,p}(\mathcal{B})$-norm, the resulting convergence order can be reduced, compared to the results within the $\mathcal{L}^2(\mathcal{B})$-norm, since also restrictions to the derivatives of the associated fields are considered.
For the continuous formulations $\mathcal{RT}_m\mathcal{P}_k$ and $\mathcal{P}_m\mathcal{P}_k$, the optimal convergence order, based on (6.27), is achieved for the compressible and the slightly incompressible material setup, see Figure 6.3. Only the displacement convergence in the $\mathcal{L}^2(\mathcal{B})$-norm for the $\mathcal{P}_1\mathcal{P}_2$ element is not able to give the optimal response with $\mathcal{O}(h^{3/2})$, which is the case for the underlying boundary value problem and not a general assumption. A comparison of the $\mathcal{RT}_m\mathcal{P}_k$ and the $\mathcal{P}_{m+1}\mathcal{P}_k$ approach show a reduction of the convergence order of the stresses using the $\mathcal{RT}$ function space. This can be explained by the incomplete polynomial order $m+1$ with $\mathcal{RT}_m = (\mathcal{P}_m)^d + \mathcal{P}_m \cdot \boldsymbol{x}$. The $\mathcal{RT}_m$ functions consists of complete polynomials only up to order m. Furthermore, the same holds for the divergence of these elements, since $\operatorname{div}[\mathcal{RT}_m] = \mathcal{P}_m$, see Boffi et al. [49]. Thus, the nonconforming approaches with $\boldsymbol{P} \in \mathcal{S}_P^{m,con}$ yield to higher convergence rates for the stresses compared to $\boldsymbol{P} \in \mathcal{S}^{m,con}$.
For the discontinuous stress element approaches, the convergence rates are constrained by the chosen stress approximation on element level. The hybrid stress formulations show the same reduced displacement convergence in the $\mathcal{L}^2(\mathcal{B})$-norm for $\mathrm{d}\mathcal{P}_1\mathcal{P}_2\mathcal{P}_n$ with $n = 0, 1$, as the continuous counterpart $\mathcal{P}_1\mathcal{P}_2$. This might lead to the conclusion that a subordinate influence of the order of Lagrange multiplier $\boldsymbol{\lambda}$ on the convergence rate is given. However, for the element $\mathrm{d}\mathcal{P}_2\mathcal{P}_2\mathcal{P}_n$, the different polynomial orders of $\boldsymbol{\lambda}$ with $n = 0, 1$ indicate such an influence of the order n on the convergence. Furthermore, the stress convergence for some of the $\mathrm{d}\mathcal{P}_k\mathcal{P}_m\mathcal{P}_n$ elements is slightly lower than the theoretically expected one, see Figure 6.6 and 6.7. This could be due to the boundary value problem, since it is not a regular problem based on the applied boundary conditions, see Rössle [194]. Nevertheless, the order of convergence is only reduced by ≈ 0.5 in all cases.
For the hybrid stress approach with $\boldsymbol{P} \in \mathcal{S}^{m,dis}$ the resulting convergence rates show a similar reduction with ≈ 0.5 in some of the rates with respect to the displacement, cf. Figure 6.4 and 6.5. Here, a comparison between $\mathrm{d}\mathcal{RT}_1\mathcal{P}_2\mathcal{P}_n$ with $n = 0, 1$ results in a reduced convergence order for $n = 0$ and in the expected one for $n = 1$. This illustrates that the order of convergence of variables on local element level depend on the chosen degree of $\boldsymbol{\lambda}$ and thus, on the enforcement of constraint condition on the skeleton. Furthermore, the $\mathrm{d}\mathcal{RT}_m\mathrm{d}\mathcal{P}_k\mathcal{P}_n\mathcal{P}_o$ yield the expected behavior, also with some small reductions. However, for the nearly incompressible setup the $\mathrm{d}\mathcal{RT}_0\mathrm{d}\mathcal{P}_2\mathcal{P}_0\mathcal{P}_1$ and $\mathrm{d}\mathcal{RT}_1\mathrm{d}\mathcal{P}_2\mathcal{P}_1\mathcal{P}_1$ elements yield no reliable solutions and diverge in the solution process.
One can conclude that the formulations provide optimal results for the majority of the analyzed elements. The deviations with a maximum of ≈ 0.5 can be explained by the choice of approximation approaches and by the not fully regular boundary value problem, which can be analyzed by the ideas in Rössle [194]. The dependence of the results on the enforcement of the constraint conditions have to be regarded in further applications. Nevertheless, an explanation of the reduced convergence rates with respect to the chosen order of the Lagrange multipliers cannot be explicitly deduced for the considered example. Furthermore, the comparison of the hybrid and LS formulation show the reduced robustness of some hybrid formulations for the imcompressilbe case at $\nu \approx 0.495$.

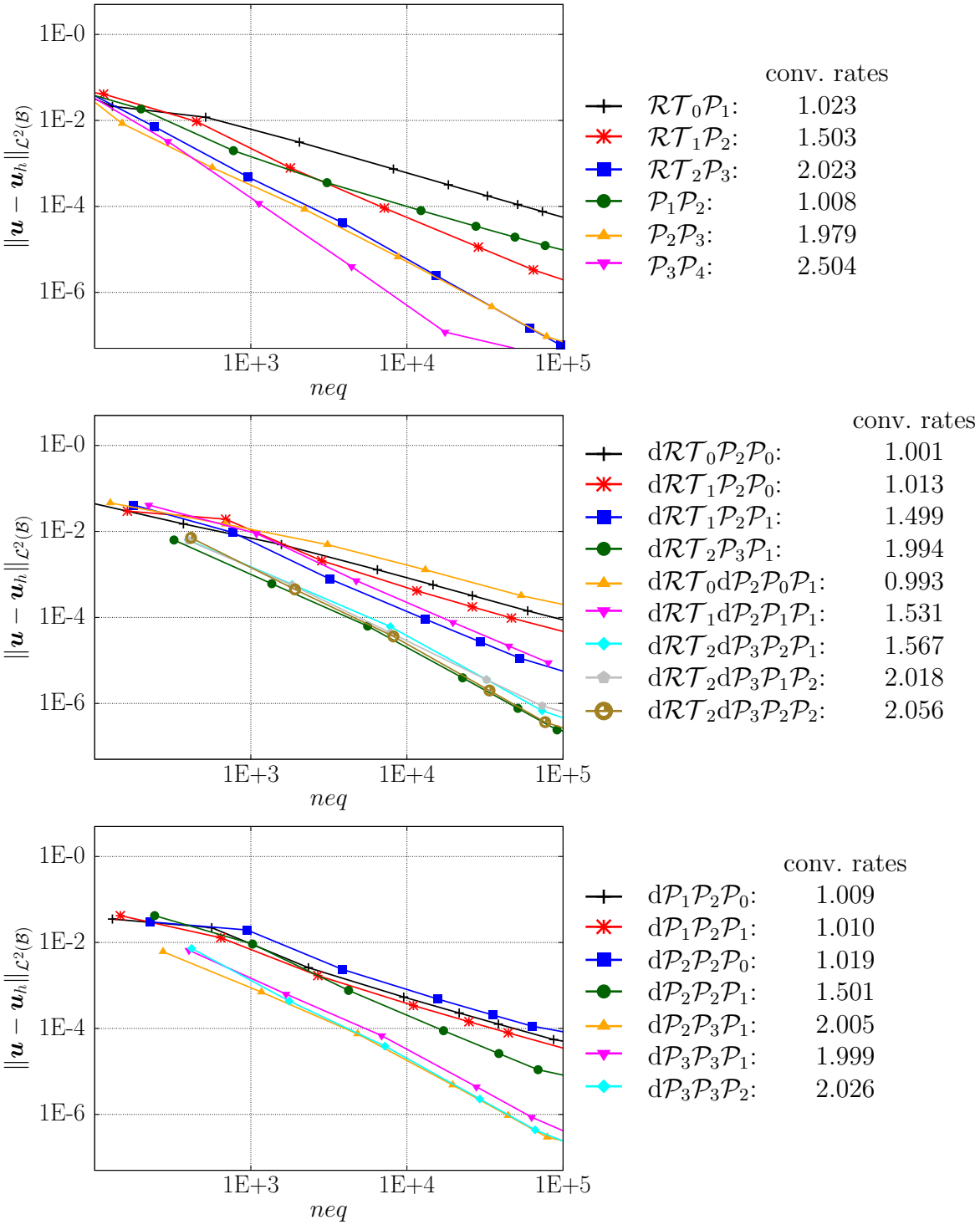

Figure 6.4: Convergence of displacements $\|\boldsymbol{u}-\boldsymbol{u}_h\|_{\mathcal{L}^2(\mathcal{B})}$ for a continuous and discontinuous stress and displacement approaches using $\lambda = 2\,\mathrm{kN/mm^2}$ ($E = 8/3\,\mathrm{kN/mm^2}, \nu = 1/3$)

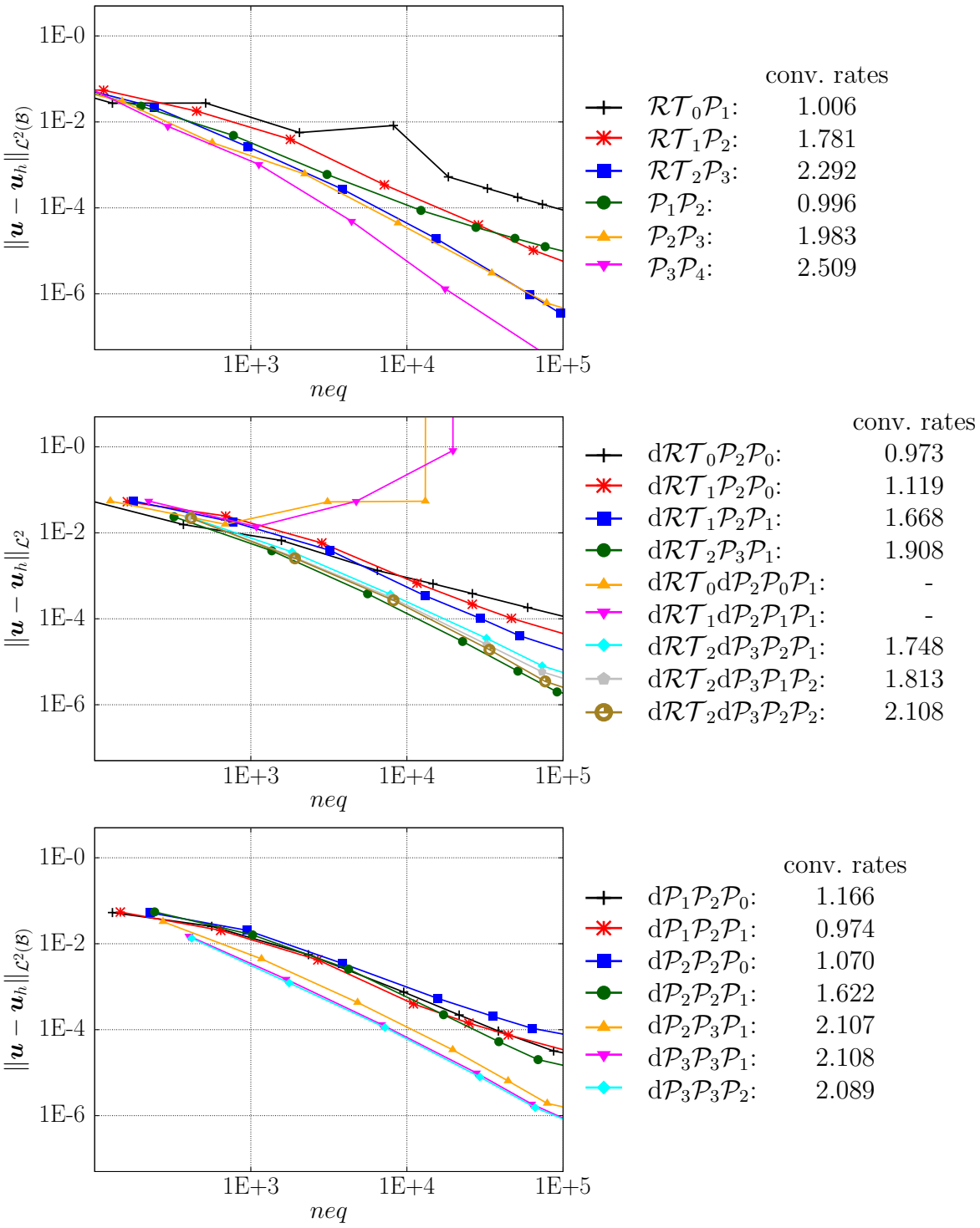

Figure 6.5: Convergence of displacements $\|\boldsymbol{u}-\boldsymbol{u}_h\|_{\mathcal{L}^2(\mathcal{B})}$ for a continuous and discontinuous stress and displacement approaches using $\lambda = 100\,\mathrm{kN/mm^2}$ ($E = 2.9901\,\mathrm{kN/mm^2}, \nu = 0.49505$)

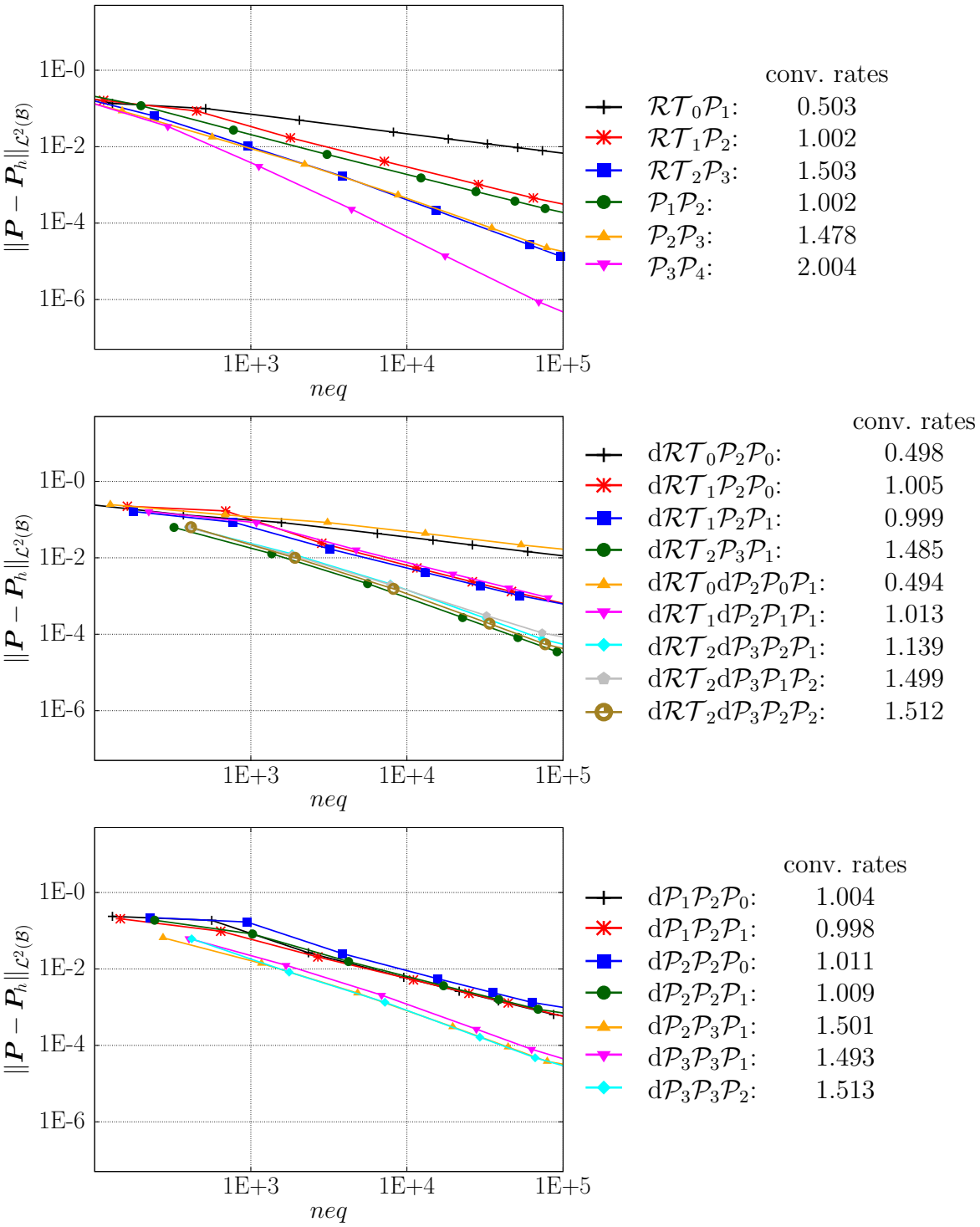

Figure 6.6: Convergence of stresses $\|\boldsymbol{P}-\boldsymbol{P}_h\|_{\mathcal{L}^2(\mathcal{B})}$ for a continuous and discontinuous stress and displacement approaches using $\lambda = 2\,\mathrm{kN/mm^2}$ ($E = 8/3\,\mathrm{kN/mm^2}, \nu = 1/3$)

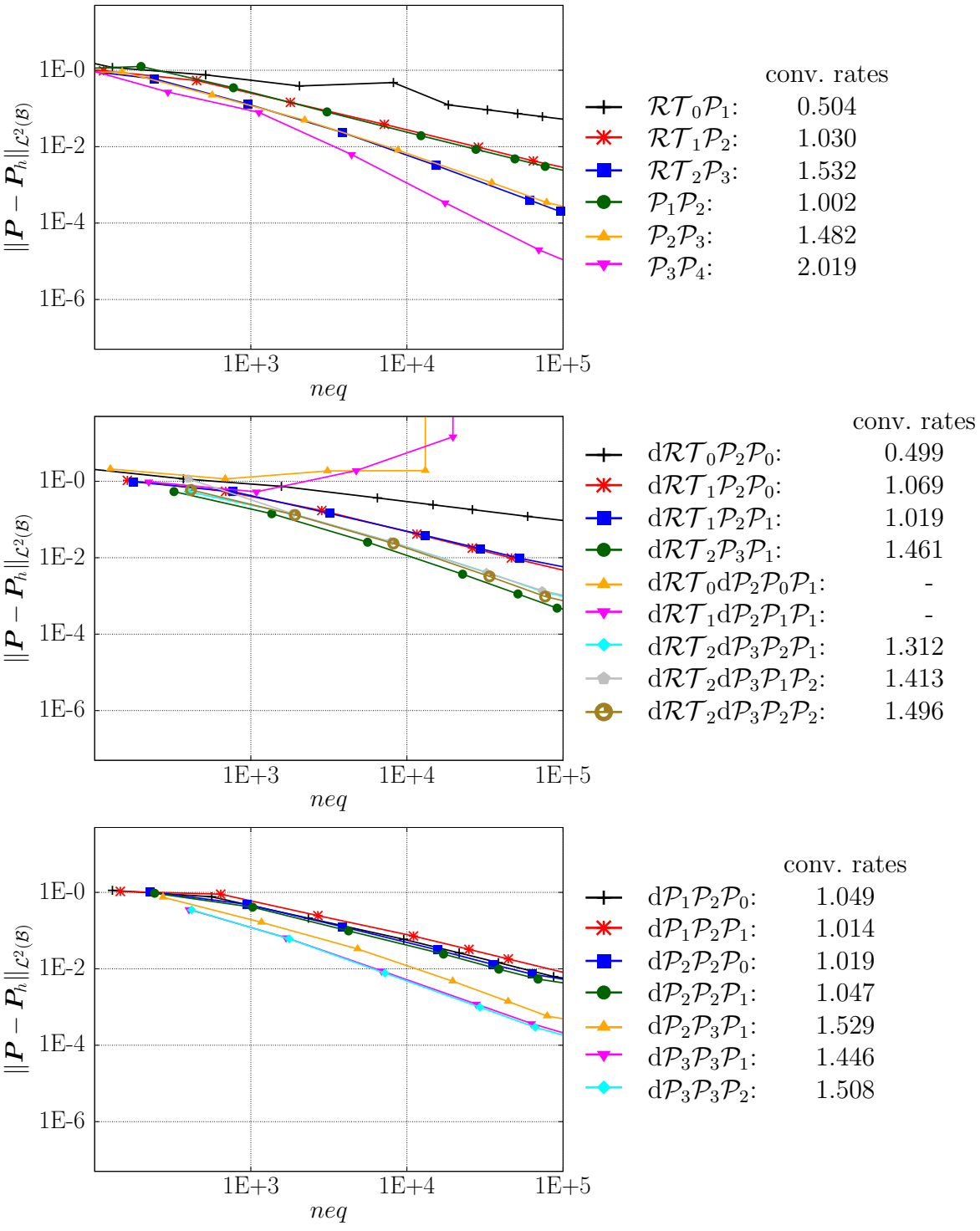

Figure 6.7: Convergence of stresses $\|\boldsymbol{P}-\boldsymbol{P}_h\|_{\mathcal{L}^2(\mathcal{B})}$ for a continuous and discontinuous stress and displacement approaches using $\lambda = 100\,\mathrm{kN/mm^2}$ ($E = 2.9901\,\mathrm{kN/mm^2}, \nu = 0.49505$)

For completeness, a static condensation of the stress field is performed for the d$\mathcal{RT}_m\mathcal{P}_k\mathcal{P}_n$ element type. As noted before, the obtained solution of the problem, see Figure 6.8, is very similar and the slightly changed convergence rates are based on the changed number of unknowns used for the calculation. In Table 6.2, the reduction of the number of equations is listed. The decreasing reduction of *neq* for finer mesh densities is natural, since for this case the degrees of freedom for $\boldsymbol{u}$ and $\boldsymbol{\lambda}$ are identical for the condensed and the original system. Thus, only the influence of the stress degrees of freedom on the total system is reduced. However, the number of equations for a continuous LS formulation of the same polynomial order m and k is even lower than the one of reduced system. Furthermore, the absolut time, dividing the calculation time of the condensed system by the time of the unreduced system, show that the reduced system is not always solved more efficiently.

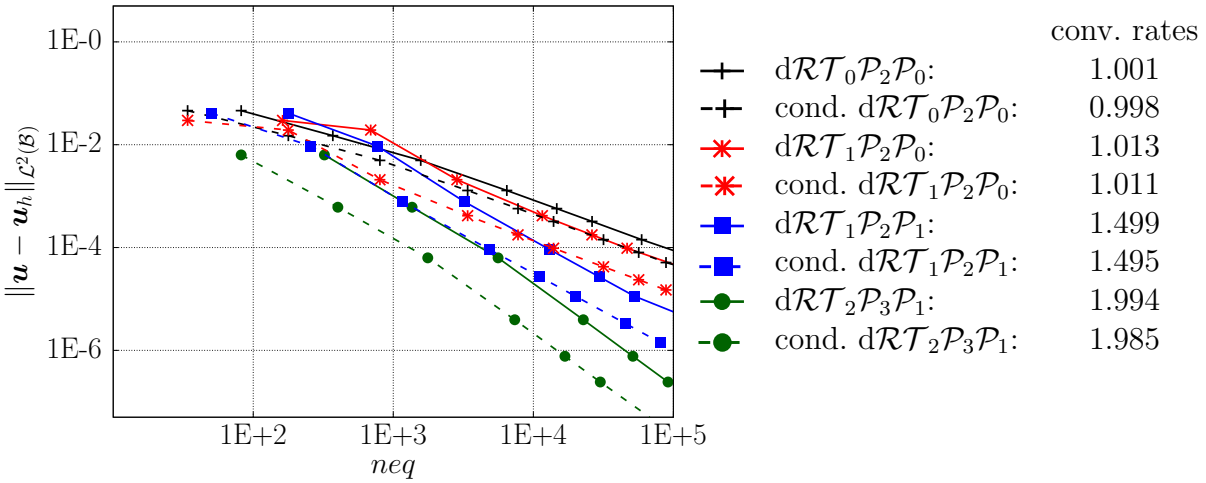

Figure 6.8: Convergence of $\|\boldsymbol{u}-\boldsymbol{u}_h\|_{\mathcal{L}^2(\mathcal{B})}$ for a discontinuous stress approach with and without static condensation of stresses using $\lambda = 2\,\mathrm{kN/mm^2}$ ($E = 8/3\,\mathrm{kN/mm^2}, \nu = 1/3$)

Table 6.2: Reduction of number of equations *neq* for d$\mathcal{RT}_m\mathcal{P}_m\mathcal{P}_n$ elements

mesh level	1	2	3	4	5	6
neq d$\mathcal{RT}_0\mathcal{P}_2\mathcal{P}_0$	82	370	1570	6466	14690	26242
neq cond. d$\mathcal{RT}_0\mathcal{P}_2\mathcal{P}_0$	34	178	802	3394	7778	13954
Reduction in %	58.54	51.89	48.92	47.51	47.05	46.83
Absolut time %	115.69	95.15	101.72	85.89	63.77	83.82
neq d$\mathcal{RT}_1\mathcal{P}_2\mathcal{P}_0$	162	690	2850	11586	26210	46722
neq cond.d$\mathcal{RT}_1\mathcal{P}_2\mathcal{P}_0$	34	178	802	3394	7778	13954
Reduction in %	79.01	74.20	71.86	70.71	70.32	70.13
Absolut time %	94.35	93.59	83.91	73.52	57.27	71.78
neq d$\mathcal{RT}_1\mathcal{P}_2\mathcal{P}_1$	178	770	3202	13058	29570	52738
neq cond.d$\mathcal{RT}_1\mathcal{P}_2\mathcal{P}_1$	50	258	1154	4866	11138	19970
Reduction in %	71.91	66.49	63.96	62.74	62.33	62.13
Absolut time %	97.57	101.39	86.47	53.77	76.19	74.310
neq d$\mathcal{RT}_2\mathcal{P}_3\mathcal{P}_1$	322	1362	5602	22722	51362	91522
neq cond. d$\mathcal{RT}_2\mathcal{P}_3\mathcal{P}_1$	82	402	1762	7362	16802	30082
Reduction in %	74.53	70.49	68.55	67.59	67.29	67.13
Absolut time %	105.09	82.21	70.49	48.59	66.18	62.82

6.6.2 Block with material interfaces

The example of a square block with material interfaces is used to illustrate that the choice of Lagrange type functions for the approximation of stresses provides the physically correct stress continuities, if a hybrid approach is applied. The approximation of stresses are naturally given in $\mathcal{W}^q(\mathrm{div}, \mathcal{B})$, since physically only normal continuity of the stresses is enforced. For a continuous LS formulation, the stress approximation $\boldsymbol{P} \in \mathcal{W}^{1,p}(\mathcal{B})$ within $\mathcal{P}_m\mathcal{P}_k$ element types lead to a continuity of all stress components. Accordingly, the requirements of the finite element space $\mathcal{W}^{1,p}(\mathcal{B})$ do not correspond to the properties of the physical quantity. Therefore, boundary value problems with material interfaces cannot represent the jumps of stress quantities correctly and are smoothed over the material interface, which is shown below.
The considered square block ($\mathcal{B} = (-1, 1) \times (-1, 1)$) consists of four material interfaces, which are defined by four different Young's moduli, each valid on a quarter of the block, cf. Figure 6.9 and Steeger [223]. The plate is subjected to a uniform elongation, where the displacements in normal direction of the outer edges are set to 1 and the shear stresses on the edges are set to 0. Based on the assumption that the Lagrange multiplier corresponds to the displacement on the element edge, $\boldsymbol{\lambda}$ in normal direction of the outer edges is set to 0, cf. Klaas et al. [132] and Schröder et al. [198]. For the numerical analysis, elements of type $\mathcal{RT}_m\mathcal{P}_k$, $\mathcal{P}_m\mathcal{P}_k$ for the continuous and $\mathrm{d}\mathcal{RT}_m\mathcal{P}_k\mathcal{P}_n$, $\mathrm{d}\mathcal{P}_m\mathcal{P}_k\mathcal{P}_n$ for the hybrid mixed approach are considered, see Table 6.1.

System setup:

Top side:	u_y	=	1 mm	Young's moduli:	E_1	=	100 kN/mm^2
Right side:	u_x	=	1 mm		E_2	=	200 kN/mm^2
Bottom side:	u_y	=	−1 mm		E_3	=	300 kN/mm^2
Left side:	u_x	=	−1 mm		E_4	=	400 kN/mm^2
				Poisson's ratio:	ν	=	0.35

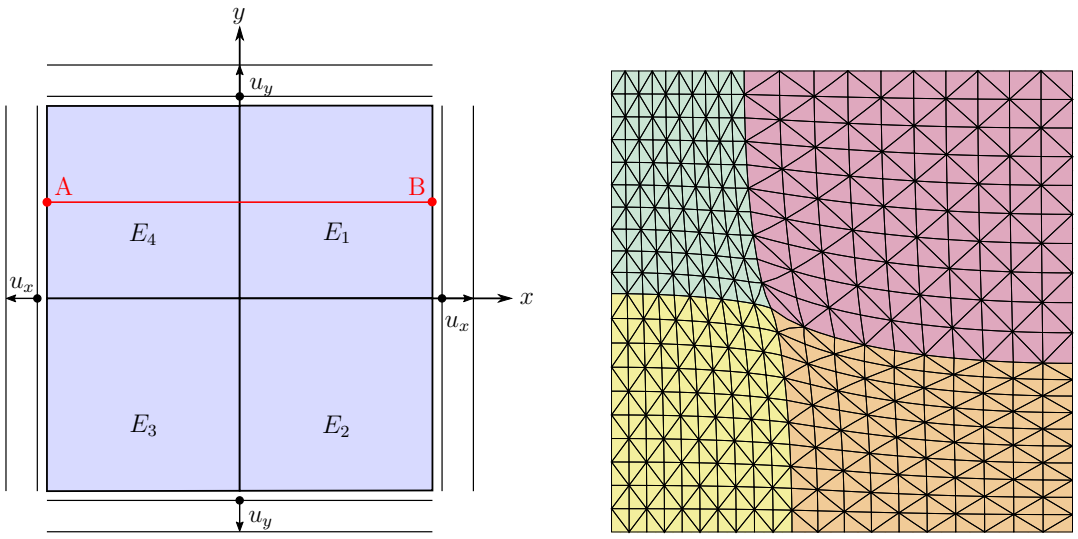

Figure 6.9: Material parameters, boundary conditions and geometry of the square block (top, bottom left) and deformed configuration with exemplarily depicted mesh consisting of 20 elements per side (bottom right)

The resulting deformation of the square block is illustrated in Figure 6.9 with an exemplarily depicted finite element mesh using 20 elements per side. Therein, the influence of the different material reactions can be clearly seen, e.g., in the comparison of the deformation of the materials with E_1 and E_4, where the softer material undergoes larger deformations.
In Figure 6.10 and 6.11 the stress distribution of P_{yy} is shown on the undeformed configuration. Obviously, the continuous stress approximation with $\boldsymbol{P} \in \mathcal{S}_P^{m,con}$ for the $\mathcal{P}_m\mathcal{P}_k$ element does not yield the physically correct results, which is due to the continuity properties of the finite element space $\mathcal{W}^{1,p}(\mathcal{B})$. From a physical point of view, the P_{yy} stresses have to be continuous for material interfaces in y-direction and discontinuous across the vertical material interface, i.e., only normal continuity of the traction is required, cf. Steeger [223]. This have to be fulfilled, since physically the normal components of the stress tensor are continuous and the tangential component could be discontinuous across material interfaces. This condition is included in the finite element space $\mathcal{W}^q(\mathrm{div}, \mathcal{B})$ and for the discontinuous elements with $\boldsymbol{P} \in \mathcal{S}^{m,dis}$ and $\boldsymbol{P} \in \mathcal{S}_P^{m,dis}$ enforced by the traction continuity on the inter-element boundaries. The course of the P_{yy} stresses at an intersection line A-B (A=(-1,0.5), B=(1,0.5)) is presented for each setup, which additionally illustrates the correct jump of the stresses and the unphysical smoothed stresses for the $\mathcal{P}_m\mathcal{P}_k$ element. The stress distribution is almost identical for the $\mathcal{RT}_m\mathcal{P}_k$, d$\mathcal{RT}_m\mathcal{P}_k$ and d$\mathcal{P}_m\mathcal{P}_k$ in Figure 6.10 and 6.11. Differences are only visible at the center of the block.

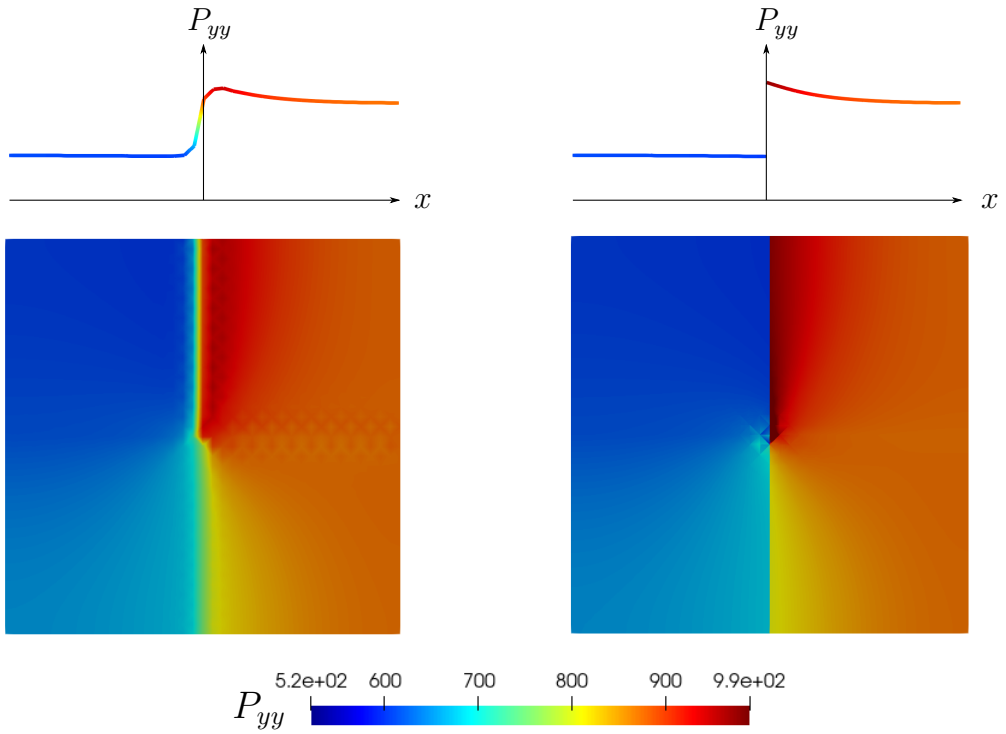

Figure 6.10: Distribution of P_{yy} stress in x-P_{yy}-plane on the intersection line A-B (top) and over the undeformed domain in x-y-plane (bottom) for element type $\mathcal{P}_2\mathcal{P}_3$ (left) and d$\mathcal{P}_2\mathcal{P}_3\mathcal{P}_1$ (right) for a mesh with 20 elements per side

Furthermore, Figure 6.12 and 6.13 depict the stress results in an "out-of-plane" value plot, which show exactly the course of the stresses on the vertical material interface. The enforced continuity of all stress components within $\mathcal{W}^{1,p}(\mathcal{B})$ can be clearly seen, where the

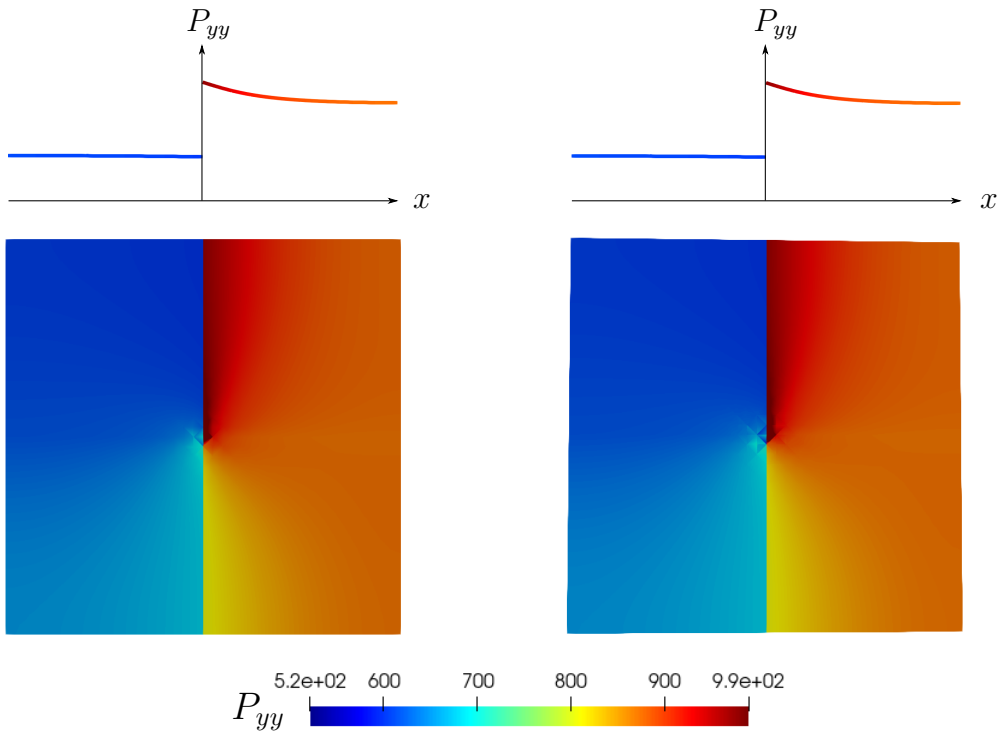

Figure 6.11: Distribution of P_{yy} stress in x-P_{yy}-plane on the intersection line A-B (top) and over the undeformed domain in x-y-plane (bottom) for element type $\mathcal{RT}_2\mathcal{P}_3$ (left) and d$\mathcal{RT}_2\mathcal{P}_3\mathcal{P}_1$ (right) for a mesh with 20 elements per side

sharp interface yields a smoothed transition of P_{yy} stresses with averaged values between the two materials. Therefore, the utilization of these element formulation has to be considered carefully, especially for stress dependent processes, e.g., elasto-plastic applications. Nevertheless, an application for homogeneous material distributions is possible. Here, the "out-of-plane" visualization illustrates the difference between the $\mathcal{RT}_m\mathcal{P}_k$, d$\mathcal{RT}_m\mathcal{P}_k$ and d$\mathcal{P}_m\mathcal{P}_k$ elements at the center of the block, where the hybrid elements show higher stress values at the stress singularity, which is also smoothed in the $\mathcal{P}_m\mathcal{P}_k$ approach.

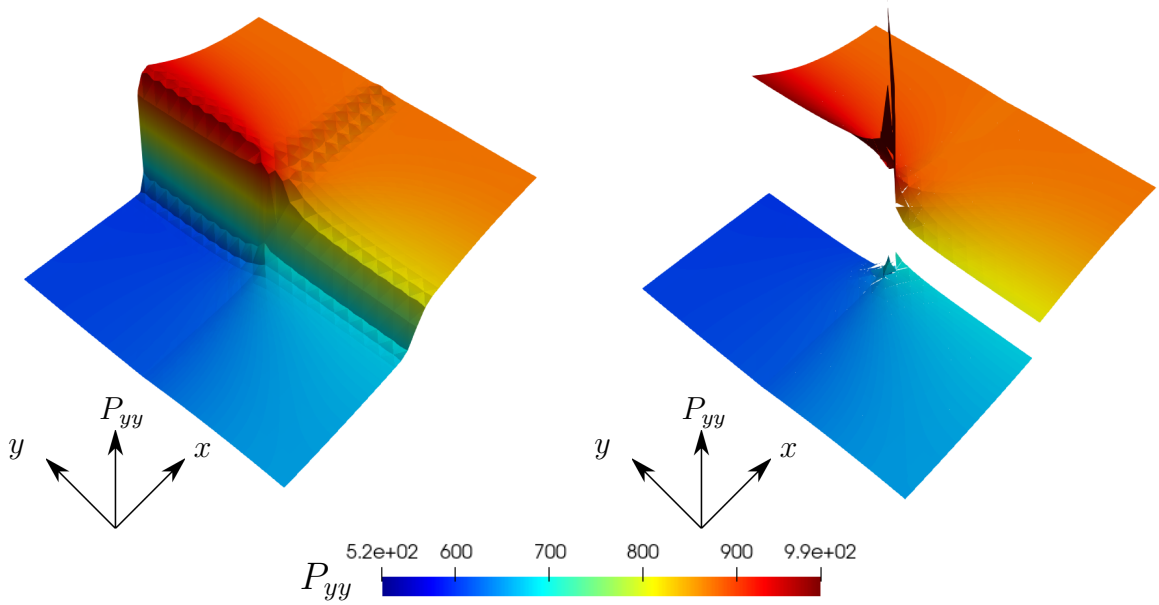

Figure 6.12: "Out-of-plane" value plot of P_{yy} stress for element type $\mathcal{P}_2\mathcal{P}_3$ (left) and d$\mathcal{P}_2\mathcal{P}_3\mathcal{P}_1$ (right) for a mesh with 20 elements per side

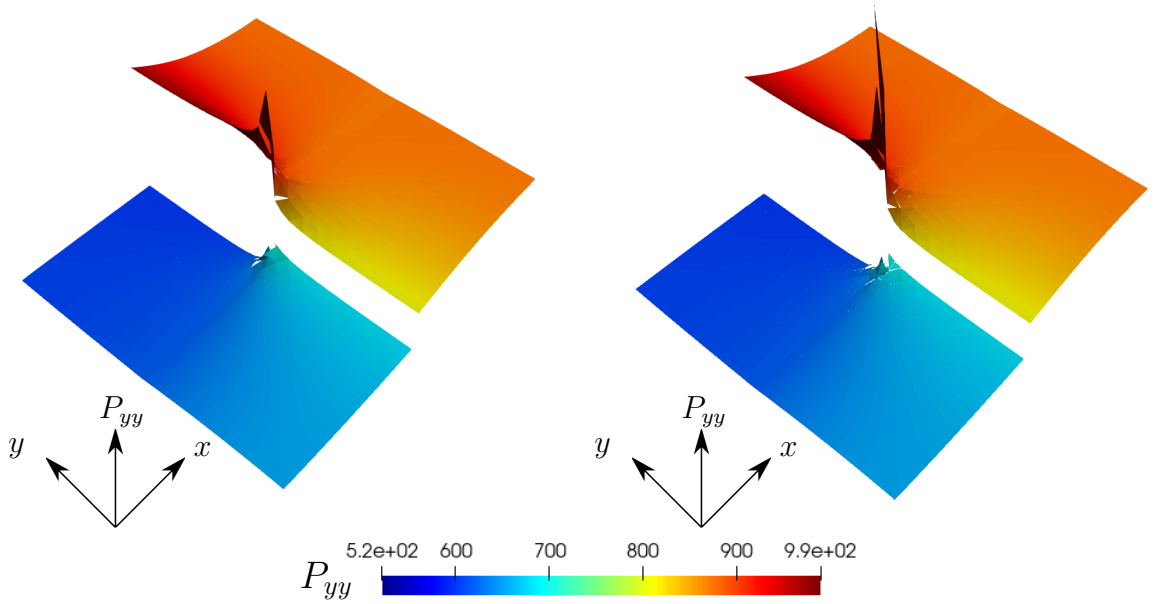

Figure 6.13: "Out-of-plane" value plot of P_{yy} stress for element type $\mathcal{RT}_2\mathcal{P}_3$ (left) and d$\mathcal{RT}_2\mathcal{P}_3\mathcal{P}_1$ (right) for a mesh with 20 elements per side

7 Conclusion and outlook

The present contribution serves for the understanding of mixed finite element formulations for applications in the field of nonlinearities, such as hyperelasticity and elasto-plasticty at small and finite strains. The introduction to the state of the art initially places the work in the field of research. In order to create the basic mechanical background for the work, kinematic relationships and stress quantities are first defined. Furthermore, the essential balance equations of continuum mechanics and the laws of material modeling are introduced. Finally, the considered nonlinear material models are presented and the derivation of the plastic constraints are carried out. Afterwards, an overview and short discussion of Galerkin and mixed Galerkin methods are given and the correlation to the mixed least-squares finite element method are introduced. In addition, mathematical terms were introduced and the basic idea of the finite element method was presented. The utilized $\mathcal{W}^{1,p}(\mathcal{B})$ and $\mathcal{W}^{q}(\mathrm{div},\mathcal{B})$ conforming finite element spaces are presented using classical approaches such as scalar-valued Lagrange functions, vector-valued Raviart-Thomas and Brezzi-Douglas-Marini functions. Examples for the construction of these functions are given and the possibility of a formulation of Raviart-Thomas approximation functions without the use of reference elements is shown. Furthermore, the co- and contravariant transformations required for vector-valued approaches are discussed and aspects on the implementation are presented for completeness. The mixed least-squares finite element method is introduced as a classical and an extended formulation for the small strain theory by means of an introductory example, where the recalculation of support reactions is considered, and examined for challenges of the method. For a preliminary consideration of elasto-plastic material behavior at small strains, the mixed primal Hellinger-Reissner principle is considered and analyzed with respect to the fulfillment of plastic constraints within the framework of mixed methods. The results are in accordance with the element-wise fulfillment of plastic constraints in Simo et al. [218] and thus no restrictions occur by a pointwise enforcement of these conditions. Taking into account the gained insights, a mixed least-squares formulation based on a hyperelastic Neo-Hookean energy function is derived. In addition to the extended least-squares formulation, which is analyzed for the consideration of the method at small deformations, a modified least-squares formulation is presented. The computational examples used are investigated based on the physical weighting factors and validated with results of the pure displacement method. This analysis and the obtained results serves as a basis for the extension of the formulation to finite J_2-plasticity, which is subsequently carried out. The non-smooth material law for rate-independent plasticity lead, within the least-squares formulation, to problems in the application of the standard Newton-Raphson method. This drawback is overcome by introducing a modified first variation, which guarantee a continuous first variation. The accordance of the obtained results with established formulations is shown for applications in $d = 2$ and $d = 3$. For exponential hardening, a subiteration for the plastic multiplier is derived. Furthermore, it is shown that the subiteration for enforcing a plane stress state provides a consistent solution for the corresponding strains in z-direction. Finally, the derivation and analysis of a mixed hybrid finite element formulation based on a least-squares approach is discussed. For this purpose, the idea of the hybrid FEM is introduced and the relaxation of continuity requirements as well as their enforcement on the inter-element boundaries is carried out with respect to stress and displacement quantities. The necessary considerations of stability properties for the resulting saddle

point problem is estimated numerically. The hybrid element formulation is analyzed for a pure discontinuous stress approach and for an approach with discontinuous stress and displacement fields. For this purpose, a problem with analytical displacement and stress solution is investigated. In addition to that, the stress approximation with Lagrange ansatz functions for problems with material interfaces is discussed and demonstrated to lead physically correct stress representations.

It is shown that the least-squares finite element method is an alternative to pure displacement and mixed formulations for nonlinear applications. However, they are only competitive with an appropriate choice of weighting factors and especially for formulations which consider extended functionals or modified first variations. The results shown can be improved further by using adaptive refinement algorithms such as Dörfler-marking or error-marking strategies, since the error estimator is provided by the least-squares functional. However, in general the corresponding proof of ellipticity of the functional has to be derived.
The great advantage of the least-squares method is given by the unrestrictedness with respect to LBB stability. It is shown that the extension to finite deformations is directly applicable and is only restricted by the non-smooth material formulation. However, this limitation can be circumvented by constructing a continuous first variation. The direct extension is not possible in this manner for the presented Hellinger-Reissner formulation. The application of mixed stress-displacement formulations in the framework of finite plasticity has not been considered so far, to the best of the author's knowledge. In general, the idea of an independent approximation of the stresses is promising in these applications, since plastic material deformations are stress driven processes. In order to show the benefit of the mixed least-squares formulation compared to Galerkin formulations, the presented idea should be used for alternative yield conditions such as Mohr-Coulomb or Drucker-Prager conditions, i.e., a yield criterion in which not only the deviatoric stress components are considered. This is due to the fact that the constraint of plastic incompressibility is already fulfilled within the applied implicit exponential time integration in combination with a J_2 yield criterion. Furthermore, since the least-squares formulation is sensitive to material and weighting parameters the consideration of a stabilization of the method, especially at finite plasticity, should be taken into account.
For the derived mixed hybrid formulation, a discussion on stability with respect to the LBB conditions must be carried out before it is applied for further problems. The direct application of Lagrange shape functions for the stress approximation avoids the need to use more sophisticated $\mathcal{H}(\mathrm{div}, \mathcal{B})$ approaches and can be applied analogously to the $d = 3$ case. Furthermore, a similar hybrid approach can be utilized with Lagrange ansatz functions for tangentially continuous quantities, instead of introducing the more sophisticated approximations in $\mathcal{H}(\mathrm{curl}, \mathcal{B})$.

8 Appendix

8.1 Appendix mixed finite element method

8.1.1 Approximation matrices

The approximation matrices are defined by

$$\mathbb{N}^j = \begin{bmatrix} N^j & 0 & 0 \\ 0 & N^j & 0 \\ 0 & 0 & N^j \end{bmatrix} \quad \text{and} \quad \mathbb{S}'^{j,i} = \begin{bmatrix} \partial_1({}_1\Psi^{j,i}) & \partial_2({}_2\Psi^{j,i}) & \partial_3({}_3\Psi^{j,i}) \\ \partial_1({}_1\Psi^{j,i}) & \partial_2({}_2\Psi^{j,i}) & \partial_3({}_3\Psi^{j,i}) \\ \partial_1({}_1\Psi^{j,i}) & \partial_2({}_2\Psi^{j,i}) & \partial_3({}_3\Psi^{j,i}) \end{bmatrix}, \tag{8.1}$$

$$\mathbb{B}^j = \begin{bmatrix} \partial_1 N^j & 0 & 0 \\ \frac{1}{2}\partial_2 N^j & \frac{1}{2}\partial_1 N^j & 0 \\ \frac{1}{2}\partial_3 N^j & 0 & \frac{1}{2}\partial_1 N^j \\ \frac{1}{2}\partial_2 N^j & \frac{1}{2}\partial_1 N^j & 0 \\ & \partial_2 N^j & 0 \\ 0 & \frac{1}{2}\partial_3 N^j & \frac{1}{2}\partial_2 N^j \\ \frac{1}{2}\partial_3 N^j & 0 & \frac{1}{2}\partial_1 N^j \\ 0 & \frac{1}{2}\partial_3 N^j & \frac{1}{2}\partial_2 N^j \\ 0 & 0 & \partial_3 N^j \end{bmatrix}, \quad \text{and} \quad \mathbb{S}^{j,i} = \begin{bmatrix} {}_1\Psi^{j,i} & 0 & 0 \\ {}_2\Psi^{j,i} & 0 & 0 \\ {}_3\Psi^{j,i} & 0 & 0 \\ 0 & {}_1\Psi^{j,i} & 0 \\ 0 & {}_2\Psi^{j,i} & 0 \\ 0 & {}_3\Psi^{j,i} & 0 \\ 0 & 0 & {}_1\Psi^{j,i} \\ 0 & 0 & {}_2\Psi^{j,i} \\ 0 & 0 & {}_3\Psi^{j,i} \end{bmatrix}. \tag{8.2}$$

The approximation matrix considering the stress approach by Pian and Sumihara [178] for two dimensions regarding plane stress conditions $\bar{\mathbb{S}}$ is denoted by

$$\bar{\mathbb{S}}^j = \begin{bmatrix} 1 & 0 & 0 & \eta & 0 \\ 0 & 1 & 0 & 0 & \xi \\ 0 & 0 & 1 & 0 & 0 \end{bmatrix}. \tag{8.3}$$

8.1.2 Construction of $\mathcal{H}(\mathrm{div}, \mathcal{B})$-conforming $\mathcal{RT}$ functions

The necessary quantities for the evaluation of $\mathcal{RT}_m$ and $\mathcal{BDM}_m$ functions are given by the outward normal vector $\hat{\boldsymbol{n}}$ in parameter space $\boldsymbol{\xi}$, the scalar and vectorial functions $\hat{p}_m$ and $\hat{\boldsymbol{p}}_{m-1}$ and the basis vector $\hat{\boldsymbol{v}}_m$ of order m. The outward normal vectors for the unit triangle, unit tetrahedral and unit quadrilateral are:

$$\hat{\boldsymbol{n}}^j = \left\{ \frac{1}{\sqrt{2}} \begin{pmatrix} 1 \\ 1 \end{pmatrix}, \begin{pmatrix} -1 \\ 0 \end{pmatrix} \begin{pmatrix} 0 \\ -1 \end{pmatrix} \right\}, \tag{8.4}$$

$$\hat{\boldsymbol{n}}^j = \left\{ \frac{1}{\sqrt{3}} \begin{pmatrix} 1 \\ 1 \\ 1 \end{pmatrix}, \begin{pmatrix} -1 \\ 0 \\ 0 \end{pmatrix}, \begin{pmatrix} 0 \\ -1 \\ 0 \end{pmatrix}, \begin{pmatrix} 0 \\ 0 \\ -1 \end{pmatrix} \right\}, \tag{8.5}$$

$$\hat{\boldsymbol{n}}^j = \left\{ \begin{pmatrix} 0 \\ -1 \end{pmatrix}, \begin{pmatrix} 1 \\ 0 \end{pmatrix}, \begin{pmatrix} 0 \\ 1 \end{pmatrix}, \begin{pmatrix} -1 \\ 0 \end{pmatrix} \right\}. \tag{8.6}$$

The normalized outward normal vector is $\boldsymbol{n}^j = \frac{1}{\|\boldsymbol{n}_g^j\|}\boldsymbol{n}_g^j$, where $\boldsymbol{n}_g$ is a normal vector on the j-th edge or face. For the evaluation of $\mathcal{RT}_m$ functions $\hat{\boldsymbol{v}}_m$, $\hat{p}_m$ and $\hat{\boldsymbol{p}}_{m-1}$ are given. The functions are constructed based on the properties of the associated edge e^j, which are $\xi = 1-\eta$ on e^1, $\xi = 0$ on e^2 and $\eta = 0$ on e^3 for the unit triangle, $\eta = -1$ on e^1, $\xi = 1$ on e^2, $\eta = 1$ on e^3 and $\xi = -1$ on e^4 for the unit quadrilateral and $\xi = 1-\eta-\zeta$ on f^1, $\xi = 0$ on f^2, $\eta = 0$ on f^3 and $\zeta = 0$ on f^4 for the unit tetrahedral.

Construction of $[\mathcal{RT}_0^{\triangle}]^2$ approximation functions:
The basic quantities for evaluation of $[\mathcal{RT}_0^{\triangle}]^2$ functions are

$$[\hat{\boldsymbol{v}}_0^{\triangle}]^2 = \begin{pmatrix} a_1 + c\,\xi \\ b_1 + c\,\eta \end{pmatrix}, \tag{8.7}$$

and the scalar function $\hat{p}_m$, chosen to be $\hat{p}_0^{1,1} = \hat{p}_0^{2,1} = \hat{p}_0^{3,1} = 1$, in combination with the associated edge relations on the unit triangle. Evaluation of (3.80) and solving the resulting system of equations yields the $[\mathcal{RT}_0^{\triangle}]^2$ functions in $\boldsymbol{\xi}$, i.e.,

$$\hat{\boldsymbol{\Psi}}_0^{j,1} = \left\{ \begin{pmatrix} \xi \\ \eta \end{pmatrix}, \begin{pmatrix} \xi - 1 \\ \eta \end{pmatrix} \begin{pmatrix} \xi \\ \eta - 1 \end{pmatrix} \right\}. \tag{8.8}$$

Construction of $[\mathcal{RT}_1^{\triangle}]^2$ approximation functions:
The basic quantities for evaluation of $[\mathcal{RT}_1^{\triangle}]^2$ functions are

$$[\hat{\boldsymbol{v}}_1^{\triangle}]^2 = \begin{pmatrix} a_1 + a_2\,\xi + a_3\,\eta + c_1\,\xi^2 + c_2\,\xi\eta \\ b_1 + b_2\,\xi + b_3\,\eta + c_1\,\xi\eta + c_2\,\eta^2 \end{pmatrix}, \tag{8.9}$$

$\hat{p}_1^{j,1} = \{\xi, \eta, 1-\xi\}$, $\hat{p}_1^{j,2} = \{\eta, 1-\eta, \xi\}$ for $j = 1, 2, 3$ and the vector function $\hat{\boldsymbol{p}}_0$ are chosen with $\hat{\boldsymbol{p}}_0^{I,1} = (1,0)^T$ and $\hat{\boldsymbol{p}}_0^{I,2} = (0,1)^T$ in combination with the associated edge relations on the unit triangle. Application of the given terms in equation (3.80) and (3.81), leads, after solving the resulting system of equations to, the $[\mathcal{RT}_1^{\triangle}]^2$ functions in $\boldsymbol{\xi}$, i.e.,

$$\begin{aligned}
\hat{\boldsymbol{\Psi}}_1^{1,1} &= \begin{pmatrix} -2\,\xi + 4\,\xi^2 \\ -\eta + 4\,\xi\eta \end{pmatrix}, & \hat{\boldsymbol{\Psi}}_1^{1,2} &= \begin{pmatrix} -\xi + 4\,\xi\eta \\ -2\,\eta + 4\,\eta^2 \end{pmatrix}, \\
\hat{\boldsymbol{\Psi}}_1^{2,1} &= \begin{pmatrix} 1 - 3\,\eta - \xi + 4\,\xi\eta \\ -2\,\eta + 4\,\eta^2 \end{pmatrix}, & \hat{\boldsymbol{\Psi}}_1^{2,2} &= \begin{pmatrix} -2 + 3\,\eta + 6\,\xi - 4\,\xi\eta - 4\,\xi^2 \\ 3\,\eta - 4\,\eta^2 - 4\,\xi\eta \end{pmatrix}, \\
\hat{\boldsymbol{\Psi}}_1^{3,1} &= \begin{pmatrix} 3\,\xi - 4\,\xi\eta - 4\,\xi^2 \\ -2 + 6\,\eta - 4\,\eta^2 + 3\,\xi - 4\,\xi\eta \end{pmatrix}, & \hat{\boldsymbol{\Psi}}_1^{3,2} &= \begin{pmatrix} -2\,\xi + 4\,\xi^2 \\ 1 - \eta - 3\,\xi + 4\,\xi\eta \end{pmatrix}, \\
\hat{\boldsymbol{\Psi}}_1^{4,1} &= \begin{pmatrix} 16\,\xi - 8\,\xi\eta - 16\,\xi^2 \\ 8\,\eta - 8\,\eta^2 - 16\,\xi\eta \end{pmatrix}, & \hat{\boldsymbol{\Psi}}_1^{4,2} &= \begin{pmatrix} 8\,\xi - 16\,\xi\eta - 8\,\xi^2 \\ 16\,\eta - 16\,\eta^2 - 8\,\xi\eta \end{pmatrix}.
\end{aligned} \tag{8.10}$$

Construction of $[\mathcal{RT}_0^{\triangle}]^3$ approximation functions:
The basic quantities for evaluation of $[\mathcal{RT}_0^{\triangle}]^3$ functions are

$$[\hat{\boldsymbol{v}}_0^{\triangle}]^3 = \begin{pmatrix} a_1 + d\,\xi \\ b_1 + d\,\eta \\ c_1 + d\,\zeta \end{pmatrix} \tag{8.11}$$

and the scalar functions $\hat{p}_0$ with $\hat{p}_0^{i,1} = 1$ for $i = 1, 2, 3, 4$ in combination with the associated edge relations on the unit tetrahedral. Application of the given terms in (3.82), yields, after solving the resulting system of equations, the $[\mathcal{RT}_0^{\triangle}]^3$ functions in $\boldsymbol{\xi}$.

$$\hat{\boldsymbol{\Psi}}_0^{j,1} = \left\{ 2\sqrt{3} \begin{pmatrix} \xi \\ \eta \\ \zeta \end{pmatrix}, 2 \begin{pmatrix} \xi - 1 \\ \eta \\ \zeta \end{pmatrix}, 2 \begin{pmatrix} \xi \\ \eta - 1 \\ \zeta \end{pmatrix}, 2 \begin{pmatrix} \xi \\ \eta \\ \zeta - 1 \end{pmatrix} \right\} \tag{8.12}$$

Construction of $[\mathcal{RT}_0^{\square}]^2$ approximation functions:
The basic quantities for evaluation of $[\mathcal{RT}_0^{\square}]^2$ functions are

$$[\hat{\boldsymbol{v}}_0^{\square}]^2 = \begin{pmatrix} a_1 + a_2\,\xi \\ b_1 + b_2\,\eta \end{pmatrix} \tag{8.13}$$

and the scalar functions $\hat{p}_0$ are chosen to be $\hat{p}_0^{j,1} = 1$ for $j = 1, 2, 3, 4$ in combination with the associated edge relations on the unit quadrilateral. Evaluation of (3.80) and (3.81), leads, after solving the resulting system of equations, to the $[\mathcal{RT}_0^{\square}]^2$ functions in $\boldsymbol{\xi}$, i.e.,

$$\hat{\boldsymbol{\Psi}}_0^{j,1} = \left\{ \begin{pmatrix} 0 \\ -\frac{1}{4} + \frac{1}{4}\,\eta \end{pmatrix}, \begin{pmatrix} \frac{1}{4} + \frac{1}{4}\,\xi \\ 0 \end{pmatrix}, \begin{pmatrix} 0 \\ \frac{1}{4} + \frac{1}{4}\,\eta \end{pmatrix}, \begin{pmatrix} -\frac{1}{4} + \frac{1}{4}\,\xi \\ 0 \end{pmatrix} \right\} . \tag{8.14}$$

Construction of $[\mathcal{RT}_1^{\square}]^2$ approximation functions:
The basic quantities for evaluation of $[\mathcal{RT}_1^{\square}]^2$ functions are

$$[\hat{\boldsymbol{v}}_1^{\square}]^2 = \begin{pmatrix} a_1 + a_2\,\xi + a_3\,\eta + a_4\,\xi\eta + a_5\,\xi^2 + a_6\,\xi^2\eta \\ b_1 + b_2\,\xi + b_3\,\eta + b_4\,\xi\eta + b_5\,\eta^2 + b_6\,\xi\eta^2 \end{pmatrix}, \tag{8.15}$$

$\hat{p}_1^{j,1} = \frac{1}{2}\big((1-\xi),(1-\eta),(1+\xi),(1+\eta)\big)$, $\hat{p}_1^{j,2} = \frac{1}{2}\big((1+\xi),(1+\eta),(1-\xi),(1-\eta)\big)$, for $j = 1, 2, 3, 4$ and the vector functions $\hat{\boldsymbol{p}}_0^{j,1}$ for $j = 5, 6, 7, 8$ are

$$\hat{\boldsymbol{p}}_0^{j,1} = \left\{ \begin{pmatrix} \frac{1}{2}(1-\xi) \\ 0 \end{pmatrix}, \begin{pmatrix} 0 \\ \frac{1}{2}(1+\xi) \end{pmatrix}, \begin{pmatrix} \frac{1}{2}(1+\eta) \\ 0 \end{pmatrix}, \begin{pmatrix} 0 \\ \frac{1}{2}(1-\eta) \end{pmatrix} \right\} \tag{8.16}$$

with the associated edge relations on the unit quadrilateral. Application of the given terms in (3.80) and (3.81), leads, after solving the resulting system of equations, to the $[\mathcal{RT}_1^{\square}]^2$

functions in $\boldsymbol{\xi}$.

$$
\begin{aligned}
\hat{\boldsymbol{\Psi}}_1^{1,1} &= \tfrac{1}{8}\,(0,\, 1+2\,\eta-3\,\eta^2-3\,\xi-6\,\xi\eta+9\,\xi\eta^2)^T \\
\hat{\boldsymbol{\Psi}}_1^{1,2} &= \tfrac{1}{8}\,(0,\, 1+2\,\eta-3\,\eta^2+3\,\xi+6\,\xi\eta-9\,\xi\eta^2)^T \\
\hat{\boldsymbol{\Psi}}_1^{2,1} &= \tfrac{1}{8}\,(-1\,+3\,\eta+2\,\xi-6\,\xi\eta+3\,\xi^2-9\,\xi^2\eta,\, 0)^T \\
\hat{\boldsymbol{\Psi}}_1^{2,2} &= \tfrac{1}{8}\,(-1-3\,\eta+2\,\xi+6\,\xi\eta+3\,\xi^2+9\,\xi^2\eta,\, 0)^T \\
\hat{\boldsymbol{\Psi}}_1^{3,1} &= \tfrac{1}{8}\,(0,\, -1+2\,\eta+3\,\eta^2+3\,\xi-6\,\xi\eta-9\,\xi\eta^2)^T \\
\hat{\boldsymbol{\Psi}}_1^{3,2} &= \tfrac{1}{8}\,(0,\, -1\,+2\,\eta+3\,\eta^2-3\,\xi+6\,\xi\eta+9\,\xi\eta^2)^T \\
\hat{\boldsymbol{\Psi}}_1^{4,1} &= \tfrac{1}{8}\,(1-3\,\eta+2\,\xi-6\,\xi\eta-3\,\xi^2+9\,\xi^2\eta,\, 0)^T \\
\hat{\boldsymbol{\Psi}}_1^{4,2} &= \tfrac{1}{8}\,(1+3\,\eta+2\,\xi+6\,\xi\eta-3\,\xi^2-9\,\xi^2\eta,\, 0)^T \\
\hat{\boldsymbol{\Psi}}_1^{5,1} &= \tfrac{1}{8}\,(3-9\,\eta-3\,\xi^2+9\,\xi^2\eta,\, 0)^T \\
\hat{\boldsymbol{\Psi}}_1^{5,2} &= \tfrac{1}{8}\,(0,\, 3-3\,\eta^2+9\,\xi-9\,\xi\eta^2)^T \\
\hat{\boldsymbol{\Psi}}_1^{5,3} &= \tfrac{1}{8}\,(3+9\,\eta-3\,\xi^2-9\,\xi^2\eta,\, 0)^T \\
\hat{\boldsymbol{\Psi}}_1^{5,4} &= \tfrac{1}{8}\,(0,\, 3-3\,\eta^2-9\,\xi+9\,\xi\eta^2)^T
\end{aligned}
\tag{8.17}
$$

Construction of $[\mathcal{RT}_1^{\triangle}]^2$ based on $[\mathcal{RT}_0^{\triangle}]^2$ and $[\mathcal{P}_1]^2$:
Here, the construction of $[\mathcal{RT}_1^{\triangle}]^2$ functions are performed, based on $[\mathcal{RT}_0^{\triangle}]^2$ and $[\mathcal{P}_1]^2$. The $[\mathcal{RT}_0^{\triangle}]^2$ functions are determined by equation (3.85) and given by

$$
\boldsymbol{\Psi}_0^{j,1} = \left\{ \sqrt{2} \begin{pmatrix} x \\ y \end{pmatrix}, \begin{pmatrix} x-1 \\ y \end{pmatrix} \begin{pmatrix} x \\ y-1 \end{pmatrix} \right\}. \tag{8.18}
$$

Considering the explanation for the evaluation of $\mathcal{RT}_m$ approximation functions on arbitrary straight-edged triangles and tetrahedral domains in Chapter 3.3.2 with the graphical representation in Figure 3.6 and 3.7 an approach for the construction is exemplarily presented in the following. Therefore, 3.89 and 3.90 are regarded with the evaluated $\mathcal{P}_1$ functions on the triangular domains T_1^1, T_1^2 and T_1^3 with:

$$
\begin{array}{lll}
T_1^1: & T_1^2: & T_1^3: \\
N_1^{1,\bar{P}^{I,1}} = 3-3\,x-3\,y\,, & N_1^{2,\bar{P}^{I,1}} = 3\,x\,, & N_1^{3,\bar{P}^{I,1}} = 3\,y\,, \\
N_1^{1,\bar{P}^{1,1}} = -1+3\,x\,, & N_1^{2,\bar{P}^{2,1}} = -1+3\,y\,, & N_1^{3,\bar{P}^{3,1}} = 2-3\,x-3\,y\,, \\
N_1^{1,\bar{P}^{1,2}} = -1+3\,y\,, & N_1^{2,\bar{P}^{2,2}} = 2-3\,x-3\,y\,, & N_1^{3,\bar{P}^{3,2}} = -1+3\,x\,.
\end{array}
\tag{8.19}
$$

The resulting functions are given by

$$\begin{aligned}
\boldsymbol{\Psi}_1^{1,1} &= \boldsymbol{\Psi}_0^{1,1}\, N_1^{1,\bar{P}^{1,1}} &&= \sqrt{2}\begin{pmatrix} -x+3\,x^2 \\ -y+3\,xy \end{pmatrix},\\
\boldsymbol{\Psi}_1^{1,2} &= \boldsymbol{\Psi}_0^{1,1}\, N_1^{1,\bar{P}^{1,2}} &&= \sqrt{2}\begin{pmatrix} -x+3\,xy \\ -y+3\,y^2 \end{pmatrix},\\
\boldsymbol{\Psi}_1^{2,1} &= \boldsymbol{\Psi}_0^{2,1}\, N_1^{2,\bar{P}^{2,1}} &&= \begin{pmatrix} 1-x-3\,y-3\,xy \\ -y+3\,xy \end{pmatrix},\\
\boldsymbol{\Psi}_1^{2,2} &= \boldsymbol{\Psi}_0^{2,1}\, N_1^{2,\bar{P}^{2,2}} &&= \begin{pmatrix} -2+5\,x+3\,y-3\,xy-3\,x^2 \\ 2\,y-3\,xy-3\,y^2 \end{pmatrix},\\
\boldsymbol{\Psi}_1^{3,1} &= \boldsymbol{\Psi}_0^{3,1}\, N_1^{3,\bar{P}^{3,1}} &&= \begin{pmatrix} 2\,x-3\,xy-3\,x^2 \\ -2-3\,x+5\,y-3\,xy-3\,y^2 \end{pmatrix},\\
\boldsymbol{\Psi}_1^{3,2} &= \boldsymbol{\Psi}_0^{3,1}\, N_1^{3,\bar{P}^{3,2}} &&= \begin{pmatrix} -x+3\,x^2 \\ 1-3\,x-y+3\,xy \end{pmatrix},\\
\boldsymbol{\Psi}_1^{4,1} &= \boldsymbol{\Psi}_0^{2,1}\, N_1^{2,\bar{P}^{I,1}} &&= \begin{pmatrix} -3\,x+3\,x^2 \\ 3\,xy \end{pmatrix},\\
\boldsymbol{\Psi}_1^{4,2} &= \boldsymbol{\Psi}_0^{3,1}\, N_1^{3,\bar{P}^{I,1}} &&= \begin{pmatrix} 3\,xy \\ -3\,y+3\,y^2 \end{pmatrix}.
\end{aligned} \tag{8.20}$$

8.1.3 Construction of $\mathcal{H}(\mathrm{div},\mathcal{B})$-conforming $\mathcal{BDM}$ functions

Construction of $[\mathcal{BDM}_1^{\triangle}]^2$ approximation functions:
The basic quantities for evaluation of $[\mathcal{BDM}_1^{\triangle}]^2$ functions are

$$[\hat{\boldsymbol{v}}_1^{\triangle}]^2 = \begin{pmatrix} a_1+a_2\,\xi+a_3\,\eta \\ b_1+b_2\,\xi+b_3\,\eta \end{pmatrix}, \tag{8.21}$$

with $\hat{p}_m$ are chosen as the lowest order Nédélec functions on a unit triangle with

$$\hat{p}_1^{j,1} = \{1-\xi,\xi,\eta\} \quad \text{and} \quad \hat{p}_1^{j,2} = \{\xi,\eta,1-\eta\} \tag{8.22}$$

in combination with the associated edge relations on the unit triangle. Application of the given terms in (3.98), leads, by solving the resulting system of equations, to the $[\mathcal{BDM}_1^{\triangle}]^2$ functions in $\boldsymbol{\xi}$ for $j=1,2,3$.

$$\begin{aligned}
\hat{\boldsymbol{\Psi}}_1^{j,1} &= \left\{ \begin{pmatrix} 2\xi \\ -\eta \end{pmatrix}, \begin{pmatrix} 1-\xi-3\eta \\ 2\eta \end{pmatrix}, \begin{pmatrix} -\xi \\ -2+3\xi+2\eta \end{pmatrix} \right\}\\
\hat{\boldsymbol{\Psi}}_1^{j,2} &= \left\{ \begin{pmatrix} -\xi \\ 2\eta \end{pmatrix}, \begin{pmatrix} -2+2\xi+3\eta \\ -\eta \end{pmatrix}, \begin{pmatrix} 2\xi \\ 1-3\xi-\eta \end{pmatrix} \right\}
\end{aligned} \tag{8.23}$$

Construction of $[\mathcal{BDM}_2^{\triangle}]^2$ approximation functions:
The basic quantities for evaluation of $[\mathcal{BDM}_2^{\triangle}]^2$ functions are

$$[\hat{\boldsymbol{v}}_2^{\triangle}]^2 = \begin{pmatrix} a_1+a_2\,\xi+a_3\,\eta+a_4\,\xi\eta+a_5\,\xi^2+a_6\,\eta^2 \\ b_1+b_2\,\xi+b_3\,\eta+b_4\,\xi\eta+b_5\,\xi^2+b_6\,\eta^2 \end{pmatrix}, \tag{8.24}$$

for $\hat{\boldsymbol{p}}_{m-1}$ the lowest order Nédélec functions with

$$\hat{\boldsymbol{p}}_1^{4,i} = \left\{ \begin{pmatrix} -\eta \\ \xi \end{pmatrix}, \begin{pmatrix} -\eta \\ \xi-1 \end{pmatrix}, \begin{pmatrix} 1-\eta \\ \xi \end{pmatrix} \right\}, \tag{8.25}$$

and $\hat{p}_2^{1,i} = \{-\xi + 2\xi^2\,, \xi - \xi^2\,, 1 - 3\,\xi + 2\,\xi^2\}$, $\hat{p}_2^{2,i} = \{2\,\eta - \eta^2\,, \eta - \eta^2\,, 1 - 3\,\eta + 2\,\eta^2\}$ $\hat{p}_2^{3,i} = \{1 - 3\,\xi + 2\,\xi^2\,, \xi - \xi^2\,, -\xi + 2\,\xi^2\}$ with $i = 1, 2, 3$, in combination with the associated edge relations on the unit triangle. Evaluation of the given terms in (3.98) and (3.99), yields, by solving the resulting system of equations, the $[\mathcal{BDM}_2^{\triangle}]^2$ functions in $\boldsymbol{\xi}$, i.e.,

$$\begin{aligned}
\hat{\boldsymbol{\Psi}}_2^{1,1} &= (-1.5\xi + 3\xi^2\,, 0.5\eta - 2\xi\eta)^T\,,\\
\hat{\boldsymbol{\Psi}}_2^{1,2} &= (-2\xi + 6\xi\eta + \xi^2,\ -2\eta + \eta^2 + 6\xi\eta)^T\,,\\
\hat{\boldsymbol{\Psi}}_2^{1,3} &= (0.5\xi - 2\xi\eta,\ -1.5\eta + 3\eta^2)^T\,,\\
\hat{\boldsymbol{\Psi}}_2^{2,1} &= (-0.5 + 4\eta - 5\eta^2 + 0.5\xi - 2\xi\eta,\ -1.5\eta + 3\eta^2)^T\,,\\
\hat{\boldsymbol{\Psi}}_2^{2,2} &= (1 - 10\eta + 10\eta^2 + 10\xi\eta - \xi^2,\ 4\eta - 5\eta^2 - 6\xi\eta)^T\,,\\
\hat{\boldsymbol{\Psi}}_2^{2,3} &= (-1.5 + 6\eta - 5\eta^2 + 4.5\xi - 8\xi\eta - 3\xi^2,\ -1.5\eta + 2\eta^2 + 2\xi\eta)^T\,,\\
\hat{\boldsymbol{\Psi}}_2^{3,1} &= (-1.5\xi + 2\xi\eta + 2\xi^2,\ -1.5 + 6\xi + 4.5\eta - 8\xi\eta - 5\xi^2 - 3\eta^2)^T\,,\\
\hat{\boldsymbol{\Psi}}_2^{3,2} &= (4\xi - 6\xi\eta - 5\xi^2,\ 1 - 10\xi + 10\xi\eta + 10\xi^2 - \eta^2)^T\\
\hat{\boldsymbol{\Psi}}_2^{3,3} &= (-1.5\xi + 3\xi^2,\ -0.5 + 4\xi + 0.5\eta - 2\xi\eta - 5\xi^2)^T\,,\\
\hat{\boldsymbol{\Psi}}_2^{4,1} &= (12\xi - 48\xi\eta - 12\xi^2,\ -12\eta + 12\eta^2 + 48\xi\eta)^T\,,\\
\hat{\boldsymbol{\Psi}}_2^{4,2} &= (12\xi - 24\xi\eta - 12\xi^2,\ -36\eta + 36\eta^2 + 48\xi\eta)^T\,,\\
\hat{\boldsymbol{\Psi}}_2^{4,3} &= (36\xi - 48\xi\eta - 36\xi^2,\ -12\eta + 12\eta^2 + 24\xi\eta)^T\,.
\end{aligned} \tag{8.26}$$

Construction of $[\mathcal{BDM}_1^{\square}]^2$ approximation functions:
For $[\mathcal{BDM}_1^{\square}]^2$ functions, the basic quantities needed are

$$[\hat{\boldsymbol{v}}_1^{\square}]^2 = \begin{pmatrix} a_1 + a_2\,\xi + a_3\,\eta + r\,\xi^2 - 2\,s\,\xi\eta \\ b_1 + b_2\,\xi + b_3\,\eta + 2\,r\,\xi\eta + s\,\eta^2 \end{pmatrix}, \tag{8.27}$$

with p_k as the Lagrange shape functions in $d = 1$ on the corresponding edge $\hat{p}_2^{j,1} = \frac{1}{2}\{(1-\xi), (1-\eta), (1+\xi), (1+\eta)\}$ and $\hat{p}_2^{j,2} = \frac{1}{2}\{(1+\xi), (1+\eta), (1-\xi), (1-\eta)\}$ for $j = 1, 2, 3, 4$ in combination with the associated edge relations on the unit quadrilateral. Evaluation of (3.98), yields, by solving the resulting system of equations, the $[\mathcal{BDM}_1^{\square}]^2$ functions in $\boldsymbol{\xi}$ with $i = 1, 2$:

$$\begin{aligned}
\hat{\boldsymbol{\Psi}}_1^{1,i} &= \tfrac{1}{8}\left\{(-3 + 3\,\xi^2,\ -2 + 2\,\eta + 6\,\xi - 6\,\xi\eta)^T\,, (3 - 3\,\xi^2,\ -2 + 2\,\eta - 6\,\xi + 6\,\xi\eta)^T\right\}\,,\\
\hat{\boldsymbol{\Psi}}_1^{2,i} &= \tfrac{1}{8}\left\{(2 - 6\,\eta + 2\,\xi - 6\,\xi\eta,\ -3\ + 3\,\eta^2)^T\,, (2 + 6\,\eta + 2\,\xi + 6\,\xi\eta,\ 3 - 3\,\eta^2)^T\right\}\,,\\
\hat{\boldsymbol{\Psi}}_1^{3,i} &= \tfrac{1}{8}\left\{(3 - 3\,\xi^2,\ 2\ + 2\,\eta + 6\,\xi + 6\,\xi\eta)^T\,, (-3 + 3\,\xi^2,\ 2 + 2\,\eta - 6\,\xi - 6\,\xi\eta)^T\right\}\,,\\
\hat{\boldsymbol{\Psi}}_1^{4,i} &= \tfrac{1}{8}\left\{(-2 - 6\,\eta + 2\,\xi + 6\,\xi\eta,\ 3 - 3\,\eta^2)^T\,, (-2 + 6\,\eta + 2\,\xi - 6\,\xi\eta,\ -3 + 3\,\eta^2)^T\right\}\,.
\end{aligned} \tag{8.28}$$

Construction of $[\mathcal{BDM}_2^{\square}]^2$ approximation functions:
The basic quantities for $[\mathcal{BDM}_2^{\square}]^2$ functions are

$$[\hat{\boldsymbol{v}}_2^{\square}]^2 = \begin{pmatrix} a_1 + a_2\,\xi + a_3\,\eta + a_4\,\xi\eta + a_5\,\xi^2 + a_6\,\eta^2 + r\,\xi^3 - 3\,s\,\xi\eta^2 \\ b_1 + b_2\,\xi + b_3\,\eta + b_1\,\xi\eta + b_2\,\xi^2 + b_3\,\eta^2 + 3\,r\,\xi^2\eta + s\,\eta^3 \end{pmatrix}, \tag{8.29}$$

$$\hat{\boldsymbol{p}}_1^{5,1} = \begin{pmatrix} \frac{1}{4}(1-\eta) \\ 0 \end{pmatrix} \quad \text{and} \quad \hat{\boldsymbol{p}}_1^{5,2} = \begin{pmatrix} 0 \\ \frac{1}{4}(1-\xi) \end{pmatrix}, \tag{8.30}$$

and $\hat{p}_2^{1,i} = \left\{\frac{1}{2}(-\xi+\xi^2), 1-\xi^2, \frac{1}{2}(\xi+\xi^2)\right\}$, $\hat{p}_2^{2,i} = \left\{\frac{1}{2}(-\eta+\eta^2), 1-\eta^2, \frac{1}{2}(\eta+\eta^2)\right\}$, $\hat{p}_2^{3,i} = \left\{\frac{1}{2}(\xi+\xi^2), 1-\xi^2, \frac{1}{2}(-\xi+\xi^2)\right\}$, $\hat{p}_2^{4,i} = \left\{\frac{1}{2}(\eta+\eta^2), 1-\eta^2, \frac{1}{2}(-\eta+\eta^2)\right\}$ for $i = 1,2,3$ in combination with the associated edge relations on the unit quadrilateral. Application of the given terms in (3.98) and (3.99), leads, by solving the resulting system of equations, to the $[\mathcal{BDM}_2^{\square}]^2$ functions in $\boldsymbol{\xi}$.

$$\begin{aligned}
\hat{\boldsymbol{\Psi}}_2^{1,1} &= \tfrac{1}{8}\left(5\,\xi - 5\,\xi^3,\ 9 - 3\,\eta - 6\,\eta^2 + 6\,\xi - 6\,\xi\eta - 15\,\xi^2 + 15\,\xi^2\eta\right)^T \\
\hat{\boldsymbol{\Psi}}_2^{1,2} &= \tfrac{1}{16}\left(-5\,\xi + 5\,\xi^3,\ -3 + 9\,\eta - 6\,\eta^2 + 15\,\xi^2 - 15\,\xi^2\eta\right)^T \\
\hat{\boldsymbol{\Psi}}_2^{1,3} &= \tfrac{1}{8}\left(5\,\xi - 5\,\xi^3,\ 3 - 3\,\eta - 6\,\xi + 6\,\xi\eta - 15\,\xi^2 + 15\,\xi^2\eta\right)^T \\
\hat{\boldsymbol{\Psi}}_2^{2,1} &= \tfrac{1}{8}\left(-9 - 6\,\eta + 15\,\eta^2 - 3\,\xi - 6\,\xi\eta + 15\,\eta^2\xi + 6\,\xi^2,\ 5\,\eta - 5\,\eta^3\right)^T \\
\hat{\boldsymbol{\Psi}}_2^{2,2} &= \tfrac{1}{16}\left(3 - 15\,\eta^2 + 9\,\xi - 15\,\eta^2\xi + 6\,\xi^2,\ -5\,\eta + 5\,\eta^3\right)^T \\
\hat{\boldsymbol{\Psi}}_2^{2,3} &= \tfrac{1}{8}\left(-3 + 6\,\eta + 15\,\eta^2 - 3\,\xi + 6\,\xi\eta + 15\,\eta^2\xi,\ 5\,\eta - 5\,\eta^3\right)^T \\
\hat{\boldsymbol{\Psi}}_2^{3,1} &= \tfrac{1}{8}\left(5\,\xi - 5\,\xi^3,\ -3 - 3\,\eta + 6\,\xi + 6\,\xi\eta + 15\,\xi^2 + 15\,\xi^2\eta\right)^T \\
\hat{\boldsymbol{\Psi}}_2^{3,2} &= \tfrac{1}{16}\left(-5\,\xi + 5\,\xi^3,\ 3 + 9\,\eta + 6\,\eta^2 - 15\,\xi^2 - 15\,\xi^2\eta\right)^T \\
\hat{\boldsymbol{\Psi}}_2^{3,3} &= \tfrac{1}{8}\left(5\,\xi - 5\,\xi^3,\ -9 - 3\,\eta + 6\,\eta^2 - 6\,\xi - 6\,\xi\eta + 15\,\xi^2 + 15\,\xi^2\eta\right)^T \\
\hat{\boldsymbol{\Psi}}_2^{4,1} &= \tfrac{1}{8}\left(3 - 6\,\eta - 15\,\eta^2 - 3\,\xi + 6\,\xi\eta + 15\,\eta^2\xi,\ 5\,\eta - 5\,\eta^3\right)^T \\
\hat{\boldsymbol{\Psi}}_2^{4,2} &= \tfrac{1}{16}\left(-3 + 15\,\eta^2 + 9\,\xi - 15\,\eta^2\xi - 6\,\xi^2,\ -5\,\eta + 5\,\eta^3\right)^T \\
\hat{\boldsymbol{\Psi}}_2^{4,3} &= \tfrac{1}{8}\left(9 + 6\,\eta - 15\,\eta^2 - 3\,\xi - 6\,\xi\eta + 15\,\eta^2\xi - 6\,\xi^2,\ 5\,\eta - 5\,\eta^3\right)^T \\
\hat{\boldsymbol{\Psi}}_2^{5,1} &= \left(1.5 - 1.5\xi^2,\ 0\right)^T \\
\hat{\boldsymbol{\Psi}}_2^{5,2} &= \left(0,\ 1.5 - 1.5\eta^2\right)^T
\end{aligned} \tag{8.31}$$

8.2 Appendix mixed finite element method at small strains

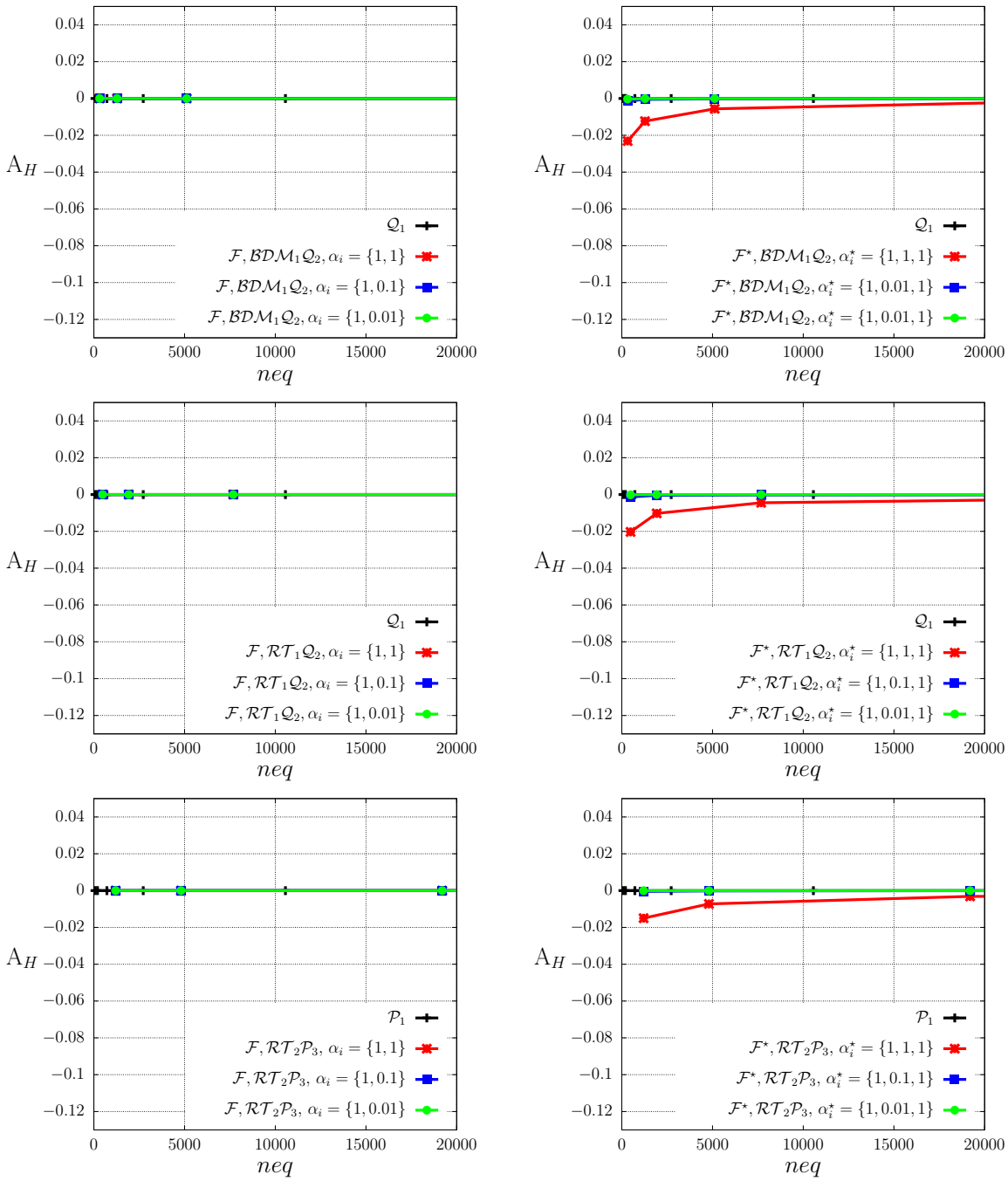

Figure 8.1: Clamped cantilever: Results for the fulfillment of equilibrium horizontal force (A_H) for $\mathcal{F}$ (left) and $\mathcal{F}^\star$ (right), considering $\mathcal{BDM}_1\mathcal{Q}_2$, $\mathcal{RT}_1\mathcal{Q}_2$ and $\mathcal{RT}_2\mathcal{P}_3$ element types

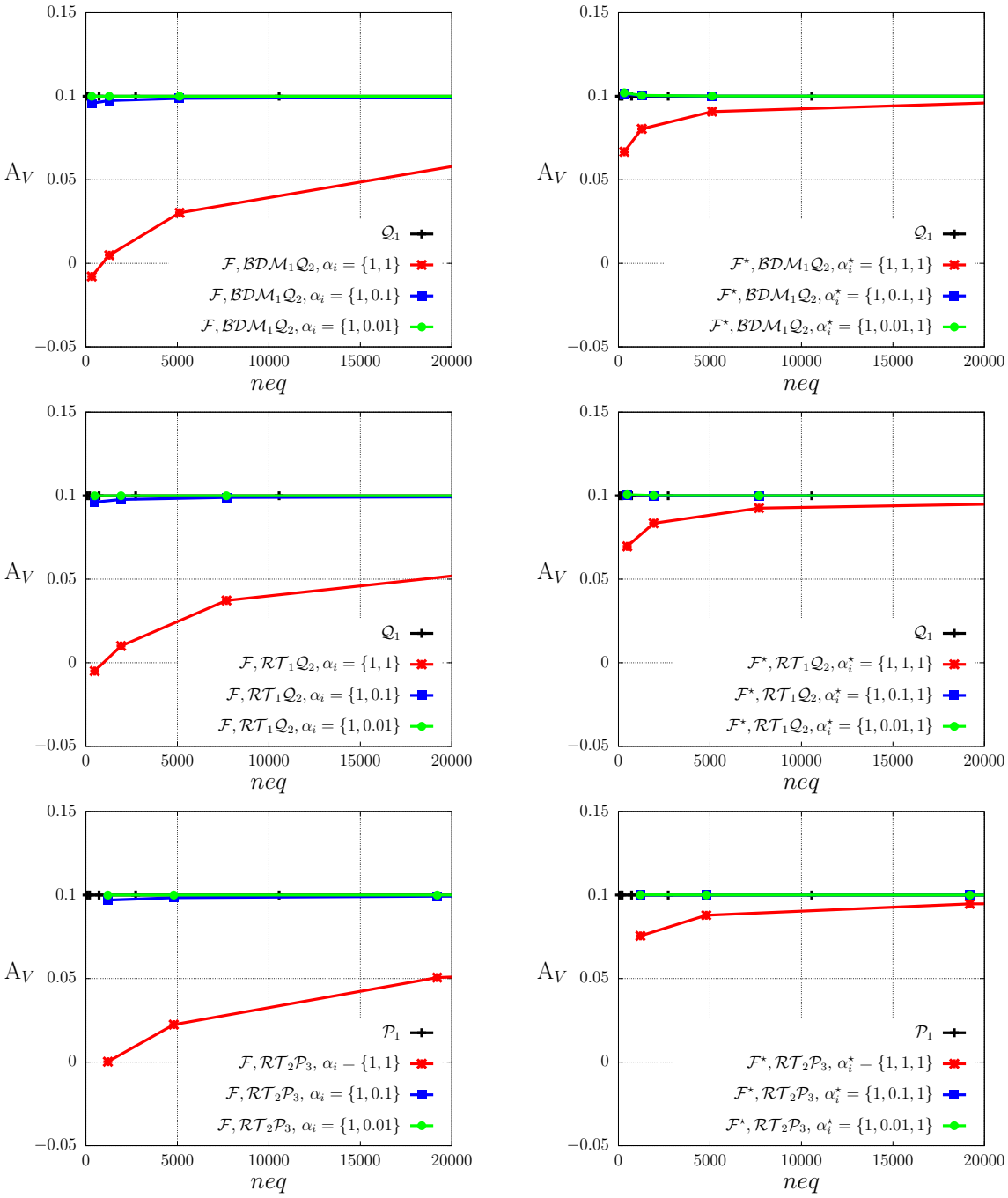

Figure 8.2: Clamped cantilever: Results for the fulfillment of equilibrium vertical force (A_V) for $\mathcal{F}$ (left) and $\mathcal{F}^\star$ (right), considering $\mathcal{BDM}_1\mathcal{Q}_2$, $\mathcal{RT}_1\mathcal{Q}_2$ and $\mathcal{RT}_2\mathcal{P}_3$ element types

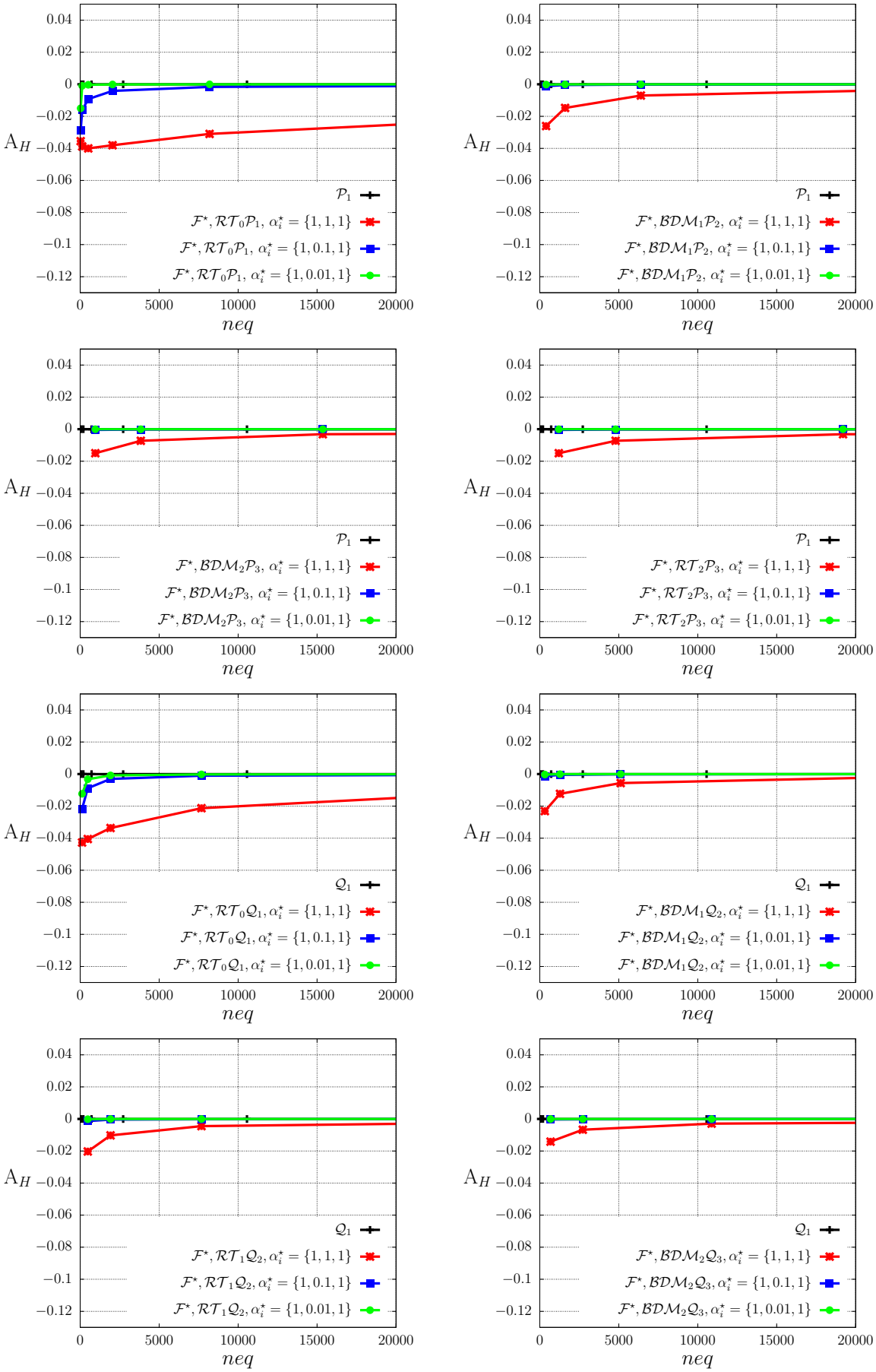

Figure 8.3: Clamped cantilever: Results for the fulfillment of equilibrium of moment A_H for LSFEM considering various finite element spaces on triangular and quadrilateral elements ($E = 70\,\mathrm{kN/mm^2}, \mu = 26.12\,\mathrm{kN/mm^2}$)

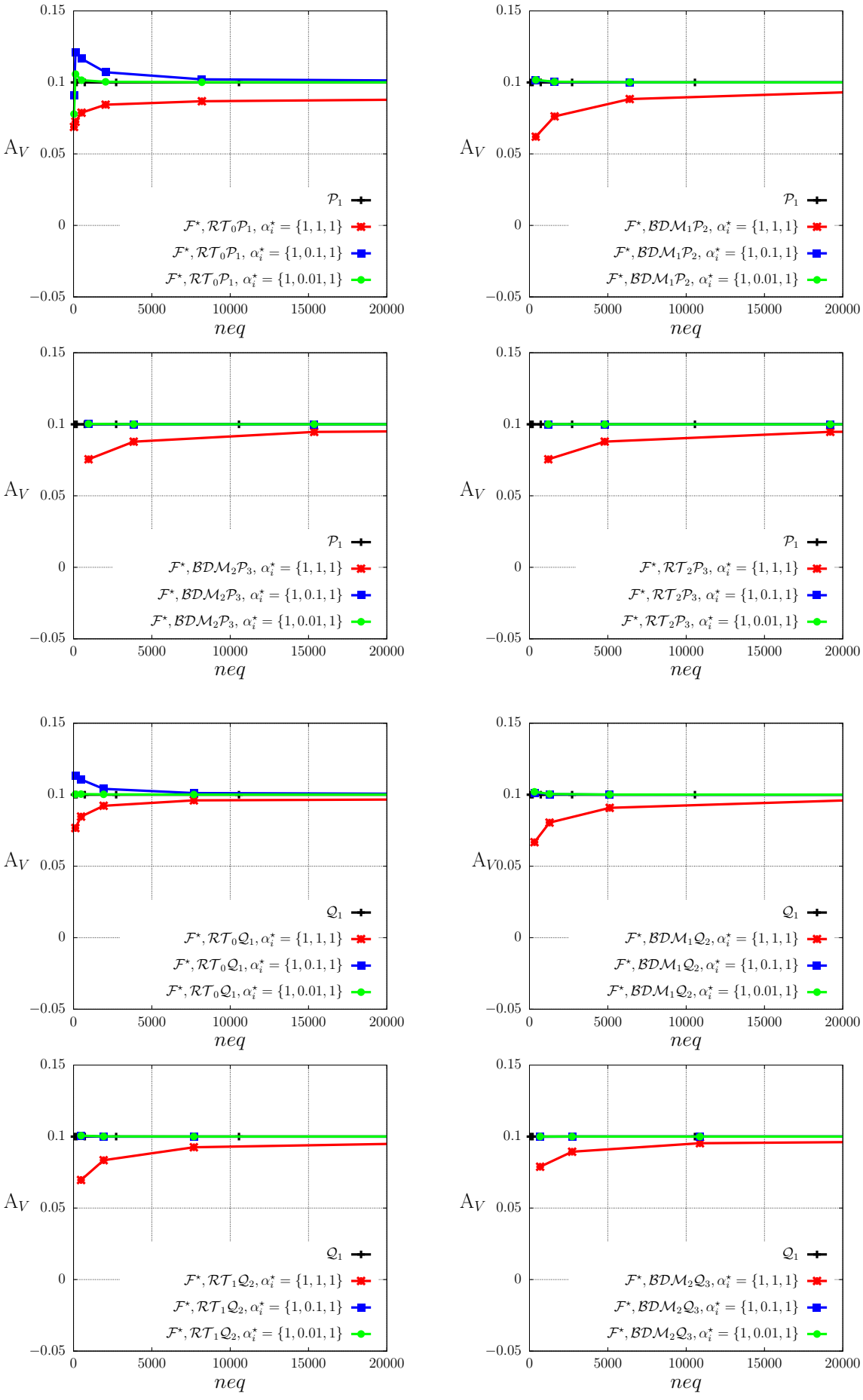

Figure 8.4: Clamped cantilever: Results for the fulfillment of equilibrium of moment A_V for LSFEM considering various finite element spaces on triangular and quadrilateral elements ($E = 70\,\mathrm{kN/mm^2}, \mu = 26.12\,\mathrm{kN/mm^2}$)

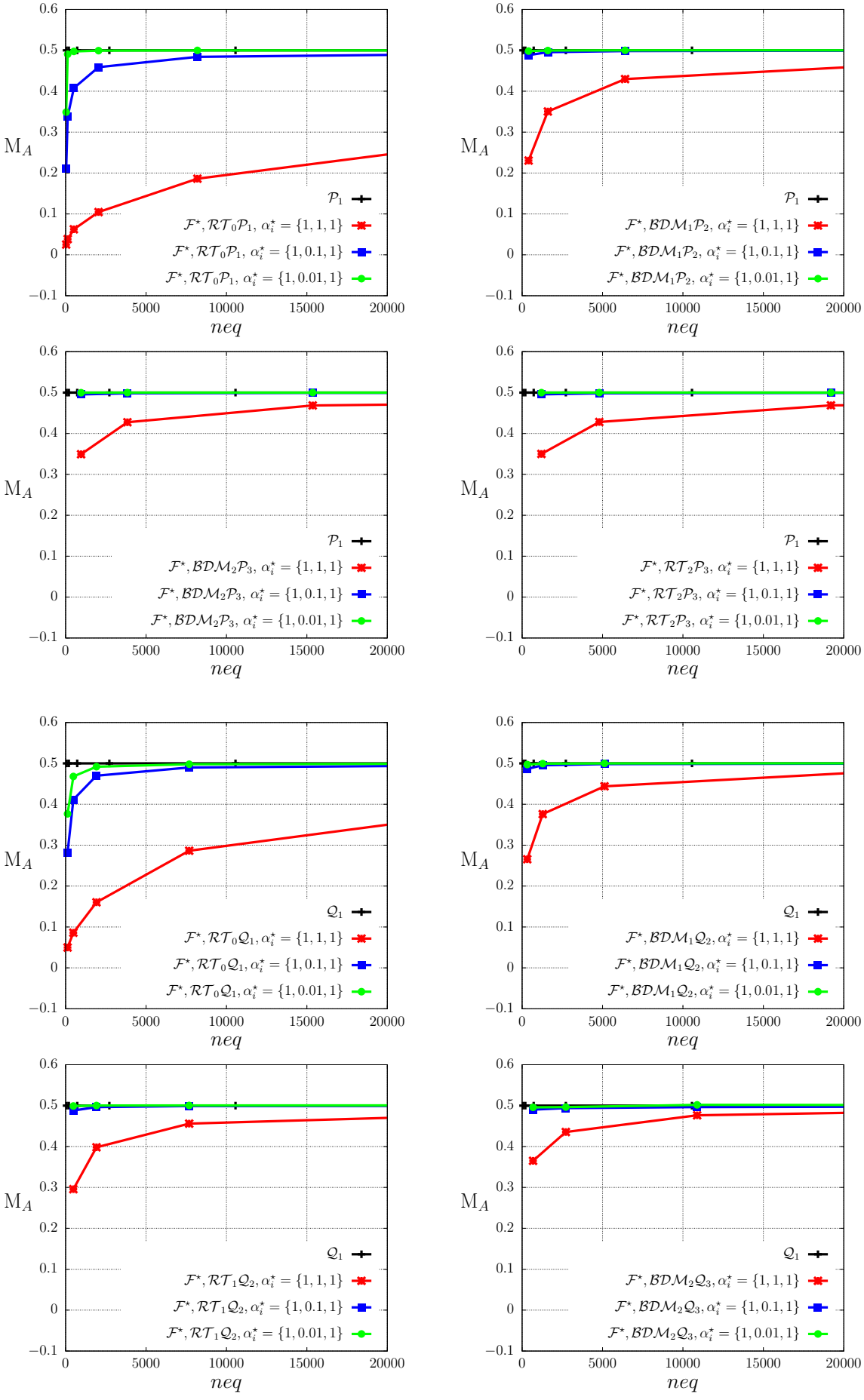

Figure 8.5: Clamped cantilever: Results for the fulfillment of equilibrium of moment A_M for LSFEM considering various finite element spaces on triangular and quadrilateral elements ($E = 70\,\mathrm{kN/mm^2}, \mu = 26.12\,\mathrm{kN/mm^2}$)

8.3 Appendix hybrid mixed finite element formulations

Representation of the applied body force for the fully constraint block example and the analytical stress components with the abbreviations $c_1 = (-1 + x^2)$, $c_2 = (-1 + y^2)$, $c_3 = (-1 + x)(1 + x)(-1 + y)(1 + y)$.

$$
\begin{aligned}
f_x = &-((-12x^{17}c_2^6(3+7y^2)^3 + 3x^{20}yc_2^7(3+7y^2)^2(13+7y^2)\\
&+ 32x^{15}c_2^6(3+7y^2)^2(7+11y^2) - 1792x^13c_2^6(3+16y^2+27y^4+14y^6)\\
&- 2x^{18}yc_2^7(1197+5637y^2+7875y^4+2891y^6)\\
&+ 40x^9c_2^4(-517-1481y^2-598y^4+130y^6-581y^8+167y^{10})\\
&+ 64x^{11}c_2^4(179+533y^2-4y^4-578y^6+301y^8+169y^{10})\\
&- 32x^7c_2^4(-759-1755y^2-650y^4-410y^6-175y^8+197y^{10})\\
&- 4xc_2^2(5+y^2)(21025-170y^2+263y^4-172y^6+79y^8-42y^{10}+9y^{12})\\
&+ 32x^5c_2^2(-1075-953y^2+873y^4-1165y^6+775y^8-507y^{10}+131y^{12}+y^14\\
&- 7680(3+7y^2)) + 128x^3c_2^2(265+250y^2+28y^4+90y^6-75y^8+38y^{10}-26y^{12}+6y^{14}\\
&+ 1280(7+11y^2)) - 24x^{14}yc_2^4(-635-498y^2+2023y^4+256y^6-1561y^8-238y^{10}\\
&+ 653y^{12}+320(39+157y^2+133y^4-49y^6))\\
&+ 2x^{12}yc_2^4(-14063-10422y^2+26867y^4+2012y^6-7113y^8-1830y^{10}+4549y^{12}\\
&- 1280(-393-1299y^2-715y^4+511y^6))\\
&+ 3x^16yc_2^4(1280(3+7y^2)^2+c_2^3(2341+9657y^2+11971y^4+4431y^6))\\
&- 2x^8yc_2^2(23275-27568y^2-4344y^4+1112y^6+23230y^8-22752y^{10}+12288y^{12}\\
&- 6600y^{14}+1359y^{16}+1280(-1312-1277y^2+2208y^4-1838y^6+320y^8+75y^{10}))\\
&+ 8x^6yc_2^2(6461-4348y^2-1880y^4-1608y^6+3310y^8-3276y^{10}+2248y^{12}-1136y^{14}\\
&+ 229y^{16}-320(1591+1335y^2-974y^4+1298y^6-969y^8+215y^{10}))\\
&- 4x^10yc_2^2(c_2^3(9027+14533y^2+5186y^4+342y^6+891y^8+165y^{10})\\
&- 640(-837-641y^2+2378y^4-510y^6-1429y^8+559y^{10}))\\
&+ y(-1280(-1525+1812y^2-2327y^4+1898y^6-883y^8+368y^{10}-129y^{12}+18y^{14})\\
&+ c_2^3(-2725+5755y^2-2845y^4+3227y^6-1943y^8+921y^{10}-423y^{12}+81y^{14}))\\
&- 2x^2y(-1280(-2191+3267y^2-3867y^4+3167y^6-1581y^8+585y^{10}-169y^{12}+21y^{14})\\
&+ c_2^3(-1515+9625y^2-5163y^4+5585y^6-3465y^8+1587y^{10}-609y^{12}+99y^{14}))\\
&+ x^4y(2560(1743-3115y^2+2715y^4-1527y^6+317y^8+591y^{10}-423y^{12}+83y^{14})\\
&- c_2^3(-23075-29291y^2+8421y^4-8763y^6+4447y^8-393y^{10}-801y^{12}+303y^{14})))\\
&/(64(-17+5y^2-7y^4+3y^6+x^2c_2^2(5+y^2)+x^6c_2^2(3+7y^2)-x^4c_2^2(7+11y^2))^2))
\end{aligned}
$$

$$
\begin{aligned}
f_y = &(4x^{18}yc_2^5(3+7y^2)^2(-1+21y^2)+x^{21}c_2^6(3+7y^2)^2(9-10y^2+21y^4)\\
&+ 512x^{14}yc_2^5(1+29y^2+87y^4+63y^6) - 4x^{16}yc_2^5(-15+1141y^2+4823y^4+4851y^6)\\
&+ 3x^{17}c_2^6(811+2392y^2+1214y^4+288y^6+1295y^8) - 2x^{19}c_2^6(333+1092y^2\\
&+ 702y^4+868y^6+2205y^8) - 32x^{12}yc_2^3(61+891y^2+570y^4-1750y^6+521y^8+507y^{10})\\
&- 8x^{10}yc_2^3(-587-6209y^2-3978y^4+3234y^6-5483y^8+1503y^{10})\\
&+ 8x^8yc_2^3(-1281-7475y^2-2670y^4-2170y^6-2385y^8+1773y^{10})\\
&+ 4y(5-14y^2+9y^4)(21025-170y^2+263y^4-172y^6+79y^8-42y^{10}+9y^{12})\\
&+ 1280x(1525-4382y^2+3486y^4-3182y^6+2624y^8-1674y^{10}+786y^{12}-234y^{14}+27y^{16})\\
&- xc_2^2(-2725-2420y^2+20960y^4-7348y^6+10894y^8-6972y^{10}+3288y^{12}\\
&- 1692y^{14}+351y^{16}) - 32x^6yc_2(-399-1535y^2+2329y^4-2975y^6+2395y^8-1445y^{10}\\
&+ 347y^{12}+3y^{14}+2560(1-21y^2))\\
&+ 4x^2yc_2(5755-3205y^2+6371y^4-3877y^6+1993y^8-935y^{10}-39y^{12}
\end{aligned}
$$

$$
\begin{aligned}
&+ 81y^{14} + 61440(3 + y^2)) + 8x^1 5c_2^4(-757 - 490y^2 + 2217y^4 - 128y^6 \\
&- 1535y^8 - 1382y^{10} + 1275y^{12} + 320(-1 + 3y^2)(3 + 7y^2)^2) \\
&- 128x^4 yc_2(140 + 347y^2 - 79y^4 + 375y^6 - 320y^8 + 211y^{10} - 125y^{12} + 27y^{14} \\
&+ 48(40 + 440y^2)) - 2x^1 3c_2^4(-6121 - 3134y^2 + 12949y^4 - 2324y^6 - 12383y^8 - 12782y^{10} \\
&+ 12915y^{12} - 640(129 + 178y^2 - 908y^4 - 1386y^6 + 147y^8)) \\
&+ 4x^1 1c_2^4(-4819 - 2326y^2 + 7499y^4 + 1668y^6 - 8757y^8 - 1806y^{10} + 4893y^{12} \\
&- 640(184 + 151y^2 - 1091y^4 - 1083y^6 + 231y^8)) - 8x^7 c_2^2(3969 - 4928y^2 - 1472y^4 \\
&+ 4180y^6 + 5390y^8 - 8136y^{10} + 6272y^{12} - 4172y^{14} + 945y^{16} \\
&- 320(-949 + 1269y^2 + 1960y^4 - 1930y^6 + 1711y^8 - 555y^{10} + 30y^{12})) \\
&+ x^5 c_2^2(28285 - 20596y^2 - 42408y^4 + 41996y^6 - 21734y^8 + 5700y^{10} + 1488y^{12} - 7644y^{14} \\
&+ 2625y^{16} - 1280(-2327 + 3080y^2 + 3057y^4 - 1072y^6 + 1699y^8 - 1176y^{10} + 195y^{12})) \\
&+ 2x^9 c_2^2(12957 - 19420y^2 - 9152y^4 + 19700y^6 + 31890y^8 - 54228y^{10} + 33320y^{12} \\
&- 10052y^{14} + 105y^{16} + 640(883 - 1396y^2 - 3041y^4 + 4392y^6 - 583y^8 - 1620y^{10} + 405y^{12})) \\
&+ 2x^3(1280(-906 + 3267y^2 - 3115y^4 + 1847y^6 - 1347y^8 + 1033y^{10} - 273y^{12} - 3y^{14} + 9y^{16}) \\
&+ c_2^2(-6965 + 240y^2 + 27412y^4 - 14496y^6 + 17714y^8 - 11280y^{10} \\
&+ 5556y^{12} - 2112y^{14} + 315y^{16}))) \\
&/(64(-17 + 5y^2 - 7y^4 + 3y^6 + x^2 c_2^2(5 + y^2) + x^6 c_2^2(3 + 7y^2) - x^4 c_2^2(7 + 11y^2))^2)
\end{aligned}
$$

$$
\begin{aligned}
P_{xx} = &(c_1\, c_2(c_4(-33 + 5x^2 - 7x^4 + 3x^6 + c_1^2(5 + x^2)y^2 - c_1^2(7 + 11x^2)y^4 \\
&+ c_1^2(3 + 7x^2)y^6)(-1 + xc_1 yc_2)(-1 + 3y^2 + x^2(3 + 7y^2))\lambda + 32(-1 + 4y^2 - 3y^4 \\
&+ x^3 yc_2^2(5 + y^2) + x^7 yc_2^2(3 + 7y^2) - x^5 yc_2^2(7 + 11y^2) - 4x^2(-1 + y^4) \\
&+ xy(-3 + y^2)(11 + 2y^2 + 3y^4) + x^4(-3 - 4y^2 + 7y^4))\mu))/ \\
&(32(-17 + 5y^2 - 7y^4 + 3y^6 + x^2 c_2^2(5 + y^2) + x^6 c_2^2(3 + 7y^2) - x^4 c_2^2(7 + 11y^2)))
\end{aligned}
$$

$$
\begin{aligned}
P_{xy} = &(-c_1^2(-1 + 3x^2)c_2^4(-33 + 5x^2 - 7x^4 + 3x^6 + c_1^2(5 + x^2)y^2 - c_1^2(7 \\
&+ 11x^2)y^4 + c_1^2(3 + 7x^2)y^6)(-1 + 3y^2 + x^2(3 + 7y^2))\lambda + 32(1 + 9x^2 + 34x^4 \\
&- 22x^6 + 13x^8 - 3x^{10} + 8(-3 + 5x^2 - 16x^4 + 10x^6 - 5x^8 + x^{10})y^2 + 2(3 - 13x^2 \\
&+ 38x^4 - 2x^6 - 17x^8 + 7x^{10})y^4 - 8c_1^4(3 + 5x^2)y^6 + 3c_1^4(3 + 7x^2)y^8)\mu)/ \\
&(128(-17 + 5y^2 - 7y^4 + 3y^6 + x^2 c_2^2(5 + y^2) + x^6 c_2^2(3 + 7y^2) - x^4 c_2^2(7 + 11y^2)))
\end{aligned}
$$

$$
\begin{aligned}
P_{yx} = &(c_1^4 c_2^2(-1 + 3y^2)(-33 + 5x^2 - 7x^4 + 3x^6 + c_1^2(5 + x^2)y^2 - c_1^2(7 + 11x^2)y^4 \\
&+ c_1^2(3 + 7x^2)y^6)(-1 + 3y^2 + x^2(3 + 7y^2))\lambda - 32(1 + 9y^2 + 34y^4 - 22y^6 + 13y^8 \\
&- 3y^{10} - 8x^6 c_2^4(3 + 5y^2) + 3x^8 c_2^4(3 + 7y^2) + 8x^2(-3 + 5y^2 - 16y^4 + 10y^6 \\
&- 5y^8 + y^{10}) + 2x^4(3 - 13y^2 + 38y^4 - 2y^6 - 17y^8 + 7y^1 0))\mu)/ \\
&(128(-17 + 5y^2 - 7y^4 + 3y^6 + x^2 c_2^2(5 + y^2) + x^6 c_2^2(3 + 7y^2) - x^4 c_2^2(7 + 11y^2)))
\end{aligned}
$$

$$
\begin{aligned}
P_{yy} = -&((c_1\, c_2(c_4(-33 + 5x^2 - 7x^4 + 3x^6 + c_1^2(5 + x^2)y^2 - c_1^2(7 + 11x^2)y^4 \\
&+ c_1^2(3 + 7x^2)y^6)(1 + xc_1 yc_2)(-1 + 3y^2 + x^2(3 + 7y^2))\lambda + 32(1 - 4y^2 + 3y^4 \\
&+ x^3 yc_2^2(5 + y^2) + x^7 yc_2^2(3 + 7y^2) - x^5 yc_2^2(7 + 11y^2) + x^4(3 + 4y^2 - 7y^4) \\
&+ 4x^2(-1 + y^4) + xy(-3 + y^2)(11 + 2y^2 + 3y^4))\mu))/ \\
&(32(-17 + 5y^2 - 7y^4 + 3y^6 + x^2 c_2^2(5 + y^2) + x^6 c_2^2(3 + 7y^2) - x^4 c_2^2(7 + 11y^2))))
\end{aligned}
$$

List of Figures

List of Tables

References

[1] J. Ahrens, B. Geveci, and C. Law. *ParaView: An End-User Tool for Large Data Visualization, Visualization Handbook*. Elsevier, version 10.1 edition, 2005. Champaign, Illinois.

[2] U. Andelfinger and E. Ramm. EAS-elements for two-dimensional, three-dimensional, plate and shell structures and their equivalence to HR-elements. *International Journal for Numerical Methods in Engineering*, 36:1311–1337, 1993.

[3] J. H. Argyris. Energy theorems and structural analysis: A generalized discourse with applications on energy principles of structural analysis including the effects of temperature and non-linear stress-strain relations. *Aircraft Engineering and Aerospace Technology*, 26:347–356, 1954.

[4] J. H. Argyris, I. Fried, and D. W. Scharpf. The TET 20 and TEA 8 elements for the matrix displacement method. *The Aeronautical Journal*, 72:618–625, 1968.

[5] F. Armero. Elastoplastic and viscoplastic deformations in solids and structures. *Encyclopedia of Computational Mechanics*, Vol. 1:Chapter 7, Wiley and Sons, 2004.

[6] D. Arnold and R. Winther. Nonconforming mixed elements for elasticity. *Mathematical Methods in Applied Science*, 13:295–307, 2003.

[7] D. Arnold, R. Falk, and R. Winther. Multigrid in $H(\mathrm{div})$ and $H(\mathrm{curl})$. *Numerische Mathematik*, 85:197–217, 2000.

[8] D. Arnold, D. Boffi, and R. Falk. Quadrilateral $H(\mathrm{div})$ finite elements. *SIAM Journal on Numerical Analysis*, 42:2429–2451, 2005.

[9] D. Arnold, R. Falk, and R. Winther. Mixed finite element methods for linear elasticity with weakly imposed symmetry. *Mathematics of Computation*, 76:1699–1723, 2007.

[10] D. N. Arnold, F. Brezzi, and J. Douglas. PEERS: A new mixed finite element for plane elasticity. *Japan Journal of Applied Mathematics*, 1:347–367, 1984.

[11] D. N. Arnold, J. Douglas, and C. P. Gupta. A family of higher order mixed finite element methods for plane elasticity. *Numerische Mathematik*, 45:1–22, 1984.

[12] D. N. Arnold, F. Brezzi, B. Cockburn, and L. D. Marini. Unified analysis of discontinuous Galerkin methods for elliptic problems. *SIAM Journal on Numerical Analysis*, 39(5):1749–1779, 2002.

[13] D. N. Arnold, G. Awanou, and R. Winther. Finite elements for symmetric tensors in three dimensions. *Mathematics of Computation*, 263:1229–1251, 2008.

[14] R. J. Asaro. Micromechanics of crystals and polycrystals. *Advances in Applied Mechanics*, 23:1–115, 1983.

[15] S. N. Atluri, R. H. Gallagher, and O. Zienkiewicz. *Hybrid and Mixed Finite Element Methods*. John Wiley & Sons, Chichester, 1983.

[16] S. N. Atluri, P. Tong, and H. Murakawa. Recent studies of hybrid and mixed finite element methods in mechanics. In S. N. Atluri, R. H. Gallagher, and O. C. Zienkiewicz, editors, *Hybrid and mixed finite element methods*, pages 51–72. John Wiley & Sons, 1983.

[17] F. Auricchio, F. Brezzi, and C. Lovadina. *Encyclopedia of Computational Mechanics*. John Wiley & Sons, Ltd., 2nd edition, 2004.

[18] F. Auricchio, L. Beirão da Veiga, C. Lovadina, and A. Reali. An analysis of some mixed-enhanced finite element for plane linear elasticity. *Computer Methods in Applied Mechanics and Engineering*, 194:2947–2968, 2005.

[19] A. Aziz, R. Kellogg, and A. Stephens. Least squares methods for elliptic systems. *Mathematics of computation*, 44(169):53–70, 1985.

[20] I. Babuška. The finite element method with Lagrangian multipliers. *Numerische Mathematik*, 20(3):179–192, 1973.

[21] I. Babuška and M. Suri. Locking effects in the finite element approximation of elasticity problems. *Numerische Mathematik*, 62(1):439–463, 1992.

[22] C. Bahriawati and C. Carstensen. Three MATLAB implementations of the lowest-order Raviart-Thomas MFEM with a posteriori error control. *Computational Methods in Applied Mathematics*, Vol. 5:333–361, 2005.

[23] R. Bank and L. Scott. On the conditioning of finite element equations with highly refined meshes. *SIAM Journal on Numerical Analysis*, 26(6):1383–1394, 1989.

[24] K.-J. Bathe. *Finite element procedures*. Prentice Hall, New Jersey, 1996.

[25] K.-J. Bathe. The inf–sup condition and its evaluation for mixed finite element methods. *Computers and Structures*, 79(2):243–252, 2001.

[26] B. Bell and K. Surana. A space-time coupled p-version least-squares finite element formulation for unsteady fluid dynamics problems. *International Journal for Numerical Methods in Engineering*, 37:3545–3569, 1994.

[27] B. Bell and K. Surana. p-version least squares finite element formulation for two-dimensional, incompressible, non-Newtonian isothermal and non-isothermal fluid flow. *International Journal for Numerical Methods in Fluids*, 18:127–162, 1994.

[28] R. Bensow and M. G. Larson. Discontinuous/continuous least-squares finite element methods for elliptic problems. *Mathematical Models and Methods in Applied Sciences*, 15(6):825–842, 2005.

[29] R. Bensow and M. G. Larson. Discontinuous least-squares finite element method for the div-curl problem. *Numerische Mathematik*, 101:601–617, 2005.

[30] J. Bergh and J. Löfström. *Interpolation Spaces - An Introduction*. Springer-Verlag, 1976.

[31] M. Berndt, T. Manteuffel, and S. McCormick. Local error estimates and adaptive refinement for first-order system least squares (FOSLS). *Electronic Transactions on Numerical Analysis*, 6:35–43, 1997.

[32] M. Berndt, T. Manteuffel, and S. McCormick. Analysis of first-order system least squares (FOSLS) for elliptic problems with discontinuous coefficients: Part II. *SIAM Journal on Numerical Analysis*, 43:409–436, 2005.

[33] M. Berndt, T. Manteuffel, S. McCormick, and G. Starke. Analysis of first-order system least squares (FOSLS) for elliptic problems with discontinuous coefficients: Part I. *SIAM Journal on Numerical Analysis*, 43:386–408, 2005.

[34] E. Bertóti. A comparison of primal- and dual-mixed finite element formulations for Timoshenko beams. *Engineering with Computers*, 31:99–111, 2015.

[35] F. Bertrand, B. Kober, M. Moldenhauer, and G. Starke. *Equilibrated stress reconstruction and a posteriori error estimation for linear elasticity*, volume 597 of *CISM International Centre for Mechanical Sciences (Courses and Lectures)*, pages 69–106. Springer, Cham., 2020.

[36] S. Bidwell, M. E. Hassell, and C. R. Westphal. A weighted least squares finite element method for elliptic problems with degenerate and singular coefficients. *Mathematics of Computation*, 82(282):673–688, 2013.

[37] M. Bischoff, E. Ramm, and D. Braess. A class of equivalent enhanced assumed strain and hybrid stress finite elements. *Computational Mechanics*, 22:443–449, 1999.

[38] P. Bochev. *Least-squares finite element methods for the Stokes and Navier-Stokes equations*. Phd thesis, Virginia Polytechnic Institute and State University, Blacksburg, Virginia, 1994.

[39] P. Bochev. Analysis of least-squares finite element methods for the Navier-Stokes equations. *SIAM Journal on Numerical Analysis*, 34:1817–1844, 1997.

[40] P. Bochev and M. Gunzburger. Accuracy of least-squares methods for the Navier-Stokes equations. *Computers and Fluids*, 22:549–563, 1993.

[41] P. Bochev and M. Gunzburger. Analysis of least squares finite element methods for the Stokes equations. *Mathematics of Computation*, 63:479–506, 1994.

[42] P. Bochev and M. Gunzburger. Least-squares methods for the velocity-pressure-stress formulation of the Stokes equations. *Computer Methods in Applied Mechanics and Engineering*, 126:267–287, 1995.

[43] P. Bochev and M. Gunzburger. *Least-Squares Finite Element Methods*. Springer-Verlag, New York, 1st edition, 2009.

[44] P. Bochev, J. Lai, and L. Olson. A locally conservative, discontinuous least-squares finite element method for the Stokes equations. *International Journal for Numerical Methods in Fluids*, 68(6):782–804, 2012.

[45] P. Bochev, J. Lai, and L. Olson. A non-conforming least-squares finite element method for the velocity-vorticity-pressure Stokes equations. *International Journal for Numerical Methods in Fluids*, 72:375–402, 2013.

[46] P. B. Bochev and J. Choi. A comparative study of least-squares, SUPG and Galerkin methods for convection problems. *International Journal of Computational Fluid Dynamics*, 15:127–146, 2001.

[47] P. B. Bochev and J. Choi. Improved least-squares error estimates for scalar hyperbolic problems. *Computational Methods in Applied Mathematics*, 1:115–124, 2001.

[48] D. Boffi, F. Brezzi, and M. Fortin. Reduced symmetry elements in linear elasticity. *Communications On Pure and Applied Analysis*, 8:95–121, 2009.

[49] D. Boffi, F. Brezzi, and M. Fortin. *Mixed Finite Element Methods and Applications*. Springer, Heidelberg, 2013.

[50] D. Braess. *Finite Elemente*. Springer-Verlag, 2007.

[51] J. Bramble, R. Lazarov, and J. Pasciak. A least-squares approach based on a discrete minus one inner product for first order systems. *Mathematics of Computation*, 66: 935–955, 1997.

[52] S. Brenner. Fourty years of the Crouzeix-Raviart element. *Numerical Methods for Partial Differential Equations*, 31:367–396, 2014.

[53] S. C. Brenner and L. R. Scott. *The mathematical theory of finite element methods*. Springer, 1994.

[54] S. C. Brenner and L. R. Scott. *The mathematical theory of finite element methods*. Springer-Verlag, 3rd edition, 2008.

[55] F. Brezzi. On the existence, uniqueness and approximation of saddle-point problems arising from Lagrangian multipliers. *Revue française d'automatique, informatique, recherche opérationnelle. Analyse numérique*, 8(2):129–151, 1974.

[56] F. Brezzi and M. Fortin. *Mixed and Hybrid Finite Element Methods*. Springer-Verlag, NewYork, 1991.

[57] F. Brezzi, J. Douglas, and L. D. Marini. Two families of mixed finite elements for second order elliptic problems. *Numerische Mathematik*, 47:217–235, 1985.

[58] F. Brezzi, J. Douglas, R. Duran, and M. Fortin. Mixed finite elements for second order elliptic problems in three variables. *Numerische Mathematik*, 51:237–250, 1987.

[59] F. Brezzi, J. Douglas, M. Fortin, and D. Marini. Efficient rectangular mixed finite elements in two and three space variables. *Mathematical Modelling and Numerical Analysis*, 21:581–604, 1987.

[60] Z. Cai and G. Starke. First-order system least squares for the stress-displacement formulation: Linear elasticity. *SIAM Journal on Numerical Analysis*, 41:715–730, 2003.

[61] Z. Cai and G. Starke. Least-squares methods for linear elasticity. *SIAM Journal on Numerical Analysis*, 42:826–842, 2004.

[62] Z. Cai and C. Westphal. A weighted $H(\mathrm{div})$ least-squares method for second-order elliptic problems. *SIAM Journal on Numerical Analysis*, 46:1640–1651, 2008.

[63] Z. Cai, T. Manteuffel, and S. McCormick. First-order system least squares for velocity-vorticity-pressure form of the Stokes equations, with application to linear elasticity. *Electronic Transactions on Numerical Analysis*, 3:150–159, 1995.

[64] Z. Cai, T. Manteuffel, and S. McCormick. First-order system least squares for the Stokes equation, with application to linear elasticity. *SIAM Journal on Numerical Analysis*, 34:1727–1741, 1997.

[65] Z. Cai, T. Manteuffel, S. McCormick, and S. Parter. First-order system least squares (FOSLS) for planar linear elasticity: Pure traction problem. *SIAM Journal on Numerical Analysis*, 35:320–335, 1998.

[66] Z. Cai, C.-O. Lee, T. Manteuffel, and S. McCormick. First-order system least squares for linear elasticity: Numerical results. *SIAM Journal on Scientific Computing*, 21: 1706–1727, 2000.

[67] Z. Cai, C.-O. Lee, T. Manteuffel, and S. McCormick. First-order system least squares for the Stokes and linear elasticity equations: Further results. *SIAM Journal on Scientific Computing*, 21:1728–1739, 2000.

[68] Z. Cai, T. Manteuffel, S. McCormick, and J. Ruge. First-order system $\mathcal{LL}^*$ (FOSLL*): Scalar elliptic partial differential equations. *SIAM Journal on Numerical Analysis*, 39(4):1418–1445, 2002.

[69] Z. Cai, J. Korsawe, and G. Starke. An adaptive least squares mixed finite element method for the stress-displacement formulation of linear elasticity. *Numerical Methods for Partial Differential Equations*, 21:132–148, 2005.

[70] G. Carey and J. Oden. *Finite Elements: A second course.* Prentice Hall, Inc., 1983.

[71] C. L. Chang and B.-N. Jiang. An error analysis of least-squares finite element method of velocity-pressure-vorticity formulation for the Stokes problem. *Computer Methods in Applied Mechanics and Engineering*, 84:247–255, 1990.

[72] C. L. Chang and J. J. Nelson. Least-squares finite element method for the Stokes problem with zero residual of mass conservation. *SIAM Journal on Scientific Computing*, 34(2):480–489, 1997.

[73] D. Chapelle and K. Bathe. The inf-sup test. *Computers and Structures*, 47:537–545, 1993.

[74] Z. Chen. *Finite element methods and their applications.* Springer, 2005.

[75] K. Chun, S. Kassenge, and W. Park. Static assessment of quadratic hybrid plane stress element using non-conforming displacement modes and modified shape functions. *Structural Engineering and Mechanics*, 29:643–658, 2008.

[76] P. Ciarlet and J. Lions. *Handbook of Numerical Analysis, Volume II, Finite Element Methods (Part I)*. Elsevier Science B.V., 1991.

[77] P. G. Ciarlet. *The Finite Element Method for Elliptic Problems*. North-Holland, 1978.

[78] P. G. Ciarlet. *Mathematical Elasticity, Volume 1: Three Dimensional Elasticity*. Elsevier Science Publishers B.V., North Holland, 1988.

[79] R. W. Clough. The finite element method in plane stress analysis. *Proceedings Second ASCE Conference on Electronic Computation, Pittsburgh, PA*, page 345, 1960.

[80] B. Cockburn, J. Gopalakrishnan, and J. Guzmán. A new elasticity element made for enforcing weak stress symmetry. *Mathematics of Computation*, 79:1331–1349, 2010.

[81] R. Cook. Improved two-dimensional finite element. *Journal of Structural Division*, 100(9):1851–1863, September 1974.

[82] R. Courant. Variational methods for the solution of problems of equilibrium and vibrations. *Bulletin of the American Mathematical Society*, 49:1–23, 1943.

[83] M. Crouzeix and P.-A. Raviart. Conforming and nonconforming finite element methods for solving the stationary Stokes equations I. *ESAIM: Mathematical Modelling and Numerical Analysis*, 7:33–75, 1973.

[84] A. Cuitino and M. Ortiz. A material independent method for extending stress update algorithms from small-strain plasticity to finite plasticity with multiplicative kinematics. *Engineering Computations*, 9:437–451, 1992.

[85] R. De Borst. The zero-normal-stress condition in plane-stress and shell elastoplasticity. *Communications in Applied Numerical Methods*, 7:29–33, 1991.

[86] E. de Souza Neto, D. Perić, and D. Owen. *Computational Methods for Plasticity: Theory and Applications*. John Wiley & Sons, Ltd., 1 edition, 2008.

[87] H. De Sterck, T. A. Manteuffel, S. F. McCormick, and L. Olson. Least-squares finite element methods and algebraic multigrid solvers for linear hyperbolic PDEs. *SIAM Journal on Scientific Computing*, 26(1):31–54, 2004.

[88] H. De Sterck, T. A. Manteuffel, S. F. McCormick, and L. Olson. Numerical conservation properties of H(div)-conforming least-squares finite element methods for the Burgers equation. *SIAM Journal on Scientific Computing*, 26(5):1573–1597, 2005.

[89] J. Deang and M. Gunzburger. Issues related to least-squares finite element methods for the stokes equations. *SIAM Journal on Scientific Computing*, 20:878–906, 1998.

[90] L. Demkowicz and J. Gopalakrishnan. Analysis of the DPG method for the Poisson equation. *SIAM Journal on Numerical Analysis*, 49:1788–1809, 2011.

[91] P. R. B. Devloo, C. O. Faria, A. M. Farias, S. M. Gomes, A. F. D. Loula, and S. M. C. Malta. On continuous, discontinuous, mixed, and primal hybrid finite element methods for second-order elliptic problems. *International Journal for Numerical Methods in Engineering*, 115:1083–1107, 2016.

[92] E. Eason. A review of least-squares methods for solving partial differential equations. *International Journal for Numerical Methods in Engineering*, 10:1021–1046, 1976.

[93] A. Eringen. *Mechanics of continua*. John Wiley & Sons, 1967.

[94] A. Ern and J.-L. Guermond. Evaluation of the condition number in linear systems arising in finite element approximations. *ESAIM: Mathematical Modelling and Numerical Analysis*, 40(1):29–48, 2006.

[95] V. J. Ervin. Computational bases for RT_k and BDM_k on triangles. *Computational Mechanics Advances*, 64(8):2765–2774, 2012.

[96] A. Eterovic and K.-J. Bathe. A hyperelastic-based large strain elasto-plastic constitutive formulation with combined isotropic-kinematic hardening using the logarithmic stress and strain measures. *International Journal for Numerical Methods in Engineering*, 30(6):1099–1115, 1990.

[97] V. Faber, T. Manteuffel, and S. Parter. On the theory of equivalent operators and application to the numerical solution of uniformly elliptic partial differential equations. *Advances in Applied Mechanics*, 11:109–163, 1990.

[98] C. Felippa. On the original publication of the general canonical functional of linear elasticity. *Journal of Applied Mechanics*, 67:217–219, 2000.

[99] G. Fix, M. Gunzburger, and R. Nicolaides. On finite element methods of the least squares type. *Computers and Mathematics with Applications*, 5:87–98, 1979.

[100] B. M. Fraeijs de Veubeke. Diffusion des inconnues hyperstatiques dans les voilures á longeron couplès. *Bull. Serv. Technique de L'Aéronautique, Imprimeríe Marcel Hayez, Bruxelles*, No. 24:56, 1951.

[101] B. M. Fraeijs De Veubeke. *Displacement and equilibrium models in the finite element method*, volume 9, pages 145–197. Wiley, New York, 1965.

[102] B. Galerkin. Series solution of some problems in elastic equilibrium of rods and plates. *Vestn. Inzh. Tech.*, 19:897–908, 1915.

[103] S. Glaser and F. Armero. On the formulation of enhanced strain finite elements in finite deformations. *Engineering Computations*, 14:759–791, 1997.

[104] J. Gopalakrishnan and J. Guzmán. Symmetric nonconforming mixed finite elements for linear elasticity. *SIAM Journal on Numerical Analysis*, 49(4):1504–1520, 2011.

[105] W. Han and B. Reddy. *Plasticity: Mathematical Theory and Numerical Analysis*. Springer Verlag New York, 1999.

[106] B. Hayburst, M. Keller, C. Cai, X. Sun, and C. R. Westphal. Adaptively weighted least-squares finite element methods for partial differential equations with singularities. *Communications in Applied Mathematics and Computational Science*, 13(1): 1–25, 2018.

[107] E. Hellinger. Die allgemeinen Ansätze der Mechanik der Kontinua. In F. Klein and C. Müller, editors, *Encyklopädie der mathematischen Wissenschaften mit Einschluss ihrer Anwendungen*, volume 4, pages 601–694. Vieweg+Teubner Verlag, Wiesbade, 1914.

[108] J.-P. Hennart, J. Jaffré, and J. E. Roberts. A constructive method for deriving finite elements of nodal type. *Numerische Mathematik*, 53:701–738, 1988.

[109] J. Heys, T. Manteuffel, S. McCormick, and J. Ruge. First-order system least-squares (FOSLS) for coupled fluid-elastic problems. *Journal of Computational Physics*, 195: 560–575, 2004.

[110] J. Heys, E. Lee, T. Manteuffel, and S. McCormick. On mass-conserving least-squares methods. *SIAM Journal of Scientific Computing*, 28(3):1675–1693, 2006.

[111] J. Heys, E. Lee, T. Manteuffel, and S. McCormick. An alternative least-squares formulation of the Navier-Stokes equations with improved mass conservation. *Journal of Chemical Physics*, 226:994–1006, 2008.

[112] J. Heys, E. Lee, T. Manteuffel, S. McCormick, and J. Ruge. Enhanced mass conservation in least-squares methods for Navier-Stokes equations. *SIAM Journal on Scientific Computing*, 31:2303–2321, 2009.

[113] R. Hill. *The mathematical theory of plasticity*. Oxford at the Clarendon Press, 1950.

[114] R. Hill. Generalized constitutive relations for incremental deformation of metal crystals by multislip. *Journal of the Mechanics and Physics of Solids*, 14(2):95–102, 1966.

[115] R. Hiptmair and J. Xu. Nodal auxiliary space preconditioning in $H(\mathrm{curl})$ and $H(\mathrm{div})$ spaces. *SIAM Journal on Numerical Analysis*, 45:2483–2509, 2007.

[116] G. A. Holzapfel. *Nonlinear solid mechanics, a continuum approach for engineering*. Wiley, 2000.

[117] H.-C. Hu. On some variational methods on the theory of elasticity and the theory of plasticity. *Scientia Sinica*, Vol. 4:33–54, 1955.

[118] M. Igelbüscher and J. Schröder. Hybrid mixed finite element formulations based on a least-squares approach. In J. Schröder and P. Wriggers, editors, *Reliable Simulation Techniques in Solid Mechanics*. Springer, 2021. (submitted).

[119] M. Igelbüscher, A. Schwarz, K. Steeger, and J. Schröder. Modified mixed least-squares finite element formulations for small and finite strain plasticity. *International Journal for Numerical Methods in Engineering*, 117:141–160, 2018.

[120] M. Igelbüscher, J. Schröder, and A. Schwarz. A mixed least-squares finite element formulation with explicit consideration of the balance of moment of momentum, a numerical study. *GAMM Mitteilungen*, 43(2):e202000009 (17 pages), 2020. doi: 10.1002/gamm.202000009.

[121] M. Igelbüscher, J. Schröder, A. Schwarz, and G. Starke. Least-squares finite element formulation for finite strain elasto-plasticity. In J. Schröder and P. Wriggers, editors, *Reliable Simulation Techniques in Solid Mechanics*. Springer, 2021. (submitted).

[122] S. Jeong and E. Lee. Weighted norm least squares finite element method for poisson equation in a polyhedral domain. *Journal of Computational and Applied Mathematics*, 299:35–49, 2016.

[123] D. Jespersen. A least-squares decomposition method for solving elliptic equations. *Mathematics of Computation*, 31:873–880, 1977.

[124] B.-N. Jiang. Non-oscillatory and non-diffusive solution of convection problems by the iteratively reweighted least-squares finite element method. *Journal of Computational Physics*, 105:108–121, 1993.

[125] B.-N. Jiang. *The Least-Squares Finite Element Method*. Springer-Verlag, Berlin, 1998.

[126] B.-N. Jiang and C. Chang. Least-squares finite elements for the Stokes problem. *Computer Methods in Applied Mechanics and Engineering*, 78:297–311, 1990.

[127] C. Johnson and B. Mercier. Some equilibrium finite element methods for two-dimensional elasticity problems. *Numerische Mathematik*, 30:85–99, 1978.

[128] O. Kayser-Herold. *Least-squares methods for the solution of fluid-structure interaction problems*. Phd thesis, Technische Universität Braunschweig, 2006.

[129] O. Kayser-Herold and H. Matthies. Least-squares FEM, literature review. *Informatik-Bericht 2005-05, TU Braunschweig, Institut für Wissenschaftliches Rechnen*, 2005.

[130] S. Kim, T. Manteuffel, and S. McCormick. First-order system least squares (FOSLS) for spatial linear elasticity: Pure traction. *SIAM Journal on Numerical Analysis*, 38:1454–1482, 2000.

[131] R. Kirby, A. Logg, M. Rognes, and A. Terrel. Common and unusual finite elements. In *Automated Solution of Differential Equations by the Finite Element Method, Lecture Notes in Computational Science and Engineering*, pages 95–119. Springer, Berlin, Heidelberg, 2012.

[132] O. Klaas, J. Schröder, E. Stein, and C. Miehe. A regularized dual mixed element for plane elasticity implementation and performance of the BDM element. *Computer Methods in Applied Mechanics and Engineering*, 121:201–209, 1995.

[133] S. Klinkel. Theorie und Numerik eines Volumen-Schalen-Elementes bei finiten elastischen und plastischen Verzerrungen. *PhD thesis, Institut für Baustatik, Universität Karlsruhe*, 2000.

[134] S. Klinkel and S. Govindjee. Using finite strain 3d-material models in beam and shell elements. *Engineering Computations*, 19(3):254–271, 2002.

[135] B. Kober and G. Starke. Strong vs. weak symmetry in stress-based mixed finite element methods for linear elasticity. In *Numerical Mathematics and Advanced Applications ENUMATH 2017*, pages 323–333. Springer International Publishing, 2019.

[136] J. Korelc. Automatic generation of finite-element code by simultaneous optimization of expressions. *Theoretical Computer Science*, 187(1):231–248, 1997.

[137] J. Korelc. Multi-language and multi-environment generation of nonlinear finite element codes. *Engineering with Computers*, 18:312–327, 2002.

[138] J. Korelc and P. Wriggers. *Automation of Finite Element Methods*. Springer International Publishing Switzerland, 2016.

[139] J. Korelc, U. Šolinc, and P. Wriggers. An improved eas brick element for finite deformation. *Computational Mechanics*, 46:641–659, 2010.

[140] M. Köster, A. Ouazzi, F. Schieweck, S. Turek, and P. Zajac. New robust nonconforming finite elements of higher order. *Applied Numerical Mathematics*, 62: 166–184, 2012.

[141] E. Kröner. Allgemeine Kontinuumstheorie der Versetzung und Eigenspannung. *Archive of Rational Mechanics and Analysis*, 4:273–334, 1960.

[142] J. Kubitz. *Gemischte Least-Squares-FEM für Elastoplastizität*. Phd thesis, Leibniz Universität Hannover, 2007.

[143] K. Kwon, S. Park, and S. Youn. The least-squares meshfree method for elastoplasticity and its application to metal forming analysis. *International Journal for Numerical Methods in Engineering*, 64:751–788, 2005.

[144] O. Ladyzhenskaya. *The mathematical theory of viscous incompressible flow*, volume 76. Gordon and Breach New York, 1969.

[145] E. Lee and D. Liu. Finite strain elastic-plastic theory particularly for plane wave analysis. *Journal of Applied Physics*, 38:1–6, 1967.

[146] E. Lee, T. Manteuffel, and C. Westphal. Weighted-norm first-order system least squares (FOSLS) for problems with corner singularities. *SIAM Journal on Numerical Analysis*, 44:1974–1996, 2006.

[147] E. Lee, T. Manteuffel, and C. Westphal. Weighted-norm first-order system least squares (FOSLS) for div/curl systems with three dimensional edge singularities. *SIAM Journal on Numerical Analysis*, 46(3):1619–1639, 2008.

[148] E. H. Lee. Elastic-plastic deformation at finite strain. *Journal of Applied Mechanics*, 36:1–6, 1969.

[149] H. Lee and T.-F. Chen. A nonlinear weighted least-squares finite element method for stokes equations. *Computers and Mathematics with Applications*, 59:215–224, 2010.

[150] J. K. Lee. *Convergence of mixed-hybrid finite element methods.* Ph. d. thesis, University of Texas at Austin, 1976.

[151] B. Li, X. Xie, and S. Zhang. New convergence analysis for assumed stress hybrid quadrilateral finite element method. *Discrete and Continuous Dynamical Systems Series B*, 22(7):2831–2856, 2017.

[152] K. Liu, T. A. Manteuffel, S. F. McCormick, J. W. Ruge, and L. Tang. Hybrid first-order system least squares (hybrid-FOSLS) finite element methods with application to Stokes equations. *SIAM Journal on Numerical Analysis*, 51:2214–2237, 2013.

[153] M. Lonsing and R. Verfürth. On the stability of BDMS and PEERS elements. *Numerische Mathematik*, 99:131–140, 2004.

[154] J. Lubliner. *Plasticity Theory.* Macmillan Publishing Company, New York, 1990.

[155] P. Lynn and S. Arya. Use of the least squares criterion in the finite element formulation. *International Journal for Numerical Methods in Engineering*, 6:75–88, 1973.

[156] P. Lynn and S. Arya. Finite elements formulated by the weighted discrete least squares method. *International Journal for Numerical Methods in Engineering*, 8: 71–90, 1974.

[157] T. Manteuffel, S. McCormick, and G. Starke. First-order system least-squares for second-order elliptic problems with discontinuous coefficients. *Proceedings of the 7th Copper Mountain Conference on Multigrid Methods, NASA*, pages 535–550, 1996.

[158] T. Manteuffel, S. McCormick, J. Schmidt, and C. Westphal. First-order system least squares (FOSLS) for geometrically nonlinear elasticity. *SIAM Journal on Numerical Analysis*, 44:2057–2081, 2006.

[159] J. Marsden and J. Hughes. *Mathematical Foundations of Elasticity.* Prentice-Hall, 1983.

[160] G. Matthies. Inf-sup stable nonconforming finite elements of higher order on quarilaterals and hexahedra. *Mathematical Modelling and Numerical Analysis*, 41:885–874, 2007.

[161] G. Maugin. *The Thermomechanics of Plasticity and Fracture.* Cambridge University Press, 1992.

[162] C. Miehe. *Kanonische Modelle Multiplikativer Elasto-Plastizität - Thermodynamische Formulierung und Numerische Implementation.* Forschungs- und Seminarberichte aus dem Bereich der Mechanik der Universität Hannover, 1992.

[163] C. Miehe and E. Stein. A canonical model of multiplicative elasto-plasticity formulation and aspects of the numerical implementation. *European Journal of Mechanics, A/Solids*, 11:25–43, 1992.

[164] M. Mooney. A theory of large elastic deformation. *Journal of Applied Physics*, 11: 582–592, 1940.

[165] B. Müller. *Mixed least squares finite element methods based on inverse stress-strain relations in hyperelasticity*. Phd thesis, Universität Duisburg-Essen, 2015.

[166] B. Müller and G. Starke. Stress-based finite element methods in linear and nonlinear solid mechanics. In J. Schröder and P. Wriggers, editors, *Advanced Finite Element Technologies*, CISM Courses and Lectures. Springer, 2016.

[167] B. Müller, G. Starke, A. Schwarz, and J. Schröder. A first-order system least squares method for hyperelasticity. *SIAM Journal on Scientific Computing*, 36:795–816, 2014.

[168] S. Münzenmaier. First-order system least squares for generalized-Newtonian coupled Stokes-Darcy flow. *Numerical Methods for Partial Differential Equations*, 31(4): 1150–1173, 2015.

[169] S. Münzenmaier and G. Starke. First-order system least squares for coupled Stokes-Darcy flow. *SIAM Journal on Numerical Analysis*, 49:387–404, 2011.

[170] J.-C. Nédélec. Mixed finite elements in $\mathbb{R}^3$. *Numerische Mathematik*, 35:315–341, 1980.

[171] J.-C. Nédélec. New mixed finite elements in $\mathbb{R}^3$. *Numerische Mathematik*, 50:57–81, 1986.

[172] J. J. Nelson and C. L. Chang. A mass conservative least-squares finite element method for the Stokes problem. *Communications in Numerical Methods in Engineering*, 11:965–970, 1995.

[173] W. Noll. *The foundations of mechanics and thermodynamics*. Springer, 1974.

[174] R. Ogden. *Non-linear elastic deformations*. Dover Publications, 1998.

[175] R. W. Ogden. Large deformation isotropic elasticity: on the correlation of theory and experiment for compressible rubber-like solids. *Proceedings of the Royal Society of London*, 326(1567):565–584, 1972.

[176] T. H. H. Pian. Derivation of element stiffness matrices by assumed stress distribution. *AIAA Journal*, 20:1333–1336, 1964.

[177] T. H. H. Pian and D.-P. Chen. Alternative ways for formulation of hybrid stress elements. *International Journal for Numerical Methods in Engineering*, 18:1679–1684, 1982.

[178] T. H. H. Pian and K. Sumihara. A rational approach for assumed stress finite elements. *International Journal for Numerical Methods in Engineering*, 20:1685–1695, 1984.

[179] T. H. H. Pian and P. Tong. Relastions between incompatible displacement model and hybrid stress model. *International Journal for Numerical Methods in Engineering*, 22:173–181, 1986.

[180] R. Piltner. An alternative version of the Pian-Sumihara element with a simple extension to non-linear problems. *Computational Mechanics*, 26:483–489, 2000.

[181] J. Pontaza and J. Reddy. Spectral/hp least-squares finite element formulation for the Navier-Stokes equations. *Journal of Computational Physics*, 190:523–549, 2003.

[182] J. P. Pontaza. *Least-squares variational principles and the finite element method: theory, form, and model for solid and fluid mechanics*. PhD thesis, Texas A&M University, 2003.

[183] G. Prange. *Das Extremum der Formänderungsarbeit*. Habilitationsschrift, Technische Hochschule Hannover, 1916.

[184] M. Proot and M. Gerritsma. Mass- and momentum conservation of the least-squares spectral element method for the stokes problem. *Journal of Scientific Computing*, Vol. 27:389–401, 2006.

[185] E. F. Punch and S. N. Atluri. Development and testing of stable, invariant, isoparametric curvilinear 2- and 3-d hybrid-stress elements. *Computer Methods in Applied Mechanics and Engineering*, 47:331–356, 1984.

[186] A. Quarteroni and A. Valli. *Numerical Approximation of Partial Differential Equations*. Springer-Verlag Berlin Heidelberg, 1994.

[187] R. Rannacher and S. Turek. Simple nonconforming quadrilateral Stokes element. *Numerical Methods for Partial Differential Equations*, 8:97–111, 1992.

[188] P. A. Raviart and J. M. Thomas. Primal hybrid finite element methods for 2nd order elliptic equations. *Report 75025, Université de Paris VI, Laboratoire Analyse Numérique*, 1976.

[189] P. A. Raviart and J. M. Thomas. A mixed finite element method for 2-nd order elliptic problems. Mathematical aspects of finite element methods. *Lecture Notes in Mathematics, Springer-Verlag New York*, pages 292–315, 1977.

[190] E. Reissner. On a variational theorem in elastictiy. *Journal of Mathematical Physics*, Vol. 29:90–95, 1950.

[191] R. S. Rivlin. Large elastic deformations of isotropic materials II. Some uniqueness theorems for pure homogeneous deformation. *Philosophical Transactions of the Royal Society of London*, 240:491–508, 1948.

[192] J. E. Roberts and J.-M. Thomas. Mixed and hybrid methods. In P. G. Ciarlet and J. L. Lions, editors, *Handbook of Numerical Analysis*, volume II, pages 523–639. Elsevier Science, 1991.

[193] M. E. Rognes, R. C. Kirby, and A. Logg. Efficient assembly of $H(\mathrm{div})$ and $H(\mathrm{curl})$ conforming finite elements. *SIAM Journal on Scientific Computing*, 31(6):4130–4151, 2009.

[194] A. Rössle. Corner singularities and regularity of weak solutions for the two-dimensional Lamé equations on domains with angular corners. *Journal of Elasticity*, 60:57–75, 2000.

[195] E. Salonen and J. Freund. Weighting in the least squares finite element method. In H. Mang, F. Rammerstorfer, and J. Eberhardsteiner, editors, *Proceedings of the Fifth World Congress on Computational Mechanics*. Vienna University of Technology, Austria, 2002.

[196] M. Sauter and C. Wieners. On the superlinear convergence in computational elasto-plasticity. *Computer Methods in Applied Mechanics and Engineering*, 200(49-52): 3646–3658, 2011.

[197] J. Schröder and M. Igelbüscher. Challenges for the least-squares finite element method in solid mechanics. In F. Aldakheel, B. Hudobivnik, M. Soleimani, H. Wessels, C. Weissenfels, and M. Marino, editors, *Current Trends and Open Problems in Computational Mechanics*. Springer, 2021. (submitted).

[198] J. Schröder, O. Klaas, E. Stein, and C. Miehe. A physically nonlinear dual mixed finite element formulation. *Computer Methods in Applied Mechanics and Engineering*, 144:77–92, 1997.

[199] J. Schröder, A. Schwarz, and K. Steeger. Least-squares finite element formulations for isotropic and anisotropic elasticity at small and large strains. In J. Schröder and P. Wriggers, editors, *Advanced Finite Element Technologies*, CISM Courses and Lectures, pages 131–175. Springer, 2016.

[200] J. Schröder, M. Igelbüscher, A. Schwarz, and G. Starke. A Prange-Hellinger-Reissner type finite element formulation for small strain elasto-plasticity. *Computer Methods in Applied Mechanics and Engineering*, 317:400–418, 2017.

[201] J. Schröder, N. Viebahn, P. Wriggers, F. Auricchio, and K. Steeger. On the stability analysis of hyperelastic boundary value problems using three- and two-field mixed finite element formulations. *Computational Mechanics*, 60(3):479–492, 2017.

[202] J. Schröder, T. Wick, S. Reese, P. Wriggers, R. Müller, S. Kollmannsberger, M. Kästner, A. Schwarz, M. Igelbüscher, N. Viebahn, H. R. Bayat, S. Wulfinghoff, K. Mang, E. Rank, T. Bog, D. DAngella, M. Elhaddad, P. Hennig, A. Düster, W. Garhuom, S. Hubrich, M. Walloth, W. Wollner, C. Kuhn, and T. Heister. A selection of benchmark problems in solid mechanics and applied mathematics. *Archives of Computational Methods in Engineering*, https://doi.org/10.1007/s11831-020-09477-3, 2020.

[203] A. Schwarz. *Least-Squares Mixed Finite Elements for Solid Mechanics*. Phd thesis, University Duisburg-Essen, 2009.

[204] A. Schwarz, J. Schröder, and G. Starke. Least-squares mixed finite elements for small strain elasto-viscoplasticity. *International Journal for Numerical Methods in Engineering*, 77:1351–1370, 2009.

[205] A. Schwarz, J. Schröder, and G. Starke. A modified least-squares mixed finite element with improved momentum balance. *International Journal for Numerical Methods in Engineering*, 81:286–306, 2010.

[206] A. Schwarz, J. Schröder, G. Starke, and K. Steeger. Least-squares mixed finite elements for hyperelastic material models. In *Report of the Workshop 1207 at the "Mathematisches Forschungsinstitut Oberwolfach" entitled "Advanced Computational Engineering", organized by O. Allix, C. Carstensen, J. Schröder, P. Wriggers*, pages 14–16, 2012.

[207] A. Schwarz, K. Steeger, and J. Schröder. Weighted overconstrained least-squares mixed finite elements for static and dynamic problems in quasi-incompressible elasticity. *Computational Mechanics*, 54(1):603–612, 2014.

[208] A. Schwarz, K. Steeger, M. Igelbüscher, and J. Schröder. Different approaches for mixed LSFEMs in hyperelasticity: Application of logarithmic deformation measures. *International Journal for Numerical Methods in Engineering*, 2018, doi.org/10.1002/nme.5838.

[209] P. Silvester. Higher order polynomial triangular finite elements for potential problems. *International Journal of Engineering Science*, 7:849–861, 1969.

[210] J. C. Simo. A framework for finite strain elastoplasticity based on maximum plastic dissipation and the multiplicative decomposition: Part I. Continuum formulation. *Computer Methods in Applied Mechanics and Engineering*, 66:199–219, 1988.

[211] J. C. Simo. A framework for finite strain elastoplasticity based on maximum plastic dissipation and the multiplicative decomposition. Part II: Computational aspects. *Computer Methods in Applied Mechanics and Engineering*, 68:1–31, 1988.

[212] J. C. Simo. Algorithms for static and dynamic multiplicative plasticity that preserve the classical return mapping schemes of the infinitesimal theory. *Computer Methods in Applied Mechanics and Engineering*, 99:61–112, 1992.

[213] J. C. Simo. Numerical analysis and simulation of plasticity. In P. Ciarlet and J. Lions, editors, *Handbook of Numerical Analysis*, volume VI, pages 183–499. North-Holland, 1998.

[214] J. C. Simo and T. J. R. Hughes. *Computational Inelasticity*. Springer-Verlag., 1998.

[215] J. C. Simo and C. Miehe. Associative coupled thermoplasticity at finite strains: Formulation, numerical analysis and implementation. *Computer Methods in Applied Mechanics and Engineering*, 96:133–171, 1992.

[216] J. C. Simo and M. S. Rifai. A class of mixed assumed strain methods and the method of incompatible modes. *International Journal for Numerical Methods in Engineering*, 29:1595–1638, 1990.

[217] J. C. Simo and R. L. Taylor. A return mapping algorithm for plane stress elastoplasticity. *International Journal for Numerical Methods in Engineering*, 22:649–670, 1986.

[218] J. C. Simo, J. G. Kennedy, and R. L. Taylor. Complementary mixed finite element formulations for elastoplasticity. *Computer Methods in Applied Mechanics and Engineering*, 74:177–206, 1989.

[219] G. Starke. An adaptive least-squares mixed finite element method for elasto-plasticity. *SIAM Journal on Numerical Analysis*, 45:371–388, 2007.

[220] G. Starke. Adaptive least squares finite element methods in elasto-plasticity. In *LSSC 2009*, volume 5910 of *Lecture Notes in Computer Science*, pages 671–678, Heidelberg, 2010. Springer.

[221] G. Starke, A. Schwarz, and J. Schröder. Analysis of a modified first-order system least squares method for linear elasticity with improved momentum balance. *SIAM Journal on Numerical Analysis*, 49(3):1006–1022, 2011.

[222] G. Starke, B. Müller, A. Schwarz, and J. Schröder. Stress-displacement least squares mixed finite element approximation for hyperelastic materials. In *Report of the Workshop 1207 at the "Mathematisches Forschungsinstitut Oberwolfach" entitled "Advanced Computational Engineering", organized by O. Allix, C. Carstensen, J. Schröder, P. Wriggers*, pages 11–13, 2012.

[223] K. Steeger. *Least-squares mixed finite elements for geometrically nonlinear solid mechanics*. Phd thesis, University Duisburg-Essen, 2017.

[224] R. Stenberg. A family of mixed finite elements for the elastic problem. *Numerische Mathematik*, 53:513–538, 1988.

[225] H. Stolarski and T. Belytschko. Limitation principles for mixed finite elements based on the Hu-Washizu variational formulation. *Computer Methods in Applied Mechanics and Engineering*, 60:195–216, 1987.

[226] L. Tang and T. Tsang. A least-squares finite element method for time dependent incompressible flows with thermal convection. *International Journal for Numerical Methods in Fluids*, 17:271–289, 1993.

[227] R. Taylor. Feap - finite element analysis program. *University of California, Berkeley*, 2008. URL `http://www.ce.berkeley/feap`.

[228] R. L. Taylor. On completeness of shape functions for finite element analysis. *International Journal for Numerical Methods in Engineering*, 4:17–22, 1972.

[229] C. Truesdell and W. Noll. *The Non-Linear Field Theories of Mechanics, Handbuch der Physik*. Springer-Verlag, Berlin, Heidelberg, New York, 3 edition, 1965.

[230] C. Truesdell and R. Toupin. The classical field theories. In S. Flügge, editor, *Encyclopedia of Physics*, III/1. Springer, 1960.

[231] K. Washizu. On the variational principles of elasticity and plasticity. *Aeroelastic and Structure Research Laboratory, Technical Report 25-18, MIT, Cambridge*, 1955.

[232] G. Weber and L. Anand. Finite deformation constitutive equations and a time integration procedure for isotropic, hyperelastic-viscoelastic solids. *Computer Methods in Applied Mechanics and Engineering*, 79:173–202, 1990.

[233] M. Wilkins. Calculation of elastic-plastic flow. In B. Adler, S. Fernback, and M. Rotenberg, editors, *Methods of Computational Physics*, volume 3, pages 211–272. Academic Press, New York, 1964.

[234] D. Winterscheidt and K. Surana. p-version least squares finite element formulation for two dimensional, incompressible fluid flow. *International Journal for Numerical Methods in Fluids*, 18:43–69, 1994.

[235] I. Wolfram Research. *Mathematica*. Wolfram Research, Inc., version 10.1 edition, 2015. Champaign, Illinois.

[236] P. Wriggers. *Nonlinear finite element methods*. Springer, 2008.

[237] P. Wriggers. Mixed finite element methods - Theory and discretization. In C. Carstensen and P. Wriggers, editors, *Mixed Finite Element Technologies*, volume 509 of *CISM International Centre for Mechanical Sciences*, pages 131–177. Springer, Vienna, 2009.

[238] P. Wriggers and J. Korelc. On enhanced strain methods for small and finite deformations of solids. *Computational Mechanics*, 18:413–428, 1996.

[239] L. A. Xue, W.-M. Karlovitz and S. N. Atluri. On the existence and stability conditions for mixed-hybrid finite element solutions based on reissner's variational principle. *International Journal of Solids and Structures*, 21:97–116, 1985.

[240] W.-M. Xue and S. N. Atluri. Existence and stability, and discrete BB and rank conditions, for general mixed-hybrid finite elements in elasticity. In *Hybrid and Mixed Finite Element Methods, ASEM, AMD*, volume 73, pages 91–112, 1985.

[241] X. Ye and S. Zhang. A discontinuous least-squares finite-element method for second-order elliptic equations. *International Journal of Computer Mathematics*, 96:601–617, 2018.

[242] S. T. Yeo and B. C. Lee. Equivalence between enhanced assumed strain method and assumed stress hybrid method based on the Hellinger-Reissner principle. *International Journal for Numerical Methods in Engineering*, 39:3083–3099, 1996.

[243] G. Yu, X. Xie, and C. Carstensen. Uniform convergence and a posteriori error estimation for assumed stress hybrid finite element methods. *Computer Methods in Applied Mechanics and Engineering*, 200:2421–2433, 2011.

[244] O. C. Zienkiewicz. Displacement and equilibrium models in the finite element method by B. Fraeijs de Veubeke, Chapter 9, Pages 145–197 of Stress Analysis, Edited by O. C. Zienkiewicz and G. S. Holister, Published by John Wiley & Sons, 1965. *International Journal for Numerical Methods in Engineering*, 52(3):287–342, 2001. doi: https://doi.org/10.1002/nme.339.

[245] O. C. Zienkiewicz and Y. K. Cheung. *Finite element method in structural and continuum mechanics*. McGraw Hill, 1967.

[246] O. C. Zienkiewicz and R. L. Taylor. *The finite element method - Volume I: The basis*. Butterworth Heinemann, 5th edition, 2000.

[247] O. C. Zienkiewicz and R. L. Taylor. *The finite element method - for solid and structural mechanics*. Elsevier, 6th edition, 2005.

[248] O. C. Zienkiewicz, D. R. J. Owen, and K. N. Lee. Least-squares finite element for elasto-static problems. Use of 'reduced' integration. *Int. J. Numer. Meth. Engng.*, 8:341–358, 1974.

[249] O. C. Zienkiewicz, S. Qu, R. L. Taylor, and S. Nakazawa. The patch test for mixed formulations. *International Journal for Numerical Methods in Engineering*, 23:1873–1883, 1986.

[250] O. C. Zienkiewicz, R. L. Taylor, and J. Z. Zhu. *The finite element method: its basis and fundamentals*. Elsevier, 2005.

Der Lebenslauf ist in der Online-Version aus Gründen des Datenschutzes nicht enthalten.

In Schriftenreihe des Instiuts für Mechanik bisher erschienene Berichte

Nr. 1 (2004) *Ein Modell zur Beschreibung finiter anisotroper elasto-plastischer Deformationen unter Berücksichtigung diskreter Rissausbreitung*, J. Löblein, Dissertation, 2004.

Nr. 2 (2006) *Polyconvex Anisotropic Energies and Modeling of Damage applied to Arterial Walls*, D. Balzani, Dissertation, 2006.

Nr. 3 (2006) *Kontinuumsmechanische Modellierung ferroelektrischer Materialien im Rahmen der Invariatentheorie*, H. Romanowski, Dissertation, 2006.

Nr. 4 (2007) *Mehrskalen-Modellierung polykristalliner Ferroelektrika basierend auf diskreten Orientierungsverteilungsfunktionen*, I. Kurzhöfer, Dissertation, 2007.

Nr. 5 (2007) *Proceedings of the First Seminar on the Mechanics of Multifunctional Materials*, J. Schröder, D.C. Lupascu, D. Balzani (Ed.), Tagungsband, 2007.

Nr. 6 (2008) *Zur Modellierung und Simulation diskreter Rissausbreitungsvorgänge*, O. Hilgert, Dissertation, 2008.

Nr. 7 (2009) *Least-Squares Mixed Finite Elements for Solid Mechanics*, A. Schwarz, Dissertation, 2009.

Nr. 8 (2010) *Design of Polyconvex Energy Functions for All Anisotropy Classes*, V. Ebbing, Dissertation, 2010.

Nr. 9 (2012) *Modeling of Electro-Mechanically Coupled Materials on Multiple Scales*, M.-A. Keip, Dissertation, 2012.

Nr. 10 (2012) *Geometrical Modeling and Numerical Simulation of Heterogeneous Materials*, D. Brands, Dissertation, 2012.

Nr. 11 (2012) *Modeling and simulation of arterial walls with focus on damage and residual stresses*, S. Brinkhues, Dissertation, 2012.

Nr. 12 (2014) *Proceedings of the Second Seminar on the Mechanics of Multifunctional Materials*, J. Schröder, D.C. Lupascu, M.-A. Keip, D. Brands (Ed.), Tagungsband, 2014.

Nr. 13 (2016) *Mixed least squares finite element methods based on inverse stress-strain relations in hyperelasticity*, B. Müller, Dissertation, 2016.

Nr. 14 (2016) *Electromechanical Modeling and Simulation of Thin Cardiac Tissue Constructs*, R. Frotscher, Dissertation, 2016.

Nr. 15 (2017) *Least-squares mixed finite elements for geometrically nonlinear solid mechanics*, K. Steeger, Dissertation, 2017.

Nr. 16 (2017) *Scale-Bridging of Elasto-Plastic Microstructures using Statistically Similar Representative Volume Elements*, L. Scheunemann, Dissertation, 2017.

Nr. 17 (2018) *Modeling of Self-healing Polymers and Polymeric Composite Systems*, S. Specht, Dissertation, 2017.

Nr. 18 (2018) *Proceedings of the Third Seminar on the Mechanics of Multifunctional Materials*, J. Schröder, D.C. Lupascu, H. Wende, D. Brands (Ed.), Tagungsband, 2018.

Nr. 19 (2018) *Least-squares finite element methods with applications in fluid and solid mechanics*, C. Nisters, Dissertation, 2018.

Nr. 20 (2018) *A two-scale homogenization scheme for the prediction of magneto-electric product properties*, M. Labusch, Dissertation, 2018.

Nr. 21 (2019) *Modeling the passive mechanical response of soft tissues: constitutive modeling approaches, efficient parameter selection and subsequent adjustments due to residual stresses*, M. von Hoegen, Dissertation, 2019

Nr. 22 (2019) *Constitutive modeling of female pelvic floor dysfunctions and reconstructive surgeries using prosthetic mesh implants*, A. Bhattarai, Dissertation, 2019

Nr. 23 (2019) *A contribution to stress-displacement based mixed galerkin finite elements for hyperelasticity*, N. Viebahn, Dissertation, 2019

Nr. 24 (2020) *Gefrier- und Auftauprozesse in gesättigten porösen Materialien - ein Modellierungskonzept im Rahmen der Theorie poröser Medien*, W.M. Bloßfeld, Dissertation, 2020

Nr. 25 (2021) *Electromechanical modelling and simulation of hiPSC-derived cardiac cell cultures*, A. Jung, Dissertation, 2021